2D Materials

TOPICAL REVIEW

2D materials: advances in regenerative medicine and human health sensing

Jasmina Lazarević[1] and Bojana Višić[1,2,*]

[1] Center for Solid State Physics and New Materials, Institute of Physics Belgrade, University of Belgrade, Pregrevica 118, Belgrade 11080, Serbia
[2] Department of Condensed Matter Physics, Jozef Stefan Institute, Jamova cesta 39, Ljubljana 1000, Slovenia
* Author to whom any correspondence should be addressed.

E-mail: bojana.visic@ijs.si

Abstract

The potential of 2D materials goes beyond the use in electronic applications, extending to regenerative medicine and noninvasive sensing. They hold great promise in these fields due to their remarkable properties, such as high surface area, electrical conductivity and modular chemistry. However, they face significant challenges related to biocompatibility, long-term safety, reproducible large-scale production and lack of standardization and clinical protocols, among others. This review presents a comprehensive overview of their application in regenerative medicine and interactions with various biological systems. We comment on the influence of their innate, but tunable properties on biological response. The chemical composition and exfoliation state of these materials also play a critical role in their bioactivity. The high sensitivity of 2D materials to humidity holds a significant promise in sensor development, which is presented here in detail. Combining them with polymer matrices can enhance the flexibility and performance of the sensors, making them suitable for wearable devices and environmental monitoring. However, challenges remain in the search for the best sensing characteristics, which can be addressed through functionalization and combining with alternative materials like metal oxide nanowires. We critically examined the key challenges (biological interactions, exposure risks, environmental changes and scalability), while assessing their potential for sustainable technologies. Despite the advancements, thorough safety assessments are needed before large-scale production and clinical deployment of 2D materials for health sensing applications.

1. Introduction

The vast, diverse and complex field of 2D materials affects nearly every aspect of life, with applications extending far beyond electronics to energy storage, coatings, cosmetics, food industry and biomedicine. Their biological and environmental interactions are of particular significance, as both living organisms and entire ecosystems ultimately become end users, whether through intentional applications or unintended exposure. Factors such as size, shape and surface characteristics of nanomaterials significantly influence the extent of their stability. These transformations can alter their physicochemical properties, which may, in turn, affect their environmental interactions and potentially modify their toxicity.

There is a notable dominance of high-quality research papers on graphene and its derivatives, likely because they were the first and most extensively studied group of 2D materials. However, inorganic layered materials, particularly MoS_2, have attracted increasing research attention into their bioactivity. In chapter 2, we discuss the recent application advances in regenerative medicine, including cardiac, neural and bone tissue regeneration from the perspective of the materials, emphasizing their functional roles while integrating both physical

principles and biological relevance. We also comment on related topics such as drug delivery, organoid culture, angiogenesis, adipogenesis and phototherapy. Composite materials were mentioned only where necessary to emphasize the specific functionalities of 2D materials, such as improving mechanical strength, electrical conductivity or biological performance relevant to regenerative applications.

The field of noninvasive sensing has been increasingly popular due to a variety of possibilities for applications, such as e-skin [1], touchless interfaces, skin patches etc. For example, skin patches can be used to monitor different types of vital human health information. Tracking the levels of humidity of human skin in real-time can provide a variety of crucial information about the health status, such as wound healing, metabolic conditions and effectiveness of cosmetic products [2]. The search for a sensor with high sensitivity, wide detection range, quick response and short recovery time is moving into the area of novel 2D materials. One of the major challenges is to achieve high and even sensitivity for the full range of humidity. 2D materials hold a lot of potential, as their high surface-to-volume ratio allows for better sensitivity to humidity changes. In chapter 3, we review the recent progress in the fabrication of humidity sensors based on 2D materials. Their performance for monitoring human breath, touch, or humidity in agriculture is discussed in chapters 4 and 5. In chapter 6, we have critically addressed key challenges of application of 2D materials, including their interactions with biological systems, exposure risks, environmental transformations, and limitations in scalability and stability, while also evaluating their potential in sustainable technologies. Finally, the last chapter focuses on the future perspectives and mitigation strategies necessary to advance these fields further.

2. 2D materials in regenerative medicine

With the world population getting older, modern medicine aims to restore tissues and organs damaged by injuries, illnesses, aging or congenital abnormalities, with stem cells (SCs) playing a key role in regenerative therapies due to their ability to self-renew, differentiate into tissue specific cells, immunomodulation properties and secretion of paracrine factors [3, 4]. Their inherent plasticity enables precise response to external cues and adoption of specific lineages. From a clinical standpoint, while embryonic SCs (ESCs) and induced pluripotent SCs (iPSCs) offer the highest differentiation potential due to their pluripotency, their use presents significant challenges. ESCs raise ethical concerns related to their isolation, while both ESCs and iPSCs carry risks of uncontrolled differentiation, tissue overgrowth and teratoma formation. On the other hand, adult SCs, such as mesenchymal

SCs (MSCs), are multipotent and widely studied due to the ease of their isolation and absence of ethical concerns [5]. It is of utmost importance to ensure SCs survival during transplantation and *in vivo* for the success of regenerative medicine approaches. Beyond regenerative medicine, MSCs serve as valuable models in drug development, offering physiologically relevant alternatives to immortalized cell lines and minimizing dependence on animal testing [6]. Given their lifelong presence, ensuring MSCs survival and functionality is crucial for both regenerative and toxicological research [7].

Although at the forefront as a tool for treating currently incurable medical conditions, SCs still need a little encouragement, and this is where 2D materials come into play. Materials reviewed in this paper, as well as their role in the field of regenerative medicine, are summarized in table 1. They offer not only physical scaffolding for transplanted cells but also actively modulate the biological microenvironment to enhance cellular responses. By mimicking key features of the native extracellular matrix (ECM), such as surface topography, stiffness and biochemical cues, 2D materials can significantly improve SC adhesion, proliferation, and lineage-specific differentiation [8, 9]. Their high surface area and tunable surface chemistry facilitate the adsorption and presentation of growth and differentiation factors, making them powerful tools for directing SC fate. The interaction at the cell-material interface, being the initial point of contact, is crucial. Nanoscale surface features of 2D materials promote focal adhesion formation and cytoskeletal reorganization, both of which are essential for mechanotransduction pathways that drive differentiation. Therefore, the integration of 2D materials into regenerative platforms holds great promise for advancing SC-based therapies by providing structural support and biological guidance within the physiologically relevant environments.

2.1. 2D materials in cardiac regeneration and angiogenesis

Regenerative strategies offer the most promising long-term solutions for cardiovascular diseases, which are the leading cause of death globally, according to the World Health Organization. They are utilizing biomaterial-based scaffolds, SCs and growth factors to repair damaged cardiac tissue, although surgical and pharmacological treatments are still the first line methods. The effectiveness of 2D materials in this context depends on their physicochemical properties, such as high electrical conductivity and surface to volume ratio, mechanical strength and flexibility; biocompatibility and immunomodulatory capabilities [8, 9].
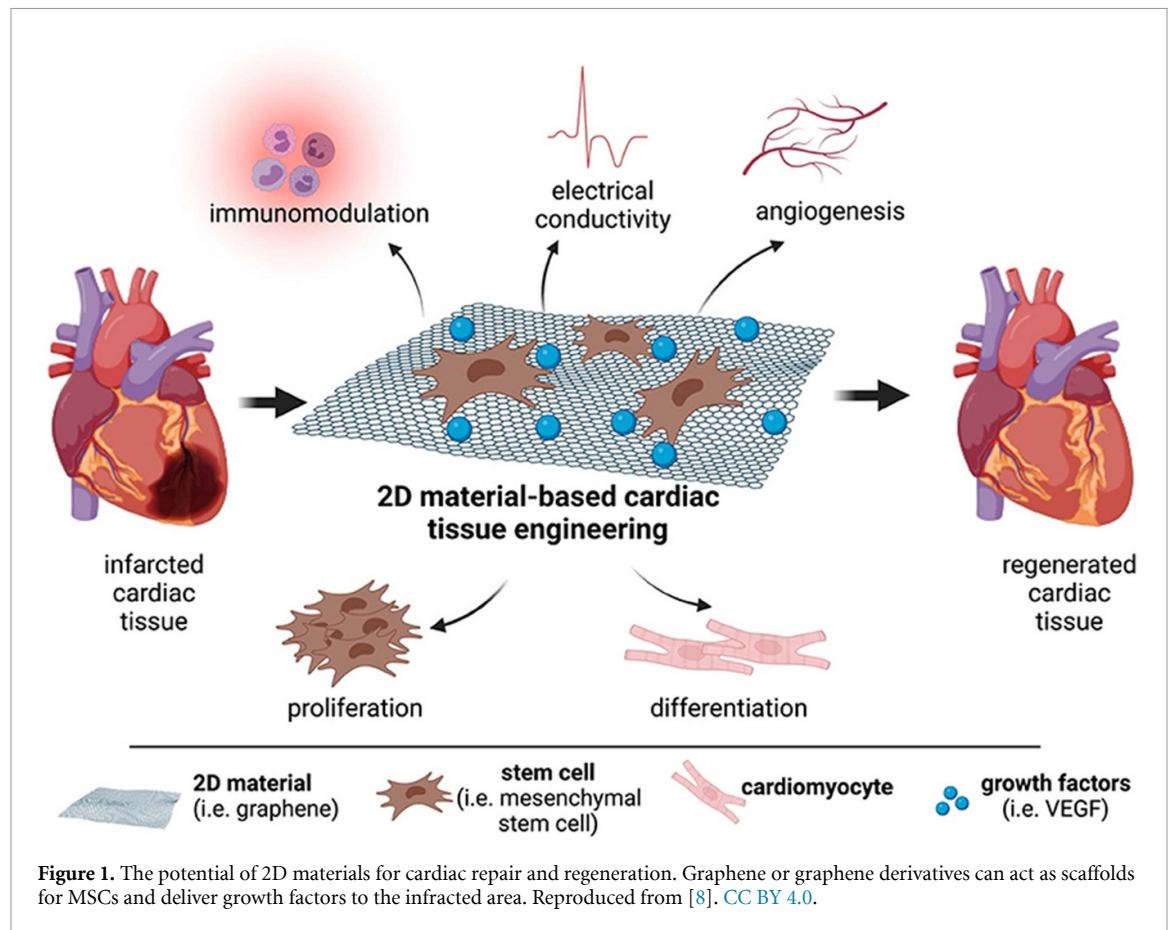
According to the literature, graphene and its derivatives, such as graphene oxide (GO) and reduced GO (rGO), are among the most extensively studied

Table 1. The summary of 2D materials discussed in this paper, their key features and the application in regenerative medicine.

2D material	Key characteristics	Role in regenerative medicine
Graphene oxide (GO)	High surface area; oxygenated functional groups; tunable electrical conductivity	Promotes osteogenesis, enhances angiogenesis, supports stem cell proliferation and differentiation in bone tissue scaffolds, neural tissue regeneration
Reduced graphene oxide (rGO)	Conductive; lower oxygen content; excellent mechanical reinforcement	Enhances osteoblast differentiation, mineralization; supports bone formation *in vivo*, scaffold for neural tissue regeneration
MXenes (e.g. $Ti_3C_2T_x$)	Metallic conductivity; hydrophilic; antioxidant (ROS scavenging); electrically conductive	Creates conductive hydrogel scaffolds for cardiac repair, supports tissue adhesion and cardiomyocyte function
Transition metal dichalcogenides (e.g. MoS_2, WS_2)	Semiconducting; photothermal properties; good biocompatibility	Promotes MSC adhesion and osteogenic differentiation; used in skin, bone and nerve regeneration
Hexagonal boron nitride (h-BN)	Chemically inert; high thermal and mechanical stability	Supports both osteogenic and adipogenic differentiation; neural tissue regeneration

materials, with a wide range of applications in modern medicine. These include their use as scaffolds and guidance materials in regenerative medicine, components in biosensors, as neural interface devices and brain implants, some of which have already entered clinical trial phases [10, 11]. They provide an excellent surface for cell attachment and proliferation, particularly for MSCs and cardiomyocytes, as shown in figure 1. The extent to which GO affects SC behavior is highly dependent on several factors, including concentration, exposure time and surface modifications. Studies suggest that altering the physicochemical properties of GO, such as functionalization with biocompatible coatings, could mitigate some of its adverse effects. In addition to the mechanical support that promotes cell differentiation and consequently, tissue regeneration and functional repair, graphene and its derivatives also guide and enhance differentiation of MSCs towards specific cardiac cell types due to their electrical features [12, 13]. Namely, these materials possess extraordinary electrical conductivity across large surface area which facilitates cell-to-cell communication and maturation by the upregulation of key cardiac markers, such as connexin 43 (a gap junction protein crucial for electrical coupling) and cardiac-specific genes, thereby enhancing the differentiation process. Moreover, the surface of GO, rich in oxygen-containing functional groups, promotes strong interactions with ECM proteins, improving SC adhesion, proliferation and survival. These interactions protect MSCs from oxidative stress and enhance their paracrine signaling, contributing to angiogenesis and tissue repair when transplanted to infracted myocardium [14, 15]. Through these mechanisms, graphene-based materials not only guide SCs differentiation, but also ensure better integration and functionality of the newly formed

cardiac tissues, offering promising strategies for cardiac tissue engineering and regenerative therapies. The conductivity of graphene closely resembles that of the native myocardium, which allows these scaffolds to effectively transmit electrical signals between cardiomyocytes, promoting synchronized contractions and improved tissue integration. Myogenic scaffolds require higher conductivity and mechanical robustness to facilitate rhythmic, force-generating contractions, whereas neurogenic scaffolds prioritize directional growth, synapse formation, and moderate signal transmission support [13]. Functionalized graphene derivatives (e.g. GO functionalized with peptides or proteins) further improve cell adhesion, viability, and differentiation into cardiac-like cells by mimicking physiological conditions in ECM [16, 17]. It was observed that graphene-coated surfaces promote cardiomyocyte alignment, mimicking the native structure of heart tissue, which is crucial for functional integration. However, recent findings of Heo *et al* [18] indicate that GO may have unintended consequences when interacting with human iPSCs generated from fibroblasts. This raises concerns about its suitability for regenerative medicine applications. One of the most critical observations is that exposure to GO of varying lateral sheet sizes (in average 150 nm, 400 nm and 1 μm) and concentrations appears to interfere with key molecular pathways that sustain pluripotency [18]. Human iPSCs rely on a strictly regulated microenvironment to maintain their undifferentiated state, and any disruption to this balance can lead to premature lineage commitment. In this study, when cultured in cardiomyocyte induction medium, the upregulation of cardiomyocyte marker NKS2.5 was evidenced. This premature differentiation is a significant challenge, as maintaining precise control over SC behavior is

Figure 1. The potential of 2D materials for cardiac repair and regeneration. Graphene or graphene derivatives can act as scaffolds for MSCs and deliver growth factors to the infracted area. Reproduced from [8]. CC BY 4.0.

essential for their successful application in regenerative therapies. When intentional, the ability to interfere with differentiation is valuable, but in this case, the lack of control could undermine the reliability of GO as a biomaterial for SC-based treatments. Additionally, GO increased both reactive oxygen species (ROSs) and caspase-3 activity as a result from cellular uptake initializing apoptotic signal in concentration of 100 μg ml^{-1}. The hiPSCs lost their pluripotency, based on significant loss in pluripotency markers OCT-4 and NANOG regardless the lateral sheet size.

GO-based 3D scaffolds (including pure and functionalized GO) provide structural support that enhances cell proliferation, differentiation and tissue formation, making them particularly valuable in regenerative medicine and organoid development [19, 20]. They offer several advantages over Matrigel, which is derived from mouse tumor ECM and shows batch-to-batch variability, undefined composition and presence of xenogeneic contaminants. GO-based scaffolds have been used in organoid cultures to create disease models that closely resemble *in vivo* conditions and are essential for studying disease mechanisms, testing new drugs and understanding tissue responses to different treatments. In a recent study, 3D liver organoids (LOs) composed of upcyte® human hepatocytes, liver sinusoidal

endothelial cells, and mesenchymal stromal cells were repeatedly exposed to GO at concentrations of 2–40 μg ml^{-1}. While the LOs maintained overall viability and structural integrity, they showed a downregulation of CYP3A4 expression, suggesting potential disruption of hepatic metabolic function [21]. These findings point out the value of LOs as physiologically relevant *in vitro* models for evaluating the long-term and cumulative effects of nanomaterials, especially under conditions resembling real-life exposure scenarios. Due to its bio functional properties, GO can also act as a drug delivery system, allowing controlled and targeted drug release in cancer therapy and regenerative applications.

The recent study by Yu *et al* highlights MXene-incorporated hydrogels as a promising platform for functional cardiac regeneration following an ischemic injury [22]. A $Ti_3C_2T_x$ MXene-based hydrogel was developed by incorporating MXene nanosheets into a GelMA–PANI matrix, achieving conductivity of 0.23 S m^{-1} and a compressive modulus of $\sim$35 kPa, closely mimicking native myocardial tissue. *In vitro*, neonatal rat cardiomyocytes cultured on the hydrogel showed enhanced viability, spreading, and expression of cardiac-specific markers (cTnT, α-actinin, connexin-43), along with synchronous contractions and improved calcium signaling. *In vivo*, MXene hydrogel treatment led to significant functional

recovery, with increases in ejection fraction (16.5%) and fractional shortening (12.8%), alongside reduced infarct size, fibrosis, and increased angiogenesis. Immunofluorescence showed better tissue preservation and cellular alignment. The MXene component also provided antioxidative and anti-inflammatory effects by scavenging ROS and reducing TNF-α and IL-6 expression. The hydrogel biodegraded over 4 weeks, aligning with tissue healing.

Enhancing angiogenesis, as focal point in tissue engineering and SC therapy, can improve the success of transplanted tissues and the repair of damaged organs, like the heart after a myocardial infarction. GO and rGO materials significantly influence the angiogenic differentiation of hUC-MSCs [12, 23]. Cells cultured on large GO flakes demonstrated a notable increase in the expression of angiogenic markers such as GATA-2, endoglin and VE-cadherin. The expression levels were up to 3.5 times higher compared to cells grown on standard culture surfaces. Interestingly, the differentiation medium did not enhance this effect further, indicating that the GO-lf surface itself played a critical role in promoting angiogenic differentiation. Additionally, cells cultured on rGO-lr-P60 surfaces (a slightly reduced form of rGO) exhibited significantly elevated expressions of angiogenic markers, particularly GATA-2, which showed a 110-fold increase in expression compared to standard culture surfaces. The promotion of angiogenesis was further supported by functional assays, where hUC-MSCs demonstrated enhanced capillary tube formation on GO and rGO surfaces, indicating improved proangiogenic capabilities.

2.2. 2D materials in bone tissue regeneration

Bone tissue engineering aims to develop materials that surpass traditional bone autografts and allografts and the process must be finely tunable and dynamic as osteogenesis and bone remodeling physiologically are. Materials used must account for age-related changes in bone microstructure and diminished regenerative capacity for elderly patients and, in contrast, pediatric applications require materials with adaptable structural properties or those that facilitate remodeling to support skeletal growth. Additionally, sex-related differences in bone microstructure and size further emphasize the need for personalized approaches. In natural bone, bioelectrical signals such as piezoelectricity, ferroelectricity and pyroelectricity are generated in response to mechanical stress, polarization and temperature variations, respectively. These signals play a crucial role in regulating cellular activities essential for bone healing, remodeling and growth [24, 25]. Piezoelectricity, produced by the deformation of collagen and other structural components, generates localized electrical charges that influence osteoblast

function and guide SC differentiation toward bone-forming pathways. Ferroelectricity, which involves reversible spontaneous polarization under an external electric field, provides continuous electroactive signals that support bone matrix mineralization. Arising from temperature-induced potential changes, pyro-electricity introduces additional electrical stimuli that may be particularly relevant during inflammatory responses or thermal fluctuations following injury. These mechanisms form a dynamic bioelectrical environment that is integral to bone regeneration and scaffolds should not only structurally support but also [24] generating bioelectrical stimuli to promote tissue regeneration. Moreover, scaffold materials in bone tissue engineering are designed to gradually degrade and be replaced by newly formed tissue that closely replicates the mechanical properties of native bone. This ensures that the regenerated bone can provide the necessary strength, stability and functionality required for long-term integration within the body. When it comes to osteogenesis, it was demonstrated that graphene can promote the osteogenic differentiation of hMSCs even without a key growth factor in bone formation, BMP-2 [26, 27]. Higher calcification was observed by alizarin red staining in the presence of graphene. Additionally, variations in osteogenesis were noted depending on the presence or absence of both graphene and BMP-2. This effect is attributed to the localized accumulation of osteogenic molecules, such as dexamethasone and β-glycerophosphate, facilitated by non-covalent interactions like $\pi-\pi$ stacking with the graphene surface [28]. A single layer GO at low doses increases the roughness and decreases the stiffness of the alginate hydrogels in which single human BMSCs have been encapsulated, as indicated by microfluidics-based approach. This enhances cell viability, proliferation and osteogenic differentiation and thus, offers a promising approach for minimally invasive injectable bone tissue transplants [29]. When Raw264.7 cells were cultured on bioactive glass/GO scaffolds, GO significantly facilitated the polarization of macrophages toward the M2 phenotype, promoting the secretion of osteogenic and angiogenic factors. This, in turn, enhanced the osteogenic differentiation of rat BMSCs and stimulated angiogenesis in endothelial cells [19]. The degradation rate of the scaffold is carefully tuned, combined with biopolymers like collagen and gelatin, to align with the pace of natural bone regeneration, preventing structural deficiencies while promoting seamless tissue remodeling [26, 30, 31]. Furthermore, 3D printed composite materials that include GO and polycaprolactone (PCL) are designed as scaffolds for application in wound healing and tissue engineering, encompassing its mechanical strength with biological functionality. In GO-PCL composite, GO adds strong antibacterial properties, disrupting bacterial membranes
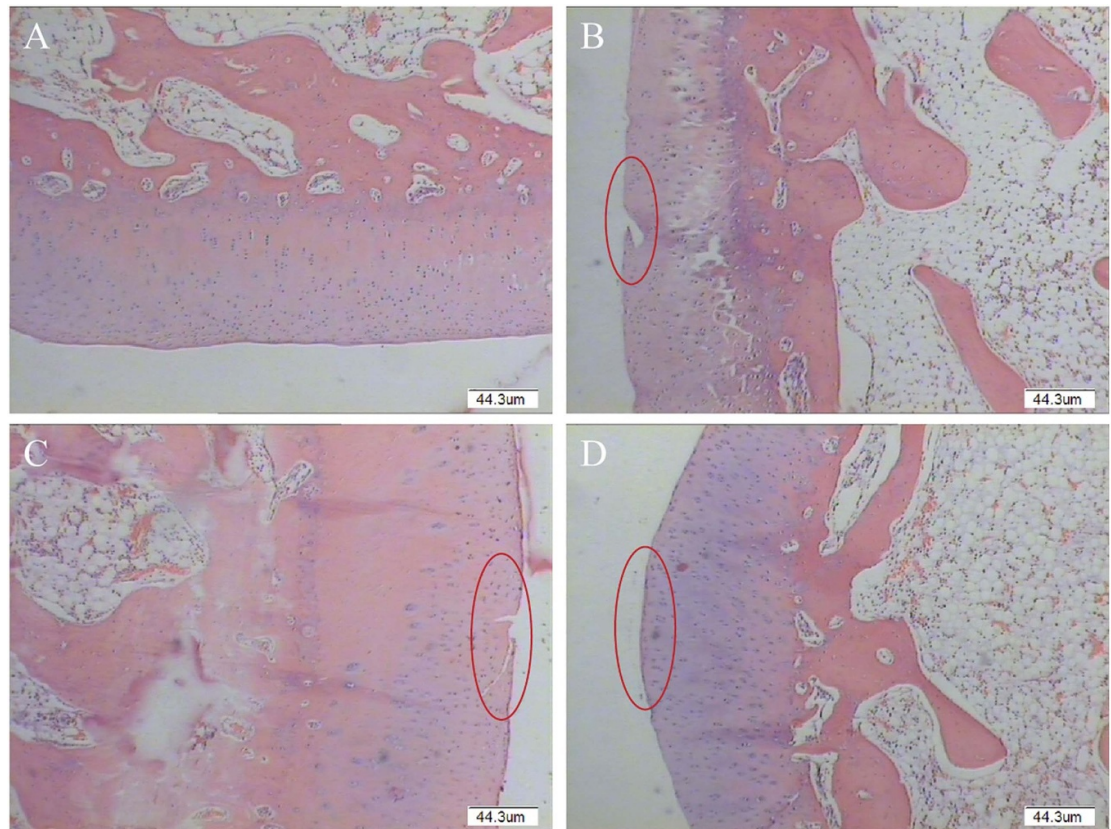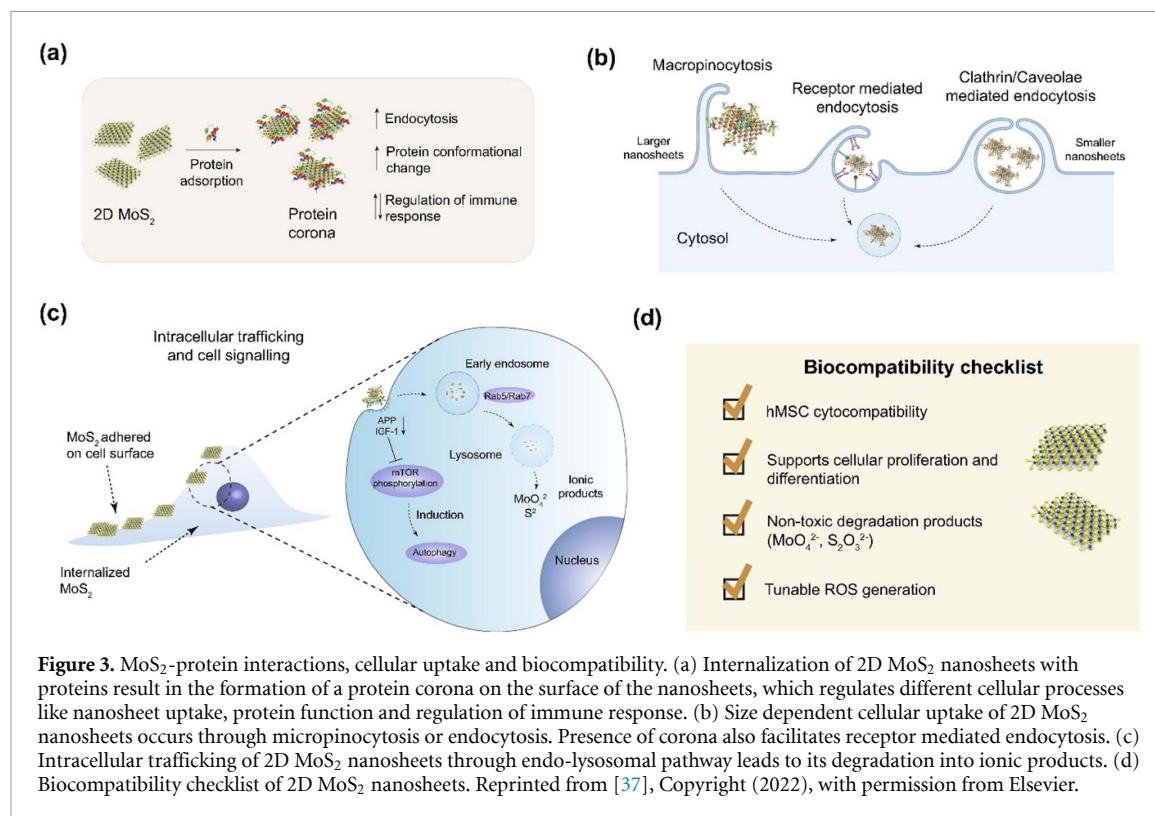
Figure 2. Patho-histological observation results of modified papain release joint injection group. (A) Blank, (B) GO group, (C) UCMSCs group, (D) GO + UCMSCs group. Red circle denotes cartilage erosion area. Reproduced from [33]. CC BY 4.0.

and inducing oxidative stress, minimizing in that way the risk of bacterial infection during the healing process [32]. On the other hand, its low cytotoxicity and high biocompatibility enhance its potential for various applications. Importantly, umbilical cord-derived MSCs (hUC-MSCs) loaded with GO granular lubricant can enhance chondrocyte secretion, lower joint inflammation, improve subchondral bone osteoporosis and support cartilage regeneration in knee osteoarthritis animal models (see figure 2) [33]. GO serves as a multifunctional reinforcing agent that not only strengthens the scaffold mechanically but also amplifies its bioelectrical functionality. When incorporated into polyvinylidene fluoride (PVDF) scaffolds produced by selective laser sintering, GO significantly promotes the transformation of the polymer's α phase to the electroactive β phase [34]. This is achieved through strong hydrogen bonding between the oxygen-containing groups of GO and the fluorine atoms in PVDF, which induces chain alignment favorable to β-phase formation. As a result, the PVDF/0.3GO scaffold demonstrated a marked increase in piezoelectric performance, achieving an output voltage of ∼8.2 V and current of ∼101.6 nA—improvements of 82.2% and 68.2%, respectively, compared to pure PVDF. In addition to enhancing electrical output, GO also reinforced the scaffold

mechanically, leading to a 97.9% increase in compressive strength and a 24.5% increase in tensile strength. These improvements are attributed to the strong interfacial interactions between GO and the PVDF matrix. Furthermore, *in vitro* studies confirmed that the enhanced electrical activity positively influenced cell behavior.

Transition metal dichalcogenides (TMDs) offer key advantages over graphene and its derivatives in regenerative medicine, primarily due to their intrinsic semiconducting properties and photothermal/photodynamic capabilities. Unlike graphene, which lacks a bandgap, TMDs enable light-responsive and electrically regulated applications, such as controlled drug release and phototherapy which enhance cell behavior and tissue repair [35]. Their broader chemical diversity, stimuli-responsiveness and ability to support cell differentiation without extensive functionalization make them especially attractive for developing smart, bioactive scaffolds. Molybdenum disulfide (MoS_2) promotes osteogenic differentiation of hMSCs by facilitating the adsorption of differentiation-inducing factors, enhancing cell adhesion and promoting differentiation into osteoblasts by upregulating osteogenic marker genes. This was confirmed through various assays, including optical microscopy and alizarin red S staining, which

Figure 3. MoS$_2$-protein interactions, cellular uptake and biocompatibility. (a) Internalization of 2D MoS$_2$ nanosheets with proteins result in the formation of a protein corona on the surface of the nanosheets, which regulates different cellular processes like nanosheet uptake, protein function and regulation of immune response. (b) Size dependent cellular uptake of 2D MoS$_2$ nanosheets occurs through micropinocytosis or endocytosis. Presence of corona also facilitates receptor mediated endocytosis. (c) Intracellular trafficking of 2D MoS$_2$ nanosheets through endo-lysosomal pathway leads to its degradation into ionic products. (d) Biocompatibility checklist of 2D MoS$_2$ nanosheets. Reprinted from [37], Copyright (2022), with permission from Elsevier.

highlighted significant mineralization, a fingerprint of osteogenic differentiation. Furthermore, gene expression analysis validated the upregulation of key osteogenic marker genes, indicating that MoS$_2$ effectively supports the osteogenic lineage. Adversely, it has minimal influence on adipogenic differentiation. Due to its photothermal properties, light-mediated modulation of SCs behavior can further influence differentiation outcomes [36]. Similar to MoS$_2$, tungsten-sulfide's (WS$_2$) surface properties enhanced the adhesion of hMSCs and facilitated their differentiation into osteocytes with minimal or no influence over adipogenesis. Both of these materials possess strong in-plane covalent bonds and weak out-of-plane van der Waals interactions, with surface roughness that promotes interactions between cells and surface, tunable for optimization. Moreover, both of these materials show minimal cytotoxicity [27]. In SC research, MoS$_2$ nanosheets provide biophysical stimuli that enhance adhesion, proliferation and differentiation. Their nanostructured surfaces mimic extracellular matrices, improving cytoskeletal organization and focal adhesion formation, as shown in figure 3 [37]. Biomolecule corona on MoS$_2$ nanosheets that dictates its biological interaction and compatibility is, unlike in graphene-protein interactions, the consequence of van der Waals energies and electrostatic interactions that regulates the conformation of the adsorbed protein [36]. That initial interaction with proteins allows cellular uptake, intracellular trafficking and immune responses. Cellular uptake of

MoS$_2$ occurs mainly via endocytosis, influenced by factors like nanosheet size, surface chemistry and functionalization. Furthermore, MoS$_2$ nanoflowers exhibits interactions with immune cells, such as macrophages and dendritic cells, modulating immune responses, leaving the space to be used as drug delivery vehicle for immunomodulation [38]. It can promote pro-inflammatory responses at higher concentrations but also shows potential in immunomodulation strategies. The *in vivo* formation of a biomolecular corona on nanoparticles (NPs) has only recently been recognized as a critical advancement in the field of nanomedicine, facilitating a range of significant biomedical applications, including the modulation of immune responses, targeted delivery through endogenous pathways and the scavenging of disease-associated biomarkers [39].

On the other hand, boron nitride (BN) as a chemically inert, thermally conductive and electrically insulating 2D material with excellent mechanical strength supported both, osteogenic differentiation and adipogenesis, but with significantly higher potential for adipogenesis, which was proved with oil red O staining and significantly elevated expression levels of adipogenic marker genes. This is explained by favoring the adsorption of adipogenic-inducing factors and relatively smoother surface which provides less mechanical stimulation and promotes lower cytoskeletal tension and rounded cell shape characteristic for adipogenesis. Moreover, BN stimulates adipogenesis-related signaling pathways like such as

the PPARγ and C/EBPα while providing insufficient mechanical or biochemical stimuli to effectively trigger osteogenic differentiation [40, 41].

2D metal carbides and nitrides (MXenes), known for their exceptional electrical conductivity, play a significant role in promoting the growth and differentiation of electrically active tissues, such as neural and cardiac tissues. Strong interlayer interactions in MXenes yield a stable aqueous colloidal suspension which allows endurance and lower cytotoxicity in biological environment [42]. Through the combined effects, photoactivated MXene promotes bone and soft tissue repair at the same time [43]. The photoactivation of MXene nanosheets (Ti$_3$C$_2$T$_x$), which converts light into localized heat, occurs through the absorption of near-infrared (NIR) light (808 nm). This photothermal activation enhances the antibacterial properties of MXene, generating sufficient heat to expose antibacterial effect on pathogenic bacteria, including methicillin-resistant *S. aureus*. The photoactivation also stimulates angiogenesis by upregulating pro-angiogenic factors (such as VEGF) while promoting cell migration and proliferation, accelerating wound healing. Moreover, MXene exposed to NIR light indirectly activates ERK signal pathway in adipose-derived SCs *in vitro*, elevating calcium mineralization by improving the activity of alkaline-phosphatase, driving osteogenic differentiation. Despite their promising potential in healthcare, MXenes face several limitations that must be addressed for successful biological application. Their tendency to oxidize in physiological environments compromises stability and functionality over time. Additionally, concerns regarding cytotoxicity, inconsistent surface terminations and unpredictable interactions with biological media raise challenges in ensuring biocompatibility and safety. The complexity of their synthesis, often involving harsh chemicals, further limits scalability and clinical translation. Therefore, comprehensive *in vivo* studies and standardized protocols are essential to fully realize MXenes' potential in biomedical settings [44]. In addition to their electrical properties, MXenes show remarkable mechanical robustness, making them ideal candidates for reinforcing scaffolds designed for load-bearing tissues, such as bone and cartilage. Their mechanical strength enhances scaffold stability, supports cellular integration and ensures better structural integrity during tissue formation.

2.3. 2D materials in neural tissue regeneration
Neural repair and regeneration are inherently slow and limited processes, particularly within the central nervous system, where neurons have a restricted ability to regenerate after injury. This limited regenerative capacity is due to factors such as inhibitory environments, the formation of scar tissue, and the complex structure of neural networks, which altogether obstruct the restoration of normal neural function [45]. Graphene-based scaffolds have demonstrated promising potential in promoting neuronal regeneration, particularly for repairing peripheral nerve injuries. In an extensive 18 month rat study, these scaffolds exhibited low toxicity, with no significant adverse effects observed in major organs such as the liver, kidneys, heart, lungs or spleen [46, 47]. These scaffolds effectively supported myelination, axonal growth and improved both locomotor and electrophysiological functions. The enhanced expression of myelin basic protein and Tuj1 highlighted the scaffolds' role in facilitating myelin and axonal regeneration. Moreover, they contributed to angiogenesis, a critical process for nutrient supply and tissue repair, by upregulating CD34 and vascular growth factor expression. Notably, graphene-based scaffolds exhibited dual regulation of Schwann cells and astroglia, positively influencing both central and peripheral nervous systems to promote neural repair. Despite these advancements, several challenges hinder clinical translation. The variability in biocompatibility results, stemming from differences in experimental models, presents a significant hurdle. Concerns about the long-term toxicity and limited biodegradability of graphene-based materials, especially at higher concentrations, also require deeper investigation. Additionally, understanding the interactions between graphene-based scaffolds and diverse cell types, alongside their effects on immune responses in large animal models, is crucial to ensure safety and effectiveness before advancing to human clinical trials. The graphene-based neural interface developed by INBRAIN Neuroelectronics represents one of the most advanced and successful examples of translating 2D material technologies from academic research into real-world medical applications [11]. By overcoming key challenges in scalability, industrial fabrication, regulatory approval and interdisciplinary collaboration, INBRAIN not only brought graphene-based devices closer to clinical use but also demonstrated a viable pathway for other emerging nanotechnologies. Their progress, culminating in FDA Breakthrough Device Designation and the launch of first-in-human clinical trials, serves as a model for how strategic partnerships, sustained funding and startup-driven innovation can bridge the critical 'lab-to-fab' gap in advanced medical technologies. Functionalization of 3D nanofibrous scaffolds made of decellularized ECM derived from porcine adipose tissue with polydopamine (PDA)-rGO enhanced its bioactivity and electrical conductivity, both very important for neural tissue engineering. Doping with PDA-rGO significantly boosted the performance of scaffolds towards neuronal differentiation, particularly in the 3D environment, which on its own created biomimetic environment that supported neural SCs adhesion, proliferation, migration and differentiation
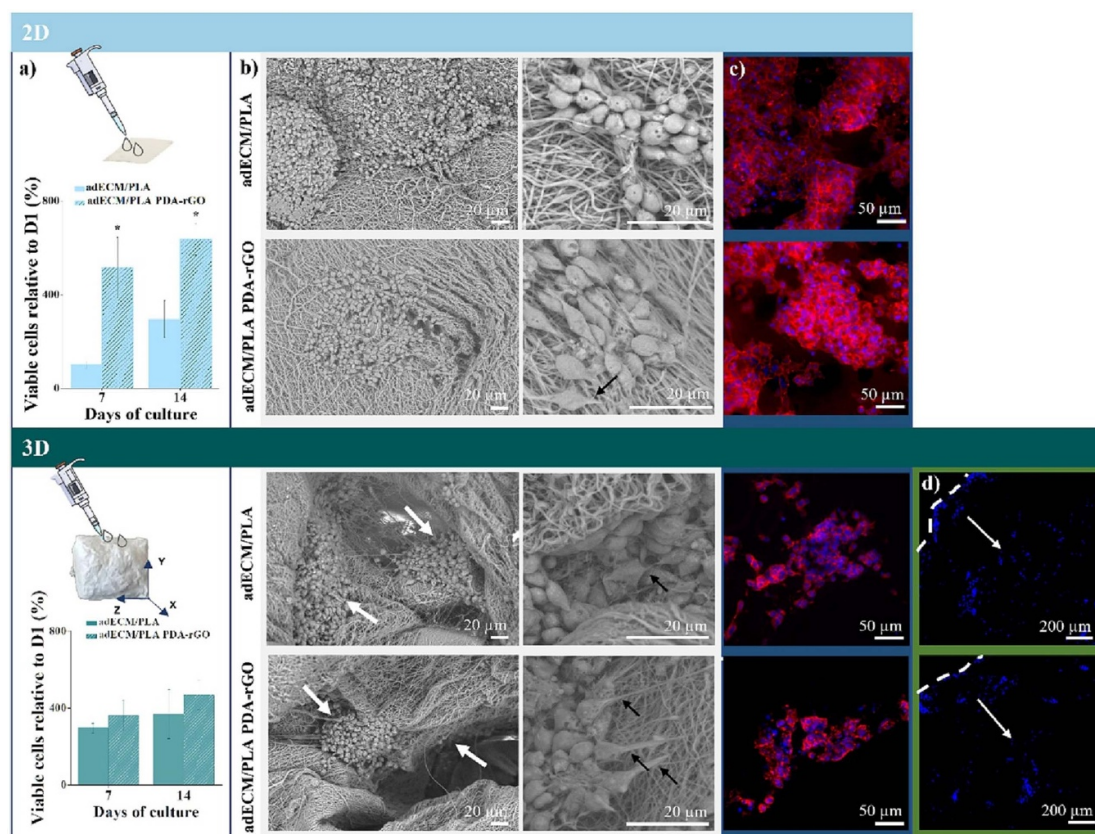
Figure 4. Proliferation and morphology of NSC-seeded bidimensional and three-dimensional platforms: (a) percentage of viable NSCs on the platforms relative to the adhered cells on day 1, after 7 and 14 d of culture and schematic illustrations of the seeding process in each platform; (b) SEM images of the NSCs-seeded platform after 7 d of culture, with white arrows highlighting the cellular clusters and black arrows pointing to the out-growing processes; (c) immunocytochemistry of actin filaments (phalloidin in red) and nuclei (DAPI in blue) of the NSC-seeded platform after 14 d of culture; (d) DAPI staining of the cross-sectioned NSC-seeded 3D platforms, with white arrows showing the cellular migration pathway. Reprinted from [48], Copyright (2023), with permission from Elsevier.

[48]. The scaffold also facilitated spontaneous differentiation, favoring a neuronal over an astrocytic lineage. In more detail, PDA-rGO in 3D platforms significantly enhanced neuronal differentiation, resulting in a 1.26-fold increase in Tuj1 levels and a 1.72-fold increase in MAP2a/b neuronal isoforms (see figure 4). Graphene, GO and rGO nanosheets, thanks to their large surface area, functionalized with molecules that enhance the ability to penetrate blood–brain barrier (BBB), can carry a variety of biomolecules, targeting the specific cell type or area in central nervous system. By serving as efficient drug delivery systems capable of crossing the BBB with ease, these nanosheets offer a promising solution to overcoming the challenges associated with drug delivery to the brain [49, 50]. The functionalization of rGO with polydopamine (PDA) has been shown to significantly influence SCs behavior, particularly by encouraging spontaneous differentiation toward the neuronal lineage [48]. This effect is observed in both 2D and 3D culture platforms, suggesting that PDA-rGO can serve as a powerful biointerface for neural tissue engineering. The gas foaming

technique offers a simple yet effective method for generating 3D nanofibrous constructs with tunable physical properties. This approach allows the creation of biomaterial-based microenvironments that closely replicate native extracellular matrices, revealing biomaterial-induced cellular responses that may remain undetected in traditional 2D cultures. By incorporating PDA-rGO into gas-foamed 3D scaffolds, its potential as a neurogenic biomaterial can be assessed, revealing new possibilities for neural tissue engineering and regenerative medicine. The ability to fine-tune material properties using gas foaming further enhances its adaptability for various biomedical applications. Additionally, excellent electrical conductivity attributed to the structure of MoS_2 with unsaturated d-orbitals, and biocompatibility create nurturing microenvironment for neural SCs differentiation, allowing their attachment to porous architecture, efficient charge transport at the cell-membrane interface, proliferation and differentiation into neural cells [51]. This differentiation is marked by the increased expression of key neural markers such as Tuj1, GFAP, and MAP2 over extended culture

periods [52]. The porous nature enables stronger protein absorption, including growth factors like EGF and FGF, which further supports the maintenance of neural SCs stemness and promotes differentiation efficiency over time.

Its structure also provides excellent template for cell elongation, which is a preferred feature in neural tissue regeneration. Moreover, 3D cylindrical scaffolds made of MoS_2-PVDF hybrid films, with randomly assembled MoS_2 nanoflakes, showed potential for nerve regeneration encompassing flexibility, conductivity and compatibility, hence mimicking natural neural structures [51]. Significant regenerative potential through the light responsive properties of 2D materials with the focus on G and derivatives and TMDs lays within their capability to finely modulate cellular response. Excellent conductivity and photothermal capabilities stimulate cell growth, differentiation and tissue regeneration, particularly in neural and muscle tissues by non-genetic optical modulation. NIR light stimulation of MoS_2 nanosheets influenced more genes related to cell migration and wound healing in MSCs than nanosheets itself, as evidenced by transcriptome sequencing [53, 54].

BN nanosheets functionalized polycaprolactone channel scaffold was evaluated for neuronal repair through piezocatalytic stimulation [55]. This 3D scaffold, produced by layer-by-layer droplet spraying method, is highly elastic, hydrophilic and biocompatible [56]. After ultrasonic actuation, the scaffold generates bioelectrical signals that promote the secretion of neurotrophic factors, enhancing Schwann cell viability and modulate ROS levels to maintain metabolic balance. Schwann cell cultured on this scaffold showcased an increased expression of proliferative and neural markers (Ki67, Tuj1 and MBP), alongside reduced oxidative stress and elevated growth factor expression. *In vivo,* improved nerve regeneration, remyelination and functional recovery in a rat sciatic nerve defect model were observed. Higher nerve conduction velocities, enhanced axonal alignment and improved muscle reinnervation compared to control groups were noted as well as promoted angiogenesis and reduced amyotrophy. High biocompatibility of the scaffold played significant role all along.

3. 2D materials as humidity sensors

The increasing interest in wearable devices, namely, flexible and transparent sensors, has expanded the demand for novel materials [57]. Electronic devices that can be attached to the skin and that are able to continuously record vital signs are going to minimize both the size and the cost of healthcare monitoring. These types of devices require developing of a variety of noninvasive sensors for monitoring of human physiological biomarkers. For example, tracking the

gas molecules that are transmitted from the body can play an important role in personalized medicine. The main requirements for these functional sensors is to be able to get comfortably attached on human skin and continuously and unobtrusively monitor human activities. Hence, this type needs to be conformable to the skin, and the substrate should not be an irritant. Some of the activities that should be uninteruptedly tracked are vital signs (respiration, pulse, blood pressure) and physiological activities (muscle movements, cognitive states). Furthermore, basic humidity sensors can have wide application in various fields outside of medical uses, such as environmental monitoring, agriculture, industrial production, process control and safety.

Some of the drawbacks of commercially available sensors is that they are mostly made of polymer films or porous ceramics, and are unable to operate at high humidity levels, have slow response time, high levels of hysteresis and a long-term drift. 2D layered materials have been extensively studied and shown great potential as resistive gas sensors due to their excellent electrical, physiochemical, and mechanical properties [58–60]. The need for these types of sensors is becoming highly important as the air pollution, caused by gases such as NO_2, SO_2, CO; VOCs and particulate matter, becomes ubiquitous. In this review, we focus on their emerging potential as humidity, human respiration and touch sensors. We firstly describe various mechanisms for humidity sensing from the aspect of sensor fabrication. In the next step, we assess the performance of different families of 2D materials, with the summary of relevant parameters.

3.1. Humidity sensing mechanisms

Humidity sensors can be fabricated through a variety of methods. While the majority of the commercially available sensors are capacitive-based, devices based on resistor/impedance response are becoming increasingly popular due to easier fabrication. In recent years, new operating mechanisms are emerging based on FET, QCM and fiber-optics. Here, we outline the most prominent sensing mechanisms and their advantages and disadvantages.

3.1.1. Capacitive

Commercially available humidity sensors are mostly based on the capacitive technique, where the dielectric constant of the active layer changes in response to humidity. The standard mechanism consists of parallel plate capacitors, where an intermediate moisture-sensitive dielectric layer is sandwiched between two metal electrodes. As the output, the change in capacitance is recorded, which occurs when the distance between the two electrodes changes (i.e. upon water molecule adsorption). The variations in capacitance also depend on the area of the electrodes and the dielectric constant of the intermediate material. The

straightforward assembly of parallel plate capacitors has led researchers to develop capacitive sensors using diverse materials, and to improve their flexibility and sensitivity. Nevertheless, capacitive sensors have several drawbacks, including hysteresis, stability at high temperatures and humidity levels, limited durability against certain organic vapors and their fabrication can be expensive.

The capacitance value is defined as:

$$C = \varepsilon A / d$$

where ε represents the dielectric constant, A the area of the capacitor, and d is the distance between the capacitor plates.

The response of the sensor is defined by the following formula:

$$\text{Response} = \frac{C - C_0}{C_0} \, x \, 100\%$$

where C_0 and C represent the capacitance measured under dry air and measured humidity, respectfully.

Sensitivity of the sensor is calculated using the equation

$$S = \frac{\Delta R}{R \Delta \% RH} X 100$$

where S is defined as the percent change in resistance divided by the percent change in relative humidity (RH), RH is defined as the ratio of 'water vapor present in a particular volume and at a particular temperature' to the 'maximum capacity of air to absorb the water molecule at the same volume and temperature'.

The response time is defined as the time required for reaching 90% of the total response value, while the recovery time is defined as the time required to return the response to 10% of the total response value.

The change in RH is detected as the change in voltage, as the conversion circuit (usually, a simple RC circuit) is transforming the change in the capacitance into change in voltage.

Capacitive-based humidity sensors have been reported on GO [61–65] and MoS$_2$ [66], which will be discussed in more detail in section 3.2. Figure 5 depicts two setups based on GO [61] and GO-PSS film [63].

3.1.2. Resistive

In contrast to capacitors, resistive humidity sensors have a simpler structure and are easier to integrate with CMOS technology. As a result, considerable research is focused on the development of resistive humidity sensors, which are expected to lower the cost per unit and offer improved long-term stability.

The sensing mechanism is based on recording the change in humidity, as the adsorbed water molecules affect the electronic density of states and the carrier concentration of the active material and change its conductivity.

The response is defined as:

$$\text{Response} = \frac{R - R_0}{R_0} x 100\%,$$

where R_0 and R represent the resistance measured under dry air and measured humidity, respectfully.

A typical response of this type of setup, prepared on a hybrid composite of rGO and MoS$_2$ [67], is shown in figure 6.

3.1.3. Impendence

Sensor with impedance output is structurally similar to the resistive sensors, whereby they consist of three parts, a substrate, interdigital electrodes, and the sensing material. The output is highly dependent on the frequency and RH. Sensors show better performance at lower frequencies, as the impedance significantly increases with the decrease in both RH and frequency. In the typical setup, the output current is measured by applying a sinusoidal voltage to the electrodes, and the impedance is calculated as the voltage/current ratio. Some of the reported impedance-based sensors used GO [68], MoS$_2$ [69, 70], MXene [71], Al$_2$O$_3$ NTs [72] as the sensing material, and their performances will be discussed in detail in section 3.2. Two typical setups are depicted in figure 7.

3.1.4. Other sensing mechanisms

Other than the previously explained mechanisms, based on resistive or capacitive effects, new approaches have been proposed. Here, we discuss the most promising ones, which bring forth better integration into electronics, or miniaturize the size of the sensing device.

QCM

Quartz crystal microbalance is a technique capable of detecting mass change as small as the sub-nanogram, making it suitable for vapor phase sensors. A thin slice of quartz crystal is placed in a circuit, and with the applied voltage, alternating compression and stretching vibrations appear [73, 74]. The change in the resonant frequency can be detected, as the adsorbed water molecules change the mass of the crystal. The amount of the adsorbed water and the resonant frequency change are correlated, allowing for the calculation of the humidity level. This type of setup is shown in the left panel of figure 8.

Potentiometric

A self-powered potentiometric mechanism was reported [75]. The sensing mechanism was based on a sandwiched material structure, made of rGO/GO/-foamed metal (such as nickel, zinc, iron and copper), and it modulates the measured potential difference between the two electrodes by humidity
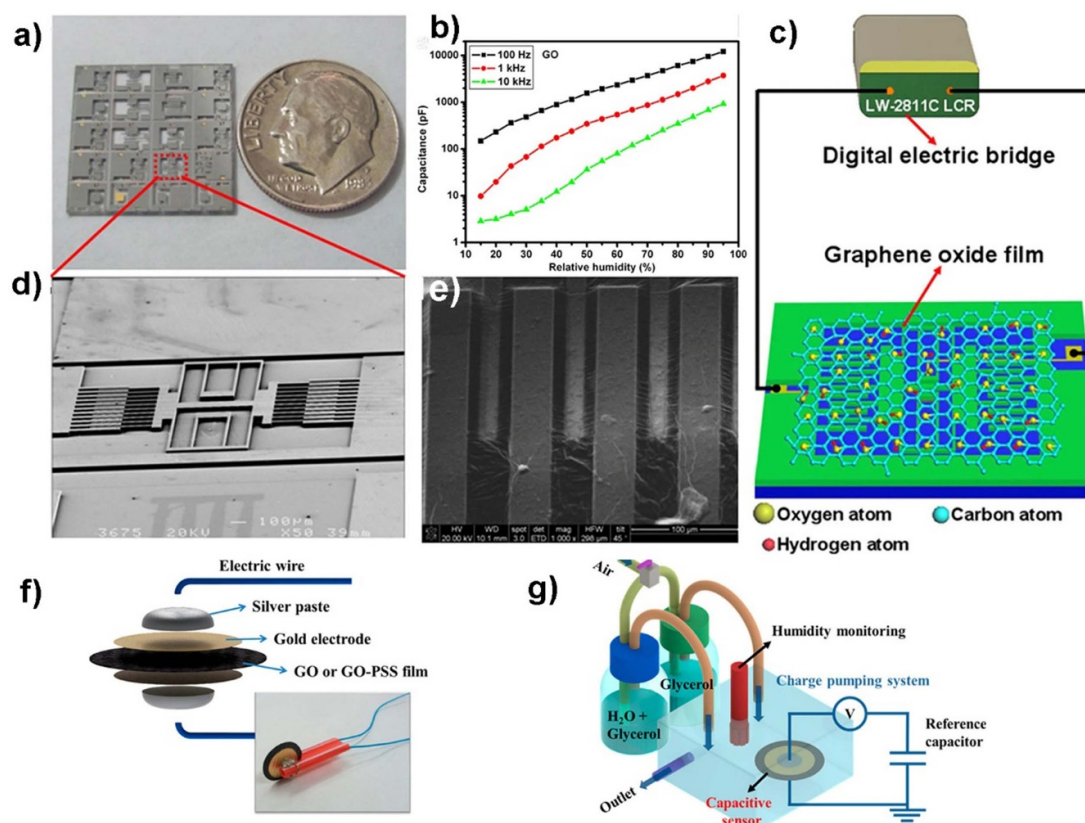
Figure 5. Capacitive-type humidity sensors based on (a)–(e) GO [61] and (f), (g) GO-PSS film [63]. (a) Digital photographs of the device, (b) SEM image of the area set off by a red dashed line, (c) output capacitances of sensors as a function of RH, (d) SEM image of interdigitated electrodes covered with GO films, (e) schematic diagram of the humidity testing system of GO as a humidity sensing material between the two sets of interdigitated electrodes. (a)–(e) Reproduced from [61], with permission from Springer Nature. (f) Sensor based on the GO and GO-PSS dielectric films. An optical image of the fabricated sensor is shown in the inset. (g) Schematic diagram of the RH controlled-environment chamber and charge pumping system. Reprinted with permission from [63]. Copyright (2014) American Chemical Society.
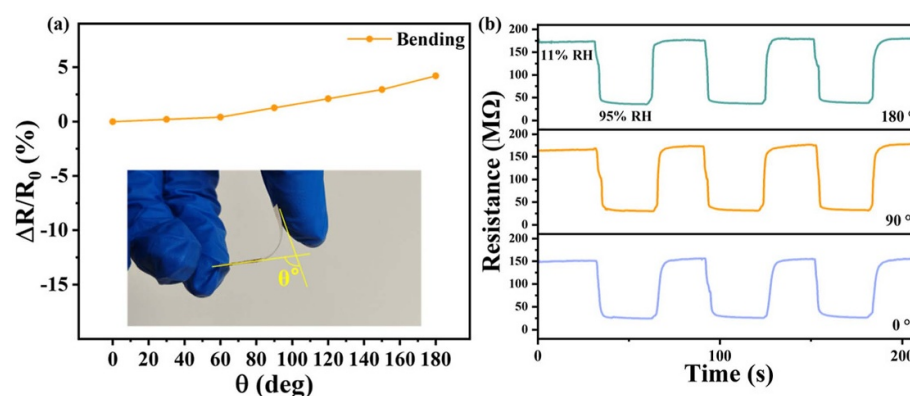
Figure 6. Resistance response of a device based on rGO and MoS_2 as it was gradually bended in the atmospheric environment. (b) Humidity experiments of a device with the relative humidity change between 11% RH and 95% RH as it was bended with different bending angles (0, 90, and 180°). Reprinted with permission from [67]. Copyright (2024) American Chemical Society.

stimulation. While the resistive or capacitive devices are difficult to miniaturize because they require an external power supply, potentiometric humidity-transduction method is able to detect both steady and rapid humidity response of multiple cycles with high response value and short response/recovery time (RRT). The external humidity stimuli can regulate the hydration across GO, as a solid electrolyte, and bring about a change in the output voltage measured between the two electrodes. The sensor showed high stability, high RRT and was able to monitor both the static and dynamic humidity stimulation.

Figure 7. Impendence-based humidity sensors. Top panel: diagram of the experimental setup and fitting of the impedance spectrum, by using the displayed equivalent circuit, for two different GO film thickness values and the conductance response of an ultrathin GO film to RH variation. Reprinted with permission from [68]. Copyright (Year) American Chemical Society. Bottom panel: SEM images of dendritic MoS_2 and impedance vs RH curves of dendritic MoS_2 and triangular MoS_2 at 100 Hz. Reprinted from [70], Copyright (2020), with permission from Elsevier.

Fiber optics

Sensors based on fiber optics are helpful for overcoming the drawbacks of electrical sensors, as they have fast response, high accuracy and long service life. They are easy to fabricate and are compatible with pre-established fiber optic systems. The sensing mechanism is based on the change in the light transmission. Namely, the water molecules adsorbed by the high refractive index (RI) coating result in a difference in the reference optical signal and the detected signal. This change can be used to calculate the humidity. For example, by overlaying WS_2 on side of a polished fiber, a first all-fiber-optics humidity sensor was developed, with rather fast RRT (1 s/5 s) [76]. This setup holds a lot of promise, and by using some other high RI materials, such as MoS_2, or the combination of materials, RRT can potentially be improved.

FET

Field effect transistor-based sensors have a standard setup of a source, drain, gate and channel materials. Channel material is the active sensing material and it bridges the source and the drain. The sensing materials absorbs or releases water, affecting the charge distribution between the layer and the gate. Graphene is not a good candidate for FET-based sensors due to low on/off ratio and zero bandgap, therefore, these

types of devices are reported on MoS_2 [69] and metallic nanowires (NWs) [77].

3.2. Sensing performance of 2D materials

Here, we assess the performance of humidity sensors for a variety of 2D materials. The summary of critical parameters, such as type of the device, material, mechanical status (whether it is rigid, flexible or stretchable), the measured humidity range, the RRT and the response/sensitivity of the device are presented in table 2. *NA* stands for parameters which were not reported (and cannot be deduced) in the paper, in the units typical for that specific measurement setup.

3.2.1. Graphene, GO and rGO

Graphene, GO and rGO [61, 62, 64, 68] were all studied as sensing materials, and their performances will be discussed here in detail.

As previously mentioned, single layer graphene has high electrical conductivity ascribed to the p-orbital electrons, which form π-bonds with neighboring atoms. On the other hand, delocalized π-electrons are sensitive to the modifications of their immediate environment, making them suitable for sensing [99]. Nevertheless, humidity sensors based on graphene alone have shown limited range and/or response times [100]. Some of these drawbacks can

Figure 8. Left panel: QCM-based sensor. Top: fabrication illustration. Reprinted from [73], Copyright (2018), with permission from Elsevier. Bottom: dynamic frequency shift of QCM sensors, inset are response values versus RH. Reprinted from [74], Copyright (2016), with permission from Elsevier. Right panel: potentiometric humidity sensor design: schematic illustration of the humidity response mechanism; response/recovery curve of open circuit voltage (V_{oc}) and short current density (I_{sc}) of rGO/GO/Ni$_{fm}$ sensor and the response/ recovery time of rGO/GO/Nifm sensor. [75] John Wiley & Sons. © 2021 Wiley-VCH GmbH.

be overcome by using CVD graphene. For example, graphene deposited on a SiO$_2$ layer on a Si wafer, was prepared as a resistive humidity sensor and showed response time comparable to GO [79]. As there has been extensive work done on graphene, we will focus more on GO and rGO.

GO film is a laminated material formed from oxygenated graphene platelets. It is a good candidate for humidity-response platforms, as it is a low-cost, easily synthesized material. It possesses a large specific surface area, which can highly improve the number of exposed atoms at the edges that can act as water molecule absorbers. It also contains diverse oxygen-containing groups on a basal plane, and carboxylic acid groups at the edges, which can increase hydrophilicity [75]. These characteristics allow GO to be utilized as humidity sensing material, as the layered and interlocked structure of GO films effectively undergoes the permeation of water molecules into the film under humid conditions [101]. Nanoscale capillaries between individual GO platelets facilitate low-friction water molecule flow on the surface, making the permeation process both rapid and reversible [102]. As a result, the interlayer distance between GO platelets increases with

increasing RH, making it possible to monitor the humidity in the environment.

The sensing mechanism based on resistivity has been developed by measuring the electrical conductance changes in the GO films upon the exposure to a humid environment [103]. Namely, electrical interactions between water molecules and GO platelets cause electrical perturbations in the GO films that can be monitored in real-time. The water molecules that are hydrogen-bonded to the oxygen groups on the GO surface easily lose a degree of rotational freedom because of the strong interactions in the layered and interlocked structure between the platelets. As a result of the confined water intercalation through exposure to humidity, there is an increase in dielectric strength and a decrease in the electrical conductivity of GO films. A capacitive-type humidity sensor was prepared, reporting high sensitivity, explained as a result of violent oxidation and a creation of large density of sulfur vacancies and hydrophilic (carboxyl, hydroxyl) functional groups [61]. Through previously mentioned basal plane and edges of GO, composed of distributed oxygen groups, the hydrophilicity is improved. Another GO humidity sensor was prepared on chemically exfoliated

Table 2. Summary of the device performance based on sensing material, mechanical status, testing RH range, response or sensitivity and response/recovery time. NA stands for non-applicable, i.e. this parameter was not evaluated.

Device	Material	Mechanical status	RH range (%)	Response/sensitivity	Response/recovery time (s)
Capacitor	GO [61]	Rigid	15–95	37 800% at 1 kHz	10.5/41
	GO/PDDA [62]	Flexible	11–97	1552 pF/% RH	108/94
	GO/PSS [63]	Flexible	20–80	NA	60/50
	GO-Au [64]	Rigid	11–97	25 809 pF/% RH	8/12
	GO [65]	Flexible	10–90	3215.25 pF/%RH	15.8/NA
	MoS_2 (liquid exf) [66]	Rigid	11–96	43 684%	30/40
Resistor	rGO [78]	Flexible	10–95	100	50/3
	Graphene [79]	Rigid	1–96	S%: 0.31 ($\Delta R/R/\%RH$)	0.6/0.4
	GO [80]	Flexible	30–95	S%: 7.9	100/NA
	rGO/PU [2]	Stretchable	10–70	$\Delta R/R_0$ 4.63 at RH = 35%)	3.5/7
	GO [81]	Rigid	8–95	124%	3/7.7
	r-CMGO [82]	Rigid	0–100	0.33%RH − 1	0.025/0.127
	rGO [83]	Rigid	11–97	NA	15/28
	MoS_2/GO [84]	Rigid	25–85	IH/IB = 1600	43/37
	rGO/MoS_2 [85]	Rigid	5–85	2494.25	6/31
	rGo/MoS_2/PI [67]	Flexible	11–95	96.7%	0.65 s/14.4
	MoS_2 (nanosheets) [86]	Rigid	10–60	NA	9/17
	MoS_2/Si NW [87]	Rigid	11–95	392%	26/15
	MoS_2/PEO [88]	Flexible	0–80	$\sim 0.7\,\Omega\,°C^{-1}$	0.6/0.3
	MoS_2 NTs [89]	Rigid	20–85	668	0,5/0,8
	MoS_2@$MoSe_2$ flowers [90]	Rigid	H_2O conc 25–12 000 ppm	NA	30/33
	WS_2 NPs [91]	Rigid	11–97	469%	12/13
	WS_2 nanosheets [92]	Rigid	8–85	IH/IB = 1300 at 85% RH	140/30
	MoS_2 NPs-plasma [93]	Rigid	20–95	NA	0.5/0.8
	SnS_2 nanoflakes [94]	Rigid	11–97	−11 300%	85/6
	SnO_2 film [95]	Flexible	15–70		
	CeO_2 NW [96]	Rigid	15–97	Rair/RRH = 6.2	3/3
	ZnO NW [97]	Rigid	17–60	4000 for 50% RH	60/3
	MXene/TPU	Flexible	11–94		12/30
Impendance	GO [68]	Flexible	35–80	NA	0.03/0.09
	MoS_2 dendrites [70]	Rigid	10–95	413 S = Im (11%)/Im (95%)]	17/24
	MoS_2—spiropyran [69]	Rigid	10–75	1.0% · (%) RH − 1	NA
	MXene/GO/COC [71]	Flexible	6–97	182 * 10^6/%RH at 1 Hz	0.8/0.9 s
	TiO_2 NW [98]	Rigid	11–95	3000%	3/7
	Al_2O_3 NT [72]	Rigid	11–95	10 000%	10/20
QCM	GO/PEI [74]	Rigid	11.3–97.3	27.3 Hz/%RH	53/18
	GO/SnO_2/PINI [73]	Rigid	0–97	29.1 Hz/%RH	7/2
Potentiometric	GO [75]	Rigid	20–90	5–20 mV/%RH	0.8/2.4
Fiber optics	WS_2 [76]	Rigid	33–85	0.1213 dB/%RH	1/5
FET	SnO_2 NW [77]	Rigid	NA	NA	120/20

large-area thin films [80]. While easier to scale-up, these films showed a slow response time of 100 s.

In another approach, a GO-based single-layered sensor chip with multiple sensing capabilities was prepared [81]. It showed potential to operate as a microheater, temperature sensor and a flow sensor. This device was fabricated on two sides of the Si wafer. On one side of the chip, a GO-based humidity sensor is fabricated, offering ultrahigh sensitivity of 124/% RH, rapid RRT, and a wide detection range (8%–95% RH). Additionally, the effect of temperature on the humidity sensing properties of GO is demonstrated using the microheater platform. On the other side of the chip, serpentine Pt micropatterns serve

as high-performance temperature and flow sensors in cold and heated states, respectively, when connected to the appropriate circuits. Low and high voltages are applied to the Pt microlines for temperature and flow sensing, respectively, generating negligible and significant Joule heating effects. As a result, the Pt micropatterns enable the realization of three distinct functionalities within a single device. The humidity was tested from 8% to 95%, with fast RRT of 3 s/7.7 s. Another technique used to increase the active surface area is to combine GO with metal NPs. For example, Ag NPs were added to GO in different concentrations, in order to improve the humidity sensitivity of capacitive-type sensors [64]. The sensing properties were tested in a 11%–97% RH range at room temperature. The best performance was achieved by the GO/Ag (2 wt%) composite-based sensors. Addition of Ag NPs increases the large specific surface area and hydrophilicity by adding the wrinkles. Beyond 2%, the initial resistance of the composites becomes too small to be dielectric, and the performance of the sensor deteriorates.

Nevertheless, sensors based on natural GO have limited sensitivity at low humidity levels. The material is also electrically insulating, but its conductivity could be partially restored if certain reduction processes are performed to remove oxygen groups. Therefore, rGO can sustain both the conductivity and the chemically active defect sites. One drawback is its relatively low surface area, which significantly hinders the sensing capabilities. Therefore, it is highly desired to prepare rGO as hierarchical nanostructures. Such a sensor was developed, whereby two-beam-laser interference was used to control the content of graphene functional groups [78]. With this approach, conductivity could be partially restored, leading to tuning of RRT due to the interaction between the water molecules and oxygen functional groups.

rGO was also prepared as a humidity sensor via modified Hummers' method, and showed faster RRT (15 s/28 s) than pure GO (18 s/31 s) [83].

Using a simple chemical modification of rGO with hydrophilic moieties can improve the sensing performance significantly. Another drawback of using rGO as a humidity sensor is the hydrophobic nature, as the reduction of GO removes the oxygen-containing functional groups. It was reported that, by using triethylene glycol chains, rGO resistive-based sensor increased the sensitivity by 31%, with ultrafast response (25 ms) and recovery (127 ms) times [82]. By using chemical functionalization of GO with carefully designed molecules allows for achieving optimal performance in humidity sensing while ensuring high selectivity to water molecules. Similar functionalization of GO and other 2D materials with specific receptors for the desired analyte, strategically selected from the well-established library of supramolecular chemistry, will enable the creation of high-performance chemical sensors for a wide range of analytes.

3.2.2. MS_2

In the covalently-bonded S–M–S (M is a transition metal such as Mo, W, Sn), MS_2-layers are bound together by van der Waals interactions. The atoms of each individual layer can be classified into basal plane sites and edge sites. The basal plane is terminated by sulfur atoms with lone-pair electrons and no dangling bonds, making it inactive. In contrast, the edge sites, where either transition metal or sulfur atoms lack coordination bonds, tend to be more active. As the analogue of graphene, semiconducting MS_2 materials, together with lower background carrier densities, are expected to display a comparative or preferable sensing performance. Furthermore, they are suited to be a good sensing platform, as this family of materials has excellent thermal stability, ideal bandgaps, very high mobility and strong electron–hole confinement. One of the first successful humidity sensors based on MoS_2 was reported in 2012, on a two- and five-layer resistor-type device, but this early work shows slow recovery and response times [104].

One of the drawbacks of the devices based on single-layer films is that they suffer from an unstable current response and are not suitable for scale-up [105]. One of the solutions is fabrication of devices based on liquid-phase exfoliated nanosheets [66]. This method of exfoliation increases the molecular adsorption area, due to the presence of dangling bonds at the edge sites and defects and vacancies. The resulting sensor showed RRT of 30/40 s. Moreover, MoS_2-based sensors show lower hysteresis than GO-based sensors, which have strong interaction between GO oxygen functionalities and the physisorbed water molecules [82]. Furthermore, few-layer nanosheets have a superior long-term stability, and they do not need to be functionalized with NPs or polymers to improve the slow recovery. Another resistive device based on a exfoliated thin film of MoS_2 was prepared by drop-casting and tested in the RH range of 0%–60% [86]. This sensor showed fast RRT of 9 s/17 s, surpassing that of bulk MoS_2. This effect can be explained by the increased surface area of the nanosheets after exfoliation, leading to more water molecules absorption sites. When MoS_2 is exfoliated into few-layer nanosheets, it exposes a significant number of low-coordination step edges, kinks, and corner atoms. These exposed edge sites play a crucial role in the material's gas sensing behavior. Another large-area few-layer MoS_2 film heterojunction was prepared with Si NWs array [87]. While the contact area of MoS_2/bulk Si is not large enough to be used as a detector, resulting in poor device performances, using NWs can increase the specific surface area, improving the sensitivity and response speed.

This sensor showed high sensitivity with the RRT of 22 s/12 s.

Although functionalization is not required for improving the stability, this process can be used to introduce other mechanisms, such as light switching. By interfacing them with organic photocromatic molecules such as spiropyran (SP), electronic characteristic of 2D materials can be modulated [69]. SP-functionalized MoS_2 light-switchable bi-functional field-effect transistors were reported [106]. SP exhibits reversible photo-isomerization from neutral (SP) form and a zwitterionic merocynine (MC) form through UV light. Owing to this effect, the functionalization of 2D surfaces with SP molecules represents a useful approach to confer to them a reversible light-controlled wettability. It was demonstrated that decorating mechanically exfoliated MoS_2 with solution-processed SP, functionalized with either ethylene glycol chains (EGO-SP) or alkyl chains (C13-SP), provides an effective approach to modulate the sensitivity of FETs to humidity changes. This is achieved by using a subtle, non-dynamic control over the interaction with environmental water molecules. The light-induced photo-switching triggers a wettability change of the SP/MoS_2 interface, which, in turn, worsens the optoelectronic properties of the MoS_2 semiconductor due to water's known role as an electron trap in MoS_2. The reversible behavior of water adsorption on the MoS_2 surface was evaluated through repeated exposure of the device to humid and dry air. It was observed that the MoS_2 device's initial performance could be partially restored after 1 h of flushing with a gentle stream of N_2 to remove the water.

While the pure MoS_2 humidity sensors suffer from low sensitivity at room temperature, coating them with metal NPs can increase their performance, but it also increases the cost. Combining GO with MoS_2 flakes to prepare a nanocomposite showed significant improvement as a chemoresistive humidity sensor [84, 85]. In the nanocomposite, water molecules attach to defect sites found in both the MoS_2 and GO layers. Additionally, the functional groups on the GO layer facilitate the adsorption of water molecules. Due to the large surface area of both MoS_2 nanoflakes and GO nanosheets, the amount of adsorbed water is significant, which in turn increases the density of charge carriers. The high response of the RGMS humidity sensor was attributed to the p–n heterojunction formed by the p-type rGO and n-type MoS_2 and the effect of the oxygen functional groups remaining on the surface of rGO.

MoS_2 can be prepared in other morphologies in order to increase the surface area. For example, MoS_2 nanoflowers were decorated with Au NPs in order to enhance electrical conductivity of the humidity sensor [107]. The prepared solution was drop casted on an electrode and mounted on a cotton mask so that it sits between the nose and the mouth and detects breathing. The sensor showed promising results with RRT of around 100 s. $MoSe_2@MoS_2$ nanoflowers were synthesized and tested as humidity sensors with a unique 3D interface structure [90]. The direct growth of MoS_2 on $MoSe_2$ nanosheets spontaneously forms a high number of n–n heterojunctions enabling more sensitive adjustment of resistivity by influencing interface electron transfer efficiency. By finding an optimal ratio of these two moieties, a sensor with improved sensitivity and response times with respect to single-phase sensors was achieved. The fastest times were 40 s/33 s for a 50:50 ratio, and the sensitivity increases almost 10 times than that of the single-phase material. Few-layer dendrites of MoS_2 were prepared via CVD method and deposited on Si/SiO_2 substrate. This fractal configuration increases the humidity sensing performance due to the increase in structural complexity and edge active sites [70]. The dendritic MoS_2 has a lower impedance and a higher rate of change for the same response time compared to the triangular MoS_2. The RRTs were 11 s/17 s and 17/24 s, respectively. Under high RH conditions, free water can penetrate the interlayer of dendritic MoS_2 nanomaterials, enhancing the dielectric constant and sensor response. The abundance of edge active sites contributes to its high conductivity and faster charge transfer, significantly improving its humidity sensing properties.

Another approach to modify and improve sensor parameters is by plasma irradiation. MoS_2 NPs were exposed to O_2 plasma, which increased the total pore volume and the specific surface area, while shifting the pore size distribution towards lower values [93]. O_2 plasma can have several effects on 1T/2H NPs. It can create defects in the crystal structure; it can act as the etching medium and remove the excessive sulfur. It is also possible that the heat generated by plasma can change the phase structure, and increase surface roughness due to formation of MoO_3. Response/recovery times for non-treated MoS_2 were 76 s/382 s, while the treated showed an increase in response time and decrease in recovery time. The decrease of the pore size slows down the diffusion of water to the pore surfaces to decrease the response time.

WS_2 was tested as humidity sensors both in the shape of nanosheets and NPs. WS_2 NPs, in the size range of 25–40 nm, were deposited on a quartz wafer [91]. The fast recovery time (13 s) is attributed to the fast desorption process of H_2O molecules from the WS_2 NP, and the slow response (12 s) is due to hydrophilic surface of the NP resulting in slow adsorption of H_2O molecules on the surface. 2D-WS_2 nanosheets were prepared via exfoliation and drop-casted on a commercial alumina substrate with Ag electrodes [92]. This resistive sensor showed RRT during a pulse between 8 and 85 RH % of 140 s and 30 s. While the reported times are not fast, the sensor showed high

stability, as it had a nearly constant response over many weeks. An all-fiber-optics sensor based on WS_2 showed rather fast RRT (1 s/5 s) [76].

SnS_2 is another layered material, where tin cations (filling the octahedral sites of the alternating layers) and sulfide anions form hexagonal structures, and it is gaining interest due to its stability. SnS_2 nanoflakes, prepared by an economically viable hydrothermal synthesis method, were tested as humidity sensors [94]. This sensor showed promising recovery time of 6 s, with the longer response time of 85 s. The response of the sensor device is most likely constrained by the strong adsorption and desorption of analyte molecules at room temperature. The thermodynamic adsorption of analyte molecules may not be highly favorable during the response time, and during the recovery phase, analyte molecules easily desorb due to their low absorption energy. As a result, the response time is significantly longer than the recovery time.

3.2.3. Flexible sensors

In order to prepare flexible sensors, TMDC materials can be introduced into flexible substrates. Given the need for permeability, biocompatibility, and comfort in wearable devices, a variety of porous materials can be utilized as flexible substrates, with the polymers being the most popular. When the nanomaterials are added to a polymer matrix to prepare a composite, unique mechanical, thermal and spectroscopic properties can be achieved that would be otherwise infeasible with the individual materials. The nanomaterials add to the improvement of the overall strength and stiffness, making them the load-bearing component, while the polymer matrix uniformly transfers the applied force to the nanomaterial, serving as a load distributor. The parameters that determine the performance of such composite are the individual properties of the constituents, their weight ratio, and the geometry and the orientation of the nanomaterial in the composite. They can improve stiffness, toughness, structural and thermal stability and tensile strength. The potential use of silicon-based nanocomposites as flexible and stretchable sensors is opening up the search for the best filler for different applications, such as motion detection, structural health monitoring, artificial electronic skin, nanosensors [108, 109]. As they can have high stretchability and sensitivity, simple manufacturing process and fast response, they can be added to wearable devices or attached directly to the skin. Nanomaterials have been shown to be superior fillers to the conventional metals and semiconductors that are limited due to their poor stretchability, brittleness and dispersion difficulties. Variety of novel nanomaterials, such as NWs [110], graphene [111–113] and metal oxides [108], have been successfully incorporated into elastomers. These fillers can be further modified to enhance their integration with polymeric matrices and substrates and to tailor

the sensing efficiency of the overall nanocomposite material.

A humidity sensor prepared from intrinsically stretchable components, instead of a combination of rigid and flexible materials, should be preferred. One of the first transparent and stretchable humidity sensors was reported on a rGO/PU (polyurethane) device [2]. This resistor-based sensor has a faster RRT than previously reported devices based on graphene and GO. It can detect the humidity of the human breath, remains stable up to a strain of 60% and after 10 000 stretching cycles at 40% strain. In other work, GO/PEI (Poly(ethyleneimine)) was sprayed on a QCM for humidity detection. This sensor exhibited high sensitivity, good RRT (53/18 s), negligible hysteresis and good repeatability [74]. QCM method was also used on a $GO/SnO_2/PANI$ nanocomposite [73]. This composite has higher surface area, accessible pore volume and pore size distribution, as well as a smaller water contact angle than the separate GO/PANI and $SnO_2/PANI$ composites. The sensing mechanism was analyzed using the Langmuir adsorption isotherm model. Water molecules are adsorbed on the $GO/SnO_2/PANI$ nanostructure through the hydroxyl, carboxyl and epoxy functional groups attached on the GO nanosheets, the amino groups on PANI nanofibers, as well as surface vacancies and defects on SnO_2 NPs. The water molecules were firstly chemisorbed on the coated film at low RH, followed by physisorption by double hydrogen bonding. At high RH, the first-layer water molecules were physisorbed through the action of double hydrogen bonding. The resulting sensor has a rather short RRT (7 s/2 s), with high stability, making this sensing mechanism promising for future applications.

Using hydrophilic polymer can improve the characteristics of GO-based sensors. PSS (poly (sodium 4-styrenesulfonate)) was added as an intercalant between individual GO platelets to enhance the water permeation characteristics [63]. The capacitive-type humidity sensor fabricated by forming metal electrodes on the film was equipped into the charge pumping system, which can produce voltage outputs as a response to humidity sensing. Compared to the pure GO sensor, GO-PSS films showed a 3 times faster response to humidity and 5 times higher voltage output. In comparison with covalent bonding in GO and RGO, non-covalent methods could offer the π bonding on graphene basal plane while retaining graphene unique electronic properties without necessarily making use of harsh chemicals. One of the approaches to non-covalently functionalize graphene was to coat it with a thin layer of hydrophilic polymer. Trough functionalization with PEI (polyethylenimine), an amine-rich polymer, the electron transfer from amine groups to graphene improved the humidity sensing performance [114]. GO/PDDA multilayer film was fabricated on a polyimide substrate using

layer-by-layer self-assembly method and tested as a capacitive humidity sensor [62]. This sensor showed high sensitivity in the 11%–97% range, as well as a fast RRTs.

MoS$_2$ flake suspended in PEO were prepared as an active layer of a resistive temperature and humidity sensor with RRT of 0.6 s/0.3 s [88]. Furthermore, compared to the bulk MoS$_2$, MoS$_2$ NPs are more promising for improving the adsorption performance of water molecules/humidity because they have a high specific surface area, which is beneficial for enhancing the number of water molecules attached on the surface of MoS$_2$. A fully-flexible humidity sensor was prepared based on a hybrid composite of rGO and MoS$_2$ with high responsivity and fast response times [67]. rGO was chemically reduced in an environmentally friendly manner, mixed with MoS$_2$ via ultrasonic dispersion and the resulting GO/MoS$_2$ dispersion was drop-casted onto a PI substrate with interdigitated electrodes. The resulting flexible humidity sensor demonstrated a responsivity of 96.7% within the RH range of 11% RH–98% RH, along with fast RRT of 0.65 s and 14.4 s, respectively.

3.2.4. MXenes

MXenes, made from thin layers of transition metal carbides, nitrides, or carbonitrides, feature alternating metal and carbon layers. To reduce or control their conductivity for humidity-sensing applications, they can be functionalized or mixed with oxides, polyelectrolytes, and polymers. Sensing mechanism of MXenes is based on the abundance of hydrophilic active sites, such as –OH and –O terminated groups for water adsorption and intercalation [115]. They are great candidates for resistive sensing, as the intercalation of water molecules within the interlayer of MXene leads to an increase of resistance. Nevertheless, the incorporation of MXenes into flexible polymers remains a challenge, as the weak affinity between MXene and polymer fibers because the hydrophilic groups of MXene is incompatible to hydrophobic nature of polymers. It usually results in the exfoliation of sensing materials during the deformation process, restricting the stability of humidity sensors. One approach to solving this issue is coating MXenes with TPU electrospun nanofibers [115]. This sensor showed RRT of 12 s/30 s, respectively, with good stability.

Using GO as the sensing layer and MXenes as the electrodes in a humidity-sensing device offers numerous advantages. While GO exhibits a strong affinity for water molecules, MXenes, known for their excellent electrical conductivity, facilitate reliable measurement of the resistance changes in the GO layer, resulting in a more sensitive humidity sensor [71]. Furthermore, GO's highly interconnected 2D layered structure facilitates rapid diffusion of water molecules, resulting in fast response times.

Its compatibility with TMNSs and flexible substrates makes it ideal for the development of flexible humidity sensors, which are well-suited for applications involving bending, molding, and mechanical stress. This type of a capacitive sensor exhibited a large response range of 6%–97%, with ultrahigh RRT of 0.8 s/0.9 s.

3.2.5. Metal oxides

Other promising humidity sensing materials are metal–oxide NWs and nanotubes [72, 77, 96–98]. While the conventional metal oxide-based sensors usually require high annealing temperatures (larger than 200 °C), NTs and NWs have many characteristic optimal for sensing, such as larger surface-to-volume ratio, higher surface activity, and better absorption performance. The tube-like nanostructures offer an increased number of efficient adsorption sites for water vapor, resulting in high surface charge densities that promote physisorption processes, thereby enhancing the sensor's sensitivity at low humidity levels. Amorphous Al$_2$O$_3$ NTs impedance-based humidity sensors were prepared, and showed promising RRT of 10 s/20 s [72]. CeO$_2$ NWs humidity sensors was reported, with the ion-type conductivity as the sensing mechanism [96]. They have a humidity-independent RRT of 3 s/3 s. LiCl-doped TiO$_2$ nanofibers [98] humidity sensors showed high RRT of 3 s and 7 s, with stability of one month with almost no changes in the impendences. Due to the 1D structure of the fibers, rapid mass transfer of water molecules to and from the interaction region is promoted, while also enhancing the rate at which charge carriers pass the barriers along the wires. Additionally, compared to 2D nanoscale films, the interfacial area between the active sensing region of the nanofibers and the underlying substrate is significantly reduced. These advantages result in a substantial improvement in the sensing signal and stability.

SnO$_2$ was used as a sensing layer and it was annealed using NIR laser, with low annealing temperature of 41 °C [95]. They were deposited on soft plastic wrap substrates. This ultra flexible SnO$_2$-based sensor can detect very small incremental changes (0.1%–2.2%) of RH in air, with RRT of 90 s/150 s. A single-NW SnO$_2$ humidity sensor was prepared as FET and tested as a humidity sensor for RH between 30% and 85% [77]. These NWs possess a large number of oxygen vacancies in the crystal; therefore, the surface is very sensitive to oxygen and water vapor in air. The RRTs were 20 s/60 s, faster than that of flat SnO$_2$. Additionally, when the sensor was kept in the moisture for about 1 h, the current still recovered to the original value, indicating that the interaction between water vapor and the surface of the NW should be dominated by physisorption, while chemisorption plays a minor role. A single ZnO NWs was deposited between gold electrodes and

placed into a chamber with humidified air [97]. These devices shows exponential change in the resistance of more than five orders of magnitude in response to a change of RH from a dry air to 60% RH air at room temperature. This is a result of a subthreshold carrier modulation in the NW core, high surface-to-volume ratio of the NW and complete exposure of the NW surface to air, due to the free standing structure. These sensors demonstrate stable behavior, reproducible switching response, with RRTs of 60 s/3 s time in response to 30% RH pulses between dry air flushes and pronounced sensitivity at elevated temperatures.

4. Human breath and touch monitoring

Respiration is one of the key human vital signs that reflects the state of the respiratory system and overall health. By monitoring respiration, health can be assessed through factors such as respiratory rate, depth, pattern, and oxygen saturation. In healthy adults, the normal respiratory rate typically ranges from 12 to 20 breaths per minute, while children tend to have a slightly higher rate. Abnormal rates can signal health issues such as anxiety, hypoxia, fever and other conditions, whereas slow breathing can be indicative of medication overdose or neurological disorders. The breathing pattern shows the regularity and rhythm of breathing. However, traditional respiratory monitoring methods often cannot provide real-time, synchronized, and comprehensive measurements. Typically, real-time monitoring requires wearing medical respiratory equipment, which can significantly interfere with normal activities. Therefore, the development of flexible respiratory monitoring e-skins is a crucial advancement in healthcare. Those novel respiratory sensors are designed to monitor human breath non-invasively by detecting, measuring and interpreting respiratory data in real-time. Some of the parameters they should track are respiratory rate and volume, and the composition of the exhaled gas. These parameters can be further used to diagnose respiratory disorders, and guide the physical activity after the recovery. For example, such wearable sensors were tested for early diagnosis of Covid-19, through non-invasive monitoring of the respiratory behavior, body temperature and blood oxygen level [116]. Graphene FETs were also able to detect SARS-CoV-2 spike protein [117]. This method of monitoring can be particularly useful for people outside of hospital settings. Specifically, humidity sensors can effectively differentiate the inhalation and exhalation phases, as well as the depth of each respiratory cycle, by detecting changes in RH during the inhale and exhale processes. Therefore, the sensor should be placed near the nostril or mouth, realizing contactless measurement. Additionally, respiratory monitoring based on RH in the airflow is minimally influenced by environmental factors such as temperature,

noise, and others, ensuring reliable data. The breathing process consists of two periodic stages: inhaling air that contains O_2 into the lungs and exhaling CO_2 through the nose or mouth. The complete cycle, from inhalation to exhalation, is referred to as a respiration cycle. The airflow can be monitored as exhaled air is warmer, has higher humidity, and contains more water molecules than inhaled air. In addition to breath monitoring, the real-time monitoring of the human skin humidity level via a skin patch can be an important development in prevention of fatal illnesses due to dehydration.

Previously mentioned first transparent and stretchable a rGO/PU sensor was able detect the humidity of the human breath [2]. The device was placed at a distance of 3 cm from the nose, and successfully detected the resistance change between dry air, ambient air and human breath. To test different environments, it was attached to the human finger, providing the feedback on the humidity of the environment, moisture of human skin and dampness of objects. A GO sensor, shown in the top left panel of figure 10, was prepared in an impedance setup and showed ultrafast RRTs of less than 100 ms for thickness of 15 nm, being among the fastest humidity sensors to be reported, comparable to the commercially available optical sensors [68]. It was further tested for speaking, breathing and whistling. The ultrafast performance of these sensors allows the capture of fine features due to moisture modulation during speech. This sensor was also capable of recognizing different whistled tunes, by capturing their distinct patterns characteristic. The patterns were then analyzed using FFT and Principal Components Analysis, resulting in clear clustering for each tune. After training the system with 10 data points per tune, each whistled tune was classified and recognized with an accuracy of approximately 90%, enabling user authentication. A GO/PDDA capacitive sensor was tested for human breath monitoring [62]. The breath response characteristics for a normal adult were measured over 45 s, during which 11 repetitive breathing cycles were observed. The capacitance response showed a sharp increase during exhalation and a drop during inhalation, corresponding to the breathing cycles. Notably, the sensor's response and recovery times were both within 1 s, enabling the capture of fine details related to moisture modulation in human breath. Another GO-based single-layered sensor chip with multiple sensing (figure 9, left panel, middle) was able to monitor human breathing, nose breath and human touch [81]. Because the three different sensors operate independently, as explained in section 3.2.1, they have good sensitivity.

MoS_2 NPs exposed to O_2 plasma were also tested as a human breath sensor and for skin monitoring [93]. The breathing test was conducted with three different conditions, including deep breath, normal
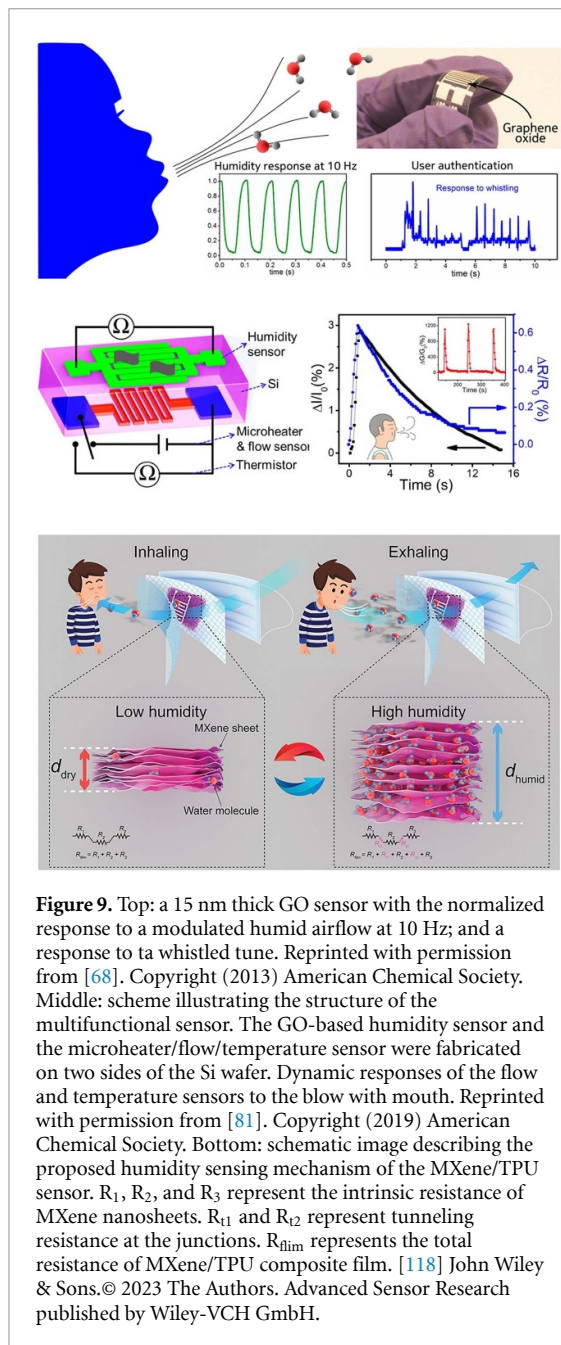
Figure 9. Top: a 15 nm thick GO sensor with the normalized response to a modulated humid airflow at 10 Hz; and a response to ta whistled tune. Reprinted with permission from [68]. Copyright (2013) American Chemical Society. Middle: scheme illustrating the structure of the multifunctional sensor. The GO-based humidity sensor and the microheater/flow/temperature sensor were fabricated on two sides of the Si wafer. Dynamic responses of the flow and temperature sensors to the blow with mouth. Reprinted with permission from [81]. Copyright (2019) American Chemical Society. Bottom: schematic image describing the proposed humidity sensing mechanism of the MXene/TPU sensor. R_1, R_2, and R_3 represent the intrinsic resistance of MXene nanosheets. R_{t1} and R_{t2} represent tunneling resistance at the junctions. R_{flim} represents the total resistance of MXene/TPU composite film. [118] John Wiley & Sons.© 2023 The Authors. Advanced Sensor Research published by Wiley-VCH GmbH.

breath, and fast breath. The breath testing indicated a good response, and the sensor also distinguished wet and dry hands clearly. Inhalation was indicated by the decrease of the resistance, and exhalation by the increase of the resistance.

A sensor based on MXenes with TPU electrospun nanofibers sensors was tested for respiratory monitoring, and embedded into the middle layer of a face mask to avoid the contamination from saliva, as shown in figure 10, left panel, bottom [118]. When a sensing material is added to a flexible and wearable face mask, its resistance has to be stable upon bending. As the MXene nanosheets are abundantly wrapped on the TPU fibers to form a conductive network, the resistance remained stable as the bending

angle increased from 0° to 210°, indicating good stability and flexibility. The sensor showed promise for distinguishing different degrees of breathing and accurately monitoring respiratory signals during different physical activities [118]. Another MXenes sensor, combined with GO, successfully detected moisture from human breath and fingertip [71]. MXene/MWCNT-sensing material was drop-coated on pristine fabric and cured by UV light. The electrical circuit was printed by conducting ink and encapsulated by polyimide to avoid short circuiting due to the water vapor. Finally, the whole sensor with the encapsulated circuit was attached inside the mask near the nose as a wearable wireless humidity sensing tag, as shown in figure 9, right panel [119]. The size of the entire tag was 2 cm × 4 cm. The fabric sensor, coupled with a flexible detecting tag, enabled the detection of respiration and the accurate identification of various breathing patterns. It was also able to record respiration signals accurately, even under deformation caused by movement for standing, walking and running. This sensor also provides a practical approach for real-time, wireless respiration monitoring using electronic fabrics.

A flexible humidity sensor, based on SnO_2 thin film, with the food plastic wrap as the substrate material, was integrated into a face mask to detect the breathing pattern [95]. Slow, normal, and fast respiratory patterns were monitored by the real-time current curves, with respiratory rates of 8, 20 and 29 breaths per minute, respectively. Sensor was put inside a glass chamber with a fixed background RH of 70%, 60%, and 50%, and the breath was released 5 cm away from the substrate.

Another fully flexible humidity sensor based on rGO/MoS_2 demonstrated finger proximity detection and non-touch switching [67]. The device was placed at 3 cm away from the human nose. When the breathing rate was 20 breaths per minute (rapid breathing), the device showed a responsivity of 70%. However, at a slower breathing rate of 10 breaths per minute, the responsivity increased to over 90%, demonstrating the good reliability. Water molecules adsorbed and desorbed quickly on the device surface in both rapid and slow breathing modes, resulting in a strong response to human breathing. Additionally, a series of finger proximity detection experiments were conducted in an atmosphere with 46% RH. The results showed that the relative resistance of the device increased gradually from 48.4% to 95.6% as the distance between the finger and the device surface decreased from 2 cm to 0.5 cm. These human respiration and finger proximity measurements demonstrate that the device has potential applications in wearable technology.

A heterojunction made of 3D $MoSe_2@MoS_2$ nanoflowers was positioned at 8 cm from human mouth to monitor respiration, and the finger was positioned
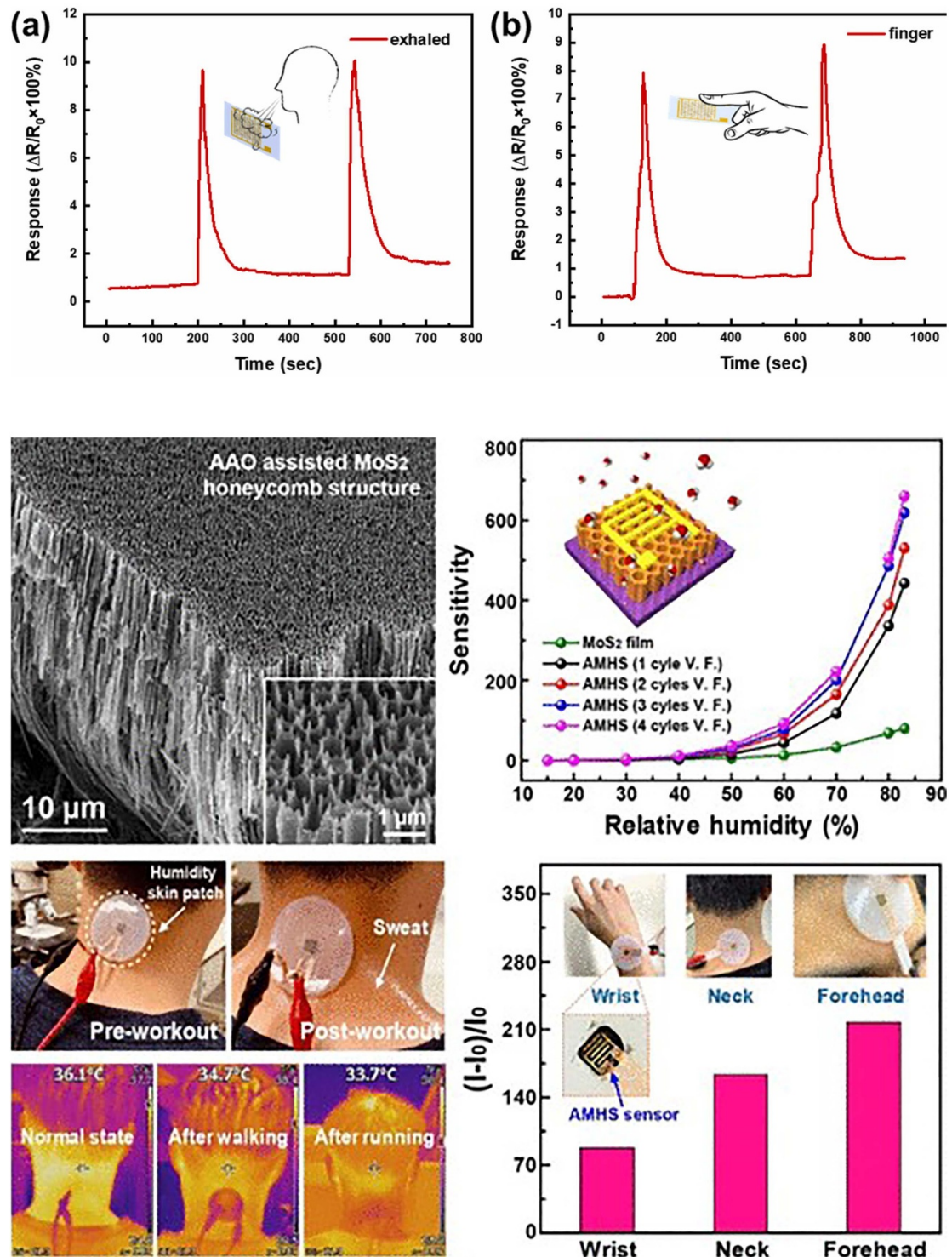
Figure 10. Top panel: (a) the continuous monitoring of the sensor to human deep breath. (b) Repeatability test of the sensor for finger approach distance of 2 cm. Reprinted from [90], Copyright (2024), with permission from Elsevier. Middle panel: FESEM image of the sensor and sensitivity as a function of RH. A bar chart in inset illustrating sensitivity dependence on the RH. Bottom panel: photograph of the attached skin humidity patch on the neck before and after sweating from exercise (top), and the variation in body temperature measured by the IR image camera (bottom). Comparison of the relative current variation in volunteers measured by the skin humidity patch from the neck at different physical conditions. Reprinted with permission from [89]. Copyright (2020) American Chemical Society.

at 2 cm to test for human touch, as shown in the top panel of figure 10 [90]. Both response curves show potential for non-contact detection.

A resistive-type humidity sensor made of a 3D-honeycomb structure based on MoS_2 NTs showed a promising response in humidity in the atmosphere, human breath and human skin in a 20%–85% RH range [89]. As a result, it can be incorporated in multifunctional sensing applications using skin humidity, human respiration pattern and speech

recognition using humidity in exhaled air. These open-ended NTs combined in a honeycomb provide a large number of absorption sites for H_2O molecules. The sensor showed ultrafast RRTs of 0.47 s/0.81 s, respectively, much faster than sensors based on 2D MoS_2. In order to test it in human skin conditions, the sensor was tested in the human body temperature range (31 °C–38 °C) at room RH condition. The sensor showed promise for non-contact applications, as the resistance change was almost negligible when it was placed at 3.8 mm above the heater, showing that it is not affected by the human body temperature, as depicted in the bottom panel of figure 10.

While reducing the MoS_2 flake size leads to formation of S-vacancies as active sites for water molecule absorption, a honeycomb structure contains an even larger number of sites. The absorbed molecules can easily diffuse into the NTs through the open pores, while the defect-rich surface with large number of S-vacancies on the open NT edges, together with the cylindrical shape, allows the water molecules to absorb and assemble easily. In addition, it was assembled into a wearable patch, detecting human skin humidity under different physical conditions and regional sweat rate.

5. Humidity sensors in agriculture

5.1. Soil moisture
Another field of use of humidity sensors is agriculture, as the estimation of soil moisture is of critical importance to avoid over-wetting or water deficiency in order to gain maximal crop production. Sensors based on 2D materials can be utilized as the capacitive devices as they can provide a direct relationship of the soil moisture content and dielectric permittivity of the soil [120]. A device prepared based on MoS_2 sheets showed good sensitivity for both black and red soil, it demonstrated stable performance over 6 months and good reproducibility with response time of 35 s [66]. In another study, a variety of 2D materials were tested as low-cost soil moisture capacitive sensors [121]. The best sensitivity (30%) was reported for MoS_2, following by MoO_3 (13%), GO (11%) and V_2O_5 (9%).

5.2. Plant transpiration monitoring
Efforts have been made to monitor the water status of plants using sensors that can be attached to leaves or placed near plants. However, these sensors with rigid designs often face mechanical incompatibility with the soft surfaces of plant leaves. In this regard, recent advancements in flexible electronics have paved the way for the development of leaf-mounted sensors, which can provide real-time and quantitative information about the water status of plants.

A flexible capacitive-type GO-based humidity sensor with low hysteresis, high sensitivity (3215.25 pF/% RH), and long-term stability was prepared in order to be directly attached onto plant leaves for real-time transpiration tracking [65]. The sensor was fabricated by laser-induced graphene (LIG) interdigital electrode on a PI film, as PI serves as both a precursor for producing LIG and a humidity sensing material. To further improve the sensor's performance, GO was incorporated as the humidity sensing material. The prepared sensor offers excellent flexibility, high sensitivity, and long-term stability, enabling multifunctional applications such as non-contact humidity sensing. Moreover, it can be attached to the surface of leaves without causing any visible damage to plants. By recording capacitance signals, real-time and long-term monitoring of plant transpiration is possible. It can be observed that the capacitance increases 1 d after watering, but over time, it significantly decreases, resembling the pristine condition. However, when the plant was watered again, the capacitance increased accordingly. These findings suggest that the humidity level on the plant surface varies depending on the plant's water conditions. Overall, these results demonstrate that the plant's response to drought can be translated into visible electrical signals, highlighting the potential of the fabricated flexible humidity sensor in the field of intelligent agriculture.

6. Human exposure and environmental impact of 2D materials

The relationship between 2D materials and biological systems is bidirectional, involving interactions where both components influence each other and undergo simultaneous changes. Human exposure to 2D materials falls into three categories: occupational, environmental and biomedical, based on three basic modes of the interactions with biological systems: chemical, mechanical and electronic (see figure 11) [122]. Occupational exposure is already occurring among researchers and is expected to become more significant for workers in nano-manufacturing industries as the field expands. In these settings, workers are primarily exposed to materials in their original synthesized form or as intermediates and byproducts during production processes, highlighting the need to study their biological interactions in these states. In contrast, environmental exposure arises from the unintentional release of these materials, which may undergo chemical transformations before re-entering human systems through air, food or water. Biomedical exposure happens in a somewhat controlled manner and undergoes rigorous investigation through processes which ensure safety, efficacy and biocompatibility before therapeutic applications or medical device approvals. Moreover, synthesis methods play a significant role. Occupational and industrial handling of 2D materials, especially in dry or

Figure 11. Exposure types and pathways for emerging 2D nanomaterials. Reproduced from [56] with permission from the Royal Society of Chemistry.
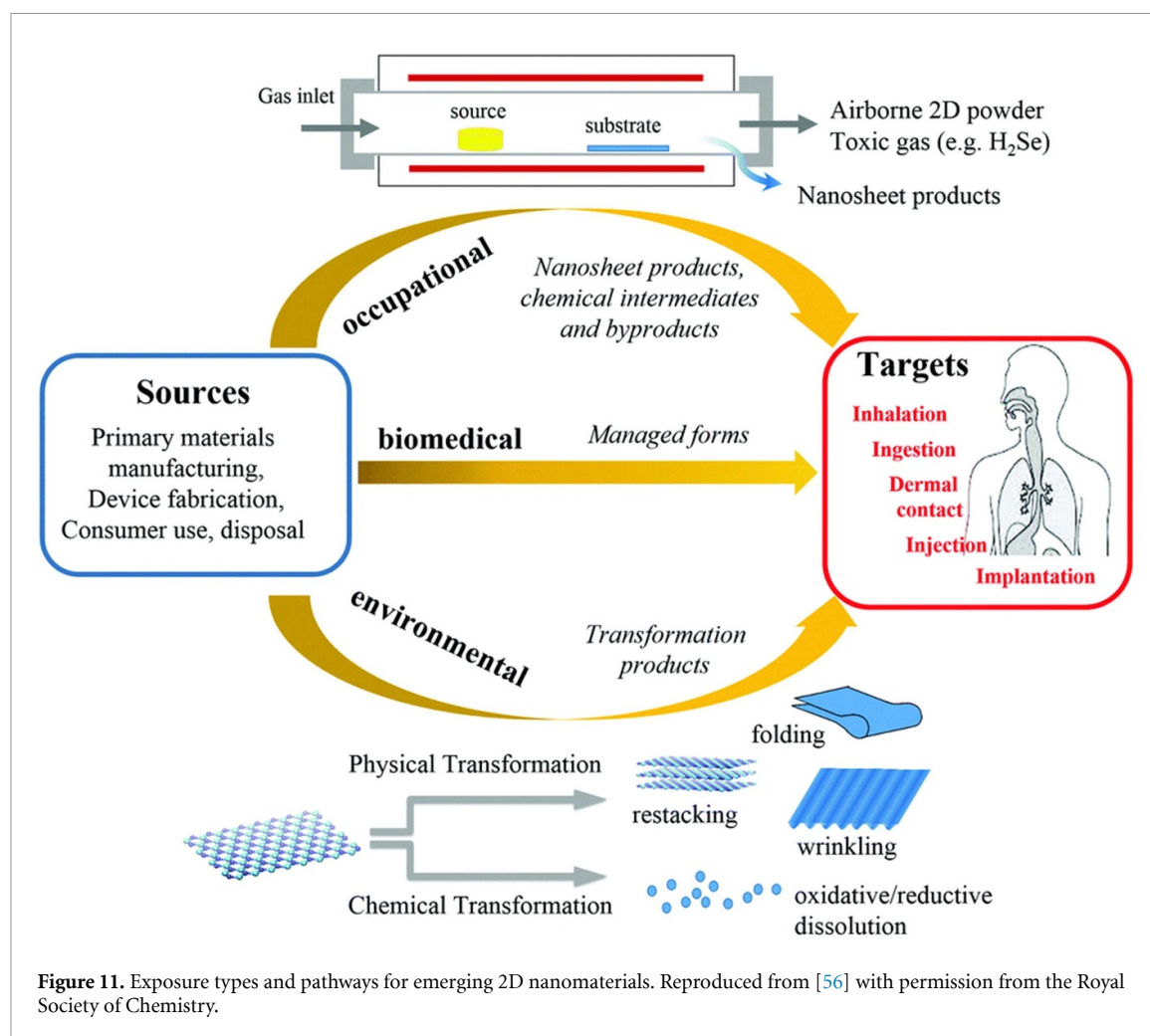
powder form, can result in airborne particles that pose inhalation risks and potential deposition into surrounding environment. Aggregation, sedimentation or restacking behaviors of 2D materials in natural systems may further affect their transport and reactivity. However, their widespread adoption is still limited by challenges including large-scale production, long-term durability and economic feasibility. The overall environmental and health risks of engineered nanomaterials are generally low, particularly when strategies like green synthesis and immobilization are applied to reduce exposure [123]. The first in-human study assessing the controlled inhalation of GO on the cardiorespiratory system demonstrated good tolerance without any adverse effects. Blood proteomics revealed minimal changes in plasma protein levels, and only a mild increase in thrombus formation was observed in an *ex vivo* arterial injury model. Overall, short-term exposure to highly purified, ultra-thin GO nanosheets did not result in any significant harm in healthy individuals. These findings support the safe implementation of human exposure studies in clinical settings and provide a foundation for evaluating the biological effects of other two-dimensional nanomaterials [124].

The potential negative impacts of 2D materials remain to be extensively explored, especially as the number of newly synthesized materials continues to grow. Even slight modifications in their composition by, for example, functionalization can significantly alter their physicochemical properties, making the range of possible effects vast and largely unpredictable. The environmental fate of 2D materials is complex due to their diverse chemistries and physical forms. Once released, these materials may undergo chemical (and physical) transformations such as oxidation, sulfidation, aggregation, dissolution, changing chemical state [125, 126] etc, induced by environmental conditions in the presence of atmospheric oxygen, moisture, sunlight and microbial species [127, 128]. Some materials, such as MoS_2, although considered to have low toxicity in bulk, in 2D and nanoscale versions can generate ROS and exhibit dose-dependent cytotoxicity. Moreover, TMDs may degrade and release heavy metals or toxic elements like selenium and tellurium, which are known to accumulate and disrupt biological functions. Their persistence, mobility and interaction with environmental components like soil, water and microbial population raise concerns about long-term

ecological effects. TMDs have been shown to degrade more rapidly under ambient conditions (exposure to air and moisture) compared to graphene-based materials, primarily due to the presence of defect sites and grain boundaries. For instance, MoS_2 undergoes gradual oxidation in air to form MoO_3, and in aqueous environments it further breaks down into soluble MoO_4^{2-} and SO_4^{2-} ions (see figure 3(d)) [128, 129]. Members of the 2D material family do not exhibit uniform resistance to oxidation, and their degradation can occur even at physiologically and environmentally relevant concentrations of oxidative compounds, such as H_2O_2, in both single- and multilayer forms, as observed with pristine graphene [130]. TMDs are also susceptible to H_2O_2-induced oxidation. This oxidative degradation can compromise their electrical, mechanical, and chemical properties, ultimately limiting their effectiveness in environmental applications. Mitigation strategies include procedures such as surface passivation, chemical functionalization and development of protective coatings and nanocomposites. Nanocomposites are particularly interesting due to the synergistic properties they offer [131]. Additionally, surface and interfacial behavior of 2D materials may also be altered by the exposure to common airborne contaminants such as hydrocarbons, water vapor and oxygen. Even at trace levels, they can impact the wettability, electrochemical performance and doping, masking the intrinsic properties of the material (i.e. hydrophobicity of graphene is largely due to adsorbed hydrocarbons rather than its true behavior) [132]. Cracking and quenching (corrosion) occur in MoS_2 and WS_2 after they are stored in the presence of water and oxygen for several months. Recently published research on WS_2 nanotubes found that material stored for a long time in protected atmosphere oxidized only marginally, while other, kept under less controllable conditions suffered severe autocatalytic oxidation [133].

Equally important is the role of these materials in environmental remediation, as a result of synergy between 2D materials and electrochemical methods (electrooxidation and electroreduction) [134, 135]. Their high surface area, tunable surface chemistry and exceptional conductivity is what make them highly effective for removing pollutants from air, water and soil. These applications include the adsorption and absorption of heavy metals, drugs, dyes and other potentially toxic compounds. United Nations' sustainable development goal 6 aims to ensure access to clean water and sanitation for all, a challenge that can be significantly addressed through the innovative use of 2D materials. With their exceptional filtration, sensing, and antimicrobial properties, 2D materials can offer solutions for efficient water purification and real-time quality monitoring [136]. Materials like graphene, MXenes, and TMDs are extensively studied for their role in electrochemical sensing,

catalytic degradation of pollutants and fabrication of advanced filtration membranes [137–139]. Notably, MXenes, particularly $Ti_3C_2T_x$, have shown excellent performance in adsorbing heavy metals like Pb^{2+}, Cr^{3+}, and Cd^{2+} due to their rich surface functional groups and high charge capacity. GO and its derivatives are widely used as membranes for water purification, thanks to their ultrahigh water permeability and chemical stability [140, 141]. Degradation of organic pollutants is also possible due to photocatalysis [142, 143]. Environmentally, the use of MoS_2 nanofertilizers reduces dependence on synthetic nitrogen inputs, thereby lowering greenhouse gas emissions and minimizing ecological impact [144]. The vision of clean energy generation is becoming increasingly achievable through the advancement of nanomaterial-based engineering approaches.

7. Outlook and future perspectives

The use of 2D materials in regenerative medicine presents immense potential, but it is held back by critical biocompatibility and toxicity challenges. Factors like size, surface charge and functionalization influence their interaction with biological systems, potentially triggering inflammatory responses, immune reactions or long-term toxicity due to accumulation. Additionally, concerns regarding mechanical stability, controlled drug release, large-scale production, regulatory approval and environmental impact necessitate advanced material engineering and thorough safety assessments to ensure their safe and effective clinical translation [31]. The overall biological impact of 2D materials is strongly governed by their chemical composition, surface characteristics and the extent of exfoliation, all of which shape their interactions with cellular systems. In the case of TMDs, both *in vitro* and *in vivo* studies highlight that their elemental composition, particularly the choice of chalcogen (e.g. sulfur, selenium, tellurium), plays a crucial role in cytotoxicity. Telluride and selenide variants generally elicit more pronounced toxic effects than sulfides, likely due to higher chemical reactivity and chalcogen release [145]. The exfoliation state further modulates bioactivity: nanosheets with high degrees of exfoliation expose more reactive surface area and edge sites, often leading to elevated cellular responses such as oxidative stress and inflammation [146, 147]. Conversely, TMDs that are well-characterized and stably dispersed, especially MoS_2, tend to exhibit lower toxicity profiles and greater biocompatibility, stressing the importance of controlled synthesis and processing in developing safe 2D materials for biomedical and environmental applications [148, 149]. Designing synthesis methods that are not only scalable and cost-effective but

also environmentally sustainable is essential for transitioning from laboratory research to industrial production. Furthermore, addressing the existing gaps in regulatory strategy and standardization is crucial to support the broader commercialization and clinical integration of nanomaterial-based technologies [150].

The previously discussed challenges in the practical utilization, from laboratory research to clinical application, can largely be described as 'cellular response heterogeneity driven by material tunability'. Overcoming these issues requires not only advancements in synthesis/production, standardization and characterization of these materials, but also hand-in-hand progress in SC biology. Recent insights into SC biology have revealed how mechanical and chemical cues from the microenvironment influence cell fate through mechanotransduction pathways [151]. This mechanotransductive signaling integrates the microenvironment, cell membrane, cytoskeleton and nucleus, ultimately guiding SCs behavior and fate. To bridge the gap between controlled laboratory settings and large-scale production, as well as for translation to clinical studies, the development of robust legal frameworks, standards, and protocols is essential. Additionally, mimicking physiological conditions through mathematical modeling, integrated data analysis, and the design of patient-specific therapies will be beneficial to the successful application of 2D materials in regenerative medicine. It offers cost-effective, ethically clean and fast solution [152].

Overall, graphene-based materials pose both risks and opportunities, with toxicity varying based on their form, properties and exposure route. Inhalation can cause lung inflammation, ingestion may disrupt gut microbiota, dermal contact might lead to irritation, and systemic exposure can result in organ accumulation and inflammation. Despite these concerns, graphene shows promise in biomedical applications such as drug delivery, antimicrobial treatments and cancer therapy [153]. Discrepancies that arise between *in vitro* and *in vivo* conditions during the evaluation of nanomaterials and their biocompatibility are the consequences of inability to replicate the complex biological environment of systemic circulation (in comparison to *in vitro* cell culture media). This mismatch, based on how the biomolecular corona differs *in vivo* and *in vitro*, can lead to biases, stressing the importance of the comprehensive approach, using advanced data analyses and machine learning [154]. While no 2D material is universally superior, GO and rGO dominate in bone, cardiac and neural applications due to their conductivity and compatibility. MXenes contribute in cardiac repair and wound healing because of their antioxidative and electroactive nature. TMDs like MoS_2 and

WS_2 show great promise in osteogenesis and neuroregeneration due to their semiconducting and photothermal properties, whereas hBN can be considered beneficial in adipogenesis and neural tissue regeneration, (see table 1). The future of regenerative medicine lies in precisely engineering these materials for specific tissue environments while ensuring long-term safety and performance.

In addition, 2D and related materials have become a fertile ground for preparation of a variety of sensors, with the humidity sensing being among the most promising. These sensors can be used in different scenarios, such as for simple monitoring of the RH of the environment, to the human health and agriculture monitoring. In the field of agriculture, these sensors can be utilized to detect soil moisture, or the transpiration cycles of plants, whereby they are coming to a direct contact with the environment. Furthermore, as they can have high stretchability and sensitivity, simple manufacturing process and fast response, they can be added to wearable devices or attached directly to the skin. This is another incentive for studying their biological activity and toxicity, as these novel devices have to be biocompatible if they are to be in contact with human skin and/or soil. This is especially important as the best sensing materials so far are exfoliated or surface modified with reactive surface area and edge sites, which usually leads to elevated cellular response.

In this review, we discussed different sensing mechanisms, and summarized the performance of different families of materials. While the standard types of sensors, such as capacitive and resistive, are relatively easy to fabricate and test, new methods are needed in order to minimize the size and the cost of the sensor. For example, sensors based on fiber optics can be easily integrated into the pre-established fiber optic systems. While developing new sensing mechanisms can lead to improved general performance of the device, another approach is to prepare a material with the best characteristics for the specific need. One way to enhance the sensitivity and RRTs is to increase the density of active edge sites of nanomaterials. This can be achieved via size control, where reducing the size leads to the increase in the density of edge sites. Another approach is shape control, where nanomaterials with unique structures, such as dendrites, nanotubes, NWs and nanoflowers, intrinsically containing a high number of edge sites, improve sensing performance. While rigid sensors based on GO and rGO showed promising characteristics and high RRTs, similar sensors based on or surface-modified or TMDC nanotubes showed superior response. For example, as summarized in table 2, sensor based on plasma-irradiated MoS_2 NPs has a far better performance than MoS_2 sheets, with sub-second RRTs [93]. The best performance was achieved by rGO

functionalized with hydrophilic moieties, with ultra-fast RRTs of 25 ms/127 ms [82]. Nevertheless, the stiffness of these materials limits their use for human health sensing.

The increasing need to move away from intrinsically rigid to flexible and wearable sensors requires finding a sensing material that responds well to mechanical deformations through a change in the electrical signal. The best way to achieve flexibility is to combine 2D and TMDC materials with polymer matrices. Some of the most promising candidates are rGO/PU [2], a combined sensing material made of rGO/MoS$_2$/PI, MXene/GO/COC [71], with the best two reported sensors being MoS$_2$-based: MoS$_2$/PEO with RRTs of 0.6 s/0.3 s [88] and MoS$_2$ NTs/Ecoflex with 0.5 s/0.8 s [89]. Therefore, a good approach to improving the performance of the polymer matrix is to use TMDC nanotubes or NWs. While the CNTs have a good potential, they have a few setbacks as well-they do not disperse well in most organic solvents, resulting in poor homogeneity when mixed with a polymer matrix, so they have to be functionalized in order to enhance the interaction with the solvent. On the other hand, various inorganic TMDC NTs promise a wide spectrum of physical effects beyond the physics of CNTs [155]. They have a high aspect ratio, high specific surface area and excellent mechanical and vibrational/acoustic properties, making them suitable as composite nanofillers as only a small amount can be used for forming a conductive path [156, 157]. The high aspect ratio can also improve the low electrical percolation of the insulating polymer matrix and form an efficient electrical network. Furthermore, MS$_2$ NTs disperse well in all commonly used solvents, simplifying the composite preparation [158]. As previously mentioned, properly stored WS$_2$ NTs oxidize only marginally even after more than 20 years [133]. Another family of nanomaterials that shows a great promise as a filler, is the family of metal oxides, as seen in table 2 [159]. Their substoichiometric MO$_{3-x}$ ($0 \leqslant x \leqslant 1$) phases grow in different shapes, such as NWs, flakes, needles and sheets. The optical, electrical and structural properties depend strongly on the degree of the reduction [160]. Together with the already reported sensors on stoichiometric CeO$_2$ [96], ZnO [97], TiO$_2$ [98] and SnO$_2$ NWs [77], W$_5$O$_{14}$ and W$_{18}$O$_{49}$, are interesting candidates due to their large aspect ratio, while the presence of photoluminescence and localized surface plasmon resonances can introduce interesting optical effects. Nevertheless, one important aspect that has to be taken into account is the cost, ease of preparation and the field of use of a specific sensor. While some applications require high sensitivity and fast RRT, for some practical uses, such as a quick diagnostic tool outside the hospital setting, the priority should be the cost and the ease of use. For example, 20 breaths per minute is defined as rapid breathing, therefore, a sensor that has a complicated and expensive synthesis method but RRT of microseconds might be superior in performance, but not necessary for practical purposes.

Future health sensing potential of these materials is vast. In addition to devices reviewed here, 2D materials have been slowly incorporated into different types of health sensors. They were reported as respiration sensors for estimation of blood oxygen saturation (SpO$_2$) [161]. LIG was placed on a PI tape, and this patch-like sensor detected the changes in mechanical deflection (such as chest movement), and measured the respiration rate in real time. Graphene-based biosensors have also been successfully integrated into an automated sensing platform for transporter protein drug delivery, showing to be biocompatible with a picomolar ionic sensitivity [162]. Furthermore, inks made of 2D materials were prepared, compatible with the standard inkjet printing. For example, water-based additive-free ink was prepared from nitrogen-doped carboxylated graphene [163]. This ink was used to fabricate fully inkjet-printed electrodes, which successfully enabled the electrochemical detection of the key neurotransmitter dopamine. The carboxyl groups in NGA ink also enable covalent attachment to biomolecules such as antibodies or aptamers, making it possible to create fully inkjet-printed biosensors.

Overall, 2D and related TMDC materials possess a variety of properties desirable for fabrication of sensors for human health monitoring. Nevertheless, their biological impact has to be thoroughly studied before they can be mass-produced.

Data availability statement

All data that support the findings of this study are included within the article (and any supplementary files).

Acknowledgments

ORCID iDs

Jasmina Lazarević ⓘ 0000-0001-8980-1688
Bojana Višić ⓘ 0000-0002-2065-0727

References

[1] Sun X, Guo X, Gao J, Wu J, Huang F, Zhang J-H, Huang F, Lu X, Shi Y and Pan L 2024 E-skin and its advanced applications in ubiquitous health monitoring *Biomedicines* **12** 2307

[2] Trung T Q, Duy L T, Ramasundaram S and Lee N-E 2017 Transparent, stretchable, and rapid-response humidity sensor for body-attachable wearable electronics *Nano Res.* **10** 2021–33

[3] McKinley K L, Longaker M T and Naik S 2023 Emerging frontiers in regenerative medicine *Science* **380** 796–8

[4] Shafiq M, Ali O, Han S-B and Kim D-H 2021 Mechanobiological strategies to enhance stem cell functionality for regenerative medicine and tissue engineering *Front. Cell Dev. Biol.* **9** 747398

[5] Pittenger M F, Discher D E, Péault B M, Phinney D G, Hare J M and Caplan A I 2019 Mesenchymal stem cell perspective: cell biology to clinical progress *npj Regen. Med.* **4** 22

[6] English K P, Mahon B J and Wood K 2014 Mesenchymal stromal cells; role in tissue repair, drug discovery and immune modulation *Concurr. Drug Deliv.* **11** 561–71

[7] Zakrzewski W, Dobrzyński M, Szymonowicz M and Rybak Z 2019 Stem cells: past, present, and future *Stem Cell Res. Ther.* **10** 68

[8] Gokce C, Gurcan C, Delogu L G and Yilmazer A 2022 2D materials for cardiac tissue repair and regeneration *Front. Cardiovasc. Med.* **9** 802551

[9] Qasim M, Chae D S and Lee N Y 2020 Bioengineering strategies for bone and cartilage tissue regeneration using growth factors and stem cells *J. Biomed. Mater. Res. A* **108** 394–411

[10] Hasnain A and Tarasov A 2023 Graphene-based electronic biosensors for disease diagnostics *Graphene Field-Effect Transistors: Advanced Bioelectronic Devices for Sensing Applications* ed O Azzaroni W Knoll (Wiley) pp 71–101

[11] Kostarelos K, Aguilar C and Garrido J A 2024 Clinical translation of graphene-based medical technology *Nat. Rev. Electr. Eng.* **1** 75–76

[12] Sekuła-Stryjewska M, Noga S, Dźwigońska M, Adamczyk E, Karnas E, Jagiełło J, Szkaradek A, Chytrosz P, Boruczkowski D and Madeja Z 2021 Graphene-based materials enhance cardiomyogenic and angiogenic differentiation capacity of human mesenchymal stem cells *in vitro*–focus on cardiac tissue regeneration *Mater. Sci. Eng. C* **119** 111614

[13] Jalilinejad N *et al* 2023 Electrically conductive carbon-based (bio)-nanomaterials for cardiac tissue engineering *Bioeng. Transl. Med.* **8** e10347

[14] Cahill T J, Choudhury R P and Riley P R 2017 Heart regeneration and repair after myocardial infarction: translational opportunities for novel therapeutics *Nat. Rev. Drug Discovery* **16** 699–717

[15] Hu X, Yu S P, Fraser J L, Lu Z, Ogle M E, Wang J-A and Wei L 2008 Transplantation of hypoxia-preconditioned mesenchymal stem cells improves infarcted heart function via enhanced survival of implanted cells and angiogenesis *J. Thoracic Cardiovasc. Surg.* **135** 799–808

[16] Lee W C, Lim C H Y, Shi H, Tang L A, Wang Y, Lim C T and Loh K P 2011 Origin of enhanced stem cell growth and differentiation on graphene and graphene oxide *ACS Nano* **5** 7334–41

[17] Ikram R, Shamsuddin S A A, Mohamed Jan B, Abdul Qadir M, Kenanakis G, Stylianakis M M and Anastasiadis S H 2022 Impact of graphene derivatives as artificial extracellular matrices on mesenchymal stem cells *Molecules* **27** 379

[18] Heo J, Choi J, Kim J Y, Jeong H, Choi D, Han U, Park J H, Park H H and Hong J 2021 2D graphene oxide particles induce unwanted loss in pluripotency and trigger early differentiation in human pluripotent stem cells *J. Hazard. Mater.* **414** 125472

[19] Qi X, Liu Y, Yin X, Zhao R, Zhang W, Cao J, Wang W and Jia W 2023 Surface-based modified 3D-printed BG/GO scaffolds promote bone defect repair through bone immunomodulation *Composites B* **257** 110673

[20] Sulaksono H L S, Annisa A, Ruslami R, Mufeeduzzaman M, Panatarani C, Hermawan W, Ekawardhani S and Joni I M 2024 Recent advances in graphene oxide-based on organoid culture as disease model and cell behavior–a systematic literature review *Int. J. Nanomed.* **19** 6201–28

[21] Romaldini A, Spanò R, Veronesi M, Grimaldi B, Bandiera T and Sabella S 2024 Human multi-lineage liver organoid model reveals impairment of CYP3A4 expression upon repeated exposure to graphene oxide *Cells* **13** 1542

[22] Yu S, Wang L, Chen M, Chen Y and Peng Z 2025 MXene-incorporated conductive hydrogel simulating myocardial microenvironment for cardiac repair and functional recovery *Biomacromolecules* **26** 2378–89

[23] Edrisi F, Baheiraei N, Razavi M, Roshanbinfar K, Imani R and Jalilinejad N 2023 Potential of graphene-based nanomaterials for cardiac tissue engineering *J. Mater. Chem. B* **11** 7280–99

[24] Zaszczyńska A, Zabielski K, Gradys A, Kowalczyk T and Sajkiewicz P 2024 Piezoelectric scaffolds as smart materials for bone tissue engineering *Polymers* **16** 2797

[25] Collins M N, Ren G, Young K, Pina S, Reis R L and Oliveira J M 2021 Scaffold fabrication technologies and structure/function properties in bone tissue engineering *Adv. Funct. Mater.* **31** 2010609

[26] Koons G L, Diba M and Mikos A G 2020 Materials design for bone-tissue engineering *Nat. Rev. Mater.* **5** 584–603

[27] Kang E-S, Kim D-S, Suhito I R, Lee W, Song I and Kim T-H 2018 Two-dimensional material-based bionano platforms to control mesenchymal stem cell differentiation *Biomater. Res.* **22** 10

[28] Yadav S, Singh Raman A P, Meena H, Goswami A G, Bhawna, Kumar V, Jain P, Kumar G, Sagar M and Rana D K 2022 An update on graphene oxide: applications and toxicity *ACS Omega* **7** 35387–445

[29] Soleymani H, Moghaddam M M, Naderi-Manesh H and Taheri R A 2024 Single-layer graphene oxide nanosheets induce proliferation and Osteogenesis of single-cell hBMSCs encapsulated in Alginate Microgels *Sci. Rep.* **14** 25272

[30] Nayak T R, Andersen H, Makam V S, Khaw C, Bae S, Xu X, Ee P-L R, Ahn J-H, Hong B H and Pastorin G 2011 Graphene for controlled and accelerated osteogenic differentiation of human mesenchymal stem cells *ACS Nano* **5** 4670–8

[31] Ma X, Luan Z and Li J 2023 Inorganic nanoparticles-based systems in biomedical applications of stem cells: opportunities and challenges *Int. J. Nanomed.* **18** 143–82

[32] Saikia N 2024 Inorganic-based nanoparticles and biomaterials as biocompatible scaffolds for regenerative medicine and tissue engineering: current advances and trends of development *Inorganics* **12** 292

[33] Liu A, Chen J, Zhang J, Zhang C, Zhou Q, Niu P and Yuan Y 2022 Intra-articular injection of umbilical cord mesenchymal stem cells loaded with graphene oxide granular lubrication ameliorates inflammatory responses and osteoporosis of the subchondral bone in rabbits of modified papain-induced osteoarthritis *Front. Endocrinol.* **12** 822294

[34] Shuai C, Zeng Z, Yang Y, Qi F, Peng S, Yang W, He C, Wang G and Qian G 2020 Graphene oxide assists polyvinylidene fluoride scaffold to reconstruct electrical microenvironment of bone tissue *Mater. Des.* **190** 108564

[35] Zhou X, Sun H and Bai X 2020 Two-dimensional transition metal dichalcogenides: synthesis, biomedical applications and biosafety evaluation *Front. Bioeng. Biotechnol.* **8** 236

[36] Carrow J K, Singh K A, Jaiswal M K, Ramirez A, Lokhande G, Yeh A T, Sarkar T R, Singh I and Gaharwar A K 2020 Photothermal modulation of human stem cells using light-responsive 2D nanomaterials *Proc. Natl Acad. Sci.* **117** 13329–38

[37] Roy S, Deo K A, Singh K A, Lee H P, Jaiswal A and Gaharwar A K 2022 Nano-bio interactions of 2D molybdenum disulfide *Adv. Drug Deliv. Rev.* **187** 114361

[38] Sun G, Yang S, Cai H, Shu Y, Han Q, Wang B, Li Z, Zhou L, Gao Q and Yin Z 2019 Molybdenum disulfide nanoflowers mediated anti-inflammation macrophage modulation for spinal cord injury treatment *J. Colloid Interface Sci.* **549** 50–62

[39] Hadjidemetriou M, Mahmoudi M and Kostarelos K 2024 *In vivo* biomolecule corona and the transformation of a foe into an ally for nanomedicine *Nat. Rev. Mater.* **9** 219–22

[40] Murali A, Lokhande G, Deo K A, Brokesh A and Gaharwar A K 2021 Emerging 2D nanomaterials for biomedical applications *Mater. Today* **50** 276–302

[41] Suhito I R, Han Y, Kim D-S, Son H and Kim T-H 2017 Effects of two-dimensional materials on human mesenchymal stem cell behaviors *Biochem. Biophys. Res. Commun.* **493** 578–84

[42] Natu V, Sokol M, Verger L and Barsoum M W 2018 Effect of edge charges on stability and aggregation of $Ti_3C_2T_z$ MXene colloidal suspensions *J. Phys. Chem. C* **122** 27745–53

[43] Qu X, Guo Y, Xie C, Li S, Liu Z and Lei B 2023 Photoactivated MXene nanosheets for integrated bone–soft tissue therapy: effect and potential mechanism *ACS Nano* **17** 7229–40

[44] Babar Z U D, Iannotti V, Rosati G, Zaheer A, Velotta R, Della Ventura B, Álvarez-Diduk R and Merkoçi A 2025 MXenes in healthcare: synthesis, fundamentals and applications *Chem. Soc. Rev.* **54** 3387–440

[45] Li K, Ji Q, Liang H, Hua Z, Hang X, Zeng L and Han H 2023 Biomedical application of 2D nanomaterials in neuroscience *J. Nanobiotechnol.* **21** 181

[46] Qian Y, Wang X, Song J, Chen W, Chen S, Jin Y, Ouyang Y, Yuan W-E and Fan C 2021 Preclinical assessment on neuronal regeneration in the injury-related microenvironment of graphene-based scaffolds *npj Regen. Med.* **6** 31

[47] Qian Y, Zhao X, Han Q, Chen W, Li H and Yuan W 2018 An integrated multi-layer 3D-fabrication of PDA/RGD coated graphene loaded PCL nanoscaffold for peripheral nerve restoration *Nat. Commun.* **9** 323

[48] da Silva D M, Barroca N, Pinto S C, Semitela Â, de Sousa B M, Martins P A, Nero L, Madarieta I, García-Urkia N and Fernández-San-Argimiro F-J 2023 Decellularized extracellular matrix-based 3D nanofibrous scaffolds functionalized with polydopamine-reduced graphene oxide for neural tissue engineering *Chem. Eng. J.* **472** 144980

[49] Fabbro A, Scaini D, León V, Vázquez E, Cellot G, Privitera G, Lombardi L, Torrisi F, Tomarchio F and Bonaccorso F 2016 Graphene-based interfaces do not alter target nerve cells *ACS Nano* **10** 615–23

[50] Bramini M, Alberini G, Colombo E, Chiacchiaretta M, DiFrancesco M L, Maya-Vetencourt J F, Maragliano L, Benfenati F and Cesca F 2018 Interfacing graphene-based materials with neural cells *Front. Syst. Neurosci.* **12** 358913

[51] Wang Z and Mi B 2017 Environmental applications of 2D molybdenum disulfide (MoS_2) nanosheets *Environ. Sci. Technol.* **51** 8229–44

[52] Zhao C, Deng W and Gage F H 2008 Mechanisms and functional implications of adult neurogenesis *Cell* **132** 645–60

[53] Lee H P and Gaharwar A K 2020 Light-responsive inorganic biomaterials for biomedical applications *Adv. Sci.* **7** 2000863

[54] Wan X, Liu Z and Li L 2021 Manipulation of stem cells fates: the master and multifaceted roles of biophysical cues of biomaterials *Adv. Funct. Mater.* **31** 2010626

[55] Qian Y, Xu Y, Yan Z, Jin Y, Chen X, Yuan W-E and Fan C 2021 Boron nitride nanosheets functionalized channel scaffold favors microenvironment rebalance cocktail therapy for piezocatalytic neuronal repair *Nano Energy* **83** 105779

[56] Merlo A, Mokkapati V, Pandit S and Mijakovic I 2018 Boron nitride nanomaterials: biocompatibility and bio-applications *Biomater. Sci.* **6** 2298–311

[57] Silvestri A, Wetzl C, Alegret N, Cardo L, Hou H-L, Criado A and Prato M 2022 The era of nano-bionic: 2D materials for wearable and implantable body sensors *Adv. Drug Deliv. Rev.* **186** 114315

[58] Ansari H R, Mirzaei A, Shokrollahi H, Kumar R, Kim J-Y, Kim H W, Kumar M and Kim S S 2023 Flexible/wearable resistive gas sensors based on 2D materials *J. Mater. Chem. C* **11** 6528–49

[59] Anwer A H, Saadaoui M, Mohamed A T, Ahmad N and Benamor A 2024 State-of-the-Art advances and challenges in wearable gas sensors for emerging applications: innovations and future prospects *Chem. Eng. J.* **502** 157899

[60] Pawar K K, Kumar A, Mirzaei A, Kumar M, Kim H W and Kim S S 2024 2D nanomaterials for realization of flexible and wearable gas sensors: a review *Chemosphere* **352** 141234

[61] Bi H, Yin K, Xie X, Ji J, Wan S, Sun L, Terrones M and Dresselhaus M S 2013 Ultrahigh humidity sensitivity of graphene oxide *Sci. Rep.* **3** 2714

[62] Zhang D, Tong J, Xia B and Xue Q 2014 Ultrahigh performance humidity sensor based on layer-by-layer self-assembly of graphene oxide/polyelectrolyte nanocomposite film *Sens. Actuators B* **203** 263–70

[63] Yu H-W, Kim H K, Kim T, Bae K M, Seo S M, Kim J-M, Kang T J and Kim Y H 2014 Self-powered humidity sensor based on graphene oxide composite film intercalated by poly (sodium 4-styrenesulfonate) *ACS Appl. Mater. Interfaces* **6** 8320–6

[64] Li N, Chen X, Chen X, Ding X and Zhao X 2017 Ultrahigh humidity sensitivity of graphene oxide combined with Ag nanoparticles *RSC Adv.* **7** 45988–96

[65] Lan L, Le X, Dong H, Xie J, Ying Y and Ping J 2020 One-step and large-scale fabrication of flexible and wearable humidity sensor based on laser-induced graphene for real-time tracking of plant transpiration at bio-interface *Biosens. Bioelectron.* **165** 112360

[66] Siddiqui M S, Mandal A, Kalita H and Aslam M 2022 Highly sensitive few-layer MoS_2 nanosheets as a stable soil moisture and humidity sensor *Sens. Actuators B* **365** 131930

[67] Ke N, Si F, Ma H, Gao Q, Ge G, Liu W, Ding J, Zhang W and Fan X 2024 Fully flexible humidity sensor with fast response and high responsivity based on rGO/MoS_2 for human respiration monitoring and nontouch switches *ACS Appl. Mater. Interfaces* **17** 2317–26

[68] Borini S, White R, Wei D, Astley M, Haque S, Spigone E, Harris N, Kivioja J and Ryhänen T 2013 Ultrafast graphene oxide humidity sensors *ACS Nano* **7** 11166–73

[69] Tamayo A, Danowski W, Han B, Jeong Y and Samorì P 2024 Light-modulated humidity sensing in spiropyran functionalized MoS_2 transistors *Small* 2404633

[70] Ren J, Guo B, Feng Y and Yu K 2020 Few-layer MoS_2 dendrites as a highly active humidity sensor *Physica E* **116** 113782

[71] Waheed W, Anwer S, Khan M U, Sajjad M and Alazzam A 2024 2D $Ti_3C_2T_x$-MXene nanosheets and graphene oxide based highly sensitive humidity sensor for wearable and flexible electronics *Chem. Eng. J.* **480** 147981

[72] Cheng B, Tian B, Xie C, Xiao Y and Lei S 2011 Highly sensitive humidity sensor based on amorphous Al_2O_3 nanotubes *J. Mater. Chem.* **21** 1907–12

[73] Zhang D, Wang D, Zong X, Dong G and Zhang Y 2018 High-performance QCM humidity sensor based on graphene oxide/tin oxide/polyaniline ternary nanocomposite prepared by *in-situ* oxidative polymerization method *Sens. Actuators B* **262** 531–41

[74] Yuan Z, Tai H, Ye Z, Liu C, Xie G, Du X and Jiang Y 2016 Novel highly sensitive QCM humidity sensor with low hysteresis based on graphene oxide (GO)/poly (ethyleneimine) layered film *Sens. Actuators B* **234** 145–54

[75] Lei D, Zhang Q, Liu N, Su T, Wang L, Ren Z, Zhang Z, Su J and Gao Y 2022 Self-powered graphene oxide humidity sensor based on potentiometric humidity transduction mechanism *Adv. Funct. Mater.* **32** 2107330

[76] Luo Y, Chen C, Xia K, Peng S, Guan H, Tang J, Lu H, Yu J, Zhang J and Xiao Y 2016 Tungsten disulfide (WS$_2$) based all-fiber-optic humidity sensor *Opt. Express* **24** 8956–66

[77] Kuang Q, Lao C, Wang Z L, Xie Z and Zheng L 2007 High-sensitivity humidity sensor based on a single SnO$_2$ nanowire *J. Am. Chem. Soc.* **129** 6070–1

[78] Guo L *et al* 2012 Two-beam-laser interference mediated reduction, patterning and nanostructuring of graphene oxide for the production of a flexible humidity sensing device *Carbon* **50** 1667–73

[79] Smith A D, Elgammal K, Niklaus F, Delin A, Fischer A C, Vaziri S, Forsberg F, Råsander M, Hugosson H and Bergqvist L 2015 Resistive graphene humidity sensors with rapid and direct electrical readout *Nanoscale* **7** 19099–109

[80] Naik G and Krishnaswamy S 2015 Room-temperature humidity sensing using graphene oxide thin films *Graphene* **5** 1–13

[81] Wu J, Wu Z, Ding H, Wei Y, Yang X, Li Z, Yang B-R, Liu C, Qiu L and Wang X 2019 Multifunctional and high-sensitive sensor capable of detecting humidity, temperature, and flow stimuli using an integrated microheater *ACS Appl. Mater. Interfaces* **11** 43383–92

[82] Anichini C, Aliprandi A, Gali S M, Liscio F, Morandi V, Minoia A, Beljonne D, Ciesielski A and Samorì P 2020 Ultrafast and highly sensitive chemically functionalized graphene oxide-based humidity sensors: harnessing device performances via the supramolecular approach *ACS Appl. Mater. Interfaces* **12** 44017–25

[83] Tripathi S, Gangwar N, Gangwar C and Shukla R 2025 Enhanced humidity sensing using graphene oxide and reduced graphene oxide synthesized via modified Hummers' method *Sens. Imaging* **26** 20

[84] Burman D, Ghosh R, Santra S and Guha P K 2016 Highly proton conducting MoS$_2$/graphene oxide nanocomposite based chemoresistive humidity sensor *RSC Adv.* **6** 57424–33

[85] Park S Y, Kim Y H, Lee S Y, Sohn W, Lee J E, Shim Y-S, Kwon K C, Choi K S, Yoo H J and Suh J M 2018 Highly selective and sensitive chemoresistive humidity sensors based on rGO/MoS$_2$ van der Waals composites *J. Mater. Chem. A* **6** 5016–24

[86] Zhang S-L, Choi H-H, Yue H-Y and Yang W-C 2014 Controlled exfoliation of molybdenum disulfide for developing thin film humidity sensor *Curr. Appl Phys.* **14** 264–8

[87] Lou Z, Wu D, Bu K, Xu T, Shi Z, Xu J, Tian Y and Li X 2017 Dual-mode high-sensitivity humidity sensor based on MoS$_2$/Si nanowires array heterojunction *J. Alloys Compd.* **726** 632–7

[88] Yousaf H Z, Kim S W, Hassan G, Karimov K, Choi K H and Sajid M 2020 Highly sensitive wide range linear integrated temperature compensated humidity sensors fabricated using electrohydrodynamic printing and electrospray deposition *Sens. Actuators B* **308** 127680

[89] Mondal S, Kim S J and Choi C-G 2020 Honeycomb-like MoS$_2$ nanotube array-based wearable sensors for noninvasive detection of human skin moisture *ACS Appl. Mater. Interfaces* **12** 17029–38

[90] Guo W, He Z, Li J, Yao L, Qiao Y, Wang F, Wang Y and Wang F 2024 3D MoSe$_2$@ MoS$_2$ heterojunction for

[91] Pawbake A S, Waykar R G, Late D J and Jadkar S R 2016 Highly transparent wafer-scale synthesis of crystalline WS$_2$ nanoparticle thin film for photodetector and humidity-sensing applications *ACS Appl. Mater. Interfaces* **8** 3359–65

[92] Leonardi S, Wlodarski W, Li Y, Donato N, Sofer Z, Pumera M and Neri G 2018 A highly sensitive room temperature humidity sensor based on 2D-WS2 nanosheets *FlatChem* **9** 21–26

[93] Taufik A, Asakura Y, Hasegawa T, Kato H, Kakihana M, Hirata S, Inada M and Yin S 2020 Surface engineering of 1T/2H-MoS$_2$ nanoparticles by O$_2$ plasma irradiation as a potential humidity sensor for breathing and skin monitoring applications *ACS Appl. Nano Mater.* **3** 7835–46

[94] Bharatula L D, Erande M B, Mulla I S, Rout C S and Late D J 2016 SnS$_2$ nanoflakes for efficient humidity and alcohol sensing at room temperature *RSC Adv.* **6** 105421–7

[95] Deb M, Chen M-Y, Chang P-Y, Li P-H, Chan M-J, Tian Y-C, Yeh P-H, Soppera O and Zan H-W 2023 SnO$_2$-based ultra-flexible humidity/respiratory sensor for analysis of human breath *Biosensors* **13** 81

[96] Fu X, Wang C, Yu H, Wang Y and Wang T 2007 Fast humidity sensors based on CeO$_2$ nanowires *Nanotechnology* **18** 145503

[97] Kiasari N M, Soltanian S, Gholamkhass B and Servati P 2012 Room temperature ultra-sensitive resistive humidity sensor based on single zinc oxide nanowire *Sens. Actuators A* **182** 101–5

[98] Li Z, Zhang H, Zheng W, Wang W, Huang H, Wang C, MacDiarmid A G and Wei Y 2008 Highly sensitive and stable humidity nanosensors based on LiCl doped TiO$_2$ electrospun nanofibers *J. Am. Chem. Soc.* **130** 5036–7

[99] Fowler J D, Allen M J, Tung V C, Yang Y, Kaner R B and Weiller B H 2009 Practical chemical sensors from chemically derived graphene *ACS Nano* **3** 301–6

[100] Ma H, Ding J, Zhang Z, Gao Q, Liu Q, Wang G, Zhang W and Fan X 2024 Recent advances in graphene-based humidity sensors with the focus of structural design: a review *IEEE Sens. J.* **24** 20289–311

[101] Buchsteiner A, Lerf A and Pieper J 2006 Water dynamics in graphite oxide investigated with neutron scattering *J. Phys. Chem. A* **110** 22328–38

[102] Nair R, Wu H, Jayaram P N, Grigorieva I V and Geim A 2012 Unimpeded permeation of water through helium-leak–tight graphene-based membranes *Science* **335** 442–4

[103] Wang D-W, Du A, Taran E, Lu G Q M and Gentle I R 2012 A water-dielectric capacitor using hydrated graphene oxide film *J. Mater. Chem.* **22** 21085–91

[104] Late D J *et al* 2013 Sensing behavior of atomically thin-layered MoS$_2$ transistors *ACS nano* **7** 4879–91

[105] Li H, Yin Z, He Q, Li H, Huang X, Lu G, Fam D W H, Tok A I Y, Zhang Q and Zhang H 2012 Fabrication of single-and multilayer MoS$_2$ film-based field-effect transistors for sensing NO at room temperature *Small* **8** 63–67

[106] Gobbi M *et al* 2018 Collective molecular switching in hybrid superlattices for light-modulated two-dimensional electronics *Nat. Commun.* **9** 2661

[107] Pujari S *et al* 2024 Au–MoS$_2$ nanoflowers sensors on interdigitated electrode for monitoring human respiration *Nano Express* (https://doi.org/10.1088/2632-959X/ad6c67)

[108] Wang B, Thukral A, Xie Z, Liu L, Zhang X, Huang W, Yu X, Yu C, Marks T J and Facchetti A 2020 Flexible and stretchable metal oxide nanofiber networks for multimodal and monolithically integrated wearable electronics *Nat. Commun.* **11** 2405

[109] Baloda S, Gupta N and Singh S 2022 A flexible pressure sensor based on multiwalled carbon nanotubes/polydimethylosiloxane composite for wearable

electronic-skin application *IEEE Trans. Electron. Devices* **69** 7011–8

[110] Panth M, Cook B, Alamri M, Ewing D, Wilson A and Wu J Z 2020 Flexible zinc oxide nanowire array/graphene nanohybrid for high-sensitivity strain detection *ACS Omega* **5** 27359–67

[111] Baloda S, Ansari Z A, Singh S and Gupta N 2020 Development and analysis of graphene nanoplatelets (GNPs)-based flexible strain sensor for health monitoring applications *IEEE Sens. J.* **20** 13302–9

[112] Irani F S, Shafaghi A H, Tasdelen M C, Delipinar T, Kaya C E, Yapici G G and Yapici M K 2022 Graphene as a piezoresistive material in strain sensing applications *Micromachines* **13** 119

[113] Xu W, Yang T, Qin F, Gong D, Du Y and Dai G 2019 A sprayed graphene pattern-based flexible strain sensor with high sensitivity and fast response *Sensors* **19** 1077

[114] Ben Aziza Z, Zhang K, Baillargeat D and Zhang Q 2015 Enhancement of humidity sensitivity of graphene through functionalization with polyethylenimine *Appl. Phys. Lett.* **107** 134102

[115] Célérier S *et al* 2018 Hydration of $Ti_3C_2T_x$ MXene: an interstratification process with major implications on physical properties *Chem. Mater.* **31** 454–61

[116] Mirjalali S, Peng S, Fang Z, Wang C H and Wu S 2022 Wearable sensors for remote health monitoring: potential applications for early diagnosis of Covid-19 *Adv. Mater. Technol.* **7** 2100545

[117] Silvestri A *et al* 2023 Ultrasensitive detection of SARS-CoV-2 spike protein by graphene field-effect transistors *Nanoscale* **15** 1076–85

[118] Liu T, Qu D, Guo L, Zhou G, Zhang G, Du T and Wu W 2024 MXene/TPU composite film for humidity sensing and human respiration monitoring *Adv. Sens. Res.* **3** 2300014

[119] Xing H, Li X, Lu Y, Wu Y, He Y, Chen Q, Liu Q and Han R P 2022 MXene/MWCNT electronic fabric with enhanced mechanical robustness on humidity sensing for real-time respiration monitoring *Sens. Actuators B* **361** 131704

[120] SU S L, Singh D N and Baghini M S 2014 A critical review of soil moisture measurement *Measurement* **54** 92–105

[121] Surya S G, Yuvaraja S, Varrla E, Baghini M S, Palaparthy V S and Salama K N 2020 An in-field integrated capacitive sensor for rapid detection and quantification of soil moisture *Sens. Actuators B* **321** 128542

[122] Wang Z, Zhu W, Qiu Y, Yi X, von Dem Bussche A, Kane A, Gao H, Koski K and Hurt R 2016 Biological and environmental interactions of emerging two-dimensional nanomaterials *Chem. Soc. Rev.* **45** 1750–80

[123] Huang X, Auffan M, Eckelman M J, Elimelech M, Kim J-H, Rose J, Zuo K, Li Q and Alvarez P J 2024 Trends, risks and opportunities in environmental nanotechnology *Nat. Rev. Earth Environ.* **5** 572–87

[124] Andrews J P *et al* 2024 First-in-human controlled inhalation of thin graphene oxide nanosheets to study acute cardiorespiratory responses *Nat. Nanotechnol.* **19** 705–14

[125] Garner K L and Keller A A 2014 Emerging patterns for engineered nanomaterials in the environment: a review of fate and toxicity studies *J. Nanopart. Res.* **16** 1–28

[126] Fojtů M, Teo W Z and Pumera M 2017 Environmental impact and potential health risks of 2D nanomaterials *Environ. Sci. Nano* **4** 1617–33

[127] Lin H *et al* 2024 Environmental and health impacts of graphene and other two-dimensional materials: a graphene flagship perspective *ACS Nano* **18** 6038–94

[128] Vranic S, Kurapati R, Kostarelos K and Bianco A 2025 Biological and environmental degradation of two-dimensional materials *Nat. Rev. Chem.* **9** 1–12

[129] Gao J, Li B, Tan J, Chow P, Lu T-M and Koratkar N 2016 Aging of transition metal dichalcogenide monolayers *ACS Nano* **10** 2628–35

[130] Yoo M J and Park H B 2019 Effect of hydrogen peroxide on properties of graphene oxide in Hummers method *Carbon* **141** 515–22

[131] Najmi P, Keshmiri N, Ramezanzadeh M, Ramezanzadeh B and Arjmand M 2023 Epoxy nanocomposites holding molybdenum disulfide decorated with covalent organic framework: all-in-one coatings featuring thermal, UV-shielding, and mechanical properties *Composites B* **260** 110785

[132] Dong W, Dai Z, Liu L and Zhang Z 2024 Toward clean 2D materials and devices: recent progress in transfer and cleaning methods *Adv. Mater.* **36** 2303014

[133] Rosentsveig R, Feldman Y, Kundrat V, Pinkas I, Zak A and Tenne R 2025 Long-term aging of multiwall nanotubes and fullerene-like nanoparticles of WS_2 *J. Solid State Chem.* **346** 125259

[134] Raza S, Hayat A, Bashir T, Chen C, Shen L, Orooji Y and Lin H 2024 Electrochemistry of 2D-materials for the remediation of environmental pollutants and alternative energy storage/conversion materials and devices, a comprehensive review *Sustain. Mater. Technol.* **40** e00963

[135] Yang J *et al* 2022 Oxidations of two-dimensional semiconductors: fundamentals and applications *Chin. Chem. Lett.* **33** 177–85

[136] Arora N K and Mishra I 2022 Sustainable development goal 6: global water security *Environ. Sustain.* **5** 271–5

[137] Garg A, Basu S, Shetti N P and Reddy K R 2021 2D materials and its heterostructured photocatalysts: synthesis, properties, functionalization and applications in environmental remediation *J. Environ. Chem. Eng.* **9** 106408

[138] Zhang C, Ma Y, Zhang X, Abdolhosseinzadeh S, Sheng H, Lan W, Pakdel A, Heier J and Nüesch F 2020 Two-dimensional transition metal carbides and nitrides (MXenes): synthesis, properties, and electrochemical energy storage applications *Energy Environ. Mater.* **3** 29–55

[139] Ikram M, Khan M, Raza A, Imran M, Ul-Hamid A and Ali S 2020 Outstanding performance of silver-decorated MoS_2 nanopetals used as nanocatalyst for synthetic dye degradation *Physica E* **124** 114246

[140] Velusamy S, Roy A, Sundaram S and Kumar Mallick T 2021 A review on heavy metal ions and containing dyes removal through graphene oxide-based adsorption strategies for textile wastewater treatment *Chem. Rec.* **21** 1570–610

[141] Ranjan P *et al* 2024 2D materials for potable water application: basic nanoarchitectonics and recent progresses *Small* **20** 2407160

[142] Junaidi N F D, Othman N H, Fuzil N S, Shayuti M S M, Alias N H, Shahruddin M Z, Marpani F, Lau W J, Ismail A F and Aba N D 2021 Recent development of graphene oxide-based membranes for oil–water separation: a review *Sep. Purif. Technol.* **258** 118000

[143] Perveen H and Zahoor I 2024 Two dimensional materials for wastewater treatment *Int. J. Chem. Biochem. Sci.* **25** 164–77

[144] Li M *et al* 2023 Molybdenum nanofertilizer boosts biological nitrogen fixation and yield of soybean through delaying nodule senescence and nutrition enhancement *ACS Nano* **17** 14761–74

[145] Teo W Z, Chng E L K, Sofer Z and Pumera M 2014 Cytotoxicity of exfoliated transition-metal dichalcogenides (MoS_2, WS_2, and WSe_2) is lower than that of graphene and its analogues *Chemistry A* **20** 9627–32

[146] Latiff N M, Sofer Z, Fisher A C and Pumera M 2017 Cytotoxicity of exfoliated layered vanadium dichalcogenides *Chemistry* **23** 684–90

[147] Chng E L K, Sofer Z and Pumera M 2014 MoS_2 exhibits stronger toxicity with increased exfoliation *Nanoscale* **6** 14412–8

[148] Guiney L M, Wang X, Xia T, Nel A E and Hersam M C 2018 Assessing and mitigating the hazard potential of two-dimensional materials *ACS Nano* **12** 6360–77

[149] Wang X, Mansukhani N D, Guiney L M, Ji Z, Chang C H, Wang M, Liao Y P, Song T B, Sun B and Li R 2015 Differences in the toxicological potential of 2D versus

aggregated molybdenum disulfide in the lung *Small* **11** 5079–87

[150] Baig N, Kammakakam I and Falath W 2021 Nanomaterials: a review of synthesis methods, properties, recent progress, and challenges *Mater. Adv.* **2** 1821–71

[151] Ferrai C and Schulte C 2024 Mechanotransduction in stem cells *Eur. J. Cell Biol.* **103** 151417

[152] Lu B *et al* 2024 When machine learning meets 2D materials: a review *Adv. Sci.* **11** 2305277

[153] Volkov Y, McIntyre J and Prina-Mello A 2017 Graphene toxicity as a double-edged sword of risks and exploitable opportunities: a critical analysis of the most recent trends and developments *2D Mater.* **4** 022001

[154] Castagnola V, Tomati V, Boselli L, Braccia C, Decherchi S, Pompa P P, Pedemonte N, Benfenati F and Armirotti A 2024 Sources of biases in the *in vitro* testing of nanomaterials: the role of the biomolecular corona *Nanoscale Horiz.* **9** 799–816

[155] Višić B, Panchakarla L S and Tenne R 2017 Inorganic nanotubes and fullerene-like nanoparticles at the crossroads between solid-state chemistry and nanotechnology *J. Am. Chem. Soc.* **139** 12865–78

[156] Evarestov R, Kovalenko A, Bandura A, Domnin A and Lukyanov S 2018 Comparison of vibrational and thermodynamic properties of MoS_2 and WS_2 nanotubes: first principles study *Mater. Res. Express* **5** 115028

[157] Sedova A, Višić B, Vega-Mayoral V, Vella D, Gadermaier C, Dodiuk H, Kenig S, Tenne R, Gvishi R and Bar G 2020 Silica aerogels as hosting matrices for WS_2 nanotubes and their optical characterization *J. Mater. Sci.* **55** 1–12

[158] Yadgarov L *et al* 2018 Strong light–matter interaction in tungsten disulfide nanotubes *Phys. Chem. Chem. Phys.* **20** 20812–20

[159] Pirker L and Višić B 2022 Recent progress in the synthesis and potential applications of two-dimensional tungsten (Sub) oxides *Isr. J. Chem.* **62** e202100074

[160] Višić B, Pirker L, Opačić M, Milosavljević A, Lazarević N, Majaron B and Remškar M 2022 Influence of crystal structure and oxygen vacancies on optical properties of nanostructured multi-stoichiometric tungsten suboxides *Nanotechnology* **33** 275705

[161] Madevska Bogdanova A, Koteska B, Vićentić T, Ilić S D, Tomić M, Spasenović M and Michel C 2024 Blood oxygen saturation estimation with laser-induced graphene respiration sensor *J. Sens.* **2024** 4696031

[162] Meincke M *et al* 2025 Integration of highly sensitive large-area graphene-based biosensors in an automated sensing platform *Measurement* **240** 115592

[163] Nalepa M-A, Panáček D, Dědek I, Jakubec P, Kupka V, Hrubý V, Petr M and Otyepka M 2024 Graphene derivative-based ink advances inkjet printing technology for fabrication of electrochemical sensors and biosensors *Biosens. Bioelectron.* **256** 116277

Wiley Analytical Science

Advancing Characterization of Materials by Multimodal 4D-STEM Analytical Methods

April 26, 11:00am - 12:00pm EDT

Development and production of new materials and semiconductor devices require morphological, structural, and chemical characterization at the nanoscale level to understand their chemico-physical properties and optimize their production process. Besides traditional electron microscopy imaging and compositional analysis techniques, 4D-STEM methods provide additional structural information about the local internal organization of atoms and molecules at each position of an acquired STEM map.

Watch this session during the WAS Virtual Conference:

Dr. Daniel Nemecek   **Dr. Tingting Yang**

Register Now

This talk is sponsored by **TESCAN** PERFORMANCE IN NANOSPACE

RESEARCH ARTICLE

ADVANCED
FUNCTIONAL
MATERIALS
www.afm-journal.de

Check for updates

Mo$_x$W$_{x-1}$S$_2$ Nanotubes for Advanced Field Emission Application

Luka Pirker,* Robert Ławrowski, Rupert Schreiner, Maja Remškar, and Bojana Višić*

Transition metal dichalcogenide (TMDC) nanotubes complement the field of low-dimensional materials with their quasi-1D morphology and a wide set of intriguing properties. By introducing different transition metals into the crystal structure, their properties can be tailored for specific purpose and applications. Herein, the characterization and a subsequent preparation of single-nanotube field emission devices of Mo$_x$W$_{x-1}$S$_2$ nanotubes prepared via the chemical vapor transport reaction is presented. Energy-dispersive X-ray spectroscopy, Raman spectroscopy, and X-ray diffraction indicate that the molybdenum and tungsten atoms are randomly distributed within the crystal structure and that the material is highly crystalline. High resolution transmission electron microscopy and electron diffraction (ED) patterns further corroborate these findings. A detailed analysis of the ED patterns from an eight-layer nanotube reveal that the nanotubes grow in the 2H structure, with each shell consists of one bilayer. The work function of the nanotubes is comparable to that of pure MoS$_2$ and lower of pure WS$_2$ NTs, making them ideal candidates for field emission applications. Two devices with different geometrical setup are prepared and tested as field emitters, showing promising results for single nanotube field emission applications.

L. Pirker, M. Remškar, B. Višić
Department of Condensed Matter Physics
Jozef Stefan Institute
Jamova cesta 39, Ljubljana 1000, Slovenia
E-mail: luka.pirker@ijs.si; bojana.visic@ipb.ac.rs
L. Pirker
Department of Electrochemical Materials
J. Heyrovsky Institute of Physical Chemistry
Dolejskova 3, 182 23 Prague 8, Czech Republic
R. Ławrowski, R. Schreiner
Faculty of Applied Natural Sciences and Cultural Studies
OTH Regensburg
Seybothstraße 2, 93053 Regensburg, Germany
B. Višić
Institute of Physics Belgrade
University of Belgrade
Pregrevica 118, Belgrade 11080, Serbia

The ORCID identification number(s) for the author(s) of this article can be found under https://doi.org/10.1002/adfm.202213869.

1. Introduction

Low-dimensional materials, based on atomically thin sheets stacked together, have become a rapidly developing field.[1] Transition metal dichalcogenides (TMDCs) with layered structure are 2D solids, which consist of molecular layers held together by weak van der Waals forces. Besides layered crystals, the TMDCs can be also found in a form of quantum dots (0D),[2] nanotubes (1D),[3,4] and monolayers (2D).[5,6] Consequently, they have a wide variety of physical and chemical properties, which depend on their crystal structure, morphology, and number of layers[7–9] and have been studied as light-emitting diodes,[10] transistors,[11] photovoltaic devices,[12] p-n junctions,[13] and more. Their properties can be further altered by constructing heterostructures[14] or by the growth of TMDC alloys.[15] By alloying, one or more elements are exchanged at either the transition metal or the chalcogen site. With this approach, not only that their properties can be tuned,[16] but the new ones, such as magnetism,[15] can emerge when different elements are added to the structure.

Nanotubes (NTs), the quasi-1D morphology, have been vastly neglected as possible alloyed TMDCs. Most of the research so far has been done on flat, 2D structures, both theoretically and experimentally.[17–20] Individual multiwalled WS$_2$ and MoS$_2$ nanotubes are having a resurgence of interest, as interesting optical and electrical properties have been reported in recent years such as quasi-1D superconductivity,[21] electroluminescence,[22] confined optical cavity modes within the nanotube core,[23,24] whispering gallery modes,[25] as well as the low-temperature Coulomb blockade,[26] field-effect transistors,[27,28] and field emitters,[29] making them promising components for nanoelectronic devices. In recent years, TMDCs have opened a new frontier in the area of field emission devices, due to their layered structure and the presence of thin and sharp edges with high aspect ratios which enhance local electric field.[30] Until now, there have been only a few reports that focused on non-carbon-based alloyed NTs.[31,32]

In this work, we present highly crystalline multiwalled Mo$_{1-x}$W$_x$S$_2$ NTs grown with the chemical vapor transport (CVT) method. Their structure and morphology were probed with scanning electron microscopy (SEM), HRTEM, ED, XRD, and atomic force microscopy (AFM). Their vibrational properties

ADVANCED
SCIENCE NEWS

www.advancedsciencenews.com

ADVANCED
FUNCTIONAL
MATERIALS

www.afm-journal.de

were measured using Raman spectroscopy, while the electrical behavior was determined by Kelvin probe force microscopy (KPFM). Single nanotube field emission devices were prepared and their performance was evaluated.

2. Results and Discussion

The material was synthesized in the form of foils, composed of thin flakes and nanotubes, as seen from SEM images as shown in **Figure 1**a. Nanotubes' diameter ranges from 10 nm up to a few hundred nm, with lengths up to several 10 µm. The NTs grow from the flakes and are usually open-ended, as seen from the inset in Figure 1a. This is similar to pure MoS_2 and WS_2 nanotubes grown via the CVT method.[26,37] The elemental composition and the ratio between Mo/W atoms were determined from EDS spectra. As shown in the EDS map of a nanotube in Figure 1b, Mo and W atoms are homogeneously distributed within the material. On average, the chemical formula of both the nanotubes and flakes is $Mo_{0.56}W_{0.44}S_2$.

The homogeneity and the composition of the material are also reflected in the Raman spectra as shown in Figure 1c. In order to assign the corresponding modes to the peaks of $Mo_{0.56}W_{0.44}S_2$, pure MoS_2 and WS_2 material was synthesized with CVT and probed with Raman spectroscopy as shown in Figure S3 (Supporting Information). The first and higher order modes are observed in both spectra due to the resonance excitation with the 633 nm laser[38,39] Peak positions are presented in Tables S1 and S2 (Supporting Information) and the

corresponding modes are assigned according to literature.[38–43] The WS_2 peak 350 cm^{-1} is assigned to 2LA, because of the resonant conditions, it is more intense than the $E^1_{2\,g}$ mode. The most intense peak, situated at 412 cm^{-1} is assigned to the A_{1g} mode, as the point group symmetry (D_{6h}) of the alloyed material should be the same as for MoS_2 and WS_2.[44] This peak is situated between the peak positions of pure MoS_2 (407.5 cm^{-1}) and WS_2 (420 cm^{-1}). The peak observed at ≈435 cm^{-1} is assigned to a down-shifted 2LA(M) mode of MoS_2 ($2LA_{MoS2}$), which appears due to the resonant excitation. The same goes for the peak situated at ≈352 cm^{-1} and assigned to the 2LA(M) mode of WS_2 ($2LA_{WS2}$), observed at the same position as in pure WS_2. The peak at 376 cm^{-1} is assigned to the $E^1_{2\,g}$ mode of MoS_2 ($E^1_{2\,g,\,MoS2}$). Other peaks present in the spectra are due to multi-phonon scattering of different in-plane, out-of-plane, and acoustic modes. The positions of individual peaks are presented in Table S3 (Supporting Information). The appearance of both MoS_2 and WS_2 characteristic modes proves that the flakes and NTs contain both Mo and W atoms.[16,44,45]

The XRD spectrum of the as synthesized $Mo_{0.56}W_{0.44}S_2$ material, that is, flakes and tubes, is shown in Figure 1d. The (00l) peaks are the most intense as the material is predominantly composed of flakes, which lay flat on the XRD sample holder. The average unit cell parameter c, calculated from the peak positions, is (1.235 ± 0.001) nm. The weak peaks, indexed as (10l) peaks, were used to calculate the unit cell parameter a, with the average value of (0.316 ± 0.002) nm. Comparing the unit cell parameters with pure 2H MoS_2 and WS_2 structures (1.229 and 1.232 nm for MoS_2 and WS_2, respectively), the unit cell parameter
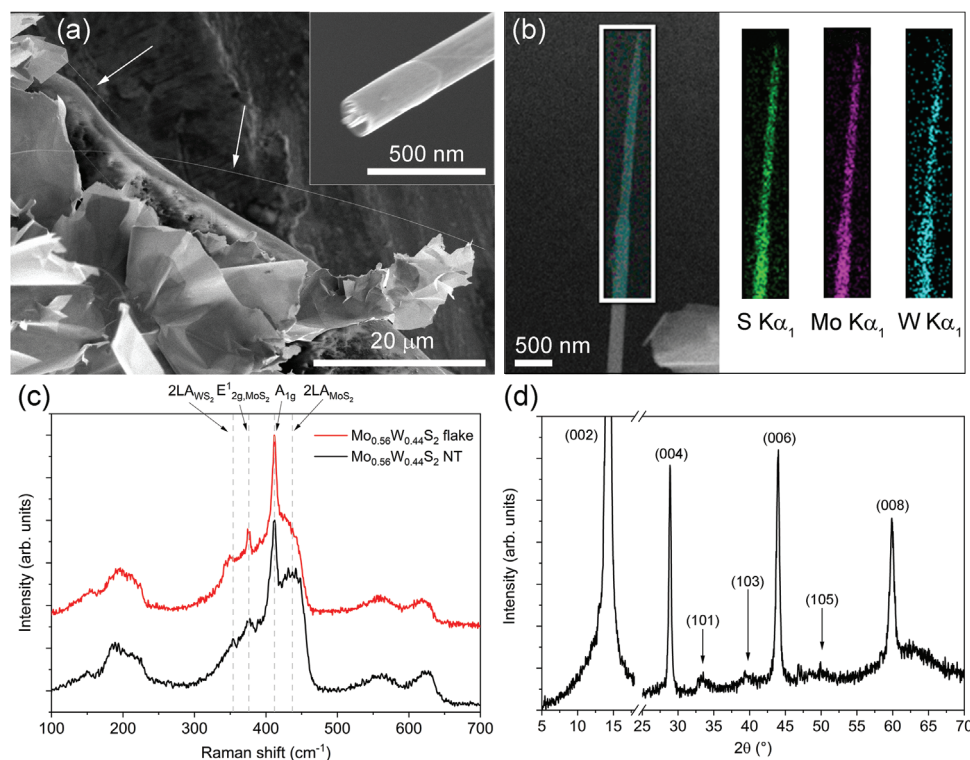
Figure 1. a) SEM image of the synthesized material. The arrows indicate individual NTs. The inset shows a NT with an approx. diameter of 100 nm, with a clearly open apex. b) SEM image and EDS maps of a single NT of $K_{\alpha1}$ emission lines for sulfur (green), molybdenum (purple), and tungsten (cyan). c) Raman spectra on a flake and a NT obtained with the 633 nm laser. d) XRD spectrum of the synthesized material.

**ADVANCED
SCIENCE NEWS**

www.advancedsciencenews.com

**ADVANCED
FUNCTIONAL
MATERIALS**

www.afm-journal.de
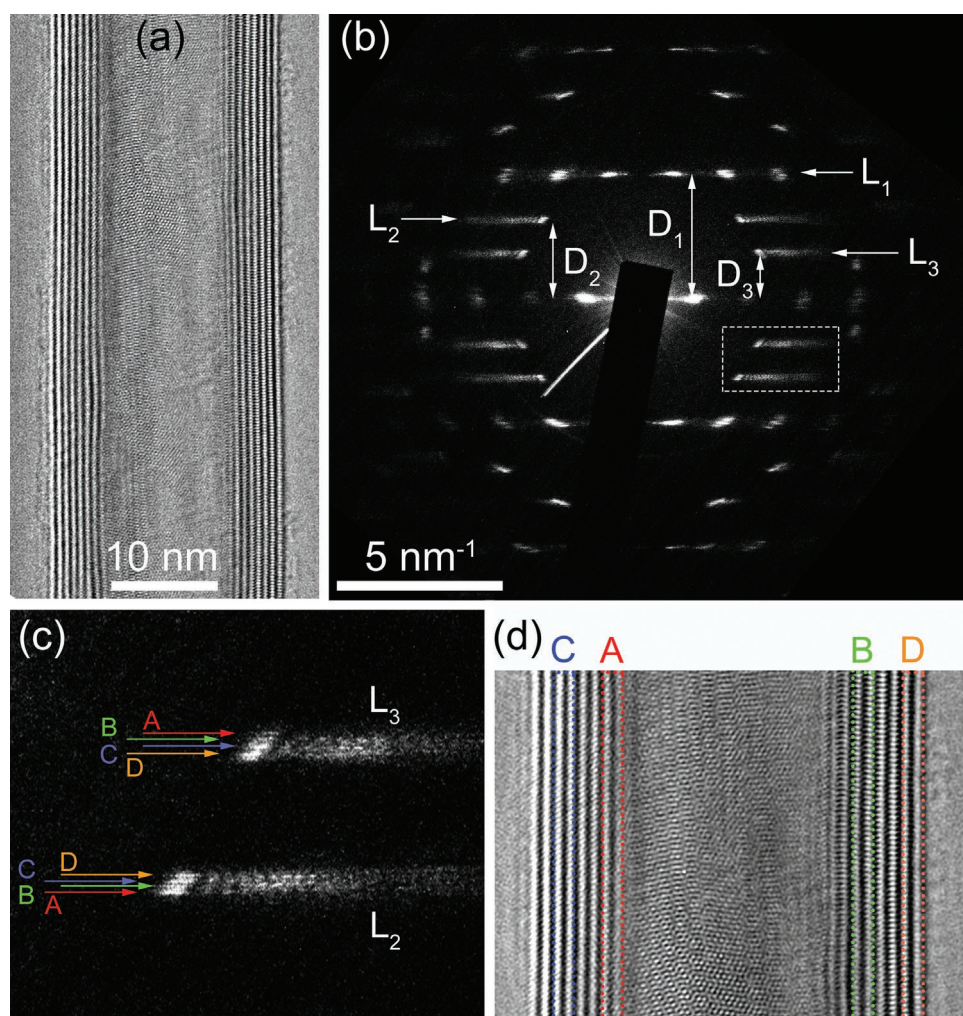
Figure 2. a) HRTEM image of an eight-shell NT with the corresponding ED pattern shown in b). The area marked with a dashed line in (b) is shown in c) with marked layer lines. d) HRTEM image of the NT with marked bilayers corresponding to each layer line in the ED.

c is closer to the WS_2 structure, while the unit cell parameter a is closer to the MoS_2 structure (0.315 nm for WS_2 (PDF2: 01-084-1398) and 0.316 nm for MoS_2 (PDF2: 03-065-0160)).

To elucidate the structure of NTs, HRTEM images and ED patterns were made. In **Figure 2**a,b, a HRTEM image and its corresponding ED pattern are shown for an eight-shell $Mo_{0.56}W_{0.44}S_2$ NT. All of the synthesized NTs are multi-walled and highly crystalline with a low number of defects. This is typical for CVT-grown nanotubes due to nearly equilibrium growth conditions.[28] As described by Youhu et al.,[46] the chiral indices (n, m) and the helical angle α of each individual shell can be deduced from the HRTEM image and ED pattern. In order to obtain this information, the diameter of each shell needs to be measured (d_i), as well as the layer line spacings (D_i) and the number of layer lines. The diameter of each shell was determined from the HRTEM image, and the values are presented in Table S4 (Supporting Information). In the next step, the ED pattern was divided into three layers (L_1, L_2, L_3), as shown in Figure 2b, and the number of layer lines was determined as shown in Figure 2c. As the nanotube was composed of eight shells, the same number of layer lines was expected in each

layer. As only four layer lines (A,B,C,D) were visible, as shown in Figure 2c, the helicity is doubly degenerated, indicating that the shells grow in pairs. It is assumed that each layer line is represented by two adjacent shells, that is, the first (with the diameter d_1) and the second (with the diameter d_2) shell grow together and have the same helicity. The average shell diameters, d_i, were calculated and presented in Table S4 (Supporting Information). For each layer, lining the principal layer line spacings D_1, D_2, and D_3 were measured in order to calculate the index ratios, m/n:[46]

$$\frac{m}{n} = \frac{D_2 - D_3}{D_2 + 2D_3} \tag{1}$$

The diffraction peaks of the layer lines in the L_2 layer presented in Table S5 (Supporting Information) follow the (ii) assignment rule in[46] and thus the smallest m/n ratio corresponds to the largest shell diameter.

To calculate the chiral indices the diameter of each shell is expressed as a function on n and m:

$$d_i = \frac{a_0}{\pi} \sqrt{n^2 + m^2 + mn} \tag{2}$$

Table 1. Parameters for measured layer lines: D_i is the principal layer line spacing, d_i is the average shell diameter, Exp. m, n, m/n, and α are values obtained from experimental measurements, Calc. m, n, and m/n are the calculated values.

Line	D_1	D_2	D_3	Average d_i	Exp. $m\,n^{-1}$	Exp. m	Exp. n	Calc. m	Calc. n	Calc. m/n	Exp. α
A	3.64	2.43	1.26	12.50	0.236	26	109	25	106	0.236	10.4
B	3.70	2.39	1.32	15.11	0.214	29	134	28	131	0.214	9.5
C	3.75	2.36	1.37	17.77	0.193	31	159	29	150	0.193	8.7
D	3.83	2.31	1.43	20.36	0.171	32	185	32	187	0.171	7.8

where a_0 is the size of the basis vector, which is equal to the unit cell parameter a. By combining Equations 1 and 2, the experimental values of indices n and m were obtained, **Table 1**. From the principal layer line spacings, the chiral angle α was calculated as well:

$$\alpha = \tan^{-1}\left(\frac{2D_2 - D_1}{\sqrt{3}D_1}\right) \quad (3)$$

The chiral indices (n, m) shown in Table 1, were further refined by finding the best combination of n and m indices that is closest to the measured values of n and m. The shells assigned to different layer lines are schematically shown in Figure 2d.

The obtained values of chiral indices and of the chiral angle imply a linear relationship with the diameter of the nanotube, similar to other reported measurements.[46] In our case, the chiral indices n and m, as well as the helical angle, scale linearly with the diameter of the nanotube as shown in Figure S4 (Supporting Information). The existence of only four layer lines in each layer implies that the NT shells grow in pairs. This effect could be a consequence of the material's tendency to crystalize in the 2H phase. Such growth has previously been observed for WS_2 nanotubes alloyed with gold.[47] As the NTs are curved and the number of atoms within a layer increases with the diameter, the phase cannot be described as a pure 2H phase with perfect translational symmetry.[48] The structure also depends on the thickness of the NT wall, as thicker NTs tend to have larger number of shells with the same chirality. In thinner NTs, similar to the one presented in Figure 2a, only single shells shared the same chirality.[49,50] The change in the shell structure can be attributed to the synthesis conditions, as the reaction times for the NTs prepared via the sulfurization of metal oxides were insufficient for full structural relaxation as in the CVT synthesis.[49]

The measured topography and contact potential difference (CPD) images of a single $Mo_{0.56}W_{0.44}S_2$ NT on highly oriented pyrolytic graphite (HOPG) are shown in **Figure 3**a,b. The NT is
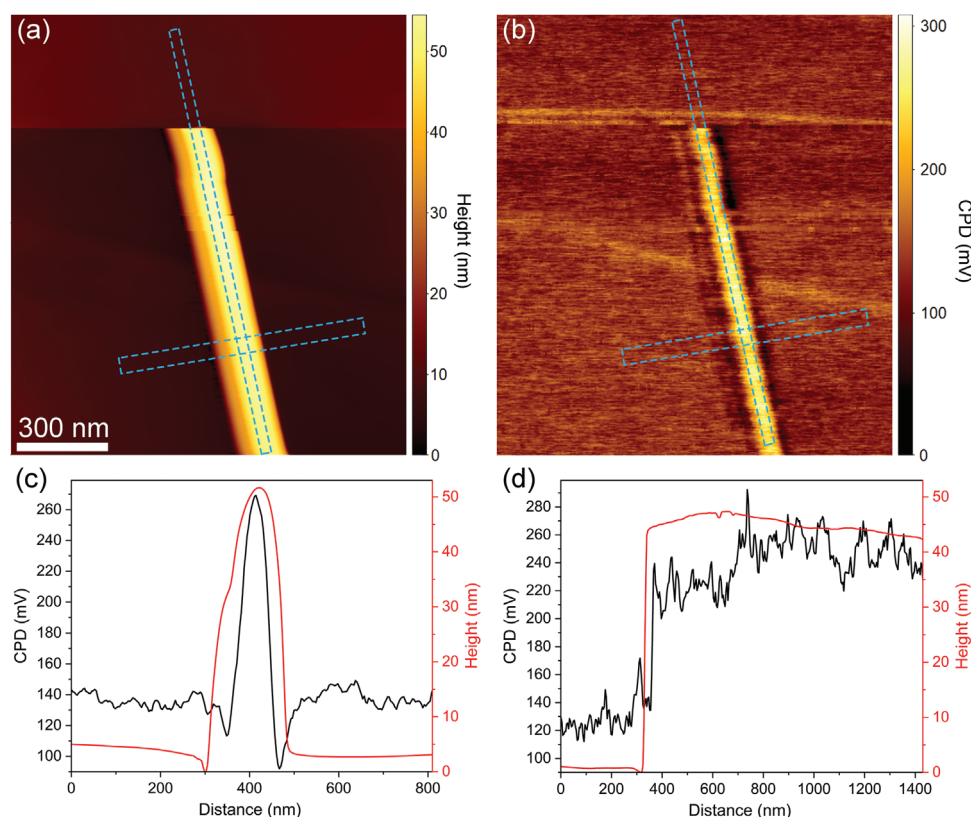
Figure 3. Topography AFM image a) of a NT on HOPG with the corresponding CPD image b). Topography and CPD line profiles perpendicular c) and parallel d) to the NT long axis.

**ADVANCED
SCIENCE NEWS**
www.advancedsciencenews.com

**ADVANCED
FUNCTIONAL
MATERIALS**
www.afm-journal.de

≈50 nm in height and 200 nm in width. However, the width is overestimated due to the tip-sample convolution effect,[51] with the true width being below 100 nm, as measured from the SEM image Figure S5 (Supporting Information). The difference between the height and width can be explained with several effects: the flattening of the NT, due to attractive forces between the substrate and the NT; its deformation from ideal cylindrical shape during sample preparation, or by the growth of the NT in a slightly elliptical shape. The KPFM measurements were performed on freshly cleaved HOPG, which has a stable work function (WF) of 4.60 ± 0.05 eV.[52,53] Figure 3c shows line profiles of the topography and CPD perpendicular to the long axis of the nanotube, while in Figure 3d the line profiles are parallel to the long axis. The CPD value of the nanotube is between 100 and 130 mV higher than that of HOPG, indicating that the WF of the NT is ≈4.7 eV (Figure S6, Supporting Information). Although we did not observe any variation in the WF of $Mo_{0.56}W_{0.44}S_2$, a slight variation was observed in the WF of pure MoS_2 NT, presented in Figure S7 (Supporting Information). The WF of the MoS_2 NT varied between 4.55 and 4.65 eV, suggesting that MoS_2 NTs have, in average, a slightly lower WF than $Mo_{0.56}W_{0.44}S_2$ NTs. Compared to WS_2 nanosheets and nanodots with the WF of 4.9 eV, $Mo_{0.56}W_{0.44}S_2$ NTs WF is significantly lower.[54] The WF does not change along the nanotube surface and has a similar value at the apex, where the inner layers are exposed, furthermore confirming a homogeneous distribution of Mo and W atoms.

As the $Mo_{0.56}W_{0.44}S_2$ NTs have a lower WF than their non-alloyed counterparts or carbon nanotubes,[55] while having an intrinsic high aspect ratio, they are prime candidates for field emission (FE) applications. For this purpose, two single nanotube devices with different geometrical setup were prepared. For the first device, a NT with the diameter of 76 nm was mounted in the upright direction on top of a Si pillar as shown in **Figure 4**a, while for the second device, a NT with the diameter of 84 nm is spanned over two pillars as shown in Figure 4b. The current–voltage-behavior of both FE devices is similar, as shown in Figure S8 (Supporting Information). For the applied voltage of 1000 V (20 MV m⁻¹), the measurement shows a maximum emission current up to 0.75 µA for the upright mounted NT and 0.80 µA for the lateral NT as shown in Figure S8 (Supporting Information). The onset voltage U_{on} for the current of 1 nA is ≈650 V (13 MV m⁻¹) for both orientations of the NTs. In addition, the FN plot shows a linear behavior for both arrangements and no deviations from the ideal Fowler–Nordheim (FN) behaviors are noticeable as shown in Figure 4c. This indicates a good electric contact and that the emission process is without saturation effects.[29] Electrostatic simulations with COMSOL Multiphysics confirmed the similarity of the emission behavior in both geometrical setups as shown in Figure S9 (Supporting Information).

To determine the field enhancement factor β and the FE parameters γ, a_{fn}, and b_{fn}, the work function of 4.7 eV, determined from KPFM, was used. From the FN plots of the measured devices, both γ and β are estimated to ≈$(6.7 ± 1.3)\ 10^4$ cm⁻¹ and 335 ± 60, respectively. For the hollow NTs with a diameter below 200 nm, ≈1/3 up to 1/2 of the diameter is the open area as shown in Figure 2a. For an upright NT with a diameter of 100 nm, this leads to a maximum estimated area of about two orders higher ($7.0 × 10^{-11}$ cm²) than the extracted area S from the plot ($1.6 × 10^{-13}$ cm²). This discrepancy can be explained with the uneven surface of the NT apex, causing that the emission does not occur over the entire surface. Hence, the smaller value of S is plausible for the upright NT. The lateral one shows a four times higher value for the emission surface, since the geometry is different.
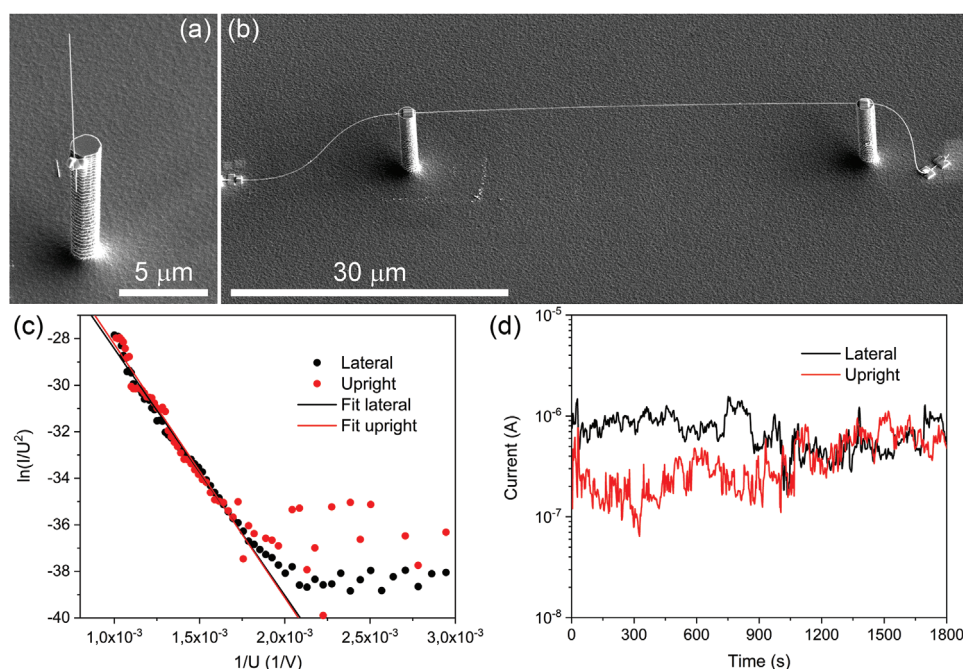
Figure 4. SEM images of the upright a) and lateral b) single NT devices. The scale bars in (a) and (b) are 5 and 30 µm, respectively. c) The FN-plot with corresponding fits. d) Current stability measurements at a constant voltage of 1000 V for both devices.

Table 2. Comparison of the emission behavior of the investigated nanotubes.

Emitter type	E_{on} [MV m^{-1}]	E_{max} [MV m^{-1}]	I_{max} [A]	I_{mean} [A]	ΔI_{rel} [A]	ΔI_{drift} [A h^{-1}]	Φ [eV]
Upright nanotube	13	20	7.51×10^{-7}	7.04×10^{-7}	$\pm 43\%$	-7.67×10^{-7}	4.7
Lateral nanotube	13	20	8.04×10^{-7}	3.65×10^{-7}	$\pm 45\%$	$+1.08 \times 10^{-6}$	4.7

Emitter type	$\approx \beta$	a_{FN} [10^{-8}]	b_{FN} [10^4]	γ [10^4 cm^{-1}]	S [10^{-13} cm^2]	R^2 [%]
Upright nanotube	338 ± 68	(2.29 ± 0.64)	$-(1.03 \pm 0.02)$	(6.77 ± 1.36)	(1.64 ± 0.80)	99.4
Lateral nanotube	332 ± 67	(1.82 ± 0.60)	$-(1.05 \pm 0.02)$	(6.63 ± 1.33)	(1.35 ± 0.71)	99.2

In order to investigate the current stability, long-term measurements (30 min) were performed for both devices as shown in Figure 4d. At a constant voltage of 1000 V, the mean current values were 0.37 and 0.70 μA, respectively. The current fluctuations are in the same range (±43% and 45%) for both orientations. However, the upright NT shows a degradation during the measurement of ≈0.7 μA h^{-1}, while the lateral NT shows a performance improvement of +1.0 μA h^{-1}. This behavior was also observed for the previously investigated MoS$_2$ NTs.[29] Due to the continuous changing of the surface conditions during the measurement, it is possible that some additional emission areas appear on the top surface of the NT, such as bent thin surface layers or cracks with sharp edges. A summary and comparison of extracted parameters of the individual samples are presented in **Table 2**.

3. Conclusion

Alloyed Mo$_{0.56}$W$_{0.44}$S$_2$ NTs were synthesized via the CVT method. The Mo and W atoms are homogenously distributed in the crystal lattice, as seen from the EDS maps as well as from Raman spectra, which contain peaks attributed to MoS$_2$ and WS$_2$. HRTEM images show that these nanotubes are highly crystalline with low density of defects. It was shown that the NT shells grow in pairs, which is reflected in the doubly degenerated helicity observed in the ED pattern. This implies that the alloyed NTs tend to crystallize in the quasi-2H phase when grown with the CTV method. The alloying also lowered the WF of the NTs, compared to pure MoS$_2$ and WS$_2$, making them a great candidate for field emission applications. Two field emission devices, with different geometrical setups, showed promising results at moderate voltages comparable with other TMDC devices.

4. Experimental Section

Synthesis: The material was synthesized by the chemical vapor transport (CVT) reaction inside quartz ampoules using MoS$_2$ and WS$_2$ powders as the precursors and iodine (1–3 mm beads, Sigma–Aldrich, St. Louis, MO, USA, 99.7%) as the transport agent. The ampoules were filled with 100 mg of iodine, 364.5 mg of WS$_2$, and 235.3 mg of MoS$_2$, which correspond to the atomic ratio of MoS$_2$ and WS$_2$ of 1. Ampoules were evacuated down to 10^{-5} mbar, sealed, and put to two-zone furnace. The material was transported from hot zone of the furnace (1133 K) to the growth zone (1009 K). The transport reaction was running for 500 h.

X-Ray Diffraction: X-ray diffraction (XRD) was performed with a D4 Endeavor diffractometer (Bruker AXS) using a quartz monochromatic Cu K$_{\alpha 1}$ radiation source ($\lambda = 0.1541$ nm) and a Sol-X dispersive detector at room temperature. The angular range (2ϑ) was from 5° to 75°, with a step size of 0.02° and collection time of 4 s.

Raman Spectroscopy: Nanotubes were studied by Micro Raman Spectroscopy on a WITec Alpha 300 RS scanning confocal Raman microscope in a backscattered geometry with a polarized Nd: YAG laser operating at a wavelength of 633 nm. The laser beam was focused through a 100x/0.9 microscope objective on an area smaller than 1 μm^2. The spectra were taken on individual nanotubes and the power was ≈0.5 mW to avoid heating and oxidation.

Electron Microscopy: Scanning electron microscopy (SEM) images were obtained using a JEOL – JSM-6510 SEM and a Helios NanoLab 650 Focused Ion Beam-scanning electron microscope (FIB). The FIB microscope was equipped with an Oxford instruments z X-max SDD detector, which was used for Energy-dispersive X-ray spectroscopy (EDS). High-resolution transmission electron microscopy (HRTEM) and electron diffraction (ED) images were acquired using a Cs probe-corrected TEM/STEM JEOL ARM 200CF microscope equipped with a cold-FEG electron source, operating at 200 kV.

AFM and KPFM: Atomic force microscopy (AFM) in non-contact mode and Kelvin probe force microscopy (KPFM) were performed with an Omicron UHV VT-AFM (Scienta Omicron, Taunusstein, Germany) operating at 10^{-9} mbar with the modulation voltage for the KPFM mode applied to the tip. Silicon Cantilevers NSG10 (NT-MDT, Moscow, Russia) with a typical force constant of 11.8 N m^{-1} were used. A single Mo$_{1-x}$W$_x$S$_2$ NT was placed on a freshly cleaved highly oriented pyrolytic graphite (HOPG) substrate with an OmniProbe manipulator 200 (with a sharp tungsten tip) in a FEI Helios Nanolab 650 SEM-FIB microscope (10^{-6} mbar). Only the electron beam was used during the procedure. The work function (WF) was calculated according to the equation in the supporting information.

Field Emission Measurement: Integral FE measurements of the mounted NTs on the structured Si substrate were performed in diode configuration with a 10 MΩ resistor in series to the electrometer with a voltage source (Keithley 6517) in a vacuum chamber at pressures of ≈ 10^{-9} mbar.[33,34] For the assembly of the electron sources, the samples are installed on a partially metallized ceramic sub mount in an aluminium framework. In addition, a metallized (Ti) fine-meshed grid with Si support structures acts as an anode, separated from the cathode by a mica spacer of 50 μm thickness. The total exposed area is ≈ 7 mm^2, due to the round opening with a diameter of 3 mm in the spacer. In order to characterize the current–voltage behavior of the samples, a voltage sweep with a slew rate of 1 V s^{-1} from 0 up to 1000 V and down to 0 V was performed. Furthermore, stability measurements at a constant voltage of 1000 V with a duration of 30 min were conducted and the mean current value, the drift, as well as the fluctuation were calculated. The upper and lower 5% of the measured values were neglected for the calculations.

From the current–voltage curve, the onset field E_{on} (for a current of 1 nA), the maximum current I_{max} for the highest applied voltage, and the corresponding electric field E_{max} can be extracted. The following simplified form describes the relation between the FE current I and the applied voltage V:[35]

$$I = a_{fn} \times U^2 \times \exp\left(-\frac{b_{fn}}{U}\right) \tag{4}$$

**ADVANCED
SCIENCE NEWS**

www.advancedsciencenews.com

**ADVANCED
FUNCTIONAL
MATERIALS**

www.afm-journal.de

where

$$a_{fn} = A \times \frac{S}{\Phi} \times \frac{\gamma^2}{\tau^2} \times \exp\left(\frac{B \times 1.44 \times 10^{-7}}{\Phi^{0.5}}\right) \text{ with } A = 1.54 \times 10^{-6} \qquad (5)$$

$$b_{fn} = B \times \mu \times \frac{\Phi^{1.5}}{\gamma} \text{ with } B = \sqrt{46.65 \times 10^{14}} \qquad (6)$$

and U is applied anode voltage in V, S is emission area in cm^2, Φ is work function in eV, τ is correction factor, μ is correction factor, and γ is voltage conversion factor in cm^{-1}. The image charge was considered and for simplification, the correction factors τ and μ were set to 1 in Equations 5 and 6. The Fowler–Nordheim (FN) plot ($\ln(I/U^2)$ against $1/U$) shows a linear behavior for an ideal metalized emitter. The FE parameter b_{fn} as well as γ correspond to the slope of the regression line in the FN plot. The consideration of the distance between the cathode and anode (50 µm) leads to the field amplification factor β. Further FE parameters, like the constant a_{fn} and the S can be estimated from the axis intercept of the regression line.

Preparation of the Field Emission Samples: In order to investigate the FE behavior of individual NTs, they were placed on structured Si substrates by using a micro manipulator and metal deposition. With these procedures, the parasitic emissions from the substrate can be excluded, due to the increased separation of the substrate from the emission area of NT emitter. Due to the enhanced aspect ratio, the field amplification can be also increased.[29]

Quadratic arrays of 4 × 4 Si pillars with a pitch of 50 µm were fabricated by several dry etching steps.[36] For this purpose, an n-type Si substrate (SIEGERT WAFER GmbH) with a diameter of 100 mm, (100)-orientation, As doped, dopant concentration of 10^{19}–10^{20} cm^3 and specific resistivity of <0.005 Ω cm with a 700 nm SiO$_2$ layer for the fabrication of the arrays was used. The lateral position of the pillars was defined by photolithography of disks with a diameter of 3 µm into AZ5214 photoresist (Microchemicals GmbH). Anisotropic reactive-ion etching (RIE) with CHF$_3$ and O$_2$ in an Oxford Plasmalab 80Plus transfers that arrangement into the SiO$_2$ layer. The resulting discs act as a mask for the etching of the pillars by RIE combined with inductive coupled plasma (ICP) using CHF$_3$ and SF$_6$ as process gases in the dry etching tool. The number of alternating passivation and etching cycles adjusts the height of the pillars. In the next step, the entire SiO$_2$ was removed by wet chemical etching with a buffered HF mixture. Afterward, the substrate was ready for the mounting of the synthesized Mo$_x$W$_{x-1}$S$_2$ NTs.

Several micrometres long NTs were picked up with an OmniProbe manipulator 200 (with a sharp tungsten tip) in a FEI Helios Nanolab 650 SEM-FIB microscope (10^{-6} mbar). For the first device, a NT with a diameter of ≈76 nm was pressed in an upright position against the Si pillar by the manipulator (Figure S1, Supporting Information). Then it was attached at multiple places by focused electron beam induced decomposition of Trimethyl-(methylcyclopentadienyl)-platinum (at 2 kV with 0.2 nA), which resulted in deposition of Pt forming the mechanical and electric contact. For the second device, a long NT (<100 µm) with a diameter of 84 nm (Figure S2, Supporting Information) was spanned over two pillars by the same method and attached to the substrate by Pt at both ends of the NT and on top of the pillars.

Supporting Information

Supporting Information is available from the Wiley Online Library or from the author.

Acknowledgements

Conflict of Interest

The authors declare no conflict of interest.

Data Availability Statement

The data that support the findings of this study are available from the corresponding author upon reasonable request.

Keywords

[1] B. Zhao, D. Shen, Z. Zhang, P. Lu, M. Hossain, J. Li, B. Li, X. Duan, *Adv. Funct. Mater.* **2021**, *31*, 2105132.

[2] S.-W. Zheng, L. Wang, H.-Y. Wang, C.-Y. Xu, Y. Luo, H.-B. Sun, *Nanoscale* **2021**, *13*, 17093.

[3] R. Tenne, L. Margulis, M. Genut, G. Hodes, *Nature* **1992**, *360*, 444.

[4] M. Remskar, A. Mrzel, Z. Skraba, A. Jesih, M. Ceh, J. Demsar, P. Stadelmann, F. Lévy, D. Mihailovic, *Science* **2001**, *292*, 479.

[5] K. S. Novoselov, D. Jiang, F. Schedin, T. J. Booth, V. V Khotkevich, S. Morozov, A. K. Geim, *Proc. Natl. Acad. Sci. USA* **2005**, *102*, 10451.

[6] I. A. M. Al-Ani, K. Ham, O. Klochan, H. T. Hattori, L. Huang, A. Miroshnichenko, *J. Opt.* **2022**, *24*, 053001.

[7] X. Zhao, Z. Shi, X. Wang, H. Zou, Y. Fu, L. Zhang, *InfoMat* **2021**, *3*, 201.

[8] K. F. Mak, C. Lee, J. Hone, J. Shan, T. F. Heinz, *Phys. Rev. Lett.* **2010**, *105*, 136805.

[9] A. Kuc, N. Zibouche, T. Heine, *Phys. Rev. B* **2011**, *83*, 245213.

[10] F. Withers, D. Pozo-Zamudio, A. Mishchenko, A. P. Rooney, A. Gholinia, K. Watanabe, T. Taniguchi, S. J. Haigh, A. K. Geim, A. I. Tartakovskii, *Nat. Mater.* **2015**, *14*, 301.

[11] B. Radisavljevic, A. Radenovic, J. Brivio, V. Giacometti, A. Kis, *Nat. Nanotechnol.* **2011**, *6*, 147.

[12] S. Roy, Z. Hu, S. Kais, P. Bermel, *Adv. Funct. Mater.* **2021**, *31*, 2100387.

[13] C.-H. Lee, G.-H. Lee, A. M. van der Zande, W. Chen, Y. Li, M. Han, X. Cui, G. Arefe, C. Nuckolls, T. F. Heinz, *Nat. Nanotechnol.* **2014**, *9*, 676.

[14] R. Dong, I. Kuljanishvili, *J. Vac. Sci. Technol. B, Nanotechnol. Microelectron.: Mater., Process. Meas., Phenom.* **2017**, *35*, 030803.

[15] Z. Hemmat, Cavin, A. Ahmadiparidari, A. Ruckel, S. Rastegar, S. N. Misal, L. Majidi, K. Kumar, S. Wang, J. Guo, *Adv. Mater.* **2020**, *32*, 1907041.

[16] Y. Chen, J. Xi, D. O. Dumcenco, Z. Liu, K. Suenaga, D. Wang, Z. Shuai, Y.-S. Huang, L. Xie, *ACS Nano* **2013**, *7*, 4610.

[17] D. O. Dumcenco, H. Kobayashi, Z. Liu, Y.-S. Huang, K. Suenaga, *Nat. Commun.* **2013**, *4*, 1.

ADVANCED
SCIENCE NEWS
www.advancedsciencenews.com

ADVANCED
FUNCTIONAL
MATERIALS
www.afm-journal.de

[18] J.-S. Kim, R. Ahmad, T. Pandey, A. Rai, S. Feng, J. Yang, Z. Lin, M. Terrones, S. K. Banerjee, A. K. Singh, *2D Mater.* **2017**, *5*, 015008.

[19] J. Xi, T. Zhao, D. Wang, Z. Shuai, *J. Phys. Chem. Lett.* **2014**, *5*, 285.

[20] D. Wang, L. Liu, N. Basu, H. L. Zhuang, *Adv. Theory Simul.* **2020**, *3*, 2000195.

[21] F. Qin, W. Shi, T. Ideue, M. Yoshida, A. Zak, R. Tenne, T. Kikitsu, D. Inoue, D. Hashizume, Y. Iwasa, *Nat. Commun.* **2017**, *8*, 1.

[22] Y. J. Zhang, M. Onga, F. Qin, W. Shi, A. Zak, R. Tenne, J. Smet, Y. Iwasa, *Optoelectron. Resp. WS2 Tubul. Pn Junct. 2D Mater.* **2018**, *5*, 035002.

[23] L. Yadgarov, B. Višić, T. Abir, R. Tenne, A. Y. Polyakov, R. Levi, T. V. Dolgova, V. V. Zubyuk, A. A. Fedyanin, E. A. Goodilin, *Phys. Chem. Chem. Phys.* **2018**, *20*, 20812.

[24] B. Višić, L. Yadgarov, E. A. A. Pogna, S. D. Conte, V. Vega-Mayoral, D. Vella, R. Tenne, G. Cerullo, C. Gadermaier, *Phys. Rev. Res.* **2019**, *1*, 033046.

[25] D. R. Kazanov, A. Poshakinskiy, V. Y. Davydov, A. N. Smirnov, I. A. Eliseyev, D. A. Kirilenko, M. Remškar, S. Fathipour, A. Mintairov, A. Seabaugh, *Appl. Phys. Lett.* **2018**, *113*, 101106.

[26] S. Reinhardt, L. Pirker, C. Bäuml, M. Remškar, A. K. Hüttel, *Phys. Status Solidi –RRL* **2019**, *13*, 1900251.

[27] S. Fathipour, H. Li, P. Paletti, M. Remskar, S. Fullerton-Shirey, A. Seabaugh, *75th Ann. Device Res. Conf. (DRC)*; IEEE, South Bend, USA **2017**.

[28] S. Fathipour, M. Remskar, A. Varlec, A. Ajoy, R. Yan, S. Vishwanath, S. Rouvimov, W. S. Hwang, H. G. Xing, D. Jena, *Appl. Phys. Lett.* **2015**, *106*, 022114.

[29] R. Ławrowski, L. Pirker, K. Kaneko, H. Kokubo, M. Bachmann, T. Ikuno, M. Remskar, R. Schreiner, *J. Vac. Sci. Technol. B* **2020**, *38*, 032801.

[30] A. Patra, M. A. More, D. J. Late, C. S. Rout, *J. Mater. Chem. C* **2021**, *9*, 11059.

[31] M. B. Sreedhara, Y. Miroshnikov, K. Zheng, L. Houben, S. Hettler, R. Arenal, I. Pinkas, S. S. Sinha, I. E. Castelli, R. Tenne, *J. Am. Chem. Soc.* **2022**, *23*, 10530.

[32] M. Nath, K. Mukhopadhyay, C. N. R Rao, *Chem. Phys. Lett.* **2002**, *352*, 163.

[33] R. Schreiner, Langer, C. Prommesberger, R. Ławrowski, F. Dams, M. Bachmann, F. Düsberg, M. Hofmann, A. Pahlke, P. Serbun, *28th Int. Vac. Nanoelectron. Conf. (IVNC)*, IEEE, South Bend, USA **2015**.

[34] M. Bachmann, F. Düsberg, C. Langer, F. Herdl, L. Bergbreiter, F. Dams, N. Miyakawa, T. Eggert, A. Pahlke, S. Edler, *J. Vac. Sci.*

[35] R. G. Forbes, J. H. B Deane, *Proc. Math. Phys. Eng. Sci.* **2007**, *463*, 2907.

[36] R. Ławrowski, C. Langer, C. Prommesberger, F. Dams, M. Bachmann, R. Schreiner, *27th Int. Vac. Nanoelectron. Conf. (IVNC)*; IEEE, South Bend, USA **2014**.

[37] M. Remškar, Z. Škraba, R. Sanjines, F. Levy, *Appl. Phys. Lett.* **1999**, *74*, 3633.

[38] N. B. Shinde, S. K. D. S. Eswaran, *J. Phys. Chem. Lett.* **2021**, *12*, 6197.

[39] M. Staiger, R. Gillen, N. Scheuschner, O. Ochedowski, F. Kampmann, M. Schleberger, C. Thomsen, J. Maultzsch, *Phys. Rev. B* **2015**, *91*, 195419.

[40] A. Rodriguez, M. Velický, M. Kalbáč, O. Frank, J. Řáhová, V. Zólyomi, J. Koltai, *Phys. Rev. B* **2022**, *105*, 195413.

[41] A. N. Barbosa, N. S. Figueroa, M. Giarola, G. Mariotto, F. L. FreireJr., *Mater. Chem. Phys.* **2020**, *243*, 122599.

[42] M. R. Molas, K. Nogajewski, M. Potemski, A. Babiński, *Sci. Rep.* **2017**, *7*, 1.

[43] J.-H. Fan, P. Gao, A.-M. Zhang, B.-R. Zhu, H.-L. Zeng, X.-D. Cui, R. He, Q.-M Zhang, *J. Appl. Phys.* **2014**, *115*, 053527.

[44] X.-F. Qiao, X.-L. Li, X. Zhang, W. Shi, J.-B. Wu, T. Chen, P.-H. Tan, *Appl. Phys. Lett.* **2015**, *106*, 223102.

[45] Y. Chen, D. O. Dumcenco, Y. Zhu, X. Zhang, N. Mao, Q. Feng, M. Zhang, J. Zhang, P.-H. Tan, Y.-S. Huang, *Nanoscale* **2014**, *6*, 2833.

[46] Y. Chen, H. Deniz, L.-C. Qin, *Nanoscale* **2017**, *9*, 7124.

[47] M. Remškar, Z. Škraba, P. Stadelmann, Levy, *Adv. Mater.* **2000**, *12*, 814.

[48] L. Houben, A. N. Enyashin, Y. Feldman, R. Rosentsveig, D. G. Stroppa, *J. Phys. Chem. C* **2012**, *116*, 24350.

[49] P. Chithaiah, S. Ghosh, A. Idelevich, L. Rovinsky, T. Livneh, A. Zak, *ACS Nano* **2020**, *14*, 3004.

[50] M. B. Sadan, L. Houben, A. N. Enyashin, G. Seifert, R. Tenne, *Proc. Natl. Acad. Sci. USA* **2008**, *105*, 15643.

[51] J. Shen, D. Zhang, F.-H. Zhang, Y. Gan, *Appl. Surf. Sci.* **2017**, *422*, 482.

[52] M. Saqib, J. Jelenc, L. Pirker, S. D. Škapin, L. de Pietro, U. Ramsperger, A. Knápek, I. Müllerová, M. Remškar, *J. Electron. Spectros. Relat. Phenom.* **2020**, *241*, 146837.

[53] F. Maeda, T. Takahashi, H. Ohsawa, S. Suzuki, H. Suematsu, *Phys. Rev. B* **1988**, *37*, 4482.

[54] T. P. Nguyen, W. Sohn, J. H. Oh, H. W. Jang, S. Y. Kim, *J. Phys. Chem. C* **2016**, *120*, 10078.

[55] M. Shiraishi, M. Ata, *Carbon* **2001**, *39*, 1913.

2213869 (8 of 8)

PAPER • OPEN ACCESS

Influence of crystal structure and oxygen vacancies on optical properties of nanostructured multi-stoichiometric tungsten suboxides

To cite this article: Bojana Višić *et al* 2022 *Nanotechnology* **33** 275705

View the article online for updates and enhancements.

Influence of crystal structure and oxygen vacancies on optical properties of nanostructured multi-stoichiometric tungsten suboxides

Bojana Višić[1,2,5] , Luka Pirker[1,5] , Marko Opačić[2], Ana Milosavljević[2], Nenad Lazarević[2], Boris Majaron[3,4] and Maja Remškar[1]

[1] Department of Condensed Matter Physics, Jozef Stefan Institute, Jamova Cesta 39, 1000 Ljubljana, Slovenia
[2] Institute of Physics Belgrade, University of Belgrade, Pregrevica 118, 11080 Belgrade, Serbia
[3] Department of Complex Matter, Jozef Stefan Institute, Jamova 39, 1000 Ljubljana, Slovenia
[4] Faculty of Physics and Mathematics, University of Ljubljana, Jadranska 19, Slovenia

E-mail: bojana.visic@ipb.ac.rs

Abstract

Four distinct tungsten suboxide (WO_{3-x}) nanomaterials were synthesized via chemical vapour transport reaction and the role of their crystal structures on the optical properties was studied. These materials grow either as thin, quasi-2D crystals with the W_nO_{3n-1} formula (in shape of platelets or nanotiles), or as nanowires (W_5O_{14}, $W_{18}O_{49}$). For the quasi-2D materials, the appearance of defect states gives rise to two indirect absorption edges. One is assigned to the regular bandgap occurring between the valence and the conduction band, while the second is a defect-induced band. While the bandgap values of platelets and nanotiles are in the upper range of the reported values for the suboxides, the nanowires' bandgaps are lower due to the higher number of free charge carriers. Both types of nanowires sustain localized surface plasmon resonances, as evidenced from the extinction measurements, whereas the quasi-2D materials exhibit excitonic transitions. All four materials have photoluminescence emission peaks in the UV region. The interplay of the crystal structure, oxygen vacancies and shape can result in changes in optical behaviour, and the understanding of these effects could enable intentional tuning of selected properties.

Supplementary material for this article is available online

Keywords: tungsten oxides, Magnèli phases, nanowires, quasi-2D materials

(Some figures may appear in colour only in the online journal)

[5] These authors contributed equally.

1. Introduction

The family of tungsten oxides, including stoichiometric WO_3 and WO_2 and substoichiometric Magnèli phases (WO_{3-x}, $0 < x < 1$), is widely studied due to numerous intriguing properties [1–5]. These tungsten (sub)oxides have been used as photodetectors [6, 7] and gas sensors [8–10], in photocatalysis and photoelectrochemical water splitting [3, 11, 12],

in smart windows [13] and optoelectronics [14]. In bulk form, WO_3 is a large indirect bandgap n-type semiconductor, with bandgap values reported in the 2.6–3.0 eV range [15–17]. In nanosized WO_3, quantum size effects appear, resulting in a blueshift of the bandgap up to 3.25 eV, with the bandwidth modulation correlated to the size of the nanoparticles [18]. This is a direct consequence of the quantum confinement effect.

Due to the crystal shear mechanism, various substoichiometric Magnèli phases with different combinations of edge- or corner-sharing WO_6 octahedra can be formed [19]. This may lead to appearance of crystal shear (CS) planes and pentagonal columns (PC), which form to accommodate oxygen vacancies [20, 21]. For less reduced suboxides (i.e. x <0.2), CS planes occur; while PCs are formed for x greater than 0.2. In the former, CS planes' corner-sharing WO_6 octahedra become edge-sharing [22], while in the latter WO_7 bipyramids are formed and share their equatorial edges with the WO_6 octahedra [23]. The degree of reduction and appearance of oxygen vacancies can be crucial for understanding the change of the optical response with respect to the fully oxidized WO_3 [8]. Furthermore, it was reported that the oxygen vacancy defect states induced by annealing can significantly improve electrical conductivity [24]. Substoichiometric WO_{3-x} are mostly found to be blue or light green, which is a structure-sensitive phenomenon and is mainly a consequence of the stoichiometry or oxygen vacancies [25, 26]. First-principles pseudopotential and total-energy projector-augmented wave method calculations showed that single oxygen vacancies and substoichiometric crystal structures modify the optical properties and generate different types of defect states in the bulk [27, 28].

For nanostructured WO_{3-x}, various phenomena may lead to different size- and shape- dependent behaviour within the same stoichiometry. This can lead to seemingly contradictory results, if only the effect of the degree of reduction is considered. It was reported that the metallic $WO_{2.83}$ nanorods ($W_{24}O_{68}$) can sustain strong localized surface plasmon resonances (LSPR), centred around 1.4 eV (corresponding to $\lambda = 900$ nm) [26]. Electrical transport measurements of $WO_{2.8}$ (W_5O_{14}) show that they exhibit metallic behaviour [29]. On the other hand, based on electrical transport measurements and photoluminescence spectra, $WO_{2.72}$ ($W_{18}O_{49}$) nanowires (NWs) show a semiconducting behaviour [30, 31].

A close relationship between the creation of oxygen vacancies and stoichiometry (i.e. degree of reduction) and morphology has been reported [32–34]. Both the stoichiometry and the amount of oxygen vacancies heavily depend on the synthesis conditions, and in turn determine the optical and electrical properties, such as photoluminescense and electrical conductivity. Therefore, a careful structural study of these materials is significant for interpreting optical spectra. In this paper, we report on optical properties of various nanostructured suboxides; namely, multistoichiometric W_nO_{3n-1} in two distinct morphologies (platelets and nanotiles), and W_5O_{14} ($WO_{2.8}$) and $W_{18}O_{49}$ ($WO_{2.72}$) nanowires.

2. Methods

2.1. Synthesis

All the materials were synthesized via chemical vapour transport reaction in a two-zone furnace, using iodine as the transport agent. The synthesis protocols are described in detail in [29, 35–37].

2.2. Electron microscopy

Scanning electron microscopy (SEM) was performed on Supra 35 VP (Carl Zeiss, Germany). High-resolution transmission electron microscopy (HRTEM) and electron diffraction (ED) images were obtained by a Cs probe-corrected TEM/STEM JEOL ARM 200CF microscope equipped with a cold-FEG electron source, operating at 200 kV. Cross-sections of the samples for TEM analysis were obtained using a Helios NanoLab 650 Focused Ion Beam-scanning electron microscope (FIB).

2.3. Photoluminescence

The solutions for the optical measurements were prepared using purified water (extinction) or ethanol (photoluminescence and Raman spectroscopy).

Photoluminescence spectra were measured using an optical spectrometer (PTI QuantaMaster 8000 by Horiba) with a continuous Xe lamp and a photomultiplier sensitive in visible and near-infrared part of the spectrum (Hamamatsu R2658). Holographic reflection gratings blazed at 300 nm were used in the dual-stage excitation monochromator, and ruled gratings (500 nm blaze) in the single-stage emission monochromator. The spectra were measured in the wavelength range of 290–450 nm (corresponding to 3.1–4.3 eV) at nominal resolution of 3 nm, with the excitation spectral band centered at 275 nm (4.51 eV). All presented spectra were corrected for spectral dependence of the instrument's excitation and emission channels.

2.4. Extinction measurements

Extinction measurements were performed with an UV–vis spectrometer (Perkin-Elmer lambda 950). The spectra were recorded with a 1 nm resolution. The solution was hand-shaken and the suspensions were measured using quartz cuvettes.

2.5. Raman scattering

The Raman scattering measurements were performed using a Tri Vista 557 Raman system in backscattering micro-Raman configuration. The 532 nm line of VerdiG solid-state (for platelets) and the 514.5 nm line of Ar^+/Kr^+ ion gas laser (for nanotiles and nanowires) were used as an excitation source. A microscope objective with ×100 magnification was used for focusing the laser beam and collecting scattered light. Laser power was kept below 0.5 mW at the sample surface, in order to minimize local heating. Spectra were recorded in parallel and crossed polarisation configuration. All measurements were performed in air, at room temperature. Spectra were corrected for the Bose factor.
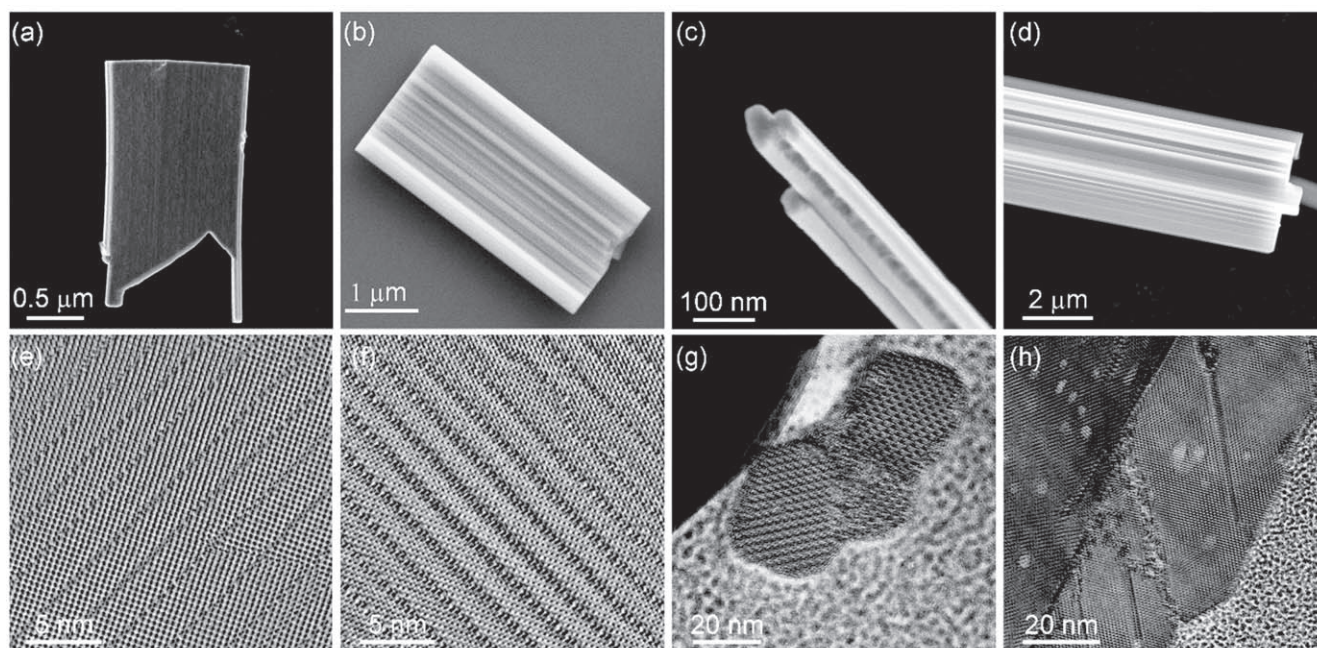
Figure 1. Electron microscopy images of (a), (e) platelets, (b), (f) nanotiles, (c), (g) W_5O_{14} NW and (d), (h) $W_{18}O_{49}$ NW. Top panel corresponds to SEM, while the bottom panel corresponds to TEM images.

Table 1. Stoichiometry of tungsten suboxide nanomaterials, their shape, thickness and lateral size (for 2D W_nO_{3n-1}) or *-diameter and length (for nanowires), and the assessed work function.

Stoichiometry	Shape	Thickness/diameter*	Lateral size/length*	Work function (eV)
W_nO_{3n-1}	Platelets	100 nm	Up to 4 μm	4.18–4.31
W_nO_{3n-1}	Nanotiles	100 nm	Up to several μm	4.94–5.30
W_5O_{14} ($WO_{2.8}$)	Nanowires	100–200 nm	Several tens μm	4.20–4.34
$W_{18}O_{49}$ ($WO_{2.72}$)	Nanowires	Up to 3 μm	Several tens μm	4.55–4.57

2.6. Kelvin probe force microscopy

The work function (WF) was measured with the Kelvin probe force microscopy (KPFM) method using a non-contact frequency-modulated atomic force microscope (NC-AFM, Omicron VT-AFM, Taunusstein, Germany) operating in ultra-high vacuum (10^{-9} mbar). The samples were dispersed in isopropanol and drop casted on a freshly cleaved highly oriented pyrolytic graphite (HOPG) substrate. The AFM and the KPFM images were taken simultaneously on the same area. KPFM was used to determine the WF of the samples by measuring the contact potential difference (CPD) between the substrate (HOPG) and the samples. As HOPG has a fairly stable WF value of 4.60 eV [38], it is commonly used as a reference material in KPFM measurements.

3. Results and discussion

3.1. Composition and morphology

The studied WO_{3-x} phases grow as thin plate-like crystals (platelets, nanotiles) or as nanowires (W_5O_{14}, $W_{18}O_{49}$). Figure 1 shows SEM and TEM images of the W_nO_{3n-1}

platelets (a), (e) and nanotiles (b), (f); W_5O_{14} nanowires (c), (g), and $W_{18}O_{49}$ nanowires (d), (h). The stoichiometry and size of all four studied WO_{3-x} phases is summarized in table 1.

The W_nO_{3n-1} platelets grow epitaxially from $W_{19}O_{55}$ nanowires. These nanowires can either get detached from the platelets by mild sonication, or remain at the long edge of the platelet, as seen in figure 1(a). The platelets grow in a rectangular geometry and are approximately 100 nm thick with the lateral size of up to 4 μm. Several W_nO_{3n-1} Magnèli phases, such as $W_{18}O_{53}$ ($WO_{2.944}$), $W_{17}O_{50}$ ($WO_{2.941}$), $W_{16}O_{47}$ ($WO_{2.938}$), $W_{15}O_{44}$ ($WO_{2.933}$), $W_{14}O_{41}$ ($WO_{2.929}$), W_9O_{26} ($WO_{2.889}$) and $W_{10}O_{29}$ ($WO_{2.9}$), were found within a single platelet [36].

The nanotiles with the length and width up to a few μm are approximately 100 nm thick. They have characteristic surface corrugations that can be several tens of nm deep. They are multi-stoichiometric, with six distinct stoichiometries within a single nanotile: $W_{16}O_{47}$ ($WO_{2.938}$), $W_{15}O_{44}$ ($WO_{2.933}$), $W_{14}O_{41}$ ($WO_{2.928}$), $W_{13}O_{38}$ ($WO_{2.923}$), $W_{12}O_{35}$ ($WO_{2.917}$), and $W_{11}O_{32}$ ($WO_{2.909}$), all having the same W_nO_{3n-1} formula [37]. In both plate-like morphologies (i.e. nanotiles and platelets), CS planes are observed, as shown in
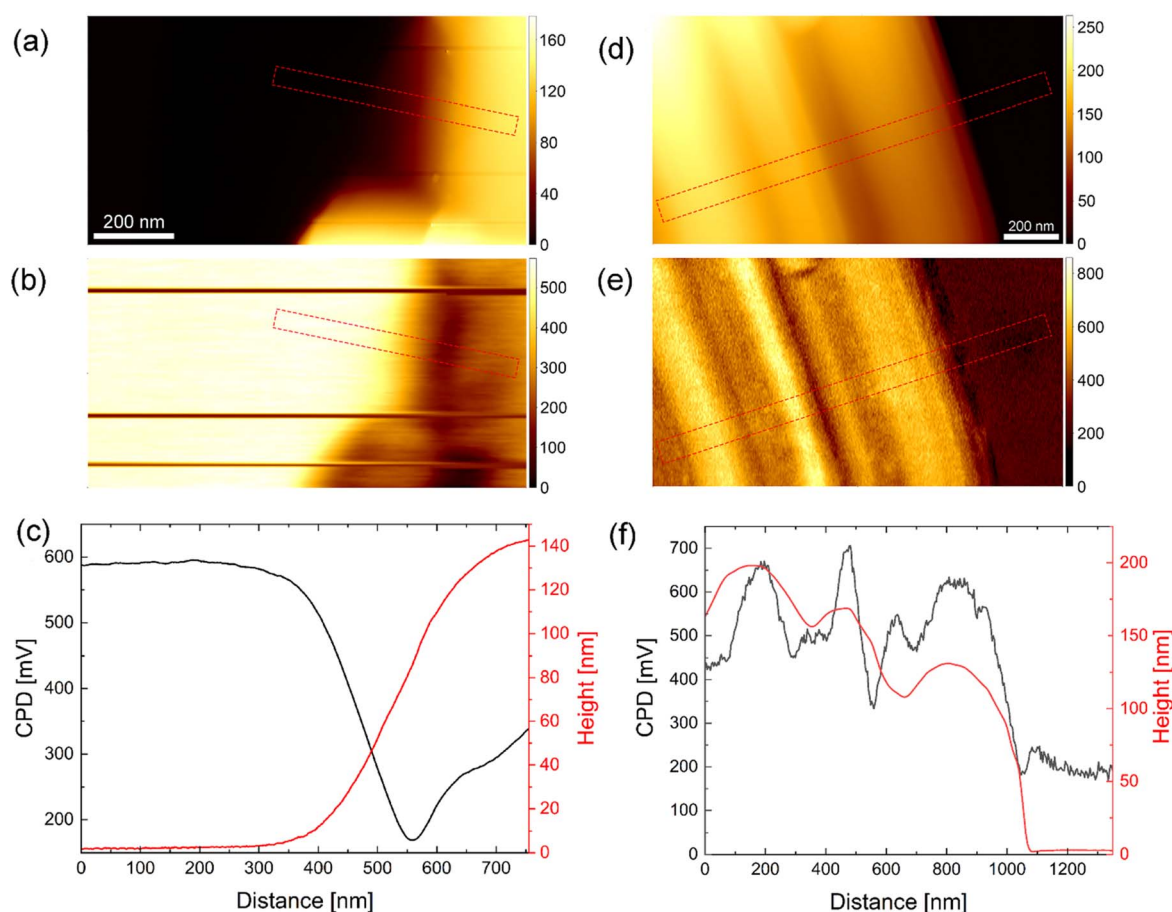
Figure 2. AFM (a), (d) and KPFM images (b), (e) of platelets and nanotiles, respectively. The CPD profiles and the matching thickness (c), (f) correspond to the areas marked with dashed rectangles.

figures 1(e), (f). The distance between the CS planes reflects the stoichiometry of a particular block.

Both W_5O_{14} and $W_{18}O_{49}$ nanowires have constant diameters along the lengths of several tens of μm. The W_5O_{14} NWs are thinner, with the mean diameter of 100–200 nm, while $W_{18}O_{49}$ NWs have significantly larger diameters of up to 3 μm, with rarely observed thin ones [35]. The cross-sectional views of such nanowires (figures 1(g), (h)) reveal that they are composed of several single-crystalline units.

3.2. Work function

The WF was measured on an individual WO_{3-x} nanotile or platelet. The results are compared with the previously published data obtained on the W_5O_{14} and $W_{18}O_{49}$ nanowires [35]. The topography and Kelvin images are shown in figure 2.

The platelet shown in figure 2(a) is around 140 nm thick. The CPD measured on the platelets was between 290 and 420 mV lower than on HOPG, corresponding to a WF of 4.18- 4.31 eV. Very similar WF values were reported earlier for W_5O_{14} nanowires (4.20–4.34 eV) [35]. On the other hand, the CPD obtained on the nanotiles was between 340 and 700 mV higher than on HOPG, indicating a WF of 4.94–5.30 eV. The WF of the nanotiles is thus substantially

higher compared to both W_5O_{14} and $W_{18}O_{49}$ nanowires (4.55–4.57 eV) [35].

The KPFM and AFM images also reveal that the WF is morphology dependent. In the case of platelets, the WF is slightly lower at the edge (figure 2(c)), similar to measurements performed on the edges of W_5O_{14} nanowires [35]. This might be due to the growth mechanism, as the platelets grow from nanowires [36], or due to band bending [39]. The WF of nanotiles also varies with location and was found to be lower inside the corrugations (figure 2(f)). The difference between the CPD at top and the bottom of the corrugation can be up to 350 meV. The summarized positions of WF values are presented in table 2.

3.3. Optical properties

3.3.1. Raman spectroscopy. Raman spectra of WO_{3-x} nanomaterials can be tentatively divided into three regions, characterized by the peaks originating from different types of vibrations. Lattice modes generally appear below 200 cm^{-1}, W–O–W bending modes between approximately 200 and 400 cm^{-1}, whereas between 600 and 900 cm^{-1} one can observe W–O stretching modes [40, 41]. Figure 3 represents room temperature Raman spectra of WO_{3-x} nanostructures measured in three polarization
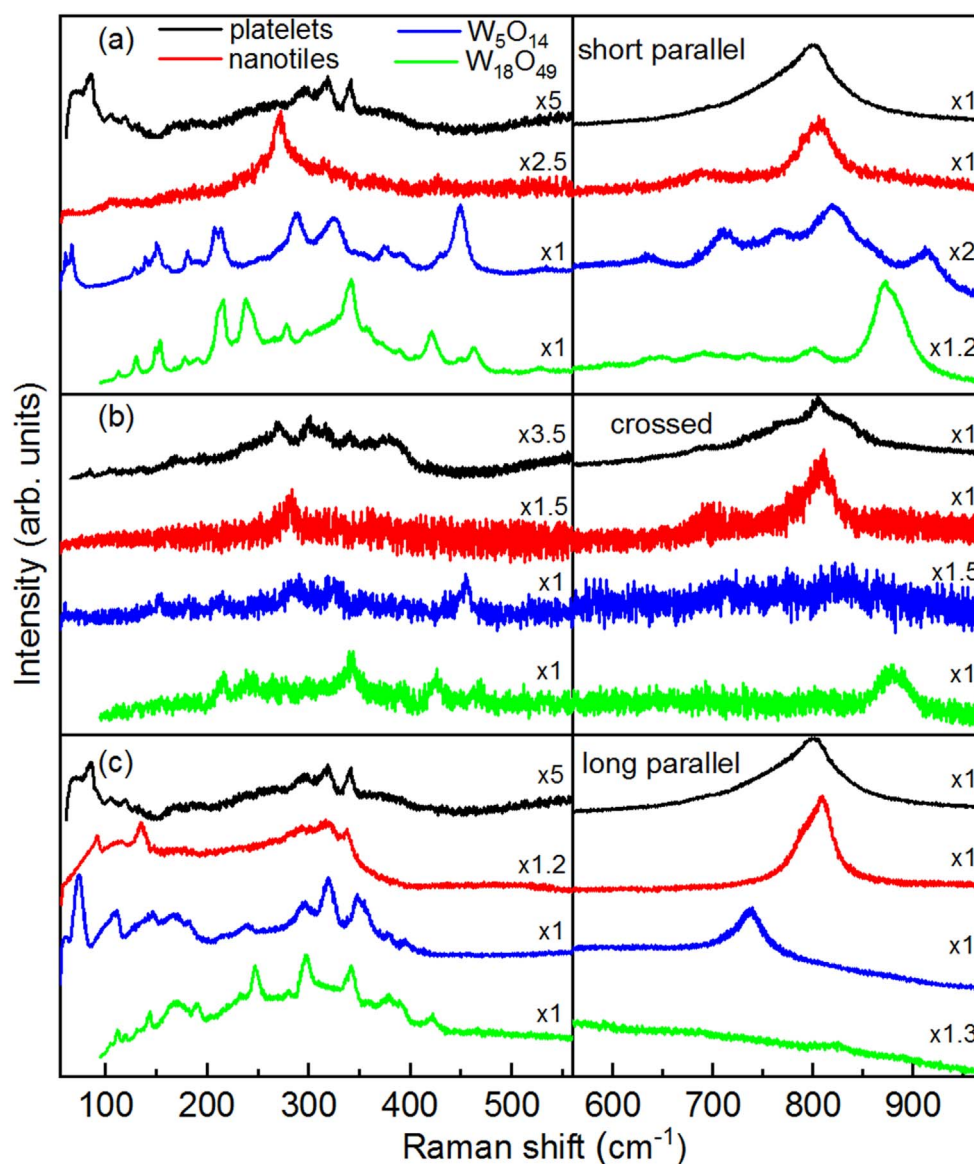
Figure 3. Raman scattering spectra of WO_{3-x} nanostructures measured at room temperature in three polarization configurations: (a) parallel, with incident and scattered light polarized along the short axis of the samples (short parallel configuration), (b) crossed, and (c) parallel, with incident and scattered light polarized along the long axis of the samples (long parallel configuration). For clarity, lower and higher-energy ranges are displayed with different scale factors.

Table 2. Summary of the assessed absorption and PL transitions, bandgap and work function values in tungsten suboxide nanomaterials.

	W_nO_{3n-1} platelets	W_nO_{3n-1} nanotiles	W_5O_{14} ($WO_{2.8}$)	$W_{18}O_{49}$ ($WO_{2.72}$)
UV–vis (nm)	207, 222, 241, 281, 323	205, 216, 240, 281, 324, 416	200, 223, 258, 326, 760	198, 208, 296, 776
PL (nm)	299, 323	302, 316	298, 324	299, 319
Bandgap (direct) (eV (nm))	4.11 (301)	4.05 (306)		
Bandgap (indirect) (eV (nm))	3.76 (330), 3.17 (391)	3.48 (356), 2.78 (446)	2.16 (574)	2.62 (473)
WF (eV)	4.18–4.31	4.94–5.30	4.20–4.34	4.55– 4.57
Average WF (eV)	4.25	5.12	4.27	4.56

configurations: short and long parallel, with incident and scattered light polarized along short and long axis of the sample respectively; and crossed, with polarisations parallel to the short and long axis of the sample but mutually orthogonal. In the case of the platelets, short and long parallel configurations are equivalent due to their symmetry.

Therefore, only two spectra were sufficient to observe all prominent modes noted in [36].

In platelets' crossed polarization configuration spectrum, there are four weak peaks, at 85, 105, 130 and 165 cm^{-1} related to lattice vibration, six peaks centred at 235, 271, 300, 319, 340 and 380 cm^{-1}, originating from W–O–W bending vibrations and one weak (690 cm^{-1}) and two strong (778 and 808 cm^{-1}) W–O stretching vibrations. In parallel configuration, one can observe few relatively weak peaks, at 85, 105, 120, 130, 297, 319 and 340 cm^{-1}, and two sharp overlapped peaks at 778 and 802 cm^{-1}. These results are in very good agreement with those from [36].

In the case of the nanotiles' short parallel polarization spectrum, only one weak peak (105 cm^{-1}) originating from lattice vibration, one strong peak at 271 cm^{-1}, a few weak peaks (at 231, 317, 331, 365 and 428 cm^{-1}) in the W–O–W bending region, and two prominent W–O stretching vibrations centred at 697 and 807 cm^{-1} are observed. In the crossed scattering configuration one can recognize the three highest intensity modes from that were also observed in the short parallel polarization (at 271, 697 and 807 cm^{-1}), whereas spectrum in long parallel polarization contains sharper and more pronounced low energy peaks, indicating good crystallinity and well-defined W–O bond length. Closer inspection revealed eight peaks, at 92, 113, 135, 175, 294, 319, 338 and 807 cm^{-1}, with the two prominent ones at 135 and 807 cm^{-1}, coinciding with the results given in [37].

Raman spectra of nanowires are qualitatively different from those of quasi-2D materials. Namely, for W$_5$O$_{14}$ NW, in short parallel polarization seven lattice (at 67, 129, 139, 151, 181, 208 and 214 cm^{-1}), six W–O–W bending (at 288, 325, 376, 391, 430 and 448 cm^{-1}) and five W–O stretching vibrations, centred around 635, 712, 767, 819 and 912 cm^{-1}, were observed. Crossed polarization revealed Raman peaks at 151, 181, 208, 288, 325, 448 and 712 cm^{-1}, whereas in long parallel polarization one can observe peaks at 73, 108, 147, 167, 181, 237, 297, 319, 350, 376, 394 and 737 cm^{-1}.

In the short parallel polarization, the W$_{18}$O$_{49}$ NW spectrum hosts a large number of peaks, at 113, 129, 149, 153, 178, 190, 211, 215, 238, 245, 278, 341, 358, 390, 422, 449, 463, 527, 644, 689, 737, 801, 871 and 882 cm^{-1}, some of which are overlapping. In crossed polarization configuration there are only a few peaks, centred at 211, 215, 238, 245, 341, 422, 463, 871 and 882 cm^{-1}, whereas the spectrum in the long parallel polarization contains modes at 113, 119, 131, 142, 168, 190, 232, 247, 280, 297, 341, 378, 390, 422 and 821 cm^{-1}. The peak positions of all four materials are summarized in tables S1–4 (available online at stacks.iop.org/NANO/33/275705/mmedia).

Unlike the spectra of the nanotiles and platelets, where the W–O stretching modes centred around 800 cm^{-1} are absolutely dominant, Raman spectra of the nanowires contain a large number of sharp peaks in the first two frequency regions, which are comparable or even more dominant than the ones from the stretching vibrations region. This indicates that 2D materials contain a higher number of W–O bonds with well-defined lengths, whereas W$_5$O$_{14}$ and W$_{18}$O$_{49}$ nanowires have better crystallinity and higher number of
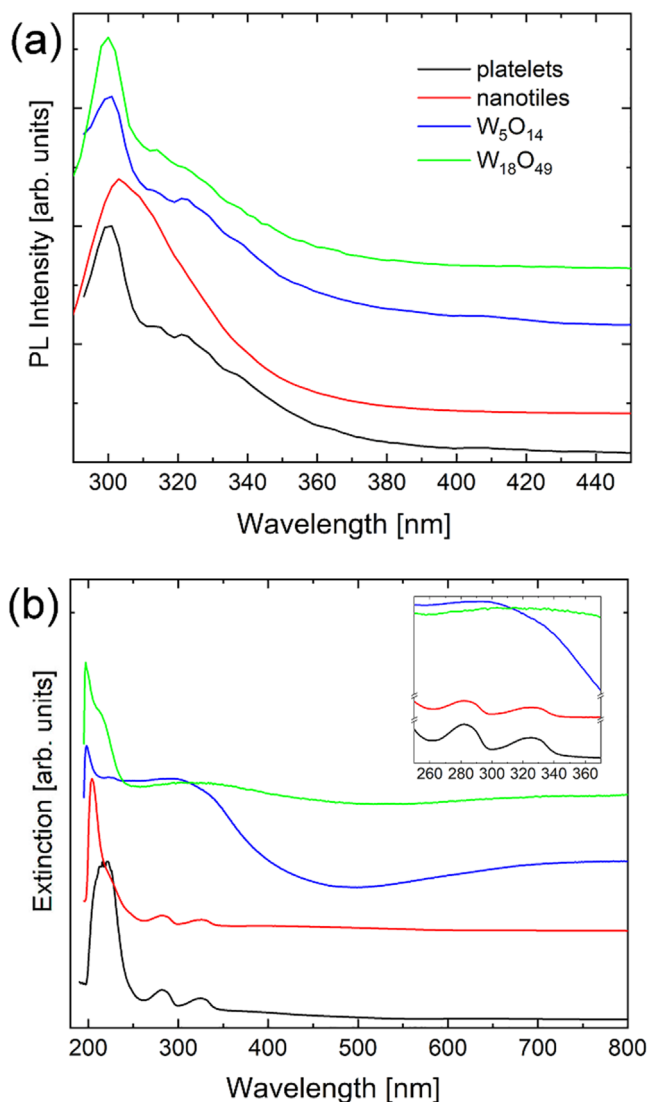
Figure 4. (a) Room temperature PL spectra and (b) UV–vis extinction spectra of platelets, nanotiles, W$_5$O$_{14}$ and W$_{18}$O$_{49}$ nanowires.

W–O–W bonds with well-defined bond angles. The fact that spectra of all the analysed materials strongly depend on the sample orientation and light polarization unequivocally confirms their anisotropic structure.

3.3.2. Photoluminescence. In figure 4(a), the PL spectra of all four materials are presented, measured with the excitation centred at 275 nm (4.51 eV). The PL spectra were deconvolved, confirming that they contain two distinct emission lines in the UV region (figure S1). All of these suboxides have a dominant, high-energy peak situated around 300 nm (4.1 eV). An additional, red-shifted component appears in the 320 nm region (∼3.9 eV), but its contribution varies. The positions of the PL peaks are summarized in table 2.

Because bulk WO$_3$ is an indirect band-gap semiconductor, its photoluminescence (PL) spectrum does not have any prominent features. In contrast, the appearance of new states in WO$_{3-x}$ materials allows distinct optical transitions, often

associated with PL emission lines. Many studies were reported on PL activity of the substoichiometric oxides [42–49], and, in general, correlated the electronic transitions to the defect states within the band gap, arising from oxygen vacancies. The two processes guiding these transitions were assigned either to the occurrence of localized states in the bandgap, stemming from oxygen vacancies or other defects; or to a band-to-band transition, arising from the electron–hole recombination induced by quantum confinement. However, there is no general consensus on interpretation of the observed emissions, as the experimental reports differ and do not unambiguously assign the observed emissions to the proposed mechanisms.

Theoretical models show that an oxygen vacancy can be in three new states, namely in a neutral (V_O^0), single- (V_O^+), or double-charged (V_O^{2+}) [25, 27, 34]. Within these models, the removal of an O atom from WO_3 structure (ReO_3-type, W^{6+}–O^{2-}–W^{6+}) results in creation of a V_O^0 state. This corresponds to creation of either a $W^{6+} + W^{4+}$ or $2W^{5+}$ defect states with levels inside or near the valence band (W^{4+}–V_O^0–W^{6+} or W^{5+}–V_O^0–W^{5+}) [25]. Removal of one additional electron, (i.e. conversion to V_O^+ (W^{5+})), leads to Coulombic repulsion between the positive vacancy and the nearest W-ion, displacing the ion and shifting the defect level into the bandgap (W^{5+}–V_O^+–W^{6+}). Removal of another electron creates a new state within the CB (W^{6+}–V_O^{2+}–W^{6+}). Therefore, the neutral state lies inside the valence band (VB), single-charged in the band gap, and the double-charged state inside the conduction band (CB). In other words, the W^{5+} states are shallow and can act as donor states, while electrons trapped in deeper states (W^{4+}) would need more energy to get excited into the CB. It is also important to note that the bandgap is closely related to the W–O bond length. When an O vacancy is introduced, structural relaxation of the lattice leads to an increase of the W–W distance. As the W ion gets displaced from the center of the WO_6 octahedron, the VB lowers and the CB rises, thus increasing the bandgap [50].

For PL spectra reported for $W_{18}O_{49}$ nanowires and nanorods, peaks appear in UV and blue spectral regions [31, 43, 45, 51]. For the nanorods, the peak located in the UV region blueshifts from 350 to 320 nm as the nanorod diameter decreases. This effect is assigned to quantum confinement, since the stoichiometry remains the same. The blue peak is situated around the absorption edge at 430 nm and does not show any size dependence, therefore it was assigned to the defect states within the bandgap [31].

Previously reported XPS measurements on these materials can provide more insight into origin of the transitions [29, 36, 37]. The valence band spectrum of the platelets indicates a semiconducting behaviour with a negligible density of states at the Fermi energy. On the other hand, the valence band spectrum of the nanotiles revealed a slightly metallic behaviour at room temperature due to a partial overlapping of a broad O 2p peak with W 5d orbitals [36, 37]. The W spectra confirm the presence of 5+ and 6+ oxidation states in both nanotiles and platelets. For the nanotiles, 6+ states represent 84% of the total W 4f, with the remaining 16% assigned to 5+, giving the average oxidation number of

5.84 and $3 - x$ value of 2.92. Similarly, the platelets spectrum is comprised of 81% of 6 + and 19% of 5+, with the oxidation number of 5.81 and $3 - x$ value of 2.91. These values are in great agreement with the stoichiometry deduced from the composition [36, 37]. Since the XPS measurements mainly correspond to the surface layers, these results confirm that the samples have no surface contaminations and that the additional defects do not accumulate at the surface layers. Similarly, 5+ and 6+ states have been observed for W_5O_{14} NW [29], while for the $W_{18}O_{49}$ NW, an additional 4+ state can appear [52, 53].

Focusing on the O 1s spectrum of nanotiles, platelets and W_5O_{14} NW, it can be observed that the peak at 533.5 eV is the most prominent for the platelets, the intensity decreases for NW while it is completely absent for the nanotiles. The WF values were increasing in the same order. This peak, together with the one at 532.0 eV, is attributed to O binding with W in lower oxidation states. HRTEM images shown in figure S3 reveal that the CS planes in the platelets appear parallel to the basal plane, which is still within the depth sensitivity of the XPS. On the other hand, the CS planes in the nanotiles are not close to the surface and are terminated in an unordered fashion, with the regular WO_3 dominating the surface. The effect of the oxidation state of the surface W can be of a great influence on the optical properties of these materials. Therefore, we can attribute the two observed emission bands in the UV to two electron–hole recombination processes, whereby the hole comes from the VB, while the electrons come from two resonant states within the CB, i.e. from two V_O^{2+} states [25, 48].

3.3.3. Extinction. As previously mentioned, both theoretical and experimental studies correlated oxygen vacancies and/or substoichiometric crystal structure to the appearance of defect states [27, 54, 55]. It was reported that up to $x = 0.1$, the optical and electrical properties of bulk WO_{3-x} are governed primarily by localized electrons involved in polarons [26]. The insulator-metal transition begins at $x = 0.1$, as the polaron wave functions start to overlap and form delocalized states [56]. As the x increases, free electrons start to dominate optical processes. In general, the indirect bandgap corresponds to the electronic transition from the filled O 2p orbitals at the top of the valence band to the empty W 5d orbitals in the conduction band [57]. Therefore, the absorption spectrum of WO_3 is essentially featureless until the photon energy reaches the bandgap value. Near the UV region, interband transitions start to take place and govern the optical properties [57].

Extinction (UV–vis) measurements, which include contributions of both absorbance and scattering processes, were performed on all four materials and the spectra are presented in figure 4(b). Although the samples were diluted in order to avoid the multi-scattering regime, the scattering effects in the near UV region cannot be completely excluded. The deconvolution of all the spectra has been performed and the positions of the individual peak contributions extracted, as shown in figure S2.

The most prominent transitions appear in the UVC range, with two contributions centred at 207 and 222 nm for the platelets and at 205 and 216 nm for the nanotiles, with another peak situated at 240 nm for both. Additionally, there are two prominent and closely positioned peaks, situated at 281 and 324 nm. These peaks may originate from exitonic transitions, as described later. A wide and less intense peak is also observed at 359 nm and 416 nm for the platelets and nanotiles, respectively. For both materials, the scattering is accounted for with a model function, as described in the SI.

On the other hand, the spectra of nanowires are significantly different compared to the quasi-2D materials. Both types of NWs have a high-energy peak around 200 nm. For $W_{18}O_{49}$ NWs, this peak can be deconvolved into two peaks positioned at 198 and 208 nm. $W_{18}O_{49}$ NWs spectrum has a higher-energy peak centred at 296 nm, ending with a broad transition at 776 nm. In addition to the peak at 200 nm, W_5O_{14} NWs have a very weak peak at 223 nm and an additional broad peak at approximately 300 nm, which can be deconvoluted into two peaks situated at 258 and 326 nm. An even broader peak appears at 760 nm in the near-IR part of the spectrum. The emergence of the near-IR peaks can be associated with LSPR due to free charge carriers. LSPR were observed previously in $W_{24}O_{68}$ ($WO_{2.83}$) and $W_{19}O_{55}$ ($WO_{2.89}$) nanorods, positioned at 900 nm and 600 nm, respectively [26, 55]. Assigning the near-IR tails to LSPR is also in agreement with earlier measurements on these NWs, which suggested metallic behaviour [29, 35].

Extinction spectra of these suboxides vary substantially in the literature, even within the same stoichiometry or morphology. For example, ultrathin (sub-nanometre) $W_{18}O_{49}$ ($WO_{2.72}$) nanowires show a large absorption tail in the visible part of the spectrum, which saturates upon oxidation [32, 51]. This effect points to the presence of a large number of oxygen vacancies or substoichiometric crystal structures. For the nanowires with larger diameter, the absorption in the visible and near-IR range drops. Nanorod bundles of the same stoichiometry have rather featureless spectra, with a steady decrease with increasing wavelength [31]. In the case of $W_{19}O_{55}$ ($WO_{2.89}$) nanorods, the extinction spectrum in UV–vis consists of one broad peak situated at 600 nm (2.07 eV) and a strong absorption band at 200–400 nm, similar to that seen in bulk WO_3 [55]. On the other hand, $W_{24}O_{68}$ ($WO_{2.83}$) nanorods support strong LSPRs, as evidenced by a broad peak centred around 900 nm [26]. WO_{3-x} reduced cubic nanosheets have a narrow peak around 220 nm, with a broader one centred around 300 nm [58]. The strong absorption in the long wavelength region is attributed to the new, oxygen vacancies-induced levels below the conduction band.

Qualitatively, the line shapes of the nanotiles and platelets spectra are similar to those of $WO_{2.9}$ ($W_{20}O_{58}$) nanoparticles [54] and WO_{3-x} quantum dots [59]. For the $WO_{2.9}$ NPs, the UV–vis spectrum consists of two shoulders at 220 and 265 nm, and a band at 320 nm with the bandgap estimated at 3.1 eV (400 nm). These NPs are also stoichiometrically the closest to platelets and nanotiles. Quantum dots have a high-intensity high-energy peak followed by broader

bands around 230 and 285 nm. Therefore, the two peaks found in the nanotiles and platelets and positioned at 281 and 323 nm are most likely a consequence of the crystal structure, i.e. the CS planes.

From the measured extinction spectra, direct and indirect optical bandgaps can be calculated using the equation [60]:

$$\alpha = \frac{A(h\nu - E_g)^n}{h\nu},$$

Here, α is the absorption coefficient, A is a constant, and E_g is the indirect bandgap for $n = 1/2$ and direct bandgap in the case of $n = 2$. The corresponding Tauc plots are presented in figure S4.

The optical bandgaps are highly sensitive to morphology and stoichiometry. In the literature, the measured optical bandgaps of bulk WO_3, bulk $WO_{2.9}$ and $WO_{2.9}$ nanowires were reported at 2.67 eV, 3.05 eV and 3.17 eV, respectively [3, 32]. For $W_{18}O_{49}$ nanorod bundles, the absorption edge is situated at 2.95 eV [31]. The decrease of the bandgap value of these nanorods by approximately 0.5 eV compared to that of the WO_3 nanoparticles of similar size (3.44 eV) [61] is assigned to the presence of new states correlated to the oxygen vacancies. The appearance of these new states can lead to the rise of two indirect absorption edges, as reported for the suboxide nanosheets (at 2.6 eV and 1.11 eV) [58]. In general, the optical bandgap of these nanostructured suboxides is governed by several different processes. The quantum confinement results in the increase of the bandgap, i.e. the smaller the particle, the larger the bandgap. A similar effect can be assigned also to the Burstein–Moss shift [62]. Namely, in the case of n-type metal oxide semiconductors, an increase of dopants (i.e. oxygen vacancies and W^{5+} atoms) shifts the absorption edge to higher energies due to filling states. Consequently, the measured bandgap, as determined from the onset of interband absorption, moves to higher energies (i.e. undergoes a blue shift). On the other hand, in heavily doped semiconductors, bandgap renormalization takes place. As the electrons start interacting with defects and impurities, their energy shifts due to a variety of effects, such as exchange interaction or Coulombic repulsion [63]. Consequently, the bandgap shrinks with increasing doping level, explaining the decrease of the band-gap with the increase of x [64]. The complex interplay of all these effects makes the value of the bandgap difficult to predict.

For both the nanotiles and platelets, an increase of the indirect bandgap is observed. However, there is an opening of another, lower energy bandgap. This bandgap appears as a consequence of the altered electronic structure due to bond length changes caused by oxygen vacancies and formation of CS planes with W atoms in lower oxidation states. The appearance of two indirect absorption edges was previously reported in suboxide nanosheets [58]. The two indirect bandgaps appear at 3.76 and 3.17 eV for the platelets and at 3.48 and 2.78 eV for the nanotiles. The former value can be assigned to the regular bandgap (between the VB and the CB), while the latter appears

between a new, defect-induced band and CB. The regular gap coincides with the transitions observed in the extinction spectra. These values lie in the upper range of the bandgaps reported in the literature, which is attributed to the distortions in the WO_6 octahedra in such sub-stoichiometric materials [12, 24].

Nanowires show the indirect bandgap values of 2.16 and 2.62 eV for W_5O_{14} and $W_{18}O_{49}$, respectively. As these materials show LSPR fingerprints and therefore free charge carriers, their bandgap decreased with respect to WO_3.

The calculated direct optical bandgap is 4.11 eV (302 nm) for the platelets and 4.05 eV (306 nm) for the nanotiles. These values are in good agreement with the dominant PL peaks that are situated at 4.15 eV and 4.11 eV for the platelets and nanotiles, respectively. As discussed previously, both recorded PL bands are in the UV region, in the 3.9–4.2 eV range and can be assigned to two resonant states introduced by oxygen vacancies [27, 47]. Namely, an electron–hole pair forms an exciton near the oxygen vacancy. When an electron is excited to a state at or above the resonance, it can be trapped. The emission bands in the UV are thus attributed to electron–hole recombination, where the electron comes from one of the two resonant levels in the CB, while the hole occupies the VB. Therefore, the direct bandgap stems from optical transitions related to the defect states. These transitions and the corresponding bandgaps are at the same positions for nanotiles and platelets, confirming their similar stoichiometry. The bang gap values and extinction peak positions are presented in table 2.

4. Conclusions

Structural and optical properties of four different WO_{3-x} nanostructures with different morphologies and/or stoichiometries are presented. While the two quasi-2D materials show polycrystallinity, nanowires are of uniform W_5O_{14} and $W_{18}O_{49}$ composition. Raman spectra reveal that less oxidized W_xO_{3x-1} stoichiometries have higher number of W–O bonds with well-defined lengths, whereas more reduced tungsten suboxides have a higher number of W–O–W bonds with well-defined bond angles. The extinction spectra reveal the appearance of excitonic states for the less oxidized W_xO_{3x-1} stoichiometries and two indirect bandgaps deduced from the Tauc plots. Both values appear in the upper range reported for suboxide materials, which can be explained by the formation of oxygen vacancies. The extinction spectra of the more reduced tungsten suboxides show the presence of LSPR in the near-IR region. Their bandgaps are lower, as they have a higher number of free charge carriers, confirmed by the LSPR-like peaks. PL spectra reveal two distinct emission peaks in the UV range, present in all four nanomaterials. They are attributed to electron–hole recombination, with the hole stemming from the VB and electron from one of the resonant states within the CB. Furthermore, the effects of stoichiometry and CS planes are discussed in relation to the understanding of the optical properties.

Data availability statement

All data that support the findings of this study are included within the article (and any supplementary files).

ORCID iDs

Bojana Višić ⬤ https://orcid.org/0000-0002-2065-0727
Luka Pirker ⬤ https://orcid.org/0000-0003-0741-0048
Boris Majaron ⬤ https://orcid.org/0000-0003-2841-8276
Maja Remškar ⬤ https://orcid.org/0000-0002-8919-1768

References

[1] Mahjabin S *et al* 2021 Effects of oxygen concentration variation on the structural and optical properties of reactive sputtered WOx thin film *Sol. Energy* **222** 202–11

[2] Thummavichai K, Xia Y and Zhu Y 2017 Recent progress in chromogenic research of tungsten oxides towards energy-related applications *Prog. Mater. Sci.* **88** 281–324

[3] Huang Z F, Song J, Pan L, Zhang X, Wang L and Zou J J 2015 Tungsten oxides for photocatalysis, electrochemistry, and phototherapy *Adv. Mater.* **27** 5309–27

[4] Pirker L and Višić B 2021 Recent progress in the synthesis and potential applications of two-dimensional tungsten (Sub) oxides *Isr. J. Chem.* (https://doi.org/10.1002/ijch.202100074)

[5] Zhang X, Wei Y and Yu R 2022 Multi-dimensional tungsten oxides for efficient solar energy conversion *Small Structures* **3** 2100130

[6] Liu J, Zhong M, Li J, Pan A and Zhu X 2015 Few-layer WO_3 nanosheets for high-performance UV-photodetectors *Mater. Lett.* **148** 184–7

[7] He Z, Liu Q, Hou H, Gao F, Tang B and Yang W 2015 Tailored electrospinning of WO_3 nanobelts as efficient ultraviolet photodetectors with photo-dark current ratios up to 1000 *ACS Appl. Mater. Interfaces* **7** 10878–85

[8] Aguir K, Lemire C and Lollman D 2002 Electrical properties of reactively sputtered WO_3 thin films as ozone gas sensor *Sensors Actuators* B **84** 1–5

[9] Zhang C *et al* 2011 Highly sensitive hydrogen sensors based on co-sputtered platinum-activated tungsten oxide films *Int. J. Hydrogen Energy* **36** 1107–14

[10] Hariharan V, Gnanavel B, Sathiyapriya R and Aroulmoji V 2019 A review on tungsten oxide (WO_3) and their derivatives for sensor applications *Int. J. Adv. Sci. Eng.* **5** 1163–8

[11] Sayama K, Mukasa K, Abe R, Abe Y and Arakawa H 2001 Stoichiometric water splitting into H2 and O2 using a mixture of two different photocatalysts and an IO3−/I− shuttle redox mediator under visible light irradiation *Chem. Commun.* **23** 2416–7

[12] Wang G, Ling Y and Li Y 2012 Oxygen-deficient metal oxide nanostructures for photoelectrochemical water oxidation and other applications *Nanoscale.* **4** 6682–91

[13] Miyazaki H, Ishigaki T and Ota T 2017 Photochromic smart windows employing WO3-based composite films *J. Mater. Sci. Res.* **6** 62–6

[14] Hai Z, Wei Z, Xue C, Xu H and Verpoort F 2019 Nanostructured tungsten oxide thin film devices: from optoelectronics and ionics to iontronics *J. Mater. Chem.* C **7** 12968–90

[15] Granqvist C G 2000 Electrochromic tungsten oxide films: review of progress 1993–1998 *Sol. Energy Mater. Sol. Cells* **60** 201–62

[16] González-Borrero P *et al* 2010 Optical band-gap determination of nanostructured WO3 film *Appl. Phys. Lett.* **96** 061909

[17] He T and Yao J 2007 Photochromic materials based on tungsten oxide *J. Mater. Chem.* **17** 4547–57

[18] Zheng H, Ou J Z, Strano M S, Kaner R B, Mitchell A and Kalantar-zadeh K 2011 Nanostructured tungsten oxide– properties, synthesis, and applications *Adv. Funct. Mater.* **21** 2175–96

[19] Polaczek A, Pekala M and Obuszko Z 1994 Magnetic susceptibility and thermoelectric power of tungsten intermediary oxides *J. Phys.:Condens. Matter* **6** 7909

[20] Tilley R 1970 The formation of shear structures in sub- stoichiometric tungsten trioxide *Mater. Res. Bull.* **5** 813–23

[21] Pickering R and Tilley R 1976 An electron microscope study of tungsten oxides in the composition range WO2. 90 · WO2. 72 *J. Solid State Chem.* **16** 247–55

[22] Magnéli A 1953 Structures of the ReO3-type with recurrent dislocations of atoms: homologous series' of molybdenum and tungsten oxides *Acta Crystallogr.* **6** 495–500

[23] Lundberg M, Sundberg M and Magnéli A 1982 The 'pentagonal column' as a building unit in crystal and defect structures of some groups of transition metal compounds *J. Solid State Chem.* **44** 32–40

[24] Mohamed A M, Amer A W, AlQaradawi S Y and Allam N K 2016 On the nature of defect states in tungstate nanoflake arrays as promising photoanodes in solar fuel cells *Phys. Chem. Chem. Phys.* **18** 22217–23

[25] Deb S K 2008 Opportunities and challenges in science and technology of WO3 for electrochromic and related applications *Sol. Energy Mater. Sol. Cells* **92** 245–58

[26] Manthiram K and Alivisatos A P 2012 Tunable localized surface plasmon resonances in tungsten oxide nanocrystals *JACS* **134** 3995–8

[27] Karazhanov S Z, Zhang Y, Mascarenhas A, Deb S and Wang L-W 2003 Oxygen vacancy in cubic WO3 studied by first-principles pseudopotential calculation *Solid State Ionics* **165** 43–9

[28] Migas D, Shaposhnikov V and Borisenko V 2010 Tungsten oxides. II. The metallic nature of Magnéli phases *J. Appl. Phys.* **108** 093714

[29] Remškar M, Kovac J, Viršek M, Mrak M, Jesih A and Seabaugh A 2007 W5O14 nanowires *Adv. Funct. Mater.* **17** 1974–8

[30] Shi S, Xue X, Feng P, Liu Y, Zhao H and Wang T 2008 Low- temperature synthesis and electrical transport properties of W18O49 nanowires *J. Cryst. Growth* **310** 462–6

[31] Su C-Y and Lin H-C 2009 Direct route to tungsten oxide nanorod bundles: microstructures and electro-optical properties *J. Phys. Chem.* C **113** 4042–6

[32] Paik T *et al* 2018 Photocatalytic hydrogen evolution from substoichiometric colloidal WO3−x nanowires *ACS Energy Lett.* **3** 1904–10

[33] Song K, Liu X, Tian C, Deng H, Wang J and Su X 2019 Oxygen defect-rich WO3−x nanostructures with high photocatalytic activity for dehydration of isopropyl alcohol to propylene *Surf. Interfaces* **14** 245–50

[34] Wang F, Di Valentin C and Pacchioni G 2011 Semiconductor- to-metal transition in WO3−x: nature of the oxygen vacancy *Phys. Rev.* B **84** 073103

[35] Saqib M *et al* 2020 Field emission properties of single crystalline W5O14 and W18O49 nanowires *J. Electron. Spectrosc. Relat. Phenom.* **241** 146837

[36] Pirker L, Višić B, Škapin S D, Dražić G, Kovač J and Remškar M 2020 Multi-stoichiometric quasi-two- dimensional Wn O 3n− 1 tungsten oxides *Nanoscale.* **12** 15102–14

[37] Pirker L, Višić B, Kovač J, Škapin S D and Remškar M 2021 Synthesis and characterization of tungsten suboxide WnO3n − 1 nanotiles *Nanomaterials.* **11** 1985

[38] Maeda F, Takahashi T, Ohsawa H, Suzuki S and Suematsu H 1988 Unoccupied-electronic-band structure of graphite studied by angle-resolved secondary-electron emission and inverse photoemission *Phys. Rev.* B **37** 4482

[39] Lanzoni E M *et al* 2021 The impact of Kelvin probe force microscopy operation modes and environment on grain boundary band bending in perovskite and Cu (In, Ga) Se2 solar cells *Nano Energy* **88** 106270

[40] Daniel M, Desbat B, Lassegues J, Gerand B and Figlarz M 1987 Infrared and Raman study of WO3 tungsten trioxides and WO3, xH2O tungsten trioxide tydrates *J. Solid State Chem.* **67** 235–47

[41] Hardcastle F D and Wachs I E 1995 Determination of the molecular structures of tungstates by Raman spectroscopy *J. Raman Spectrosc.* **26** 397–405

[42] Johansson M B, Zietz B, Niklasson G A and Österlund L 2014 Optical properties of nanocrystalline WO3 and WO3−x thin films prepared by DC magnetron sputtering *J. Appl. Phys.* **115** 213510

[43] Lee K, Seo W S and Park J T 2003 Synthesis and optical properties of colloidal tungsten oxide nanorods *JACS* **125** 3408–9

[44] Feng M *et al* 2005 Strong photoluminescence of nanostructured crystalline tungsten oxide thin films *Appl. Phys. Lett.* **86** 141901

[45] Hong K, Xie M, Hu R and Wu H 2007 Synthesizing tungsten oxide nanowires by a thermal evaporation method *Appl. Phys. Lett.* **90** 173121

[46] Wang J, Lee P S and Ma J 2009 Synthesis, growth mechanism and room-temperature blue luminescence emission of uniform WO3 nanosheets with W as starting material *J. Cryst. Growth* **311** 316–9

[47] Luo J Y, Xu N S, Zhao F L, Deng S Z and Tao Y T 2011 Ultraviolet superfluorescence from oxygen vacancies in WO3−x nanowires at room temperature *J. Appl. Phys.* **109** 024312

[48] Wang B, Zhong X, He C, Zhang B, Cvelbar U and Ostrikov K 2021 Nanostructure conversion and enhanced photoluminescence of vacancy engineered substoichiometric tungsten oxide nanomaterials *Mater. Chem. Phys.* **262** 124311

[49] Wang D *et al* 2013 High-performance gas sensing achieved by mesoporous tungsten oxide mesocrystals with increased oxygen vacancies *J. Mater. Chem.* A **1** 8653–7

[50] Walkingshaw A D, Spaldin N A and Artacho E 2004 Density- functional study of charge doping in WO3 *Phys. Rev.* B **70** 165110

[51] Xi G *et al* 2012 Ultrathin W18O49 nanowires with diameters below 1 nm: synthesis, near-infrared absorption,

photoluminescence, and photochemical reduction of carbon dioxide *Angew. Chem. Int. Ed.* **51** 2395–9

[52] Guo C, Yin S, Dong Q and Sato T 2012 The near infrared absorption properties of $W_{18}O_{49}$ *RSC Adv.* **2** 5041–3

[53] Guo C, Yin S, Yan M, Kobayashi M, Kakihana M and Sato T 2012 Morphology-controlled synthesis of $W_{18}O_{49}$ nanostructures and their near-infrared absorption properties *Inorg. Chem.* **51** 4763–71

[54] Barreca F, Acacia N, Spadaro S, Curro G and Neri F 2011 Tungsten trioxide (WO_{3-x}) nanoparticles prepared by pulsed laser ablation in water *Mater. Chem. Phys.* **127** 197–202

[55] Qian J, Zhao Z, Shen Z, Zhang G, Peng Z and Fu X 2016 Oxide vacancies enhanced visible active photocatalytic W 19 O 55 NMRs via strong adsorption *RSC Adv.* **6** 8061–9

[56] Salje E and Güttler B 1984 Anderson transition and intermediate polaron formation in WO_{3-x} Transport properties and optical absorption *Philos. Mag.* B **50** 607–20

[57] Hjelm A, Granqvist C G and Wills J M 1996 Electronic structure and optical properties of WO_3, $LiWO_3$, $NaWO_3$, and HWO_3 *Phys. Rev.* B **54** 2436

[58] Fang Z *et al* 2017 Synthesis of reduced cubic phase WO_{3-x} nanosheet by direct reduction of $H_2WO_4 \cdot H_2O$ *Mater. Today Energy* **6** 146–53

[59] Wang Y *et al* 2017 Simultaneous synthesis of WO_{3-x} quantum dots and bundle-like nanowires using a one-pot template-free solvothermal strategy and their versatile applications *Small* **13** 1603689

[60] Pankove J I 1971 *Optical Processes in Semi-Conductors* (Mineola, NY: Dover Publications, Inc)

[61] He T *et al* 2002 Photochromism of WO_3 colloids combined with TiO_2 nanoparticles *J. Phys. Chem.* B **106** 12670–6

[62] Sarkar A, Ghosh S, Chaudhuri S and Pal A 1991 Studies on electron transport properties and the Burstein-Moss shift in indium-doped ZnO films *Thin Solid Films* **204** 255–64

[63] Walsh A, Da Silva J L and Wei S-H 2008 Origins of band-gap renormalization in degenerately doped semiconductors *Phys. Rev.* B **78** 075211

[64] Smith W, Zhang Z-Y and Zhao Y-P 2007 Structural and optical characterization of WO_3 nanorods/films prepared by oblique angle deposition *J. Vac. Sci. Technol.* B **25** 1875–81

Dynamical Nature of Exciton-Polariton Coupling in WS$_2$ Nanoparticles

Sudarson Sekhar Sinha,[a] Bojana Višić,[b, c] Archana Byregowda,[d] and Lena Yadgarov*[d]

Abstract: Semiconducting transition metal dichalcogenides can be synthesized in a wide range of structures and geometries, including closed cage nanostructures, such as nanotubes or fullerene-like nanoparticles (NSs). The latter is especially intriguing due to the stability, enhanced light-matter interactions, and ability to sustain exciton-polaritons (EPs) in ambient conditions, i.e., strong coupling of excitonic resonances to the optical cavity. Here we investigate the dynamics of EPs formation in WS$_2$ NPs in the time domain using femtosecond transient extinction spectroscopy. We develop a gamut of analytical methods and models with time-dependent parameters to extract the underlying non-equilibrium dynamics of EPs formation. We find that the formation of EPs in WS$_2$ NPs is not instantaneous but a gradual process that occurs only after several picoseconds. Specifically, for the short delay times, the light-matter interaction is guided by excitonic absorption, whereas for the long delay times, the process is controlled by polaritonic scattering. We discover that the coupling strength is a time-dependent entity and not a constant as is usually defined. Namely, there is a nonlinear coupling between excitonic and external modes and a notable transition from weak to strong coupling limit. Our results show that the time-dependent phenomenological dynamical model quantitatively reproduces the nonlinear dynamical coupling as well as the effects of the pump fluence on the coupling strength.

Keywords: 2D materials · inorganic fullerene like nanoparticles · polaritons · excitons · femtosecond spectroscopy · strong coupling

Introduction

Extensive research efforts have been devoted to understanding and utilizing the unique optical properties of semiconductor nanostructures (NSs). Much effort has been placed on their ability to confine light into nanoscale dimensions,[1] which subsequently increases the field strength. In turn, this effect enhances light-matter interactions and leads to nonlinearities, large photonic forces, and enhanced emission and absorption probabilities.[2] In general, semiconductor NSs support cavity modes if their scales are comparable to the wavelength of light in vacuum. However, semiconductors with a refractive index that is much larger than that of their surroundings can also efficiently confine light into subwavelength dimensions.[1b,2–3] The cavity modes are generated by the confinement of the light into small volumes and the Fabry-Perot recirculation.[1b] The resonance conditions in nanocavities depend on the refractive index of the medium and the semiconductor, the nanostructure's dimensions, and geometry, as well as the polarization of the optical field. Together with their ability to sustain cavity-mode resonances, semiconductor NSs can generate excitons and can thus create quasi-particles known as exciton-polaritons (EPs).[4] EPs are formed as a result of strong coupling between the excitons and the optical modes of the nanocavity (photon).

The interactions between excitons and cavity mode resonances are usually studied in the weak and strong coupling regimes. The energy spectrum of the coupled systems is modified such that the frequencies of the new modes are different from the original oscillator modes. The frequencies shift or the spectral change depends on the strength of coupling.[5] Typically, the weak coupling manifests itself as a narrow asymmetric dip and a negligible shift at the resonance frequency of the uncoupled oscillators.[5] Under the weak coupling regime, the energy transfer rate between the two modes is lower than the relaxation rate of the system.[6]

In the strong coupling regime, the interaction between the modes is strong enough and significantly modifies the energy levels. Strong coupling induces a significant spectral shift of

[a] S. S. Sinha
Department of Materials and Interfaces, Weizmann Institute of Science, Rehovot, 7610001 Israel

[b] B. Višić
Institute of Physics Belgrade, University of Belgrade, Pregrevica 118, 11080 Belgrade, Serbia

[c] B. Višić
Solid State Physics Department, Jozef Stefan Institute, Jamova cesta 39, 1000 Ljubljana, Slovenia

[d] A. Byregowda, L. Yadgarov
The Department Chemical Engineering, Ariel University, Ramat HaGolan St 65, 4077625 Ariél
E-mail: lenay@ariel.ac.il

the resonances and manifests itself as well-separated peaks in the energy spectrum. Here, the new hybridized energies correspond to hybrids of the original modes of the interacting oscillators.[5,7] The strong interaction between the coupled modes leads to an ultrafast oscillation between the two excited states.[6b] The period of this oscillation is known as the Rabi oscillation period and should be much faster than the decoherence time of the excitation.[8] The spectral splitting induced by the strong coupling is inferred as Rabi energy splitting.[9] The hybrid nature of EPs opens possibilities for applications associated with information transfer, photonic and quantum technologies, and more.[10]

Owing to their sizable bandgaps, strongly bound excitons, and high oscillator strength, the transition metal dichalcogenides (TMDs) are a promising platform to explore EP formation dynamics. Layered TMDs compounds are two-dimensional (2D) materials and have been studied intensively for a decade in the context of electrical, optical, and mechanical applications.[11] The lattice of layered TMDs materials, e.g., MoS_2, consists of a 2D S–M–S sandwich structure, where M is the transition metal atom that binds to six chalcogen (S=S, Se or Te) atoms via strong covalent bonds. The MS_2 (M=Mo, W) layers are stacked together by weak van der Waals (vdW) forces.[12] MS_2 exhibits a bandgap in the visible range, rendering it suitable for exploitation in solar cells, photodegradation of toxic materials, photovoltaics, and numerous other electronic applications. The indirect bandgap of bulk and multilayer MS_2 transforms into a direct bandgap in a single-layer material.[12d] The properties of 2D-TMD semiconductors can be engineered through mechanical or structural changes. For instance, due to coupling between their mechanical and electrical properties,[13] the electronic structures can be altered by introducing curvature to the 2D topology.[14]

MS_2-type TMD materials feature A, B, and C exciton transitions in the visible light range. The excitonic transitions arise from the interlayer interactions and spin-orbit splitting, where the magnitude of the A–B splitting is independent of the number of layers (down to a few layers).[15] Due to their sizable bandgaps, strongly bound excitons, and high oscillator strength, these materials can sustain stable polaritons under ambient conditions. Namely, the MS_2-type TMDs can trap optical cavity modes, resulting in a strong interaction of photonic modes and the excitons. Indeed, it was shown that MS_2 embedded in microcavities exhibited signatures of strong exciton-polariton coupling.[16] The strong coupling in the Fabry-Perot microcavity configuration was observed for monolayer[17] and multilayer systems.[12a,16b,17–18] As these strong light-matter interactions occur at ambient conditions, TMDs polaritonic materials generate a considerable interest in the field of nanodevices.[12c,19]

The fact that EP can exist in multilayered TMD materials under ambient conditions inspired a renewed interest in the optical properties of MX_2 closed-cage layered nanostructures, such as nanotubes (NTs) and fullerene-like nanoparticles (NPs). Nanotubes and fullerene-like nanoparticles have been synthesized in substantial amounts and their properties were widely studied.[20] These studies resulted in numerous applications, and led to their rapid commercialization.[21] The multi-wall closed-cage MX_2 nanostructures preserve the semiconductor nature of their bulk counterparts and are usually indirect bandgap semiconductors.[22] Using tight-binding model calculations, it was shown that the zig-zag (n,0) single-wall NTs exhibit a direct bandgap whereas the lowest transition of armchair (n,n) NTs exhibits indirect bandgap.[23] The experimental results indicates that the bandgap of these closed-cage nanomaterials shrinks with the decrease in diameter.[24] Moreover, due to the chiral nature of the NTs, the quasi 1D superconductivity, Little-Parks oscillations, photovoltaic effects, and the ambipolar transition behavior in ionic liquid and strong electroluminescence is observed.[25]

Interestingly, MoS_2 and WS_2 closed-cage nanomaterials are emerged to be unique systems that support polaritonic features even when dispersed in aqueous solutions without an external cavity.[12a,26] Moreover, the strong-coupling effects in WS_2 nanotubes (NTs) exist even when dispersed in aqueous solutions, where EPs modes occur due to strong coupling between excitons and cavity modes confined in the nanotubes.[12a,18] The use of such closed-cage nanostructures allows remarkable tunability of light-matter interactions, such that by varying the diameter of the NTs we can shift from pure excitonic to polaritonic features.[18b]

Although light-matter interaction of bulk and single layers of MS_2 materials is studied intensively, their closed-caged counterparts have not been thoroughly explored yet. Notwithstanding, the study of excitons coupled with light in multi-layered closed-cage 3D materials could provide broader perspectives for the fundamental properties of EPs in sub-wavelength dimensions. Their ability to sustain 3D cavity modes, stability and the lack of the dangling bonds can suppress exciton capture at non-radiative recombination centers. Moreover, WS_2 NPs are expected to serve as an extraordinary platform for applications and fundamental research in the field of TMDs polaritonics.

Here, we provide a time-dependent study of the coupling between exciton resonances and intrinsic optical cavity modes. We employ femtosecond (fs) broadband optical pump-probe spectroscopy to examine the response of WS_2 NPs in aqueous dispersion and explore time-dependent coupled states formation between exciton resonances and an intrinsic cavity mode. Using a simplistic comparison of the steady-state absorbance and extinction derivatives with the transient extinction spectra, we find that in the fs time-limit, the light-matter interaction is guided by the excitonic absorption, whereas at picoseconds (ps) time-delays, the process is controlled by polaritonic scattering. Moreover, by expressing the transient signals as the difference of the transmission with and without pump, we discover temporal transition from weak to strong coupling limit as the excited excitons relax into the coupled (polaritonic) state. Namely, we find that the formation of EPs in WS_2 NPs is not instantaneous but a gradual process that occurs only after several ps. Using these findings, we propose a model for

the time-dependent coupling of exciton and cavity modes with phenomenological dynamics. The temporal evolution of the model parameters clarifies the nonlinear dynamical coupling and the effects of the pump fluence on the coupling strength. The gamut of proposed models can hereafter be utilized to guide the experimental observation of exciton-polariton formation and coupling evolution dynamics. Moreover, the obtained results can be applied in the field of TMDs polaritonics for exploring genuinely unique physical scenarios and exploiting these new phenomena in technology in areas such as nanoscale lasing, quantum optics, and nanomanipulation.

Results and Discussion

The studied WS_2 fullerene-like nanoparticles consist of 20-40 concentric shells and span diameters from 30 to 100 nm.[27] This somewhat high size distribution can be narrowed down using a simple dispersion-fractionation technique.[18b] Figures 1a present the SEM and TEM images of such nanoparticles. The size and high degree of crystalline order of the NPs can be appreciated from these figures. The absorbance was measured using an integrating sphere which allows excluding the scattering contribution. The absorbance spectra exhibit distinct resonances at 630 nm and 530 nm (Figure 1b, **red line**) assigned to the A and B excitonic transitions, respectively.[28] In contrast to the absorbance, the extinction spectra of the dispersed WS_2 NPs (Figure 1b, **black line**) introduce maxima at 680, 580, 510 nm, which are red-shifted compared to the A, B, and C excitonic transitions of the WS_2 NPs and the bulk.[28–29] The extinction measurements are performed by a standard UV-Vis spectrophotometer, hence the spectra include absorbance and scattering features.[30] The difference between absorbance and extinction spectra can be assigned to the scattering related phenomena – polaritons. It

was shown that WS_2 nanostructures with a diameter > 60 nm, sustain cavity modes that are strongly coupled to the A and B excitons and generate polaritonic modes.[18a,b, 19b, 31] Thus it can be concluded that the unusual extinction spectrum of the dispersed WS_2 NP is of polaritonic nature.

To study the formation of exciton-polariton (EP) quasiparticles, the ultrafast relaxation dynamics of WS_2 NP were investigated using femtosecond pump-probe optical spectroscopy. Here, the electron system is driven out of the equilibrium by the femtosecond pump pulse. The ultrafast motion is then captured by a broadband probe pulse with delay. This setup is used to determine the relative change in transmittance ($\Delta T/T$) as a function of pump-probe delay and wavelength. The ultrafast transient response of the states at 97 mW of pump is shown in Figure 2. The main features obtained from the femtosecond $\Delta T/T$ spectra are the two photo-bleaching and photo-induced absorption peaks. Photobleach (PB) and photo-induced absorption (PA) peaks correspond to decreased and increased transmittance (PB $= -\Delta T/T$; PA $= \Delta T/T$), respectively. The $\Delta T/T$ spectra of WS_2 NP at the short delay (0.3 ps) show PB at 625 and 525 nm and PA at 662 and 550 nm, corresponding to A and B excitonic resonances.[32] At longer delays, most features are already significantly shifted, thus excitons can no longer be considered as the primary photoexcitation species. Specifically, from short (0.3 ps) to long (100 ps) delays, there is a 13 nm blue shift in the PB and PA states, i.e., the PA and PB shifted from 662 to 649 nm and 625 to 612 nm, respectively. (Figure S1, SI). The blue shift occurs mainly during the first 30 ps and is very high compared to the one reported for the few-layered WS_2 (~ 4 nm).[32a] (Figure S2, SI) That considerable shift at shorter delay times, followed by decay at longer delays times, suggests two distinct processes and some coupling between them. Indeed, it was confirmed before that excitons in few-layered WS_2 are the primary photoexcitation species, dissociating into charge pairs with a time constant of ~1.3 ps.[32a]
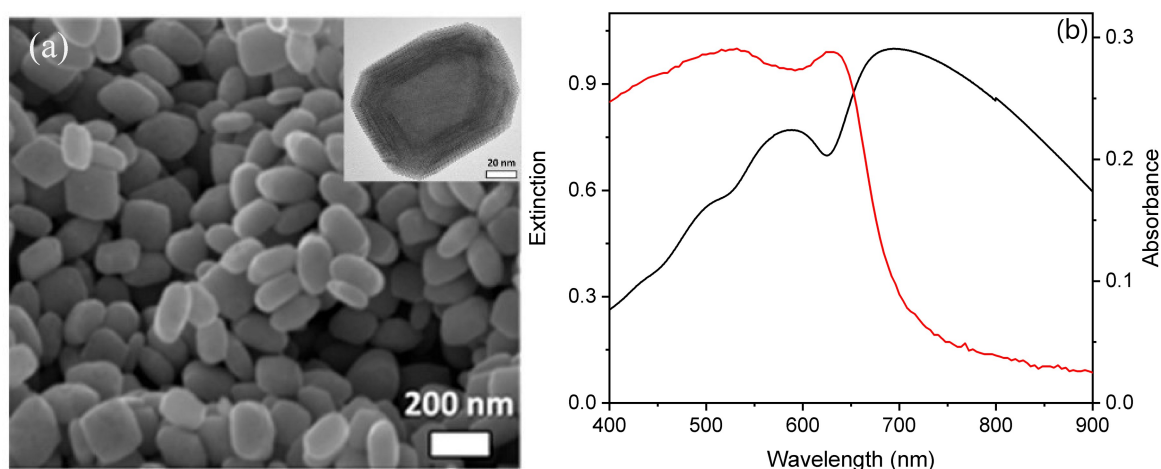
Figure 1. (a) SEM image of WS_2 NP; (inset) TEM image of WS_2 NP (b) extinction (black line) and absorption (red line) spectra of the dispersed WS_2 NP.
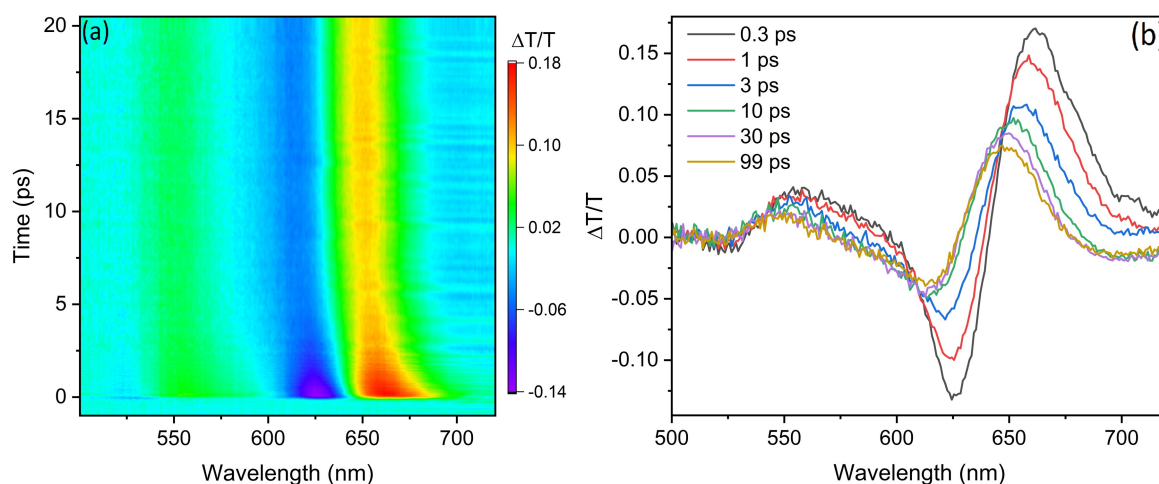
Figure 2. (a) Transient transmission trace $\left(\frac{\Delta T}{T}\right)$ of WS$_2$ NPs for 97uW pump power. (b) Temporal evolution of transient spectra $\left(\frac{\Delta T}{T}\right)$ at different pump-probe delay. Note the shift in photo-absorption and photo-bleach states in exciton (625 nm and 663 nm) to polariton (616 nm and 650 nm) states.

Moreover, it was found that in WS$_2$ nanotubes, the exciton resonances shift on the femto- and picosecond time scales due to the many-body effects of the photogenerated charge carriers and their population dynamics.[18a] Generally, it was established that in WS$_2$ and MoS$_2$ nanotubes the transient spectra are dominated by the coupling of the exciton resonances to the cavity mode resonances.[18a,c] In another work, it was shown that, while WS$_2$ nanotubes of an average diameter >80 nm support polaritonic modes, the extinction of nanotubes with smaller diameter controlled mainly by excitonic features. [ref. Shina size] Note that the influence of the size distribution on the polariton dynamics is not discussed here, and will be presented in the future work. As most of the electro-optical properties of WS$_2$ NPs are comparable to their nanotubes counterparts, the dynamics of NP with diameter >80 nm are expected to be similar to the latter, i.e., dominated by strong coupling of exciton resonances to the cavity mode resonances.

To understand the coupling between exciton and polariton, it is necessary to observe the photophysical processes on different time scales. The transient absorption spectroscopy produces a dynamical differential absorption spectrum, and the PB and PA processes are the main observables. Generally, the energy of the PB/PA processes is constant in time, except when intermediate dynamical processes occur. These processes are usually manifested by a spectral shift of the PB/PA picks.[33] Intriguingly, in the case of dispersed WS$_2$ NP, the short time spectra (~ 0.3 ps) are very different from the long time (~ 100 ps) differential absorption spectra. To elucidate this phenomenon, let us calculate the differential spectra using steady-state extinction and absorbance measurements by Eq. 1 and 2, respectively.

$$\frac{dT_A}{d\lambda} = d\left(10^{-A(\lambda)}\right)/d\lambda = -T_A \frac{d\alpha_A}{d\lambda} \tag{1}$$

$$\frac{dT_E}{d\lambda} = d\left(10^{-\varepsilon(\lambda)}\right)/d\lambda = -T_E \frac{d\alpha_E}{d\lambda} \tag{2}$$

Here α_E and α_A correspond to the extinction and absorption coefficient at wavelength λ, respectively. The T_E and T_A are the transmittances in extinction and absorption measurements. Note that extinction coefficients contain scattering and absorbance contribution, whereas the absorption coefficient is a pure absorption process with no scattering. The comparison of the steady-state derivatives to $\Delta T/T$ spectra at short and long delay times (0.03 ps and 98.9 ps) to the absorption and extinction derivatives are presented in Figure 3. The PB and PA peak positions at the shortest delays correspond to the maxima and minima of the absorbance derivatives. (Figure 3a, Eq. 1) Generally, the ground state bleaching and its absorption are the dominant processes at instantaneous excitation ($t \sim 0$), so the derivative of absorbance coefficient and the $\Delta T/T_{(t=0)}$ are expected to match. Indeed, there is a good overlap between $dT_A/d\lambda$ and $\Delta T/T_{(t=0)}$ at 660 nm. The PA is red-shifted by 15 nm compared to $dT_A/d\lambda$ minima (~ 610 nm). This shift can be explained by the response of the excitons or non-thermal hot electrons to the higher polar excited state.[32a,34] At the longest delay ($t = 98.9$ ps), the PB and PA peaks do not match with the $dT_A/d\lambda$ but almost completely overlap with the features of the extinction derivative, $dT_E/d\lambda$. (Figure 3b, Eq. 2) The extinction features of the dispersed WS$_2$ NP are governed by the polaritonic modes.[18a,19b,31a,b] Thus the match between the extinction derivative and the $\Delta T/T$ ($t = 98.9$ ps) implies that the latter is dominated by the polaritonic states.[18a,b] In over words, the formation of EPs in WS$_2$ NPs is not instantaneous but a gradual process that occurs only after several ps. Moreover, the PA and PB of the coupled states are considerably shifted compared to the excitonic features. Interestingly, the somewhat simplistic comparison of the
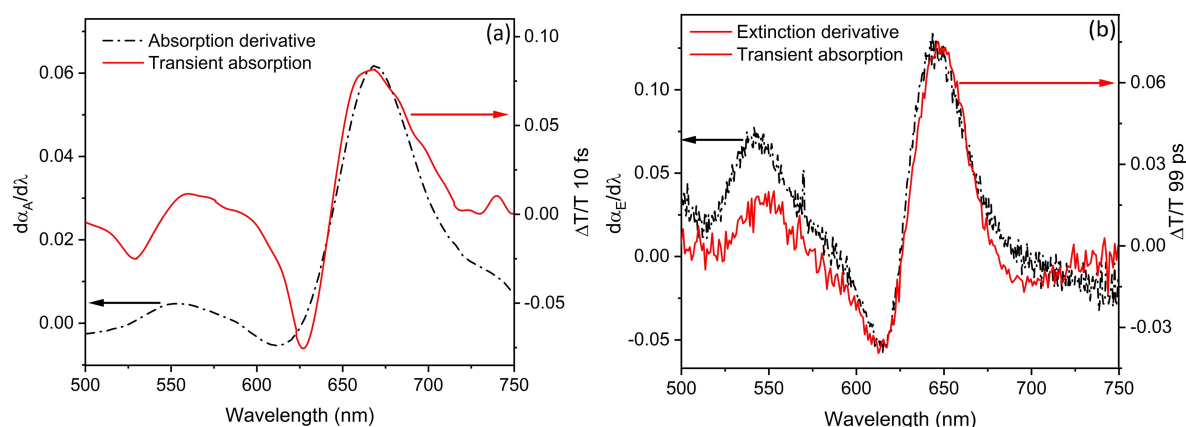
Figure 3. (a) A comparison plot of the short time (~10 fs, red solid line) experimental transient transmission $\left(\frac{\Delta T}{T}\right)$ and absorption derivative $\left(\frac{d\alpha_A}{d\lambda}\right)$ of steady-state signal (dash-dotted black line) calculated using Equation 1 of WS$_2$ NPs. (b) A comparison plot of the long time (~99 ps, black solid line) experimental transient transmission $\left(\frac{\Delta T}{T}\right)$ and the extinction derivative $\left(\frac{d\alpha_E}{d\lambda}\right)$ of steady-state signal (dash-dotted black line) calculated using Equation 2 of WS$_2$ NPs.

derivatives (Eq. 1, 2) with the ΔT/T spectra provides immediate assignment of the short- and long-delay processes. The results of the spectra comparison (Figure 3) infer that for the short delay times, the photophysical process is guided by the excitonic absorption, whereas for the long delay times, the process is controlled by polaritonic scattering. Furthermore, the matching of the derivatives with the ultrafast profile at short- and long-delay times reveals that the temporal dynamics of the quasi-systems strongly depend on the state of their coupling.

To comprehend the dynamics of exciton-polariton coupling, we consider the spectral shift and the change in spectral width observed in the transient absorption spectra of the dispersed WS$_2$ NP. (Figure 2b) These phenomena are not prevalent in pump-probe spectroscopy of molecules and semiconductors, yet they occur in WS$_2$ nanostructures due to many-body effects.[18a,c,35] The blue shift of the PB and PA and the change in their spectral width can be considered as shifts of an individual exciton.[36] Considering the spectral feature of the transitions as Gaussian, the transient signals from pump-probe spectroscopy can be expressed as the difference of the transmission in the presence and absence of the pump. (Eq. 3)

$$\Delta T(\lambda,\ t) = a_e(t) exp\left[-\left(\frac{\lambda - \lambda_0 - \Delta\lambda(t)}{\gamma + \Delta\gamma(t)}\right)^2\right]$$

$$-a_g(t)\ \exp\left[-\left(\frac{\lambda - \lambda_0}{\gamma}\right)^2\right] \qquad (3)$$

where a, λ_0, and γ are the amplitude, peak position of the exciton transition, and spectral width, respectively. The subscripts g and e represent the ground state and the excited state, respectively. The pre-exponential factors (a_e and a_g) indicate the temporal population for the excited and ground state. The shifts in spectral position and width from the steady-state values are denoted as Δλ and Δγ, respectively. These fitting

parameters are varied to obtain the best fit of $\Delta T(\lambda,\ t)$ to the measured ΔT/T. The time-dependent shifts of Δλ and Δγ are the indicators of the bandgap renormalization and the distribution of the excited electrons.[18a]

Figure 4a represents the comparison between measured and the fitted spectral evolution of the transient spectra ΔT/T at the different pump-probe delays. The photo-absorption (PA) states are observed at 662 nm and 556 nm and correspond to the components of A and B excitons, respectively. The prominent photo-bleach (PB) state at 625 nm corresponds to the component of A exciton. The decay time relaxations of an individual A and B excitons are 1.2 and 2.1 ps, respectively. These values were derived from the fitting parameter – spectral shift (Δλ(t)). (Figure 4b, Eq. 3) The A exciton decays faster than the B exciton due to stronger coupling with the cavity modes of the former. The dynamical nature of the spectral shift is apparent here, indicating the relaxation of the excitons to the coupled (polaritonic) state. The change in spectral width (Δγ(t)) further emphasizes the mechanism of the A and B excitons' relaxation into the coupled state. (Figure 4b, inset) Note that the spectral width is directly correlated with the coupling constant (g). The approach used for Eq. 3 assumes that the shift of spectral width is constant with time. However, from the poor linear fit presented in the inset of Figure 4b, it is evident that this approach is not sufficient to describe the nonlinear change in spectral width. Thus, we consider an additional model to account for the unusual coupling in WS$_2$ NP further.

In order to understand the individual dynamics of PB and PA processes of polaritons and excitons, the temporal evolution dynamics have to be explored in detail. Driving by this requirement, the dynamics of different states were extracted by fitting the decay transients. To fit the photo-excitation dynamics, we recall that the recorded differential transmission of temporal dynamics can be represented as $\Delta T(\lambda, t) = T_p(\lambda,\ t) - T_{np}(\lambda,\ t)$. Where T_p and T_{np} are the
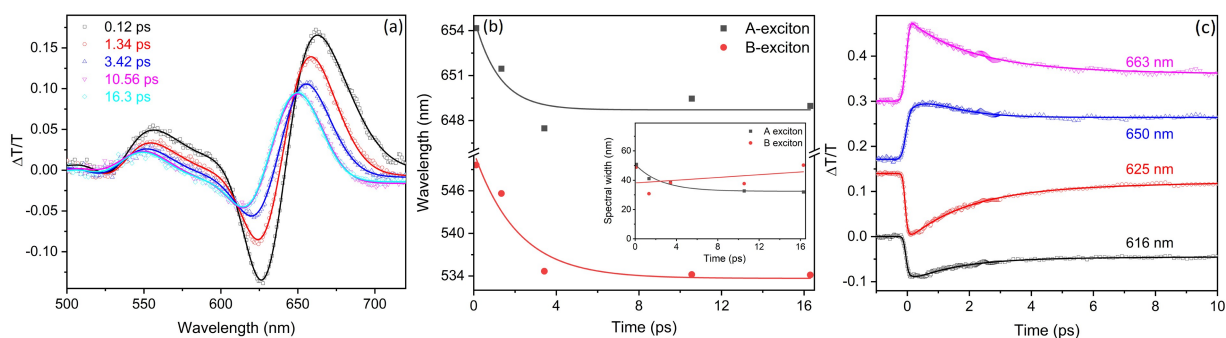
Figure 4. (a) Fitted plot of transient spectra $\left(\frac{\Delta T}{T}\right)$ at different pump-probe delay presented in Figure 2. he symbols represent the experimental data points and the solid lines are the fitted curve using Eq. 3. **(b)** Plot of temporal variation spectral shift ($\Delta\lambda(t)$) of the A and B exciton with varied delay time, calculated from the fitting parameters of Eq. 3. The transition from A and B excitons to the polaritonic states can be realized from this shift. **(Inset)** Plot of temporal variation of spectral width ($\Delta\gamma(t)$) with delay time. The spectral width of A exciton shows an exponential delay whereas B exciton shows a linear shift due to hybridization of upper and lower polaritons. **(c)** Transient dynamics of PB states and PA states of excitons and polaritons of WS$_2$ NPs for 97uW pump power. The transients are fitted using Eq. 4 and presented as solid lines.

wavelengths (λ) dependent transmission signal at the different pump-probe delay (t) in the presence (p) and absence (np) of the pump laser, respectively. For each examined λ, the dynamics follow exponential decay or rise, thus the decay transients can be fitted as follows (Eq 4):[37]

$$\frac{\Delta T(\lambda,\ t)}{T} = \sum_{i} a_i(\lambda, t)\exp\left(-\frac{t}{\tau_i}\right) \qquad (4)$$

here a_i and τ_i are the pre-exponential factors (or the amplitude) and decay lifetime of the ith decay process (a particular state at a specific λ). Due to the low signal-to-noise ratio, only the signal around the A exciton is considered. The comparison of the experimental and the fitted transient dynamics of PA and PB states, lifetimes, and amplitudes are presented in Figure 4c and S3. The free parameters of the fit results are presented in Table 1. There are two PA states, 662 nm for A exciton and 650 nm for polariton, and two PB states, 625 nm for A exciton and 616 nm for polariton. The fastest PA component (τ_{1A}) of the exciton A is due to coupling with the non-polaritonic state.[32a] The PA of the polariton shows two distinct decay components. The longer component (τ_{2_PB}) can be ascribed to the longer charge recombination processes or the effect of the strong cavity pumping.[38] The long charge recombination process suggests that these polaritonic materials are suitable for photonic applications. The PB process presents two decay

components for the excitons, whereas the polaritons show a rise component along with two decay components. The rise component of the polaritons is induced by the coupling of the cavity modes to the excitons. The decay times can be assigned to the recombination processes.[39] The result of the fitted decay dynamics reveals that both: the excitons and the polaritons have more than one lifetime. This finding suggests the existence of multiple coupled states associated with the exciton-polariton decays.

To understand the fascinating coupling dynamics, the experimental results of power-dependent dynamics were analyzed using the time-dependent coupling model.[40] Here the exciton density in the excited state is considered to be proportional to the pump fluence. Therefore, the polariton density also increases with the pump power. The population of polaritons depends on the coupling constant between the exciton and the cavity modes. Thus, the polariton density also changes with time. However, the coupling between the exciton and the cavity shows time-dependent coupling and depends on the pump fluence.[35b] The dynamical equations of these interacting systems are presented in Equation 5 a–c.[40]

$$\frac{dN_{exc}(t)}{dt} = -k_1 N_{exc}(t) - g(t)N_{exc}(t) - \gamma\ N_{exc}^2(t) + I(t) \qquad (5a)$$

Table 1. The summary of the fitting parameters of temporal dynamics presented in Figure 4b. The longer lifetime of the polaritonic states implies the longer recombination rate, the stability of the charged states.

		T_1 (ps)	T_2 (ps)	T_3 (ps)
PA of the A exc.	662 nm	0.02 (67%)	2.04 (21%)	99.8 (12%)
PA of the polariton	650 nm	0.16	$>10^4$	–
PB of the A exc.	616 nm	−0.18 (*rise component*)	1.6	233.1
PB of the polariton	625 nm	2.0	24.3	–

$$\frac{dN_P(t)}{dt} = -k_2 N_P(t) + g(t)N_{exc}(t) \quad (5b)$$

$$\frac{dg(t)}{dt} = \beta I_0 N_{exc}(t)(1 - e^{-k_{12}t})e^{-k_3 t} \quad (5c)$$

Here N_{exc}, N_P, and g represent the population density of excitons and polaritons and the coupling strength, respectively. I_0 represent the pump fluence (corelated to power). The constants k_1 and k_2 are the intrinsic decay of the exciton and polariton density, respectively. The constant k_{12} determines the strength of spatial coupling between exciton and cavity to form the polaritonic states. The increase in polariton density is controlled by the temporal coupling strength. The effect of the pump fluence on the dynamics of the coupling was modeled using Equation 5 d. Here $I(t)$ is the pump profile (pump shape) which is corelated to the intensity of an ultrafast pulsed electromagnetic source and can be considered as follows:[41]

$$I(t) = \sqrt{\frac{4\ln(2)}{\pi}} \frac{(1-R)\alpha I_0}{t_p} exp\left[-4\ln(2)\left(\frac{t-2t_p}{t_p}\right)^2\right] \quad (5d)$$

where R, α, and t_p are reflectance, absorbance, and pulse width, respectively. In this model, the coupling strength is not fixed but rather evolves with time. The temporal coupling of the excitons to the cavity modes infers the spatial dynamics of excitons and polaritons.[42] Due to the low signal-to-noise ratio, only the interactions between the A exciton and the cavity mode are considered here.

The exciton decay and the formation of polariton due to the temporal coupling of exciton and the cavity modes is presented in Figure 5a for the pump fluence of 97 μJ and 26 μJ (inset). Using the temporal coupling approach, we learn that the saturation time of the polariton strongly depends on the pump fluence. Namely, the coupling strength of cavity and

exciton is much higher with pump power. The saturation time of the polariton is longer at lower pump fluence (I_0), and the cavity modes are more pronounced at higher I_0. The dynamics of exciton and the polariton, and the transient transmission spectra at different pump power, are shown in Figure S4, 5. Figure 5b presents the evolution of the coupling strength (**g**) as a function of pump fluence at several delay times. For a shorter delay time, **g** linearly increases with the increase in the pump fluence. For longer delay times, the change in **g** is nonlinear and approaches saturation (constant value). Another insight drawn from the developed temporal coupling model is that at shorter delays, due to the low coupling strength only the excitonic behavior prevails. Thus, as the pump fluence increases, **g** increases, and the exciton decays into polariton much faster. For longer delay times, the dynamics are guided by polariton as the **g** becomes saturated.

Conclusions

In this work, we have reported on the ultrafast nonequilibrium light-matter interaction in WS$_2$ nanoparticles in aqueous dispersion, providing a time-dependent study of the coupled states formation between exciton resonances and an intrinsic cavity mode. We have shown that the simplistic comparison of the steady-state absorbance and extinction derivatives with the ΔT/T spectra provides an instantaneous assignment of the short- and long-delay decay processes. For short delay times (∼0.3 ps), the transient spectra are related to the derivative of the absorbance while at long delay time (∼100 ps) it is related to the derivative of the extinction. There is, for the short delay times, the light-matter interaction is guided by the excitonic absorption, whereas for the long delay times, the process is controlled by polaritonic scattering. In over words, the
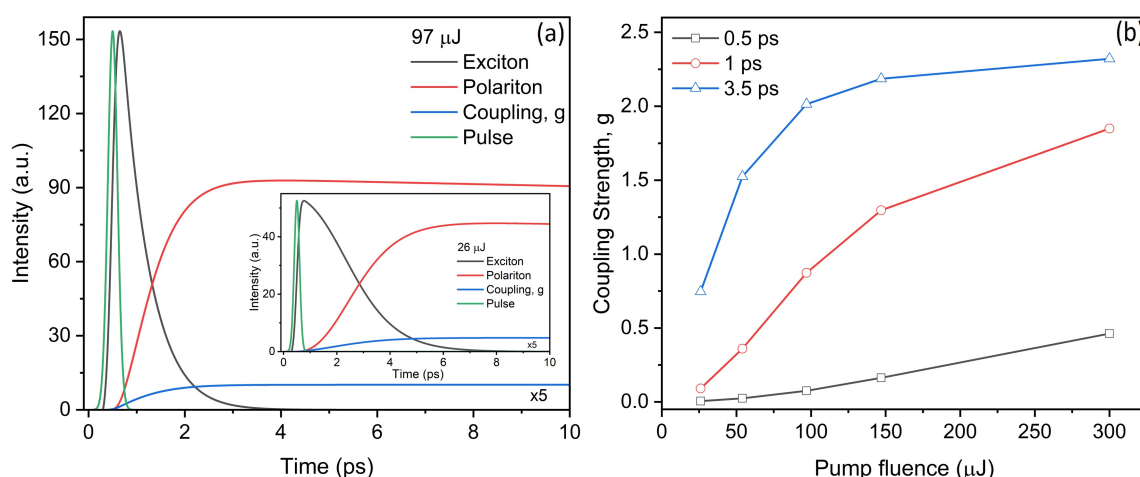
Figure 5. (a) The dynamics of exciton, polariton and the temporal coupling of exciton-cavity modes at the pump fluence of 97 μJ and 26 μJ (inset). The coupling strength is amplified (x5) for the presentation. (b) The pump-fluence dependence of coupling strength at different delay time. Note the nonlinear relation of coupling strength with pump fluence and the delay time.

formation of EPs in WS_2 NPs is not instantaneous but a gradual process that occurs only after several ps.

We find an additional indication of the temporal nature of polariton formation when we observe the blue shift and broadening of the maxima in the transient spectra ($\triangle T/T$) at the different pump-probe delays. By expressing the transient signals as the difference of the transmission in the presence and absence of the pump, we discover the nonlinear coupling (Δg) between excitonic and external mode and eminent transition from weak to strong coupling limit. The dynamical nature of the spectral shift indicates the relaxation of the excitons to the coupled (polaritonic) state. The change in spectral width is an additional indication of the relaxation mechanism of EPs, where A and B excitons decay into the coupled state. Also, we found that the A exciton decays faster than the B exciton due to stronger coupling with the cavity modes of the former. Using the results of the fitted decay dynamics, we determined the existence of multiple coupled states associated with the exciton-polariton decays.

To elucidate the dynamic nature of the EPs formation further, we modeled the time-dependent coupling of exciton and cavity modes using the phenomenological dynamics. We found that the developed model explains the nonlinear dynamical coupling as well as the effects of the pump fluence on the coupling strength. We find that the saturation time of the polariton is longer at lower pump fluence (I_0), while the cavity modes are more pronounced at higher I_0. Thus, as the pump fluence increases, g increases, and the exciton decays into polariton much faster. Namely, the coupling strength of cavity and exciton increases as the pump power increases. For the longer delay times, the dynamics are guided by the polariton as the g becomes saturated.

Our findings shed light on the dynamic and non-linear phenomena of the coupling processes in EPs. The methods and models developed in this work can hereafter be utilized to guide the experimental observation of exciton-polariton formation and coupling evolution dynamics. Moreover, the obtained knowledge can be readily utilized in the field of TMDs polaritonics for exploring genuinely unique physical scenarios and exploiting these new phenomena in technology in areas such as nanoscale lasing, quantum optics, and nanomanipulation.

Experimental

Materials

The multiwall WS_2 fullerene-like nanoparticles (NPs) were synthesized according to the procedure reported by Tenne et al.[27b] The synthesis was carried out at $840\,°C$ using WO_3 as a precursor and the resulted NPs were annealed for 20 hours at $840\,°C$ to remove the remaining oxide.[27] The XRD pattern of the annealed sample is presented in ref.[27] and shows ~2% remaining oxide after the annealing process. The average size of these NPs is 50 to 200 nm and the number of WS_2 shells depends on the synthetic conditions. TEM and SEM analyses reveal that the WS_2 NPs are somewhat oblate (Figure 1a). The solutions for all the current measurements were prepared using purified water (Milli-Q RG, Millipore).

Steady-State Absorption and Extinction Spectra

UV–vis extinction measurements were carried out on a Cary-5000 spectrometer (Varian). Samples were prepared by adding 0.6 mg of the WS_2 NP into 9 ml of purified water. The mixture was shaken by hand and then sonicated twice for 1–3 min using an ultrasonic bath. All suspensions were measured using quartz cuvettes. Scanning electron microscope (SEM) and Transmission electron microscope (TEM) analyses demonstrate that the WS_2 NPs remain unaffected by this mild sonication procedure.

Decoupled absorption spectra, used to separate scattering and absorption processes from the total extinction spectra, were measured using an integrated sphere (Hamamatsu Quantaurus absolute QY system).[43] This instrument directly measures the amount of absorbed light by placing the sample inside an integrating sphere. The system was calibrated using a sample with known absorbance to extract the optical absorbance. A calibration for counting the single-pass absorption photons was performed to avoid the full extinction which also includes photons that are scattered a few times before being detected.

Femtosecond Pump-Probe Spectroscopy

Femtosecond (fs) pump-probe spectroscopy was used to resolve the character of polaritonic features as a function of excitation time. Here, the setup is driven by an amplified Ti: sapphire laser (Coherent Libra 2) producing 4 W, 150 fs, 800 nm pulses at a 2 kHz repetition rate. To generate a single Filament white light continuum used as a probe, a fraction of the pulse energy is focused in a 3 mm thick sapphire plate. Another fraction of the pulse energy was doubled in a second harmonic (SH) crystal, serving as the pump pulse. Pump and probe are non-collinearly focused on the sample. The transmitted probe spectrum is detected by a spectrometer that is working at the full 2 kHz repetition rate of the laser. The spectra ($\Delta T/T$) of the dispersed NP were recorded with a time resolution of 150 fs set by the cross-correlation of pump and probe pulses and sensitivity of $1–2\times10^{-5}$. With the OPA one can reach a higher time resolution of 100 fs. The fs pump-probe measurements were carried out for WS_2 NP dispersed in H_2O (0.15 mg per ml). The dispersions were sonicated twice for two minutes before the measurement itself. The excited sample was probed at varying delays by a white-light continuum, covering the visible-near infrared (400–800 nm) region.

Research Article

Glossary for Abbreviations and Acronyms

NSs   nanostructures
NPs   fullerene-like nanoparticles
2D   two-dimensional
NTs   nanotubes
EPs   exciton-polaritons
PA   photo-induced absorption
Fs   femtosecond
PB   photo-bleach
G coupling strength
Ps   picosecond
I_0 pump fluence
TMDs transition metal dichalcogenides

Data Availability Statement

The data that support the findings of this study are available on request from the corresponding author. The data are not publicly available due to privacy or ethical restrictions.

References

[1] a) A. P. Alivisatos, *Science* **1996**, *271*, 933; b) K. J. Vahala, *Nature* **2003**, *424*, 839–846; c) R. K. Chang, A. J. Campillo, in *Advanced Series in Applied Physics, Vol. 3*, World scientific, **1996**, p. 448.

[2] L. Cao, J. S. White, J.-S. Park, J. A. Schuller, B. M. Clemens, M. L. Brongersma, *Nat. Mater.* **2009**, *8*, 643–647.

[3] J. Hu, C. R. Menyuk, *Adv. Opt. Photonics* **2009**, *1*, 58–106.

[4] a) N. Rivera, I. Kaminer, *Nat. Rev. Phys.* **2020**, *2*, 538–561; bE. J. Dias, F. J. G. de Abajo, *Optik* **2021**, *8*, 520–531.

[5] P. Törmä, W. L. Barnes, *Rep. Prog. Phys.* **2015**, *78*, 013901.

[6] a) R. R. Chance, A. Prock, R. Silbey, in *Adv. Chem. Phys., Vol. 37* (Eds.: I. Prigogine, S. A. Rice), **1978**, p. 65; b) L. Novotny, *Am. J. Phys.* **2010**, *78*, 1199–1202.

[7] S. Haroche, in *Les Houches Summar School Session* (Ed.: J. D. e. al), Amsterdam: North Holland, **1992**, pp. 767–940.

[8] J. Bellessa, C. Bonnand, J. C. Plenet, J. Mugnier, *Phys. Rev. Lett.* **2004**, *93*, 036404.

[9] B. Munkhbat, D. G. Baranov, M. Stührenberg, M. Wersäll, A. Bisht, T. Shegai, *ACS Photonics* **2019**, *6*, 139–147.

[10] a) C. Weisbuch, M. Nishioka, A. Ishikawa, Y. Arakawa, *Phys. Rev. Lett.* **1992**, *69*, 3314; b) H. Gibbs, G. Khitrova, S. Koch, *Nat. Photonics* **2011**, *5*, 273–273; c) F. Tassone, F. Bassani, L. Andreani, *Phys. Rev. B* **1992**, *45*, 6023.

[11] a) E. P. T. Tyndall, *Phys. Rev.* **1923**, *21*, 162–180; b) A. Zak, L. Sallacan-Ecker, A. Margolin, M. Genut, R. Tenne, *NANO* **2009**, *04*, 91–98; c) E. Hossain, A. A. Rahman, R. D. Bapat, J. B. Parmar, A. P. Shah, A. Arora, R. Bratschitsch, A. Bhattacharya, *Nanoscale* **2018**, *10*, 16683–16691; d) M. Nath, A. Govindaraj, C. N. R. Rao, *Adv. Mater.* **2001**, *13*, 283–286.

[12] a) L. Yadgarov, B. Višić, T. Abir, R. Tenne, A. Y. Polyakov, R. Levi, T. V. Dolgova, V. V. Zubyuk, A. A. Fedyanin, E. A. Goodilin, T. Ellenbogen, R. Tenne, D. Oron, *Phys. Chem. Chem. Phys.* **2018**, *20*, 20812–20820; b) R. Friend, A. Yoffe, *Adv. Phys.* **1987**, *36*, 1–94; c) Q. H. Wang, K. Kalantar-Zadeh, A. Kis, J. N. Coleman, M. S. Strano, *Nat. Nanotechnol.* **2012**, *7*, 699–712; d) L. Yuwen, F. Xu, B. Xue, Z. Luo, Q. Zhang, B. Bao, S. Su, L. Weng, W. Huang, L. Wang, *Nanoscale* **2014**, *6*, 5762–5769.

[13] A. H. Castro Neto, F. Guinea, N. M. R. Peres, K. S. Novoselov, A. K. Geim, *Rev. Mod. Phys.* **2009**, *81*, 109–162.

[14] a) N. Levy, S. Burke, K. Meaker, M. Panlasigui, A. Zettl, F. Guinea, A. C. Neto, M. F. Crommie, *Science* **2010**, *329*, 544–547; b) D. Allan, A. Kelsey, S. Clark, R. Angel, G. Ackland, *Phys. Rev. B* **1998**, *57*, 5106.

[15] a) R. Coehoorn, C. Haas, R. De Groot, *Phys. Rev. B* **1987**, *35*, 6203–6206; b) H. Zeng, G.-B. Liu, J. Dai, Y. Yan, B. Zhu, R. He, L. Xie, S. Xu, X. Chen, W. Yao, X. Cui, *Sci. Rep.* **2013**, *3*, 1608.

[16] a) X. Liu, T. Galfsky, Z. Sun, F. Xia, E.-c. Lin, Y.-H. Lee, S. Kéna-Cohen, V. M. Menon, *Nat. Photonics* **2015**, *9*, 30–34; b) K. F. Mak, J. Shan, *Nat. Photonics* **2016**, *10*, 216–226; c) S. Dufferwiel, T. Lyons, D. Solnyshkov, A. Trichet, F. Withers, S. Schwarz, G. Malpuech, J. Smith, K. Novoselov, M. Skolnick, *Nat. Photonics* **2017**, *11*, 497–501.

[17] X. Liu, T. Galfsky, Z. Sun, F. Xia, E.-c. Lin, Y.-H. Lee, S. Kéna-Cohen, V. M. Menon, *Nat. Photonics* **2014**, *9*, 30.

[18] a) B. Višić, L. Yadgarov, E. A. A. Pogna, S. Dal Conte, V. Vega-Mayoral, D. Vella, R. Tenne, G. Cerullo, C. Gadermaier, *Phys. Rev. Res.* **2019**, *1*, 033046; b) S. S. Sinha, A. Zak, R. Rosentsveig, I. Pinkas, R. Tenne, L. Yadgarov, *Small* **2020**, *16*, 1904390; c) S. S. Sinha, L. Yadgarov, S. B. Aliev, Y. Feldman, I. Pinkas, P. Chithaiah, S. Ghosh, A. Idelevich, A. Zak, R. Tenne, *J. Phys. Chem. C* **2021**, *125*, 6324–6340; d) A. Sedova, B. Višić, V. Vega-Mayoral, D. Vella, C. Gadermaier, H. Dodiuk, S. Kenig, R. Tenne, R. Gvishi, G. Bar, *J. Mater. Sci.* **2020**, *55*, 7612–7623.

[19] a) B. Radisavljevic, A. Radenovic, J. Brivio, V. Giacometti, A. Kis, *Nat. Nanotechnol.* **2011**, *6*, 147–150; b) Q. Wang, L. Sun, B. Zhang, C. Chen, X. Shen, W. Lu, *Opt. Express* **2016**, *24*, 7151–7157; c) Z. Fei, M. E. Scott, D. J. Gosztola, J. J. Foley, J. Yan, D. G. Mandrus, H. Wen, P. Zhou, D. W. Zhang, Y. Sun, J. R. Guest, S. K. Gray, W. Bao, G. P. Wiederrecht, X. Xu, *Phys. Rev. B* **2016**, *94*, 081402; d) A. A. Murthy, Y. Li, E. Palacios, Q. Li, S. Hao, J. G. DiStefano, C. Wolverton, K. Aydin, X. Chen, V. P. Dravid, *ACS Appl. Mater. Interfaces* **2018**, *10*, 6799–6804; e) Y. Li, E. C. Moy, A. A. Murthy, S. Hao, J. D. Cain, E. D. Hanson, J. G. DiStefano, W. H. Chae, Q. Li, C. Wolverton, X. Chen, V. P. Dravid, *Adv. Funct. Mater.* **2018**, *28*, 1704863; f) F. Hu, Y. Luan, M. E. Scott, J. Yan, D. G. Mandrus, X. Xu, Z. Fei, *Nat. Photonics* **2017**, *11*, 356–360.

[20] a) R. Tenne, L. Margulis, M. Genut, G. Hodes, *Nature* **1992**, *360*, 444–446; b) M. Hershfinkel, L. Gheber, V. Volterra, J. Hutchison, L. Margulis, R. Tenne, *J. Am. Chem. Soc.* **1994**, *116*, 1914–1917; c) Y. Feldman, E. Wasserman, D. Srolovitz, R. Tenne, *Science* **1995**, *267*, 222.

[21] a) Y. Golan, C. Drummond, M. Homyonfer, Y. Feldman, R. Tenne, J. Israelachvili, *Adv. Mater.* **1999**, *11*, 934–937; b) L. Rapoport, V. Leshchinsky, I. Lapsker, Y. Volovik, O. Nepomnyashchy, M. Lvovsky, R. Popovitz-Biro, Y. Feldman, R. Tenne, *Wear* **2003**, *255*, 785–793; c) R. Rosentsveig, A. Gorodnev, N.

Feuerstein, H. Friedman, A. Zak, N. Fleischer, J. Tannous, F. Dassenoy, R. Tenne, *Tribol. Lett.* **2009**, *36*, 175–182; d) R. Rosentsveig, A. Margolin, A. Gorodnev, R. Popovitz-Biro, Y. Feldman, L. Rapoport, Y. Novema, G. Naveh, R. Tenne, *J. Mater. Chem.* **2009**, *19*, 4368–4374; e) J. Tannous, F. Dassenoy, I. Lahouij, T. Le Mogne, B. Vacher, A. Bruhács, W. Tremel, *Tribol. Lett.* **2011**, *41*, 55–64; f) L. Yadgarov, V. Petrone, R. Rosentsveig, Y. Feldman, R. Tenne, A. Senatore, *Wear* **2013**, *297*, 1103–1110.

[22] a) C. Ballif, M. Regula, P. Schmid, M. Remškar, R. Sanjines, F. Levy, *Appl. Phys. A* **1996**, *62*, 543–546; b) L. Yadgarov, R. Rosentsveig, G. Leitus, A. Albu-Yaron, A. Moshkovich, V. Perfilyev, R. Vasic, A. I. Frenkel, A. N. Enyashin, G. Seifert, *Angew. Chem. Int. Ed.* **2012**, *51*, 1148–1151; *Angew. Chem.* **2012**, *124*, 1174–1177.

[23] a) G. Seifert, H. Terrones, M. Terrones, G. Jungnickel, T. Frauenheim, *Phys. Rev. Lett.* **2000**, *85*, 146–149; b) G. Seifert, H. Terrones, M. Terrones, G. Jungnickel, T. Frauenheim, *Solid State Commun.* **2000**, *114*, 245–248.

[24] a) G. L. Frey, S. Elani, M. Homyonfer, Y. Feldman, R. Tenne, *Phys. Rev. B* **1998**, *57*, 6666–6671; b) L. Scheffer, R. Rosentzveig, A. Margolin, R. Popovitz-Biro, G. Seifert, S. R. Cohen, R. Tenne, *Phys. Chem. Chem. Phys.* **2002**, *4*, 2095–2098.

[25] a) F. Qin, W. Shi, T. Ideue, M. Yoshida, A. Zak, R. Tenne, T. Kikitsu, D. Inoue, D. Hashizume, Y. Iwasa, *Nat. Commun.* **2017**, *8*, 14465; b) Y. J. Zhang, T. Ideue, M. Onga, F. Qin, R. Suzuki, A. Zak, R. Tenne, J. H. Smet, Y. Iwasa, *Nature* **2019**, *570*, 349–353; c) Y. J. Zhang, M. Onga, F. Qin, W. Shi, A. Zak, R. Tenne, J. Smet, Y. Iwasa, *2D Mater.* **2018**, *5*, 035002.

[26] R. Verre, D. G. Baranov, B. Munkhbat, J. Cuadra, M. Käll, T. Shegai, *Nat. Nanotechnol.* **2019**, *14*, 679–683.

[27] a) Y. Feldman, G. Frey, M. Homyonfer, V. Lyakhovitskaya, L. Margulis, H. Cohen, G. Hodes, J. Hutchison, R. Tenne, *J. Am. Chem. Soc.* **1996**, *118*, 5362–5367; b) L. Rapoport, Y. Bilik, Y. Feldman, M. Homyonfer, S. Cohen, R. Tenne, *Nature* **1997**, *387*, 791–793; c) L. Rapoport, Y. Feldman, M. Homyonfer, H. Cohen, J. Sloan, J. Hutchison, R. Tenne, *Wear* **1999**, *225*, 975–982.

[28] G. L. Frey, R. Tenne, M. J. Matthews, M. S. Dresselhaus, G. Dresselhaus, *J. Mater. Res.* **1998**, *13*, 2412–2417.

[29] C. Ballif, M. Regula, F. Levy, *Sol. Energy Mater. Sol. Cells* **1999**, *57*, 189–207.

[30] C. F. Bohren, D. R. Huffman, *Absorption and Scattering of Light by Small Particles*, John Wiley & Sons, Hoboken, NJ, USA, **2007**.

[31] a) B. Munkhbat, D. G. Baranov, M. Stührenberg, M. Wersäll, A. Bisht, T. Shegai, *ACS Photonics* **2019**, *6*, 139–147; b) L.

Yadgarov, B. Višić, T. Abir, R. Tenne, A. Y. Polyakov, R. Levi, T. V. Dolgova, V. V. Zubyuk, A. A. Fedyanin, E. A. Goodilin, *Phys. Chem. Chem. Phys.* **2018**, *20*, 20812–20820; c) L. C. Flatten, Z. He, D. M. Coles, A. A. Trichet, A. W. Powell, R. A. Taylor, J. H. Warner, J. M. Smith, *Sci. Rep.* **2016**, *6*, 1–7.

[32] a) V. Vega-Mayoral, D. Vella, T. Borzda, M. Prijatelj, I. Tempra, E. A. A. Pogna, S. D. Conte, P. Topolovsek, N. Vujicic, G. Cerullo, D. Mihailovica, C. Gadermaier, *Nanoscale* **2016**, *8*, 5428–5434; b) J. Wilson, A. Yoffe, *Adv. Phys.* **1969**, *18*, 193–335.

[33] a) T. Arlt, S. Schmidt, W. Kaiser, C. Lauterwasser, M. Meyer, H. Scheer, W. Zinth, *Proc. Natl. Acad. Sci. USA* **1993**, *90*, 11757–11761; b) J. T. Kennis, A. Y. Shkuropatov, I. H. Van Stokkum, P. Gast, A. J. Hoff, V. A. Shuvalov, T. J. Aartsma, *Biochemistry* **1997**, *36*, 16231–16238.

[34] C. Reichardt, *Chem. Rev.* **1994**, *94*, 2319–2358.

[35] a) M. M. Brister, L. E. Piñero-Santiago, M. Morel, R. Arce, C. E. Crespo-Hernández, *J. Phys. Chem. Lett.* **2016**, *7*, 5086–5092; b) K. Tvrdy, P. A. Frantsuzov, P. V. Kamat, *Proc. Natl. Acad. Sci. USA* **2011**, *108*, 29–34.

[36] A. Mondal, J. Aneesh, V. K. Ravi, R. Sharma, W. J. Mir, M. C. Beard, A. Nag, K. Adarsh, *Phys. Rev. B* **2018**, *98*, 115418.

[37] R. Sharma, J. Aneesh, R. K. Yadav, S. Sanda, A. Barik, A. K. Mishra, T. K. Maji, D. Karmakar, K. Adarsh, *Phys. Rev. B* **2016**, *93*, 155433.

[38] M. Zürch, H.-T. Chang, L. J. Borja, P. M. Kraus, S. K. Cushing, A. Gandman, C. J. Kaplan, M. H. Oh, J. S. Prell, D. Prendergast, C. D. Pemmaraju, D. M. Neumark, S. R. Leone, *Nat. Commun.* **2017**, *8*, 15734.

[39] K. E. Knowles, M. D. Koch, J. L. Shelton, *J. Mater. Chem. C* **2018**, *6*, 11853–11867.

[40] A. Stokes, A. Nazir, *Phys. Rev. Res.* **2021**, *3*, 013116.

[41] J. K. Chen, D. Y. Tzou, J. E. Beraun, *Int. J. Heat Mass Transfer* **2006**, *49*, 307–316.

[42] *Note: The nonlinear Auger effects only for very high pump fluence can be considered by the parameter γ, but can be neglected for 97 μJ. The higher order polaritonic modes are beyond the scope of the article.*

[43] K. Suzuki, *Nat. Photonics* **2011**, *5*, 247.

Recent Progress in the Synthesis and Potential Applications of Two-Dimensional Tungsten (Sub)oxides

Luka Pirker[a] and Bojana Višić*[a, b]

Abstract: While WO_3 is one of the most studied metal-oxides in bulk, it is increasingly gaining interest as a two-dimensional (2D) material as it exhibits different behaviour compared to bulk. In addition, many substoichiometric WO_{3-x} ($0 \leq x \leq 1$) phases exist both in bulk and 2D form. These Magneli phases have different physical and chemical properties than their WO_3 counterparts. By introducing oxygen vacancies, the physical and chemical properties of 2D tungsten (sub)oxide nanomaterials can be further altered. This review focuses on synthesis pathways of 2D tungsten (sub)oxides reported so far, and their subsequent use for various applications. The different stoichiometries and additional oxygen vacancies that appear in these materials, combined with their low thickness and high surface area, make them interesting candidates for gas sensing, catalytic application or in electronic devices.

Keywords: two-dimensional materials · metal oxides · tungsten suboxides · synthesis · applications

1. Introduction

Tungsten (VI) oxide (WO_3) is one of the most investigated transition metal oxides due to various potential applications, such as in photochromic smart windows,[1] in optoelectronics,[2] gas sensing and photocatalysis,[3] as supercapacitors,[4] as nanostructured thermoelectrics,[5] etc. The WO_3 forms a rich variety of crystal structures composed of corner-sharing WO_6 octahedra, which differ in tilting angles, displacements of the W cation from the centre of the octahedron, and rotation of WO_6 octahedra with respect to ideal cubic (ReO_3 type) structure.[5] In bulk, partially reversible inter-phase transformations occur upon heating in addition to the formation of a metastable phase.[6] At nanoscale, phase transitions occur at temperatures lower than in bulk and depend mostly on the size of WO_3 nanoparticles.[7]

Recently, two-dimensional (2D) nanostructures, including 2D-WO_3, have attracted a lot of attention among researchers due to their novel physical and chemical properties, which differ from their bulk counterparts.[8] High surface area, appearance of crystalline planes/surfaces that are not available in bulk materials, and stability of crystal phases declared as metastable in bulk systems are just some of the examples. Due to their low-dimensional nature, quantum confinement effects come into play, changing their electronic properties. This is providing a great opportunity for their use as components in novel sensors, energy conversion devices, transistors, to name a few. Different particular particle shapes, such as pseudo-spherical nanometre-sized particles, nanowires, nano-discs and flakes, were already synthesized with various growth techniques.[9]

Besides the stoichiometric WO_3, many substoichiometric WO_{3-x} phases exist, where $0 \leq x \leq 1$. The electrical, optical, and structural properties of tungsten suboxides depend strongly on the degree of reduction (i. e. x) and consequently differ from stoichiometric WO_3.[10] Moreover, for additional tuning of their properties, oxygen vacancies can be induced in WO_3 or WO_{3-x}. The abundance of tungsten ore in combination with the low-dimensional nature, a wide range of substoichiometric phases that can be further altered by inducing oxygen vacancies, 2D tungsten (sub)oxides offer a platform with diverse and tuneable properties for a great variety of applications.

This review focuses on current synthesis approaches to obtaining 2D tungsten (sub)oxide materials. In addition, the progress in their utilization in various applications, such as gas sensing, catalysis and photodetection, is discussed in terms of current state of the art and future outlook.

2. Synthesis, Morphology and Structure

One of the first 2D-WO_3 crystals was prepared more than 15 years ago, when monoclinic WO_3 nanosheets were synthesized by a solvothermal reaction.[11] The square nanosheets were 150 nm in size and thin enough for a direct HRTEM

[a] *Dr. L. Pirker, B. Višić*
Solid State Physics, Jozef Stefan Institute
Jamova cesta 39, 1000 Ljubljana, Slovenia
[b] *B. Višić*
Institute of Physics Belgrade, University of Belgrade
Pregrevica 118, 11080 Belgrade, Serbia
Phone: +381113713000
Fax: +381113162190
E-mail: bojana.visic@ipb.ac.rs

analysis. In the following years, different methods of synthesis were reported. The 2D-WO_3 nanoparticles were crystallized in the monoclinic WO_3 phase via wet chemical synthesis,[12] topochemical conversion,[13] hydrothermal,[8] solvothermal,[14] exfoliation and oxidation of WS_2,[15] and microwave irradiation,[16] to name a few. The morphologies of synthesized nanoparticles range from rectangular nanoplates,[13] irregularly shaped nanodisks,[13] leaf-like nanoplatelets,[17] and nanoflakes,[18] with the sizes ranging from 20 nm to 500 nm in lateral dimensions and from 5 nm to 60 nm in thickness. An example of a nanoplate is shown in Figure 1 a, b).

Although at room temperature only the monoclinic WO_3 phase is stable in bulk, other crystal structures were stabilized in form of 2D-WO_3 crystals. Hexagonal WO_3 nanosheets were synthesized from the colloidal suspension of $BaWO_4$-PAA[19] orthorhombic WO_3 nanoplates were synthesized using sodium tungsten $Na_2WO_4*_2H_2O$ as precursor by a simple free template precipitation method,[20] triclinic WO_3 nanoparticles were synthesized through a hydrothermal route,[21] and cubic WO_3 nanosheets were synthesized by direct reduction.[22] Novel octahedral molecular sieves (h'-WO_3) with the diameter between 20 and 80 nm and thickness of 3–10 nm were also synthesized and are shown in Figure 1 c).[23]

With various synthesis methods, different crystal facets could be exposed, which are not available in bulk materials. It was reported that (100), (010), and (001) facets could be exposed with the use of different surfactants,[12,24] solvents,[21] specific precursors,[13,25] or the synthesis method. Their atomic structure and electronic properties differ due to the nature of the crystal structure, and thus play an important part in the physical and chemical properties of the material.[26] For example, it was reported that (100) facets show higher evolution rate of O_2 in water splitting than WO_3 without a preferred crystal face.[26b]

As stated in the Introduction, the stoichiometric WO_3 can also be reduced into substoichiometric WO_{3-x} using different techniques such as chemical vapor transport (CVT),[27] heating under controlled atmosphere,[28] and electron beam irradiation in a TEM microscope.[28b,29] The substoichiometric WO_{3-x} can
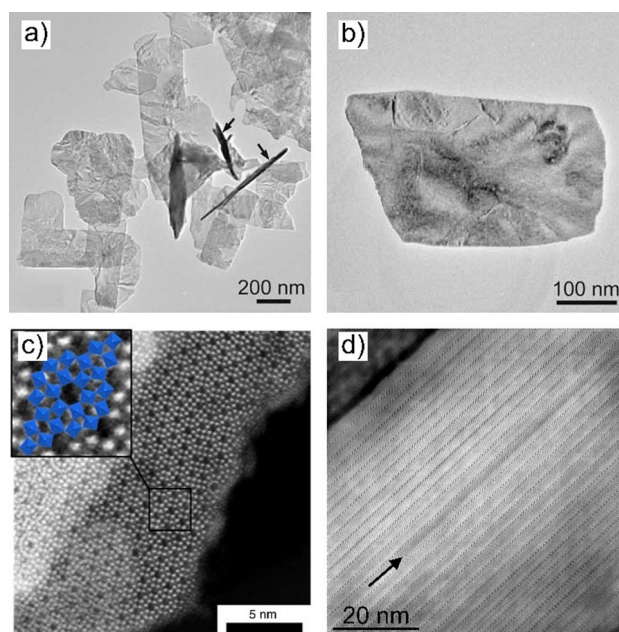
Figure 1. a) Low-magnification and b) high magnification TEM images of WO_3 nanoplates (Reprinted from reference [13] with permission from John Wiley and Sons); c) HAADF-STEM micrograph of a h'-WO_3 framework. The inset shows the arrangement of tungsten octahedra (Reprinted from reference [23] with permission from Springer Nature); d) HRTEM image of a cross-section lamella showing semi-regularly distributed CS planes in a W_nO_{3n-1} tungsten suboxide. The arrow points to a defect (Reprinted from reference [10] with permission from the Royal Society of Chemistry.)

be synthesized with a wide variety of hydrothermal and solvothermal methods,[30] layer deposition methods, such as atomic layer deposition (ALD) and chemical vapour deposition (CVD).[31] These suboxides grow in different structures such as films,[32] needles,[33] nanowires,[27] nanorods[34] and nanodots[35] and can crystallize in similar structures as tungsten bronzes with a general formula A_xWO_3, where A is an electropositive element.[36] While in the tungsten bronzes W^{5+}

Dr. Luka Pirker obtained his BS and MSc in physics at the Faculty of Mathematics and Physics, University of Ljubljana in Slovenia. He finished his PhD in physics at the Faculty of Mathematics and Physics, University of Ljubljana in Slovenia in 2020 under the supervision of prof. Maja Remškar. He is currently working at Jozef Stefan Institute, Slovenia. During his PhD he investigated the structural, optical, and electrical properties of low-dimensional tungsten suboxides. He is also interested in low-dimensional transition metal dichalcogenides and their structural, optical, and electrical properties.
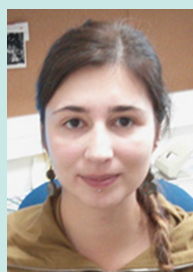
Assoc. Res. Prof. Bojana Višić completed her BS and MSc at the Faculty of Physics, Belgrade, Serbia in 2007 and 2008, respectively. She received her PhD at Faculty of Mathematics and Physics, Ljubljana, Slovenia in 2013, under the guidance of Prof. Maja Remškar. Afterwards she joined the groups of prof. Reshef Tenne (Weizmann Institute of Science, Israel) and prof. Maja Remškar (Jozef Stefan Institute, Slovenia) as a postdoctoral fellow in 2013–2017 and 2017–2018. In December 2018, she joined the Center for Solid State Physics and New Materials at the Institute of Physics, Belgrade, Serbia. Her main research interests focus on low-dimensional materials, namely inorganic nanotubes, their characterization and optical properties.

Review

state appears due to the presence of the electropositive element, in WO_{3-x} it occurs through the intrinsic oxygen vacancies. It has been shown that even when x in WO_{3-x} is less than 0.0001, the oxygen atoms are not removed randomly but form ordered structures.[28a] Within the material, crystallographic shear (CS) planes, pentagonal columns (PC), and oxygen vacancy walls (OVW) are formed to accommodate the oxygen vacancies, as shown in Figure 2.

The term crystallographic shear comes from the shearing of two adjacent blocks of WO_3. In a CS plane, corner sharing WO_6 octahedra that are a part of the CS plane become edge sharing WO_6 octahedra.[38] While a single CS plane is considered a defect, an array of equally spaced CS planes forms a WO_{3-x} crystal with a defined stoichiometry. The CS planes can be described in terms of $\{hkl\}_r$ planes of WO_3, which crystallize in the ReO_3 type structure.[39] For $x < 0.007$, the $\{102\}r$ CS planes are randomly distributed.[28a] The increase of the degree of reduction (i.e. increasing x) increases the density of CS planes, resulting in a formation of their ordered arrays, which form the W_nO_{3n-1} tungsten suboxides. When x approaches 0.1, the formation of $\{103\}_r$ CS planes become favourable over the formation of $\{102\}_r$ CS planes, forming the W_nO_{3n-2} tungsten suboxides. While CS planes are observed in less reduced WO_{3-x} ($x \leq 0.2$), PC structures form only in more reduced WO_{3-x} ($x \geq 0.2$). The PC are periodic structures of WO_7 bipyramids that share their equatorial edges with WO_6 octahedra.[40] Within structures with PC, three-, four-, five- and six-sided tunnels can also form as in the case of $W_{18}O_{49}$ or W_5O_{14}.[27,41] Although OVW were proposed as the precursors of CS planes, there are very few articles where these were experimentally observed.[42] The abundance of CS planes and PCs largely depends on the degree of reduction.

With sufficiently low reduction, single oxygen vacancies can be produced.[43] In this case, oxygen atoms are removed from the surface, forming oxygen vacancies. To minimize the surface energy, single PCs appear on the surface, stabilizing the structure. Although technically oxygen vacancies reduce WO_3 into WO_{3-x}, in the majority of the materials reported in the literature, it is not clear what kind of structure formed within the material. Thus, the term substoichiometric tungsten oxides (WO_{3-x}) is used interchangeably in literature for materials with ordered CS and PC structures, as well as for materials with induced oxygen vacancies.

For 2D-WO_{3-x} materials, different stoichiometries were identified, such as $W_{18}O_{49}$[44] and $W_{10}O_{29}$ nanosheets,[45] as well as materials with mixed stoichiometry,[30b] multi-stoichiometric nanoplates,[10,46] and nanomaterials with unknown stoichiometries.[47] Similarly to 2D nanoparticles, 2D-WO_3 and 2D-WO_{3-x} thin films can be made using atomic layer deposition,[31a] molecular beam epitaxy,[48] and vapor-phase deposition.[31b] Different stoichiometries can be prepared, from monoclinic WO_3,[31a] to $W_{18}O_{49}$,[49] and $WO_2 + O$ bilayer structure,[31b] with the thickness ranging from a monolayer up to several tens of nm. Owing to the large area of deposited films, they can be used in many applications such as electrochromic displays, solar cells, and supercapacitors.[50] Due to the formation of CS planes, as shown in Figure 1 d), the electronic and optical properties differ from monoclinic WO_3 and they may have an advantage in applications such as water splitting,[37,51] near-infrared shielding,[44] as anode materials for high-performance Li-ion batteries,[52] photocatalysis,[53] and in domain boundary engineering.[54]

Although the majority of the reported stoichiometries were determined from XRD measurements, it is not the most suitable and precise method to use in the case of tungsten suboxides, as the differences between phases are too small to be detected.[39] Only for highly crystalline samples, where the diffraction peaks from the low index (hkl) planes are observed, can the stoichiometry be determined by using XRD as the main tool. HRTEM images and electron diffraction patterns can be used to further elucidate the true crystal structure of tungsten (sub)oxides.

A short summary of the synthesis methods, particle sizes, crystal structures, exposed faces, and applications of 2D-WO_3 and 2D-WO_{3-x} is presented in Table 1.

3. 2D-WO_{3-x} for Applications

Among the biggest advantages of the 2D morphology are the large specific surface area, increased number of active sites and confined thickness, which make these nanostructures promising candidates for gas sensing, catalytic applications and electronic or photonic devices. Additionally, the 2D-WO_3 and 2D-WO_{3-x} are interesting from the aspect of defect engineering, where finding the optimal concentration of oxygen vacancies could lead to fine bandgap tuning, increased amount of charge carriers and photocurrents, whilst maintaining the crystallinity. Nevertheless, ultrathin WO_{3-x} nanosheets have not been sufficiently studied in terms of applications, despite their substantial amount of reactive (002) crystal facets and a high specific surface area.
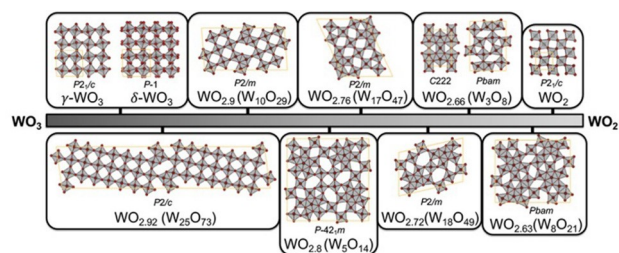
Figure 2. Crystal structures of some stoichiometric and sub-stoichiometric tungsten oxides. Reprinted with permission from reference [37]. Copyright 2021 American Chemical Society.

Table 1. A short summary of the synthesis methods, particle sizes, crystal structures, exposed faces, and applications of 2D-WO_{3-x} nanomaterials.

Synthesis method	Lateral size (nm)	Thickness (nm)	Crystal structure	Exposed faces	Application	Morphology
Wet chemical[12]	200–1000	7–18	Monoclinic WO_3	(010)	Water splitting	nanodisks
topochemical conversion[13]	200–500	10–30	Monoclinic WO_3	(001)	Water splitting	nanoplates
hydrothermal[55]	A few 100	~10	Monoclinic WO_3	(200)	NO_2 gas detection	nanosheets
Laser ablation[17]	600–1800 μm	30	Monoclinic WO_3	(001)	/	leaf-like nanoplatelets
Aqueous Synthesis[19]	Several 100	5–60	Hexagonal WO_3	(001)	/	nanosheets
wet chemical[20]	Up to 175	~40	Orthorhombic WO_3	(010)	CO oxidation	nanoplatelets
hydrothermal[21]	<200 nm	30–175	Triclinic WO_3	(100), (010), (001)	Gas sensing	nanosheets
thermal decomposition[56]	Up to a few 10	/	$W_{18}O_{49}$	(020)	Photocatalytic decomposition	nanosheets
CVT[10]	Up to 4000	10–100	W_nO_{3n-1}	(001)	/	nanoplates
direct current sputtering[49]	/	>52	$W_{18}O_{49}$	/	water splitting	film
ALD[31a]	/	~42	Monoclinic WO_3	(002)	Gas sensor	film
Vapor-phase deposition[31b]	9–4	monolayer	$WO2+O$ bilayer	/	/	clusters

3.1 Gas Sensing

Materials preferred in gas sensing applications tend to have a good adsorption-desorption mechanism and a pore-rich morphology. This makes 2D-WO_3 and 2D-WO_{3-x} promising candidates, since the oxygen vacancies play an important role in adsorption-desorption phenomena. In order to obtain the enhanced gas-sensing performances, morphology and surface design are required. Other important parameters for optimisation of sensor performance are sensitivity, stability, selectivity, adsorption and desorption ability, crystal structure, electronic and chemical properties etc. In addition, since these reactions rely closely on the interaction of the surface of the material and the target molecules, the performance depends strongly on the exposed facets and surface area. Different facets of the same structure can have different dangling bonds and electronic structure, exhibiting different physical and chemical properties. As seen in Section 2, tuning the synthesis can expose selected facets[26b], with which the gas sensing ability can be optimized. When it comes to gas sensing capabilities of metal oxides, they are mostly based on the oxidation-reduction reaction of the detected gases.[57] As the oxidation-reduction reaction takes place on the surface, the physical and chemical properties of the facets play an important role. If the planes are terminated with positive ions, they are able to adsorb the oxygen species and target molecules due to unsaturated oxygen coordination, improving gas sensing capabilities. It was shown that for the monoclinic WO_3, (002) crystal facets exhibit enhanced photocatalytic CO_2 reduction and photoelectrochemical (PEC) water splitting capabilities compared to (200) and (020) facets, due to improved photoinduced charge carrier separation efficiency.[26a] Another important factor for gas sensing is selectivity. The sensor has to be able to discriminate the selected gas in a mixture of gases, and this is determined by the adsorption and subsequent chemical oxidation on the surface of the potential sensor material. The sensitivity is largely affected by geometrical and chemical heterogeneities of the reacting surface. Materials with higher amount of surface defects, where adsorption and catalytic reaction may take place, are preferred.

Reducing NO_2 emissions is an important task, as very low concentrations (1 ppm) can induce respiratory issues.[58] Since NO_2 sensors should operate in the ambient oxygen environment, materials under consideration need to have good air durability, as well as high selectivity and sensitivity, fast response and recovery time. 150 nm thick WO_3 films were shown to be good candidates for NO_2 sensing.[59] Here, Cantalini *et al.* showed that the sensor sensitivity increases with the increase in surface defects concentration, while the long-term stability depends on the optimization of the annealing process of the films. In this case, the films were more stable when annealed for longer times, which stabilizes the surface defects.[55] In a different study, 10 nm thick WO_{3-x} nanosheets showed high sensitivity and selectivity to NO_2. The best performance was obtained at 50 ppb NO_2 at 140 °C with response and recovery times of 140 s and 75 s, respectively. With a further reduced thickness, Khan *et al.* made physisorption-based NO_2 sensors from 4 nm thick substoichiometric WO_{3-x} nanosheets.[60] The optimal operating temperature for samples annealed at different temperatures was 150 °C. This temperature is significantly lower than for the conventional chemisorptive metal oxide gas sensors, which operate above 200 °C. As the operating temperature increased, the response decreased. In this regime, the rate of adsorption is lower than the rate of desorption. The best responsivity (here, the input/output ratio of the electrical resistance) to 40 ppb was reported to be 30, which is more than an order of magnitude higher than for the nanocrystals.[60] This work furthermore empha-

sizes the influence of the stoichiometry on performance and properties. These materials were tested in the NO_2 concentration range of 20 to 2000 ppb, but the sample annealed at 225 °C was overly sensitive, reaching saturation beyond 120 ppb. The saturation occurs because as the concentration of the NO_2 increases, these surface-adsorbed molecules act as acceptors available to take electrons from the suboxide and at a certain concentration, there are no electrons left. The sample annealed at 225 °C has the $WO_{2.96}$ stoichiometry, which is known to be semiconducting, while the unannealed and annealed at 450 °C have the $WO_{2.92}$ stoichiometry that is more metallic and requires more electron transfer for full off/on switching. Therefore, the changes in crystal structure and stoichiometry can result in different performance of sensors. The same samples were studied for NH_3, H_2S, CO_2, H_2 and humidity sensing, but showed far less promise. This is explained with greater molecule-surface binding energies for NO_2 and WO_3.

In another study, WO_3 nanosheets prepared by microwave irradiation method showed promise as humidity sensors.[61] With the relative humidity working range of 10–90 %, the maximum sensitivity was estimated to be 98 %, with the response and recovery time of 25 and 15 s, respectively. They showed high stability, with only a 3 % drop in performance after three months, making them suitable candidates for high performance sensing.

Ultrathin (5 nm) WO_3 sheets were successfully used as gas sensing material for the detection of xylene, a volatile organic compound that has adverse effects on human health.[3] The sensing mechanism can be explained as follows: oxygen molecules from air get adsorbed on the surface of WO_3 and get chemisorbed into O^{2-}, O^- or O_2^- by capturing electrons from the material's conduction band. Upon xylene introduction, it reacts with these species, releasing the trapped electrons. In the case of thin sheets, these charge layers may cover the entire surface, increasing the material's sensitivity.[3] This sensing mechanism is depicted in Figure 3 a).

2D-WO_3 nanoplatelets with 10–50 nm thickness were used as hydrogen sensors.[62] The most efficient interaction of WO_3 with the molecules that contain hydrogen atoms is through intercalation. The intercalated H^+ ions embed themselves into WO_3 lattice, and the electrons released from the lattice are transferred to the lowest unoccupied energy levels. This in turn changes the band structure of the metal oxide and increases the conductivity, which can be used for sensing applications. The mechanism of H_2 sensing is based on the changes in electrical conductance, which strongly depends on the content of oxygen vacancies and $H+$ ions. The oxygen adsorbing capabilities in turn depend on the surface area of the material, morphology and the operating temperature. As the oxygen species adsorbed on the surface capture electrons from the material, the hole concentration increases, forming an electron-depleted layer at the surface of the platelets.[62]

Triclinic WO_3 nanosheets with 35 nm thickness were synthesized in a process that enables the control of the exposed facets.[21] These nanosheets were used as l-butylamine sensors,
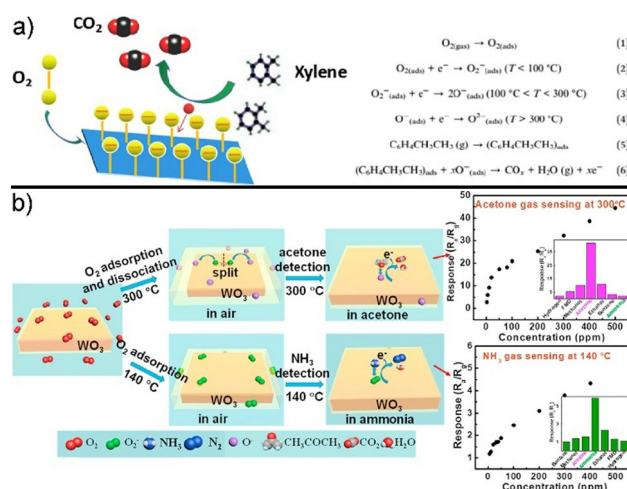
Figure 3. Schematic illustrations of the sensing mechanism of 2D-WO_3 towards a) xylene (Reprinted from reference [3], with permission from Elsevier) and b) acetone and ammonia (Reprinted from reference [24], with permission from Elsevier).

and the sheets with the exposed (010) facets demonstrated the best performance. It was shown that (001) and (100) facets have more O-terminated planes, while (010) have more W atoms exposed at the surface. Therefore, as it has more positive ions than other facets, it has better gas sensing capabilities.

As n-type semiconductors, WO_{3-x} materials are good candidates for ethanol sensing.[63] When the platelets are exposed to air, the oxygen molecules from the atmosphere can get adsorbed on the surface. They can subsequently capture electrons from the conduction band of WO_{3-x}, forming adsorbed oxygen ions (O^{2-}, O^-, O_2^-), producing an electron-depletion layer on the surface. When the sensor gets exposed to ethanol, the ethanol molecules get chemisorbed on the surface and oxidized by the adsorbed oxygen ions.[63] The oxidation promotes the return of the depleted electrons back to the conduction band, resulting in the decrease of the thickness of the electron-depletion layer. As a result, upon ethanol exposure, electrical current increases. The sensors of WO_3 nanoplates annealed at different temperatures were tested at the operating temperature of 300 °C for various ethanol concentrations.[64] It was shown that the sensitivity improved as the gas concentration increased. The gas sensor made of nanoplates with 500–1000 nm in lateral size and 50 nm thickness annealed at 450 °C had the best alcohol sensing performance, due to the high crystallinity of the nanoplates. The sensor maintained the initial response upon seven successive tests to 100 ppm of ethanol, showing good stability and reproducibility. The plate-like morphology and high crystallinity enable effective adsorption and rapid diffusion of the ethanol molecules. WO_3 platelets, produced by laser-assisted synthesis and with 70 nm thickness, were tested as ethanol sensors both in their pristine form and decorated with 8 nm Au nanoparticles.[65] The pure platelet sensor reached the

maximum response (current ratios through the sensor with and without the target gas) of 28 at 390 °C for 100 ppm of ethanol. With the added Au particles, the optimal temperature was lowered to 300 °C, with the 3.5-fold increase of the response value. The difference is attributed to the increased thickness of the electron-depletion layer, whereby Au nanoparticles accelerate the reaction between the ethanol molecules and adsorb oxygen ions.

Nanoplatelets of monoclinic WO_3 with 70–100 nm in lateral size and 30 nm of thickness were investigated as acetone and ammonia sensors due to their high crystallinity and smooth 2D surface.[24] These nanoplatelets do not have oxygen vacancies, but an abundance of surface chemisorbed oxygen. Those properties make them excellent gas sensors towards acetone at 300 °C, with response and recovery times of 3 s and 7 s, respectively, at 10 ppm of acetone. Additionally, this sensor showed a wide response range (1–500 ppm), detection concentration as low as 1 ppm and good selectivity and stability. It was shown that active O^- plays a leading sensing role for acetone. In the case of ammonia sensing, the optimal operating temperature was found to be 140 °C, with the response and recovery times of 39 s and 10 s, respectively; response region of 5–500 ppm and high selectivity. The sensing mechanism and the sensor response are shown in Figure 3 b).

3.2 Electrical Properties: Conductivity and 2D Photodetectors

The presence of the free electrons in the conduction band is the dominant factor in the electrical conductivity of these materials. These free electrons mainly come from CS planes, PC structures, oxygen vacancies, and other defects.[66] Even in the case of a single crystal, the electrical conductivity can span five orders of magnitude (10^{-4}–10 S cm^{-1}), depending on the stoichiometry,[67] with the charge carrier concentrations spanning the similar range (10^{17}–10^{22} cm^{-3}).[68] The amount of oxygen vacancies and the stoichiometry strongly depend on synthesis conditions and structural factors, which heavily influence the conductivity. This makes tungsten (sub)oxides interesting in terms of tailoring the material properties for specific electrical applications.

Bulk monoclinic WO_3 is a wide bandgap n-type semiconductor.[1a,69] The n-type semiconductor properties stem from oxygen vacancy-type defects. Bandgap corresponds to the difference between the top of the valence band (filled O 2p orbitals) and the bottom of the conduction band (empty W 5d orbitals), and is typically reported as 2.62 eV.[70] Bulk, stoichiometric WO_3 is therefore transparent in the visible wavelength range. Another thing to consider when designing optical devices based on WO_3, is its large refractive index of up to 2.5.[71] On the other hand, oxygen vacancies due to true, point-like defects in WO_3, are major contributors in the improved photocurrent density.[72] In n-type metal oxides, these oxygen vacancies act as shallow donors. These electrons may fill the acceptor states below the conduction band minimum,

making inter-bandgap states. If these shallow defect states remain unfilled, they can act as electron traps, resulting in the increased photoelectron lifetimes.[73] Due to the quantum confinement effects, 2D-WO_3 have a larger bandgap and more positive conduction and valence band edges.[25,74] For nano-structured semiconductors, the bandgap generally increases with the decrease in size,[75] resulting in the blueshift of the optical absorption band edge. It should be pointed out that the quantum confinement effect can occur in two different regimes.[76] In the strong regime, the size of the material has to be much smaller than its Bohr radius, which is estimated as 3 nm for WO_3.[77] The bandgap is significantly altered because the electron wavefunctions are perturbed directly. In the weak regime, when the crystallite size is larger than the Bohr radius, the bandgap energy changes are subtler, as the wavefunctions are indirectly perturbed. Therefore, the crystallite size plays an important role in bandgap engineering.

In bulk and in form of nanowires, WO_3 photodetectors showed a relatively slow response time and low on/off ratios.[78] It is to be expected that 2D nanosheets have an improved performance.

50 nm layers thick WO_3 layers were deposited on a graphene back electrode (on a PET substrate), in order to engineer a transparent, flexible UV detector, as shown in Figure 4 a).[74] These photodetectors were subsequently tested under 325 nm UV light or an alternating on and off UV source in 10 s intervals. The detector had a typical p-type Schottky contact barrier I–V response. The time responses are highly stable and reproducible, with no degradation after tens of on-
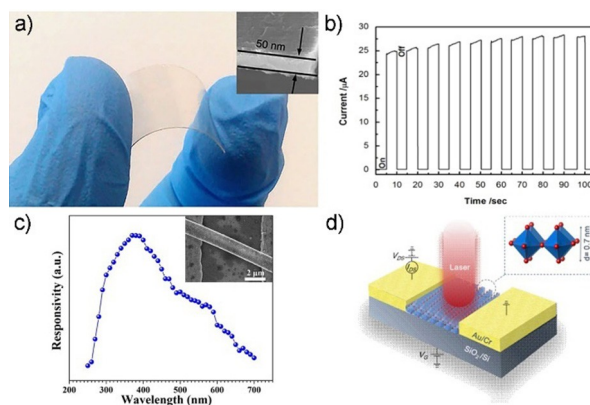
Figure 4. a) The fabricated flexible photodetector made of a WO_3 nanosheet on PET substrate (Reprinted from reference [74], with permission from Springer); b) The time-resolved photocurrent of the photodetector in response to light on/off at an irradiance of 131 mW cm^{-2} with 365 nm light (Reprinted from reference [79], with permission from Elsevier); c) Spectroscopic photoresponse of the WO_3 nanobelt photodetector (shown in inset) measured at various wavelengths ranging from 250 to 700 nm at a bias of 1 mV. (Reprinted with permission from reference [80]. Copyright {2015} American Chemical Society); d) Three-dimensional schematic view of the monolayer WO_3 photodetector and the focused laser beam used to probe the device. (Reprinted from reference [82], with permission from Elsevier).

off switching cycles. Interestingly, there was an increase in photocurrent with prolonged irradiation time, possibly due to its photochromic effect under UV radiation.[74]

A 12 nm (approximately 16 molecular sheets) thick WO_3 nanosheets photodetector, with two Cr/Au electrodes, was irradiated with a 365 nm monochromatic light.[79] This source was chosen as it is approximately at the position of the bandgap. The device exhibited a reversible on/off ratio of 2000, making it a high-quality photosensitive switch. The rise and the decay time were estimated to be 40 ms and 80 ms, respectively, which is much faster than that of the nanowires (20 s). The decay time was longer than the rise time, due to the presence of several recombination processes, such as surface and Auger recombination. Spectral responsivity, defined as the photocurrent generated per unit power of incident light on the effective area of a photodevice, was estimated as 293 AW^{-1}. The time-resolved photocurrent in response to on/off light is shown in Figure 4 b).

Additionally, polycrystalline WO_3 200–300 nm thick nanobelts were successfully used as a building block of a UV photodetector.[80] One individual belt consisted of dense nanoparticles of 20 nm in size. Using gold electrodes, this photodetector was assembled on a SiO_2/Si substrate and the photoresponse was recorded for the light excitation between 250 and 700 nm, as shown in Figure 4 c), with the maximum sensitivity observed at 400 nm. The photoresponse has a slight drop for the wavelengths shorter than 400 nm, as explained by the enhanced absorption of the high-energy photons near the surface, while the increase in the longer wavelengths was attributed to the transition of the carriers from defect states to the conduction band.[81] I–V curves recorded in dark and under illumination are nonlinear, indicating Shottky contact between the sample and the electrodes. The photoexcited currents were much greater than dark currents, with a photo-dark current ratio of 1000. The superior performance compared to monocrystalline WO_3 was attributed to the abundance of grains and boundaries that supress the dark currents, and the increased photocurrent due to band-gap modulation.

Finally, a monolayer WO_3, produced by atomic layer deposition on a SiO_2/Si wafer, as shown in in Figure 4 d), was used for UV-A (315–400 nm) spectrum detection, which represents 95% of the UV radiation that reaches the Earth's surface.[82] This detector was shown to have an extremely fast response time ($\leq 40\ \mu s$, 400 times faster than in the case of WO_3 nanosheets[79]), stability of more than 200 cycles and photoresponsivity of 0.33 AW^{-1}. This value is more than two orders of magnitude greater than for the previously reported WO_3 photodetectors, with the reduced thickness as the most important factor for such an improvement in performance. Additionally, the photodetector was tested under 320 nm light for different bias and back-gate voltages. In the dark, with no bias, a depletion sub-layer near the surface of the monolayer is formed, as the surrounding O_2 adsorbs on the material. With the applied bias, the current through the monolayer is low as the conductivity is low because of the depletion layer. When the device was put under the UV radiation, the photogenerated holes moved to the surface and desorbed the oxygen, in turn decreasing the width of the depletion sublayer and increasing the number of free charge carriers. This whole process is sped up due to the small thickness.

Ultrathin (less than 10 nm) WO_{3-x} nanoflakes were intercalated with H^+ and tested as field-efect-transistor (FET) based devices.[83] Zhuiykov *et al.* reported that devices prepared this way reach charge-carrier mobility of 319 $cm^2 V^{-1} s^{-2}$, comparable to those of MoS_2 and WS_2, while for the nanoflakes before intercalation the mobility was 275 $cm^2 V^{-1} s^{-2}$. Both results are great improvements compared to the bulk WO_3, that had the reported charge-carrier mobility of 12 $cm^2 V^{-1} s^{-2}$.[83] By changing the thickness of the material (from 50 nm to 2.5 nm), the bandgap was modulated from 2.60 to 2.40 eV. It is believed that the intercalated H^+ ions interact with the corner-sharing oxygen atoms in the first monolayer, while the remaining ions get transferred deeper into the structure and repeat the same interaction. This fuels the formation of H_2O molecules that get released, leaving lone oxygen vacancies. The additional electron gets delocalized within the layers, giving rise to a mid-gap state. Furthermore, it was shown that H^+ intercalation reduces the bandgap from 2.6 to 2.5 eV.

3.3 Photocatalysis and Photoelectrochemical (PEC) Water Splitting

Pristine WO_3 does not have the photocatalytic activity high enough for practical use. Therefore, many approaches have been undertaken to improve the photocatalytic performance, with the most efficient ones being the introduction of the oxygen vacancies and/or using lower dimensional WO_{3-x}.

The photocatalytic reduction of CO_2 is an important route for its transformation to organic compounds as well as CO. Semiconductors have been used for photocatalysis with the absorption of a photon with the energy greater than its bandgap. This process induces an interband transition, whereby conduction band electrons and valence band holes are formed. The electrons and holes diffuse to the surface of the material, but only a fraction reaches it due to the recombination. In addition, the free charge carriers that reach the surface may be trapped before the interfacial charge transfer. Lastly, the photogenerated electrons reduce the CO_2 adsorbed on the catalyst surface into CO, HCOOH etc, while the holes oxidize H_2O to O_2. One of the most important steps is the facilitation of the electron-hole separation, since the charge recombination happens on a much faster timescale (10^{-9} s) than the reaction process (10^{-3}–10^{-8} s).[84] Using the lower-dimensional WO_{3-x} can potentially improve the catalytic behaviour. Namely, in the case of bulk WO_3, the photogenerated electrons in the conduction band have a lower, more positive, band-edge position.[25] Therefore, in bulk, this material cannot be used for the reduction of CO_2 or H_2O. On the other hand, 5 nm thick WO_3 nanosheets could catalyse the photoreduction of CO_2 with H_2O into CH_4. For such ultrathin material, the bandgap

increased from 2.63 eV to 2.79 eV, while the conduction band edge moved from 0.05 eV to −0.42 eV (versus normal hydrogen electrode, NHE), becoming more negative than the CO_2/CH_4 redox potential at −0.24 eV.[25–26] This demonstrates how a specific morphology can change the position of the conduction and/or the valence band, making the material a more suitable candidate for CO_2 reduction.

Liang *et al.* studied 5 nm thick WO_3 sheets' photocatalytic activity by degradation of methyl orange (MO) under simulated sunlight.[3] They showed that the nanosheets have superior photocatalytic activity compared to nanoparticles or bulk material, due to their high specific surface area. Ultrathin (5 nm) WO_{3-x} nanosheets with abundant surface oxygen vacancies were also tested as PEC devices, by degradation of MO under visible light.[14] After 90 min of irradiation, 70% of the solution was degraded, making them good candidates for this type of catalysis.

WO_{3-x} nanosheets with up to 300 nm lateral size and 15 nm thickness were tested as photocatalysts by using methylene blue (MB) and congo-red (CR) dyes under visible light irradiation.[61] In 100 min, 99.5% of MB and 92% of CR was photodegraded by the nanosheets, a significant improvement compared with the nanorods (76% and 70%). The superior photocatalytic performance of the nanosheets is explained by the increase in the active surface, the smaller bandgap and oxygen deficiencies.

Both pristine WO_3 and 20–30 nm thick WO_3 nanosheets with oxygen vacancies were tested for their photocatalytic activity for the degradation of rhodamine B (RhB) under visible light irradiation.[47a] While the pristine oxide decomposed only 9% of RhB after 320 min, WO_3 nanosheets with oxygen vacancies had increased photocatalytic efficiency of 77%. The latter sample had enhanced visible light absorption, and the plasmonic resonance with the peak at 800 nm. The oxygen vacancies act as electron donors and contribute to the enhanced donor density, increasing the charge transport and enhancing the photocatalytic activity.[47a] Hydrothermally prepared WO_3 platelets with 50 nm thickness and up to 170 nm in lateral size were tested for the similar activity.[85] It was shown that after 70 min of irradiation, the characteristic absorption peak of RhB almost disappeared, suggesting good photocatalytic activity.

Photoelectrochemical (PEC) water splitting is an increasingly popular technique for the efficient hydrogen generation. While the hydrogen is produced at the photocathode part of the PEC cell, photoanode material is responsible for the oxygen evolution reaction. Suitable photoanode candidates need to have appropriate band alignments (valence band more positive than water oxidation and conduction band more negative than hydrogen reduction) and to be absorbent in the visible light. WO_3 has a bandgap that can capture approximately 12% of the solar spectrum and absorb light up to 500 nm in the visible spectrum,[86] while being chemically stable and environmentally friendly. In the case of the suboxides, the W^{5+} present in CS and PC structures as well as oxygen vacancy-induced electron traps can extend the photo-

electron lifetimes, improving their performance as photocathodes for water splitting.[87] As a result, the photogenerated holes in the valence band have more time to move to the electrode and participate in the reaction. The W^{5+} and oxygen vacancies are not just active centres which capture charges to block recombination, they may also reduce the activation energy. On the other hand, samples with high number of defects may have decreased crystallinity. This can result in an overall decrease of photocurrents due to increase in scattering effects. Since the hole diffusion length in WO_3 is 150 nm,[88] if the thickness of the samples is of an approximately similar size, it can play a significant role in decreasing charge carrier recombination. If this is fulfilled, the photogenerated holes can reach the surface more easily and participate in water splitting before recombining.

The free-standing pore-rich sub-4 nm thick WO_3 nanosheets were obtained by using a chemical topology transformation strategy.[86] It was demonstrated that they have more photogenerated holes, shorter migration path and stronger oxidation ability than thicker samples. The measured photocurrent density of this sample is 2.14 mA cm^{-2}.

Mohamed *et al.* investigated both the stoichiometric and nonstoichiometric WO_3, using an electrochemical method to study the nature of the defect states.[72] Annealing the samples under different atmospheres resulted not only in different number, but in different nature of vacancies, making this a suitable approach to defect engineering. The highest photocurrent density was obtained on the nanoflakes annealed in air (1.3 mA cm^{-2}), with the optical band gap of 2.88 eV. It was demonstrated that the nonstoichiometric samples had higher photocurrents, indicating the presence of the shallow surface states, that feed the conduction band with electrons and form interband states. When the deep defect states become more dominant, they push the Fermi level away from the conduction band minimum, having damaging effect on the photocurrent. It can be concluded that the moderate concentration of oxygen vacancies results in appearance of W^{5+} shallow donor states that increase the photoactivity, while the deep trap W^{4+} states arise with the increase in oxygen vacancies, with the detrimental effect on photocurrent. This subtle interplay explains the contradictory results for the same material prepared under different conditions.

Soltani *et al.* designed 50 nm thick highly porous WO_{3-x} nanoplates with dual oxygen and tungsten vacancies for PEC water splitting.[87] The number of oxygen vacancies and the film design were optimised to provide a large surface area for efficient charge collecting, which led to a photocurrent density of 4.12 mA cm^{-2} at 1.6 V vs Ag/AgCl. The stability time was reported as 1 h.

4. Summary and Outlook

In this review, an overview of the recent progress in the preparation of quasi-two-dimensional tungsten (sub)oxides was discussed. In recent years, a wide range of techniques

Review

were developed to synthesize such materials. To a certain degree, the crystal phase, morphology and stoichiometry can be controlled but there is still room for improvement. For example, as discussed above, different facets have unique physical and chemical properties, which can be exploited in a wide range of chemical reactions and sensing devices. As of now, only a few 2D-WO$_3$ nanomaterials were synthesized with the certain facets exposed intentionally. Although the majority of the tungsten oxide nanomaterials appears in one form of the WO$_3$ crystal structure, substoichiometric tungsten oxides (WO$_{3-x}$) show a great variety of structures. Furthermore, they hold great promise due to their W^{5+} states that act as electron donors. By varying the stoichiometry of WO$_{3-x}$ or the number of oxygen vacancies on the surface of tungsten (sub)oxides, their electrical and optical properties can be tuned for specific devices and chemical reactions.

It has to be pointed out that in the majority of publications, the material's reported stoichiometry was determined exclusively from XRD measurements, which is not a suitable method as the differences between the WO$_{3-x}$ phases are too small to be unambiguously detected. Furthermore, it should be emphasized that the WO$_{3-x}$ materials containing CS and PC structures should not be interchanged with materials with surface oxygen vacancies. Although individual oxygen vacancies can be produced, in order to minimize the surface energy, PC structures are formed while single CS planes appear when the material is further reduced. It would be beneficial if the reports on tungsten suboxide materials contained a thorough examination with HRTEM and electron diffraction techniques in order to determine the true nature and structure of oxygen vacancies. Only when this is achieved, further spectroscopic methods, such as Raman spectroscopy and optical measurements, can be utilized properly.

When it comes to potential applications, three of the most important factors that are responsible for the performance are the sample thickness, stoichiometry, and the oxygen vacancies. While the nanostructured suboxides in the shape of nanorods, nanowires and various other types of nanoparticles have been under numerous application-based studies, the similar research for their 2D counterparts is still in its infancy. For example, their charge-carrier densities are comparable to those of transition metal dichalcogenides, but the amount of reports of FETs based on these suboxides has been incomparably small. The control of the thickness, stoichiometry, and the introduction of the oxygen vacancies can be used as general strategies for increasing the electrical conductivity and photocatalytic activity. One of the major challenges could be the quantification and the effect on the crystal structure of the oxygen vacancies, and the deep understanding of their effect on optical and electronic properties, and the resulting performance in various applications.

References

[1] a) C. G. Granqvist, *Sol. Energy Mater. Sol. Cells* **2000**, *60*, 201–262; b) H. Miyazaki, T. Ishigaki, T. Ota, *J. Mater. Sci. Res.* **2017**, *6*, 62–66.

[2] Z. Hai, Z. Wei, C. Xue, H. Xu, F. Verpoort, *J. Mater. Chem. C* **2019**, *7*, 12968–12990.

[3] Y. Liang, Y. Yang, C. Zou, K. Xu, X. Luo, T. Luo, J. Li, Q. Yang, P. Shi, C. Yuan, *J. Alloys Compd.* **2019**, *783*, 848–854.

[4] S. S. Thind, X. Chang, J. S. Wentzell, A. Chen, *Electrochem. Commun.* **2016**, *67*, 1–5.

[5] H. Zheng, J. Z. Ou, M. S. Strano, R. B. Kaner, A. Mitchell, K. Kalantar-zadeh, *Adv. Funct. Mater.* **2011**, *21*, 2175–2196.

[6] a) T. Vogt, P. M. Woodward, B. A. Hunter, *J. Solid State Chem.* **1999**, *144*, 209–215; b) B. Gerand, G. Nowogrocki, J. Guenot, M. Figlarz, *J. Solid State Chem.* **1979**, *29*, 429–434.

[7] M. Boulova, G. Lucazeau, *J. Solid State Chem.* **2002**, *167*, 425–434.

[8] Z. Zhang, X. Hao, S. Hao, X. Yu, Y. Wang, J. Li, *Molecular Catalysis* **2021**, *503*, 111427.

[9] V. Hariharan, B. Gnanavel, R. Sathiyapriya, V. Aroulmoji, *Int J Adv Sci Eng Inf Technol.* **2019**, *5*, 1163–1168.

[10] L. Pirker, B. Višić, S. D. Škapin, G. Dražić, J. Kovač, M. Remškar, *Nanoscale* **2020**, *12*, 15102–15114.

[11] H. G. Choi, Y. H. Jung, D. K. Kim, *J. Am. Ceram. Soc.* **2005**, *88*, 1684–1686.

[12] A. Wolcott, T. R. Kuykendall, W. Chen, S. Chen, J. Z. Zhang, *J. Phys. Chem. B* **2006**, *110*, 25288–25296.

[13] D. Chen, L. Gao, A. Yasumori, K. Kuroda, Y. Sugahara, *Small* **2008**, *4*, 1813–1822.

[14] X. Zhou, X. Zheng, B. Yan, T. Xu, Q. Xu, *Appl. Surf. Sci.* **2017**, *400*, 57–63.

[15] A. Azam, J. Kim, J. Park, T. G. Novak, A. P. Tiwari, S. H. Song, B. Kim, S. Jeon, *Nano Lett.* **2018**, *18*, 5646–5651.

[16] K. D. McDonald, B. M. Bartlett, *RSC Adv.* **2019**, *9*, 28688–28694.

[17] H. Zhang, G. Duan, Y. Li, X. Xu, Z. Dai, W. Cai, *Cryst. Growth Des.* **2012**, *12*, 2646–2652.

[18] W. Li, P. Da, Y. Zhang, Y. Wang, X. Lin, X. Gong, G. Zheng, *ACS Nano* **2014**, *8*, 11770–11777.

[19] Y. Oaki, H. Imai, *Adv. Mater.* **2006**, *18*, 1807–1811.

[20] N. Dirany, M. Arab, V. Madigou, C. Leroux, J. Gavarri, *RSC Adv.* **2016**, *6*, 69615–69626.

[21] X. Han, X. Han, L. Li, C. Wang, *New J. Chem.* **2012**, *36*, 2205–2208.

[22] Z. Fang, S. Jiao, B. Wang, W. Yin, S. Liu, R. Gao, Z. Liu, G. Pang, S. Feng, *Mater. Today* **2017**, *6*, 146–153.

[23] J. Besnardiere, B. Ma, A. Torres-Pardo, G. Wallez, H. Kabbour, J. M. González-Calbet, H. J. Von Bardeleben, B. Fleury, V. Buissette, C. Sanchez, *Nat. Commun.* **2019**, *10*, 1–9.

[24] G. Liu, L. Zhu, Y. Yu, M. Qiu, H. Gao, D. Chen, *J. Alloys Compd.* **2021**, *858*, 157638.

[25] X. Chen, Y. Zhou, Q. Liu, Z. Li, J. Liu, Z. Zou, *ACS Appl. Mater. Interfaces* **2012**, *4*, 3372–3377.

[26] a) Y. P. Xie, G. Liu, L. Yin, H.-M. Cheng, *J. Mater. Chem.* **2012**, *22*, 6746–6751; b) N. Zhang, C. Chen, Z. Mei, X. Liu, X. Qu, Y. Li, S. Li, W. Qi, Y. Zhang, J. Ye, *ACS Appl. Mater. Interfaces* **2016**, *8*, 10367–10374.

[27] M. Remškar, J. Kovac, M. Viršek, M. Mrak, A. Jesih, A. Seabaugh, *Adv. Funct. Mater.* **2007**, *17*, 1974–1978.

[28] a) J. Allpress, R. Tilley, M. Sienko, *J. Solid State Chem.* **1971**, *3*, 440–451; b) S. Iijima, *J. Solid State Chem.* **1975**, *14*, 52–65.

[29] W. Merchan-Merchan, M. F. Farahani, Z. Moorhead-Rosenberg, *Micron* **2014**, *57*, 23–30.

[30] a) S. Lee, Y.-W. Lee, D.-H. Kwak, M.-C. Kim, J.-Y. Lee, D.-M. Kim, K.-W. Park, *Ceram. Int.* **2015**, *41*, 4989–4995; b) B. Wang, X. Zhong, C. He, B. Zhang, U. Cvelbar, K. Ostrikov, *J. Alloys Compd.* **2021**, *854*, 157249; c) B. Wang, X. Zhong, C. He, B. Zhang, U. Cvelbar, K. Ostrikov, *Mater. Chem. Phys.* **2021**, *262*, 124311.

[31] a) M. Mattinen, J.-L. Wree, N. Stegmann, E. Ciftyurek, M. E. Achhab, P. J. King, K. Mizohata, J. Räisänen, K. D. Schierbaum, A. Devi, *Chem. Mater.* **2018**, *30*, 8690–8701; b) N. Doudin, D. Kuhness, M. Blatnik, G. Barcaro, F. Negreiros, L. Sementa, A. Fortunelli, S. Surnev, F. Netzer, *J. Phys. Chem. C* **2016**, *120*, 28682–28693.

[32] M. B. Johansson, B. Zietz, G. A. Niklasson, L. Österlund, *J. Appl. Phys.* **2014**, *115*, 213510.

[33] M. Dobson, R. Tilley, *Acta Crystallogr. Sect. B* **1988**, *44*, 474–480.

[34] S. Heo, J. Kim, G. K. Ong, D. J. Milliron, *Nano Lett.* **2017**, *17*, 5756–5761.

[35] L. Wen, L. Chen, S. Zheng, J. Zeng, G. Duan, Y. Wang, G. Wang, Z. Chai, Z. Li, M. Gao, *Adv. Mater.* **2016**, *28*, 5072–5079.

[36] a) P. Labbe, in *Key Engineering Materials, Vol. 68*, Trans Tech Publ, **1992**, p. 293; b) R. Tilley, *J. Solid State Chem.* **1976**, *19*, 53–62.

[37] Y.-J. Lee, T. Lee, A. Soon, *Chem. Mater.* **2019**, *31*, 4282–4290.

[38] A. Magnéli, *Acta Crystallogr.* **1953**, *6*, 495–500.

[39] L. Bursill, B. Hyde, *J. Solid State Chem.* **1972**, *4*, 430–446.

[40] M. Lundberg, M. Sundberg, A. Magnéli, *J. Solid State Chem.* **1982**, *44*, 32–40.

[41] a) A. Magneli, *Arkiv Kemi* **1949**, *1*, 223–230; b) R. Pickering, R. Tilley, *J. Solid State Chem.* **1976**, *16*, 247–255.

[42] T. Miyano, M. Iwanishi, C. Kaito, M. Shiojiri, *Japanese J. Appl. Phys.* **1983**, *22*, 863.

[43] J. Meng, Z. Lan, I. E. Castelli, K. Zheng, *J. Phys. Chem. C* **2021**, *125*, 8456–8460.

[44] Z. Zhao, Y. Bai, W. Ning, J. Fan, Z. Gu, H. Chang, S. Yin, *Appl. Surf. Sci.* **2019**, *471*, 537–544.

[45] W. Zhang, P. Xu, Y. Shen, J. Feng, Z. Liu, G. Cai, X. Yang, R. Guan, L. Su, L. Yue, *J. Environ. Chem. Eng.* **2021**, *9* (6), 106493.

[46] L. Pirker, B. Višić, J. Kovač, S. D. Škapin, M. Remškar, *Nanomaterials* **2021**, *11*, 1985.

[47] a) S. Chen, Y. Xiao, W. Xie, Y. Wang, Z. Hu, W. Zhang, H. Zhao, *Nanomaterials* **2018**, *8*, 553; b) X. Ming, A. Guo, G. Wang, X. Wang, *Sol. Energy Mater. Sol. Cells* **2018**, *185*, 333–341.

[48] F. Negreiros, T. Obermüller, M. Blatnik, M. Mohammadi, A. Fortunelli, F. Netzer, S. Surnev, *J. Phys. Chem. C* **2019**, *123*, 27584–27593.

[49] A. Mohamedkhair, Q. Drmosh, M. Qamar, Z. Yamani, *Catalysts* **2020**, *10*, 526.

[50] a) Z. Hai, M. K. Akbari, Z. Wei, C. Xue, H. Xu, J. Hu, S. Zhuiykov, *Electrochim. Acta* **2017**, *246*, 625–633; b) S. Balasubramanyam, A. Sharma, V. Vandalon, H. C. Knoops, W. M. Kessels, A. A. Bol, *J. Vac. Sci. Technol.* **2018**, *36*, 01B103.

[51] S. Yu, Y. Ling, J. Zhang, F. Qin, Z. Zhang, *Int. J. Hydrogen Energy* **2017**, *42*, 20879–20887.

[52] Y. Li, K. Chang, H. Tang, B. Li, Y. Qin, Y. Hou, Z. Chang, *Electrochim. Acta* **2019**, *298*, 640–649.

[53] K. Pan, K. Shan, S. Wei, K. Li, J. Zhu, S. H. Siyal, H.-H. Wu, *Compos. Commun.* **2019**, *16*, 106–110.

[54] E. K. Salje, *Condens. Matter* **2020**, *5*, 32.

[55] Z. Wang, D. Wang, J. Sun, *Sens. Actuators B* **2017**, *245*, 828–834.

[56] W. Zhu, F. Huang, E. Chen, Q. Wu, J. Xu, C. Lu, Y. Wang, *Che. Asian J.* **2017**, *12*, 524–529.

[57] A. Dey, *Mater. Sci. Eng. B* **2018**, *229*, 206–217.

[58] M. Guarnieri, J. R. Balmes, *The Lancet* **2014**, *383*, 1581–1592.

[59] C. Cantalini, L. Lozzi, M. Passacantando, S. Santucci, *IEEE Sens. J.* **2003**, *3*, 171–179.

[60] H. Khan, A. Zavabeti, Y. Wang, C. J. Harrison, B. J. Carey, M. Mohiuddin, A. F. Chrimes, I. A. De Castro, B. Y. Zhang, Y. M. Sabri, *Nanoscale* **2017**, *9*, 19162–19175.

[61] M. Parthibavarman, M. Karthik, S. Prabhakaran, *Vacuum* **2018**, *155*, 224–232.

[62] M. B. Rahmani, M. H. Yaacob, Y. M. Sabri, *Sens. Actuators B* **2017**, *251*, 57–64.

[63] M. Horprathum, T. Srichaiyaperk, B. Samransuksamer, A. Wisitsoraat, P. Eiamchai, S. Limwichean, C. Chananonnawathorn, K. Aiempanakit, N. Nuntawong, V. Patthanasettakul, *ACS Appl. Mater. Interfaces* **2014**, *6*, 22051–22060.

[64] J. Ma, J. Zhang, S. Wang, T. Wang, J. Lian, X. Duan, W. Zheng, *J. Phys. Chem. C* **2011**, *115*, 18157–18163.

[65] E. Dai, S. Wu, Y. Ye, Y. Cai, J. Liu, C. Liang, *J. Colloid Interface Sci.* **2018**, *514*, 165–171.

[66] K. Aguir, C. Lemire, D. Lollman, *Sens. Actuators B* **2002**, *84*, 1–5.

[67] V. Makarov, M. Trontelj, *J. Eur. Ceram. Soc.* **1996**, *16*, 791–794.

[68] a) X. Liu, Y. He, S. Wang, Q. Zhang, M. Song, *Int. J. Refract. Met. Hard M.* **2012**, *34*, 47–52; b) K. Patel, C. Panchal, V. Kheraj, M. Desai, *Mater. Chem. Phys.* **2009**, *114*, 475–478; c) M. Regragui, V. Jousseaume, M. Addou, A. Outzourhit, J. Bernede, B. E Idrissi, *Thin Solid Films* **2001**, *397*, 238–243.

[69] P. González-Borrero, F. Sato, A. Medina, M. L. Baesso, A. C. Bento, G. Baldissera, C. Persson, G. A. Niklasson, C. G. Granqvist, A. Ferreira da Silva, *Appl. Phys. Lett.* **2010**, *96*, 061909.

[70] M. Gillet, K. Aguir, C. Lemire, E. Gillet, K. Schierbaum, *Thin Solid Films* **2004**, *467*, 239–246.

[71] D. Davazoglou, A. Donnadieu, *Thin Solid Films* **1987**, *147*, 131–142.

[72] A. M. Mohamed, A. W. Amer, S. Y. AlQaradawi, N. K. Allam, *Phys. Chem. Chem. Phys.* **2016**, *18*, 22217–22223.

[73] L. J. Antila, M. J. Heikkilä, V. Mäkinen, N. Humalamäki, M. Laitinen, V. Linko, P. Jalkanen, J. Toppari, V. Aumanen, M. Kemell, *J. Phys. Chem. C* **2011**, *115*, 16720–16729.

[74] Z. Sun, T. Liao, Y. Dou, S. M. Hwang, M.-S. Park, L. Jiang, J. H. Kim, S. X. Dou, *Nat. Commun.* **2014**, *5*, 1–9.

[75] S. Gullapalli, R. Vemuri, C. Ramana, *Appl. Phys. Lett.* **2010**, *96*, 171903.

[76] A. D. Yoffe, *Adv. Phys.* **1993**, *42*, 173–266.

[77] R. A. May, L. Kondrachova, B. P. Hahn, K. J. Stevenson, *J. Phys. Chem. C* **2007**, *111*, 18251–18257.

[78] L. Li, Y. Zhang, X. Fang, T. Zhai, M. Liao, X. Sun, Y. Koide, Y. Bando, D. Golberg, *J. Mater. Chem.* **2011**, *21*, 6525–6530.

[79] J. Liu, M. Zhong, J. Li, A. Pan, X. Zhu, *Mater. Lett.* **2015**, *148*, 184–187.

Review

[80] Z. He, Q. Liu, H. Hou, F. Gao, B. Tang, W. Yang, *ACS Appl. Mater. Interfaces* **2015**, *7*, 10878–10885.

[81] J. Jie, W. Zhang, Y. Jiang, X. Meng, Y. Li, S. Lee, *Nano Lett.* **2006**, *6*, 1887–1892.

[82] Z. Hai, M. K. Akbari, C. Xue, H. Xu, L. Hyde, S. Zhuiykov, *Appl. Surf. Sci.* **2017**, *405*, 169–177.

[83] S. Zhuiykov, E. Kats, B. Carey, S. Balendhran, *Nanoscale* **2014**, *6*, 15029–15036.

[84] M. R. Hoffmann, S. T. Martin, W. Choi, D. W. Bahnemann, *Chem. Rev.* **1995**, *95*, 69–96.

[85] H. Zhang, J. Yang, D. Li, W. Guo, Q. Qin, L. Zhu, W. Zheng, *Appl. Surf. Sci.* **2014**, *305*, 274–280.

[86] Y. Liu, L. Liang, C. Xiao, X. Hua, Z. Li, B. Pan, Y. Xie, *Adv. Energy Mater.* **2016**, *6*, 1600437.

[87] T. Soltani, A. Tayyebi, H. Hong, M. H. Mirfasih, B.-K. Lee, *Sol. Energy Mater. Sol. Cells* **2019**, *191*, 39–49.

[88] R. Solarska, R. Jurczakowski, J. Augustynski, *Nanoscale* **2012**, *4*, 1553–1556.

Article

Synthesis and Characterization of Tungsten Suboxide W_nO_{3n-1} Nanotiles

Luka Pirker [1,†] , Bojana Višić [1,2,*,†] , Janez Kovač [1] , Srečo D. Škapin [1] and Maja Remškar [1,3]

1   Jožef Stefan Institute, Jamova Cesta 39, 1000 Ljubljana, Slovenia; luka.pirker@ijs.si (L.P.);
janez.kovac@ijs.si (J.K.); sreco.skapin@ijs.si (S.D.Š.); maja.remskar@ijs.si (M.R.)
2   Institute of Physics Belgrade, University of Belgrade, Pregrevica 118, 11080 Belgrade, Serbia
3   Faculty for Mathematics and Physics, University of Ljubljana, Jadranska Ulica 19, 1000 Ljubljana, Slovenia
*   Correspondence: bojana.visic@ipb.ac.rs
†   These authors contributed equally.

Abstract: W_nO_{3n-1} nanotiles, with multiple stoichiometries within one nanotile, were synthesized via the chemical vapour transport method. They grow along the [010] crystallographic axis, with the thickness ranging from a few tens to a few hundreds of nm, with the lateral size up to several μm. Distinct surface corrugations, up to a few 10 nm deep appear during growth. The $\{102\}_r$ crystallographic shear planes indicate the W_nO_{3n-1} stoichiometries. Within a single nanotile, six stoichiometries were detected, namely $W_{16}O_{47}$ ($WO_{2.938}$), $W_{15}O_{44}$ ($WO_{2.933}$), $W_{14}O_{41}$ ($WO_{2.928}$), $W_{13}O_{38}$ ($WO_{2.923}$), $W_{12}O_{35}$ ($WO_{2.917}$), and $W_{11}O_{32}$ ($WO_{2.909}$), with the last three never being reported before. The existence of oxygen vacancies within the crystallographic shear planes resulted in the observed non-zero density of states at the Fermi energy.

Keywords: tungsten oxides; nanotiles; nanomaterials

1. Introduction

In the family of transition metal oxide materials, semiconducting WO_3 is among the most studied, due to its promising practical applications. It has already been successfully used as a catalyst for water splitting [1], in gas/temperature sensors [2,3], in optoelectronics [4], or as a component in supercapacitors [5]. The crystal structure of WO_3 is usually described in terms of corner-sharing WO_6 octahedra. The structure can differ from the ideal cubic ReO_3 type structure due to different tilting angles, displacement of the W cation, and rotation of WO_6 octahedra. Its phase transitions have been thoroughly studied [6–9], and various nanometre-sized particles, nanowires and flakes were synthesized [10,11].

The sub-stoichiometric tungsten oxide phases, WO_{3-x}, with $0 < x < 1$, provide the opportunity to synthesize and study nanoparticles with great variety of shapes, sizes and physical properties. According to the literature, for $x \leq 0.2$, the WO_{3-x} crystallize into phases with the chemical formula W_nO_{3n-1} or W_nO_{3n-2}, which are often referred to as Magnéli phases [12,13]. The W_nO_{3n-1} stoichiometry crystallizes in the P2/a symmetry with a monoclinic unit cell containing two W_nO_{3n-1} moieties, while the W_nO_{3n-2} crystallizes in the P2/m symmetry in a monoclinic unit cell with one W_nO_{3n-2} moiety. The oxygen deficiency present in WO_{3-x} is compensated with the formation of crystallographic shear (CS) planes, where some of the corner-sharing WO_6 octahedra become edge-sharing. In W_nO_{3n-1} structures, four WO_6 octahedra are joined by edges, while in W_nO_{3n-2} the number of these octahedra is six. With further reduction ($x > 0.2$), edge and face-sharing WO_6 octahedra emerge, forming pentagonal columns and hexagonal tunnels [14]. The crystal structures of these materials are found to be orthorhombic for $W_{32}O_{84}$ and W_3O_8, monoclinic for $W_{18}O_{49}$, $W_{17}O_{47}$, $W_{20}O_{58}$, and $W_{25}O_{73}$, and tetragonal for W_5O_{14} [15]. These varieties stem from different oxygen deficiencies within the nanostructures [16,17].

Here, we report on new tungsten suboxide nanostructures crystallized in the form of nanotiles. The nanotiles are composed of different W_nO_{3n-1} stoichiometries, three of which were observed for the first time. High-resolution transmission electron microscopy (HRTEM), scanning electron miscroscopy (SEM), X-ray diffraction (XRD), Raman spectroscopy, X-ray photoelectron spectroscopy (XPS) and atomic force microscopy (AFM) were used to characterize the nanotiles.

2. Materials and Methods

2.1. Synthesis

The nanotiles were synthesized via the chemical vapour transport reaction (CVT). Iodine was used as the transport agent and nickel as the growth promoter. Quartz ampules were filled with 352.7 mg of WO_3 powder (Sigma-Aldrich, St. Louis, MO, USA, 99.99%), 37.5 mg of nickel (metal foil) and 562 mg of iodine (1–3 mm beads, Sigma-Aldrich, St. Louis, MO, USA, 99.7%). Ampules were evacuated down to 10^{-5} mbar, and the transport reaction was running for 500 h. The material was transported from hot zone of the furnace (1133K) to the growth zone (1009K).

2.2. X-ray Diffraction

X-ray diffraction (XRD) was performed using a D4 Endeavor diffractometer (Bruker AXS GmbH, Karlsruhe, Germany) at room temperature. A quartz monochromator Cu Ka1 radiation source (λ = 0.1541 nm) and a Sol-X energy dispersive detector were used. The angular range (2ϑ) was in the range from $10°$ to $70°$, with a step size of $0.02°$ and collection time of 4 s.

2.3. Raman Spectroscopy

Raman spectra of the nanotiles were recorded by an Alpha300 R (WITec, Ulm, Germany) confocal Raman imaging system. Measurements were performed in backscattered geometry using a frequency doubled Nd:YAG laser (532 nm). The laser power was kept under 5 mW for standard measurements (to prevent oxidation and damage of the material). For laser power dependence studies, the power was varied from 0.06 mW to 24.7 mW. The sample was dispersed in ethanol and drop-casted on a chromium plate as a substrate with a featureless Raman spectrum.

2.4. Scanning Electron Microscopy

Scanning electron microscopy (SEM) images and cross-sections of the samples for TEM analysis were obtained using a Helios NanoLab 650 (Thermo Fisher, Waltham, MA, USA) Focused Ion Beam-scanning electron microscope (FIB). The nanotiles were drop-casted on a silicon wafer for SEM studies.

2.5. High-Resolution Transmission Electron Microscopy and Electron Diffraction

High-resolution transmission electron microscopy (HRTEM) and electron diffraction (ED) images were acquired using a Cs probe-corrected TEM/STEM JEOL ARM 200CF (JEOL, Peabody, MA, USA) microscope equipped with a cold-FEG electron source, operating at 200 kV. Distances between atomic columns and angles between their rows were measured using Digital Micrograph software. An accuracy of 0.04 Å in distance and $0.5°$ in angle was achieved. All HRTEM images were filtered using the Average Background Subtraction Filter method described in [18].

2.6. Atomic Force Microscopy

Atomic force microscopy (AFM) in contact mode was performed with an Omicron UHV VT-AFM (Scienta Omicron, Taunusstein, Germany) operating at 10^{-9} mbar. Silicon Cantilevers CSG10 (NT-MDT, Moscow, Russia) with a typical force constant of 0.11 N/m were used.

2.7. X-ray Photoelectron Spectroscopy

X-ray photoelectron spectroscopy XPS analysis was carried out on the PHI-TFA XPS spectrometer produced by Physical Electronics, Chanhassen, MN, USA. Samples were mounted on the metallic sample holder and introduced in ultra-high vacuum spectrometer. The vacuum during the XPS analyses was in the range of 10^{-9} mbar. The analysed area was 0.4 mm in diameter and the analysed depth was about 3–5 nm. Sample surfaces were excited by X-ray radiation from monochromatic Al source at photon energy of 1486.6 eV. The high-energy resolution spectra were acquired with energy analyser operating at resolution of about 0.6 eV and pass energy of 29 eV. The accuracy of binding energies was about ± 0.2 eV. Three places on every sample were analysed. High resolution spectra were fitted with Gauss-Lorentz functions and Shirley function was used for background removal. For the XPS measurements, the ethanol suspension of nanotiles was deposited on an oxidized Si wafer, dried at room temperature and inserted into ultra-high vacuum of the spectrometer.

### 3. Results

3.1. Electron Microscopy

The nanotiles, depicted in Figure 1, grow on the ampule walls in the form of a blue powder. A single nanotile usually grows in a rectangular shape, a few micrometres in width and up to 10 μm in length, as shown in Figure 1. The thickness of the nanotiles varies from a few 10 nm up to a few 100 nm, as seen in Figure S1 and Figure 1. They have distinct corrugations, which can be up to a few 10 nm deep, as seen in Figure 2. To determine the structure of the nanotiles, two cross-section lamellas perpendicular and parallel to the corrugations were prepared for further TEM analysis, as shown in Figure 1a.
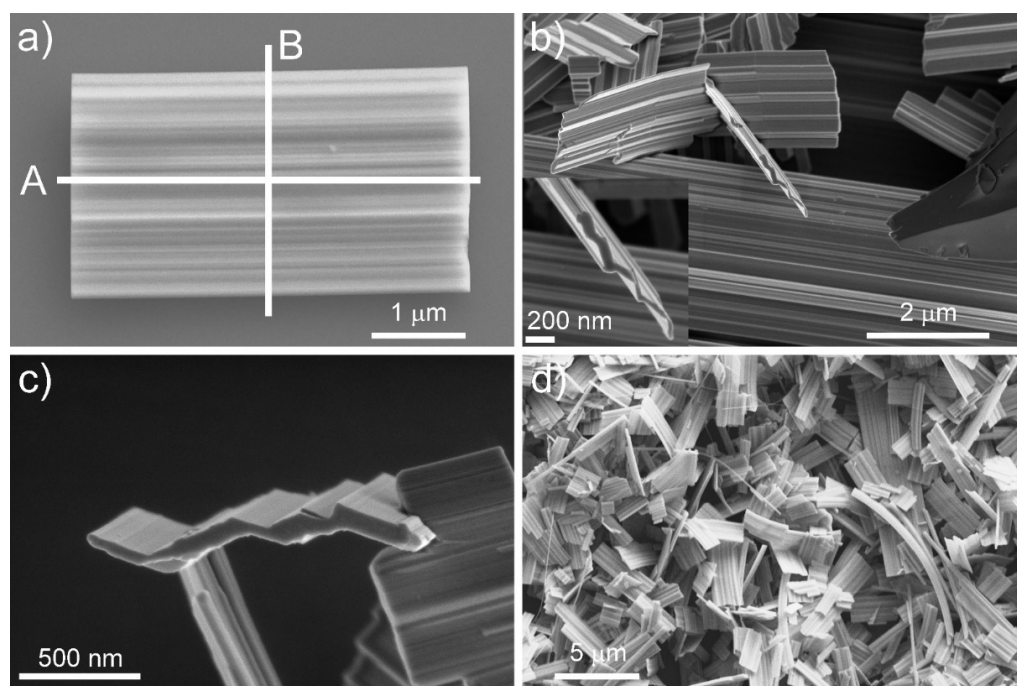

Figure 1. (**a**) A single nanotile, with lines A and B representing the direction of the cross-sections for the TEM lamellas; (**b**–**d**) SEM images of different nanotiles.

An HRTEM image of the cross-section lamella B is shown in Figure 3a and Figure S2. Figure 3a was taken along the [010] direction, and was used to determine the stoichiometry of the nanotiles. The parallel contrast lines are crystallographic shear (CS) planes, which are characteristic for W_nO_{3n-1} and W_nO_{3n-2} phases. Only $\{102\}_r$ CS planes were observed, indicating that only W_nO_{3n-1} structures grow inside the nanotiles [12,19]. Six stoichiometries were determined by measuring the unit cell parameters *a*, *c*, and β: $W_{16}O_{47}$ ($WO_{2.938}$),

$W_{15}O_{44}$ ($WO_{2.933}$), $W_{14}O_{41}$ ($WO_{2.928}$), $W_{13}O_{38}$ ($WO_{2.923}$), $W_{12}O_{35}$ ($WO_{2.917}$), and $W_{11}O_{32}$ ($WO_{2.909}$), of which the last three were not experimentally observed to date [20]. The unit cell parameters *a*, *c*, and β of the observed phases are presented in Table 1. The *a* axis is oriented along the CS planes, while the *c* axis is directed towards the CS plane at the angle β, relative to axis *a*. An electron diffraction was performed on lamella A, Figure 3b. The reflections (010), $(40\bar{3})$ and $(41\bar{3})$ correspond to interlayer distances of 3.79 Å, 3.56 Å, and 2.61 Å, respectively. The first estimation of the unit cell parameter *b* was determined from the (010) reflection with the value of 3.79 Å. The second value for *b* (3.86 Å) was determined from the average distance between the tungsten atoms that are not part of the CS planes. The mean value of the unit cell parameter *b* is 3.83 Å. The theoretical tungsten atom positions and unit cell parameters for the newly observed phases were calculated using the model proposed in ref. [12]. The parameters d and e used in the model were determined from the HRTEM and electron diffraction images and are schematically shown in Figure S3: (i) interatomic distance between tungsten atoms that are not part of the CS plane that should equal unit cell parameter *b* (d = 3.83 Å); (ii) interatomic distance between tungsten atoms that are part of the CS plane, where the tungsten octahedra are joined by edges (e = 2.92 Å). The experimental unit cell parameters are in good agreement with the calculated ones. The unit cells are schematically drawn on the HRTEM and simulated structure images and are shown in Figure 4.
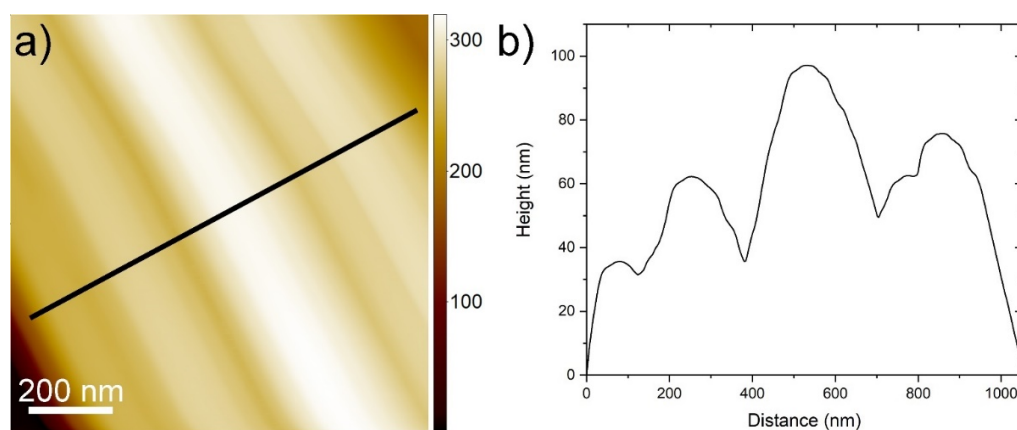

Figure 2. (**a**) An AFM image of a nanotile with a line profile showing corrugations in (**b**).
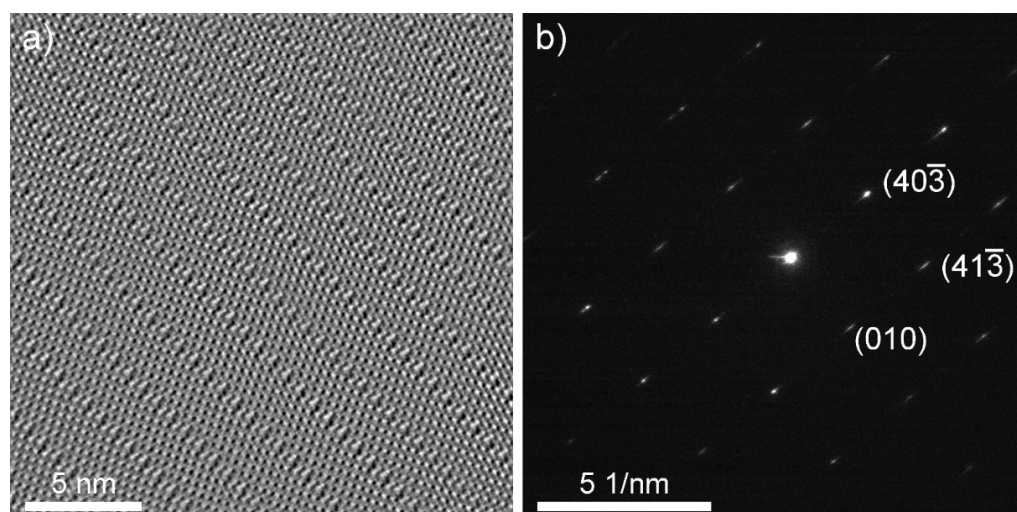
Figure 3. (**a**) HRTEM image along the [010] direction (lamella B). (**b**) An electron diffraction of the [304] zone (lamella A).

Table 1. Measured and calculated unit cell parameters for observed phases.

Structure	Measured				Calculated			
	a (Å)	b (Å)	c (Å)	β (°)	a (Å)	b (Å)	c (Å)	β (°)
$W_{11}O_{32}$	17.3	3.83	18.9	79.3	17.1	>3.83	19.2	72.2
$W_{12}O_{35}$	17.3	3.83	20.2	89.6	17.1	>3.83	20.0	87.9
$W_{13}O_{38}$	17.3	3.83	22.5	103.7	17.1	>3.83	22.1	101.5
$W_{14}O_{41}$	17.3	3.83	24.5	74.2	17.1	>3.83	24.6	72.0
$W_{15}O_{43}$	17.3	3.83	25.6	88.0	17.1	>3.83	25.2	84.4
$W_{16}O_{47}$	17.3	3.83	27.5	98.3	17.1	>3.83	26.9	95.7
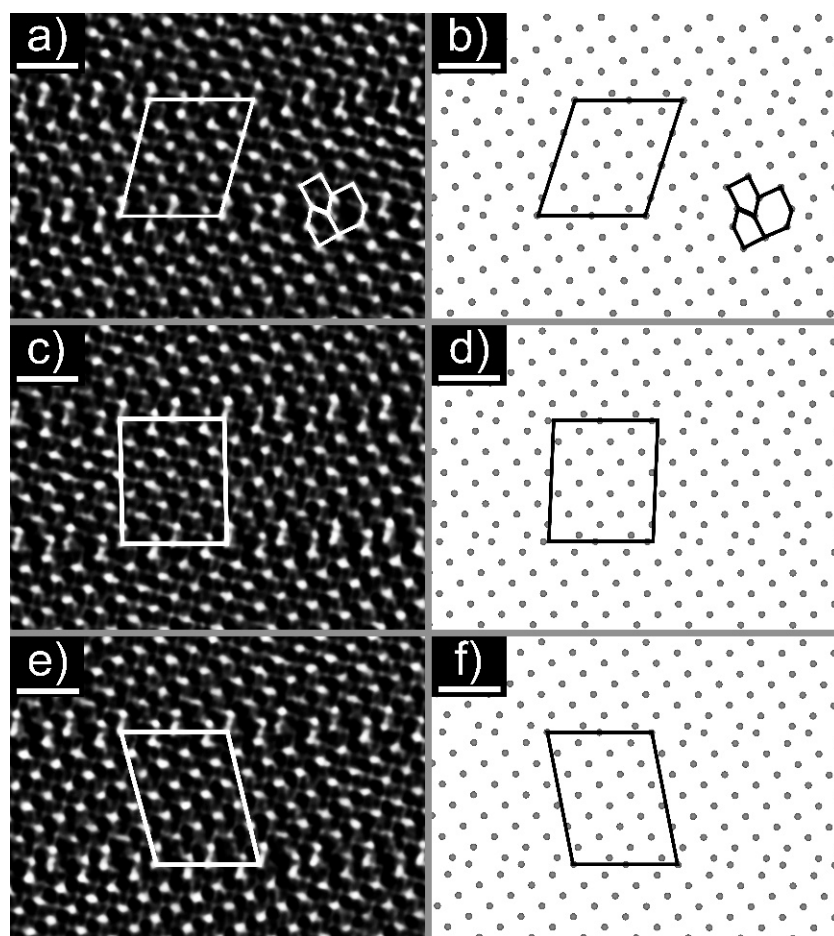
Figure 4. HRTEM images of: (**a**) $W_{11}O_{32}$, (**c**) $W_{12}O_{35}$, and (**e**) $W_{13}O_{38}$ with the proposed unit cell. The scale bar is 1 nm. Simulated structures of: (**b**) $W_{11}O_{32}$, (**d**) $W_{12}O_{35}$, and (**f**) $W_{13}O_{38}$ with the proposed unit cell.

3.2. X-ray Diffraction

The XRD pattern of the nanotiles is shown in Figure 5. Due to their multi-stoichiometric structure, the XRD pattern is composed of diffraction lines corresponding to all tungsten suboxide phases present in the nanotiles. The low-angle diffraction lines were used to determine the most prominent phase, as they are different for each stoichiometry and do not overlap with the m-WO_3 phase. The measured diffractogram had the best match with the $W_{14}O_{41}$ ($WO_{2.928}$) stoichiometry, indicating that this is the phase the majority of the nanotiles crystallize in. The position of the diffraction lines, their relative intensities and the assigned (hkl) indices, are presented in Table 2. Additionally, the (010) line closely matches with the *b* unit cell parameter obtained from the HRTEM images. In Figure 5, the measured XRD pattern is compared to the m-WO_3 one (PDF2: 01-072-1465).
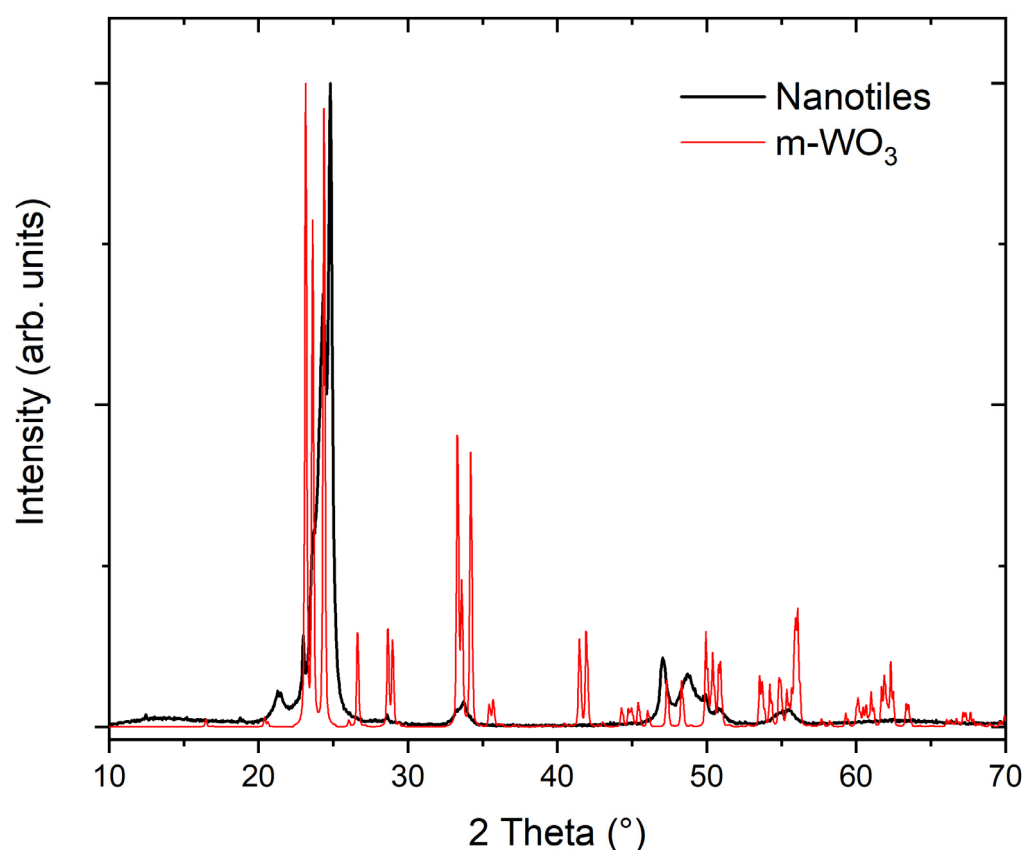
Figure 5. XRD pattern of the WO_{3-x} nanotiles and of m-WO_3 (PDF2: 01-072-1465).

Table 2. Measured XRD diffraction lines (positions in ° and Å) and their relative intensities compared with the calculated d values using parameters obtained from HRTEM images and the assigned (hkl) indices.

	Measured		Theoretical $W_{14}O_{41}$	
2 Theta (°)	d (Å)	Rel. Int.	Assigned Index (hkl)	d (Å)
12.5	7.08	0.02	$(20\bar{3})$	7.04
18.8	4.70	0.01	(005)	4.68
21.5	4.13	0.05	(403)	4.17
23.2	3.84	0.14	(010)	3.83
23.9	3.73	0.30	(110)	3.73
24.5	3.63	0.66	(112)	3.63
25.0	3.56	1.00	$(40\bar{2})$	3.52
28.9	3.09	0.02	(407)	3.09
34.2	2.62	0.04	$(21\bar{5})$	2.62
48.5	1.88	0.10	$(71\bar{2})$	1.88
50.3	1.81	0.08	(322)	1.81
52.7	1.74	0.03	$(12\bar{5})$	1.74
57.6	1.60	0.02	$(52\bar{2})$	1.60

3.3. X-ray Photoelectron Spectroscopy

Figure 6 shows the W 4f and O 2p spectra, the survey spectrum, and the valence band spectrum of the nanotiles. The energy distribution of W 4f core levels is presented in Figure 6a. The spectrum can be deconvoluted into two doublets, with the additional fifth component (around 41.1 eV) corresponding to the W 5p photoelectrons. The main peaks, representing 84% of total W 4f, appear at 35.5 and 37.6 eV, corresponding to $4f_{7/2}$ and $4f_{5/2}$, respectively, of W in 6+ oxidation state [21]. The remaining 16% are attributed to a doublet positioned at 34.3 and 36.4 eV of the $4f_{7/2}$ and $4f_{5/2}$ of W in 5+ oxidation

states [22,23]. We can disregard the presence of WO_2 in the nanotiles, as there are no peaks corresponding to 4 + oxidation states (doublets at 33.3 and 35.5 eV) or metallic tungsten (31.2 and 33.4 eV) [24,25].
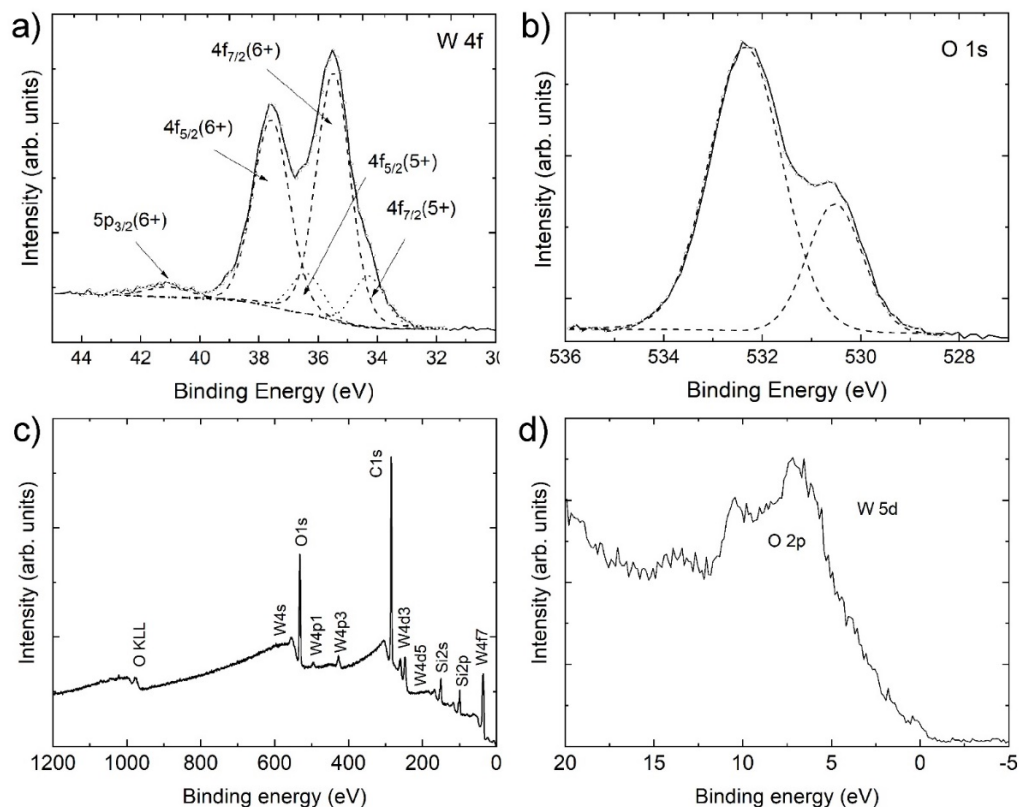

Figure 6. XPS spectra of the nanotiles: (**a**) the W 4f spectrum; (**b**) the O 1s spectrum; (**c**) XPS survey spectrum; and (**d**) the valence band spectrum.

The oxygen O 1s spectrum can be deconvoluted into two peaks, as shown in Figure 6b. Peak at 530.5 eV, attributing 26% to the O 1s photoelectrons, corresponds to O^{2-} bonded to W^{6+} in WO_3 [26]. Peak at 532.3 eV may correspond to oxygen O^{2-} bonded to SiO_2 (substrate), C-O bonds or lower oxidation states of O in W-O bonds. The survey spectrum presented in Figure 6c shows no impurities other than carbon, while the silicon peaks arise due to the SiO_2 substrate. The valence band spectrum presented in Figure 6d shows a broad O 2p peak with non-negligible density of states at the Fermi energy.

3.4. Raman Spectroscopy

Raman spectra of the nanotiles are shown in Figure 7a. The spectra were taken with the laser polarisation parallel and perpendicular to the corrugations (i.e., *b* axis). The peak positions and their normalized intensities are presented in Table 3. The Raman spectrum of the nanotiles with the polarisation parallel to the *b* axis reveals six peaks at 136.5, 322.5, 341.5, 426.5, 722, and 810 cm^{-1}. The peak at 136.5 cm^{-1} is attributed to the relative translational or rotational motions of WO_6 octahedral units in the same unit cell (lattice modes), the 322.5, 341.5, and 426.5 peaks to the W-O-W bending modes, while the 722 and 810 cm^{-1} peaks are attributed to the W-O stretching modes [7,27]. On the other hand, Raman spectrum of the nanotiles with the polarisation perpendicular to the *b* axis has nine peaks at 136, 180, 232.5, 271.5, 331.5, 367, 428, 702, and 810 cm^{-1}. In both cases the 810 cm^{-1} peak is the most intense one. The dependency of the Raman spectra on orientation is a direct evidence of material anisotropy. Similarly to the previously reported spectra, [20] the spectrum where the polarisation is parallel to the *b* axis has sharper and more pronounced peaks, pointing to a crystal structure with fewer defects and a higher

number of W-O bonds with well-defined lengths. The Raman spectrum recorded with the polarisation perpendicularly to the *b* axis has a greater number of peaks in the lattice (<200 cm^{-1}) and bending mode (200–400 cm^{-1}) region, while the peaks associated with W-O stretching modes (600–900 cm^{-1}) are broader, indicating that multiple bond lengths are present [27,28]. The spectra of the nanotiles are compared with the precursor WO_3 powder, with the most prominent peaks at 72, 135, 273, 372, 716, and 807 cm^{-1}. These peaks match the monoclinic γ-phase with the space group $P2_1/n$, and the total of 48 Raman active modes [29]. Compared with the m-WO_3 spectrum, the most intense peak at 810 cm^{-1} is slightly red-shifted towards longer wavelengths with regard to the 807 cm^{-1} in m-WO_3, indicating slightly shorter bonds [7,30]. The peaks at 702 and 428 cm^{-1} are blue-shifted, indicating slightly longer bonds (i.e., shorter wavelengths) compared to the m-WO_3 peaks situated at 715 cm^{-1} and 434 cm^{-1}, respectively.
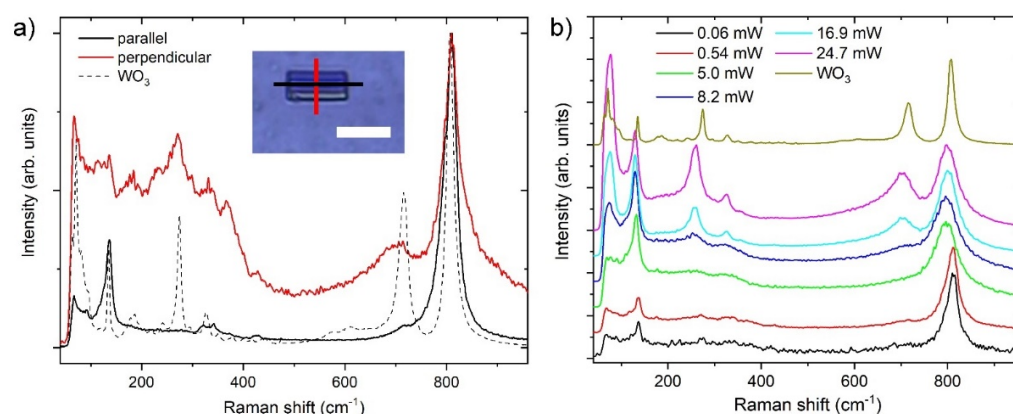
Figure 7. (a) Raman spectra of the WO_{3-x} nanotiles taken parallel and perpendicular to the corrugations, and of m-WO_3 (dashed line). Inset shows an optical image of the nanotile with the red and black line representing the direction of the laser polarisation. **(b)** Power dependency of the Raman spectra.

Table 3. Raman peak position and normalized intensity of the nanotiles and WO_3.

Modes	Parallel Raman Shift	Int	Perpendicular Raman Shift	Int	WO$_3$ Powder Raman Shift	Int
					71	0.65
Lattice modes	136.5	0.26	136	0.14	135	0.29
			180	0.09	186.5	0.06
			232.5	Sh	241	0.03
W-O bending			271.5	0.19	273	0.41
	322.5	0.02	331.5	0.12	327	0.07
	341.5	0.03	367	0.05	350	0.02
					417	0.01
	426.5	0.01	428	0.02	437	0.01
W-O stretching	722	sh	702	0.17	716	0.49
	810	1.00	810	1.00	807	1.00

As these materials tend to be oxidized or damaged under the laser irradiation in ambient conditions, a stepwise laser power dependency measurement was performed. The powers at which the sample underwent change and damage can be easily inferred from the spectra shown in Figure 7b. The spectra in the power range between 0.06 and 0.54 mW are indistinguishable, while at 5 mW the 810 cm^{-1} peak shifts to 798 cm^{-1} and becomes broader, the 136 cm^{-1} peak becomes more intense and shifts to 130 cm^{-1}, and the shoulders between 200 and 400 cm^{-1} become more prominent. At this point the sample remains visually undamaged, as concluded from its optical image. The power of 8.2 mW marks the start of the sample damage. This is accompanied with the peak at 130 cm^{-1} becoming the

most prominent, the appearance of a new peak at 73 cm^{-1}, and a shoulder appears around 710 cm^{-1}. At 16.9 mW, the spectrum becomes very similar to that of the WO$_3$ precursor, marking the complete oxidation of the nanotile due to the heating in ambient oxygen. This is evidenced by a clear appearance of the peak at 702 cm^{-1}, albeit blue-shifted and broader (716 cm^{-1} for m-WO$_3$). The two shoulders between 200 and 400 cm^{-1} transform into peaks at 258 and 325 cm^{-1} (274 and 327 cm^{-1} for m-WO$_3$). Additionally, the peak at 76 cm^{-1} becomes the most intense one. For higher laser powers, no other new peaks appear.

4. Discussion

The reported nanotiles are composed of multiple W$_n$O$_{3n-1}$ phases, with three of those not observed to date. As previously reported, the multiphase nature of a single nanotile could stabilize the W$_n$O$_{3n-1}$ phases [20]. In our previous report, the similar multi-stoichiometric platelets had a flat, corrugation-free surface, while the nanotiles have distinct corrugations with tens of nm in depth. The change in the morphology could be explained with a slightly different overall stoichiometry. Another reason for this change may be because the nanotiles did not have a template from which to grow, while the platelets grew epitaxially from a nanowire [20]. Similar corrugations are also present in other tungsten suboxides [31–33] and could contribute to the stabilization of different phases. It is presumed that the nanotiles grow faster along the [010] crystallographic axis (along the corrugations), as the length of the nanotiles varies, while the width is remaining quite uniform.

The XRD pattern of the nanotiles differs from a typical XRD pattern of the m-WO$_3$ especially in the low-angle region. Due to the P2/a symmetry of the W$_n$O$_{3n-1}$ stoichiometries, only (2n,0,l) and (2n,0,0) diffraction lines should be visible [12]. At approximately 2θ > 30°, diffraction lines from W$_n$O$_{3n-1}$ and m-WO$_3$ overlap and thus cannot be used to determine the structure or the stoichiometry.

The valence band spectrum shows some density of states at the Fermi energy. The near-Fermi bands are formed due to 5d- and W 6s-like states taking part in the formation of the shortened W-W bonds [34] or due to trap states created by defects [35]. This could indicate a slightly metallic behaviour at room temperature, instead of a semiconducting one. DFT calculation on similar stoichiometries shows that the 5d-orbitals of tungsten atoms, which are part of the CS planes, are responsible for the conductivity and other effects related to the states near the Fermi surface [17,36].

The Raman spectra of the nanotiles have peaks of similar shape and position to those from the literature [20]. The spectra taken at the polarisation along the *b* axis have fewer peaks in the lattice and bending mode region than when the polarisation is perpendicular to the *b* axis. Compared to some other Raman spectra of WO$_{3-x}$ nanomaterials [24,37,38], our spectra show narrower peaks, pointing to a higher degree of crystallinity. When the laser power is increased, the nanotiles oxidize to m-WO$_3$ [24,37].

Due to the intrinsic oxygen vacancies and formation of CS planes, the electronic and optical properties of tungsten suboxides differ from m-WO$_3$. Such properties may provide an advantage in applications such as water splitting [39], near-infrared shielding [40], in anode materials for high-performance Li-ion batteries [41], field-effect-transistors [42], photocatalysis [43], and in-domain boundary engineering [44]. As it was shown [35], sub-stoichiometric WO$_{3-x}$ nanosheets can be used as physisorption-based NO$_2$ sensors. A slight difference in the stoichiometry can change the WO$_{3-x}$ materials from a semiconductor to a metal, which can result in a poorer performance of such sensors. As pristine WO$_3$ does not have a high photocatalytic activity, introducing oxygen vacancies and/or using lower dimensional WO$_{3-x}$ can improve its performance. In several studies [45,46], the WO$_{3-x}$ materials outperformed pristine WO$_3$ in the degradation of dyes such as methylene blue, congo red, and rhodamine B. The oxygen vacancies act as electron donors, increasing the charge transport and thus enhancing the photocatalytic activity. Sub-stoichiometric materials also outperform m-WO$_3$ when it comes to water splitting [47]. By annealing the samples under different atmospheres, the number and nature of oxygen vacancies were

altered. It was concluded that the moderate concentration of oxygen vacancies results in appearance of W^{5+} shallow donor states that increase photoactivity, while the deep trap W^{4+} states have a detrimental effect on photocurrent. Being able to determine the stoichiometry and with it the electrical and optical properties of WO_{3-x} nanomaterials offers new opportunities for a wide range of applications.

5. Conclusions

Multi-stoichiometric nanotiles were synthesized using the CVT method. The thickness of the nanotiles ranged from a few 10 to a few 100 nm, and they grew up to a few μm in the lateral size. The formation of $\{102\}_r$ CS planes indicates, that only W_nO_{3n-1} phases grow inside the nanotiles. Three new stoichiometries were identified from HRTEM images: $W_{13}O_{38}$ ($WO_{2.923}$), $W_{12}O_{35}$ ($WO_{2.917}$), and $W_{11}O_{32}$ ($WO_{2.909}$). Measured unit cell parameters agreed well with the calculated ones. The valence band spectrum showed some density of states at the Fermi energy, making the material slightly metallic. Obtained Raman spectra showed multiple peaks and are direct evidence of the material anisotropy. Increasing the laser power during Raman spectroscopy promoted the oxidation of the platelets into m-WO_3.

References

1. Sayama, K.; Kazuaki, M.; Ryu, A.; Yoshimoto, A.; Hironori, A. Stoichiometric water splitting into H_2 and O_2 using a mixture of two different photocatalysts and an IO_3^-/I^- shuttle redox mediator under visible light irradiation. *Chem. Comm.* **2001**, *23*, 2416–2417. [CrossRef]
2. Ho, J. Novel nitrogen monoxides (NO) gas sensors integrated with tungsten trioxide (WO_3)/pin structure for room temperature operation. *Solid-State Electron.* **2003**, *47*, 827–830. [CrossRef]
3. Reyes, L.F.; Hoel, A.; Saukko, S.; Heszler, P.; Lantto, V.; Granqvist, C.G. Gas sensor response of pure and activated WO_3 nanoparticle films made by advanced reactive gas deposition. *Sens. Actuators B Chem.* **2006**, *117*, 128–134. [CrossRef]
4. Hai, Z.; Wei, Z.; Xue, C.; Xu, H.; Verpoort, F. Nanostructured tungsten oxide thin film devices: From optoelectronics and ionics to iontronics. *J. Mater. Chem.* **2019**, *7*, 12968–12990. [CrossRef]
5. Thind, S.S.; Chang, X.; Wentzell, J.S.; Chen, A. High-performance based supercapacitor on tantalum iridium oxides supported on tungsten oxide nanoplatelets. *Electrochem. Commun.* **2016**, *67*, 1–5. [CrossRef]
6. Cazzanelli, E.; Vinegoni, C.; Mariotto, G.; Kuzmin, A.; Purans, J. Low-Temperature Polymorphism in Tungsten Trioxide Powders and Its Dependence on Mechanical Treatments. *J. Solid State Chem.* **1999**, *143*, 24–32. [CrossRef]
7. Daniel, M.F.; Desbat, B.; Lassegues, J.C.; Gerand, B.; Figlarz, M. Infrared and raman study of WO_3 tungsten trioxides and WO_3, xH_2O tungsten trioxide tydrates. *J. Solid State Chem.* **1987**, *67*, 235–247. [CrossRef]
8. Filipescu, M.; Ion, V.; Colceag, D.; Ossi, P.M.; Dinescu, M. Growth and characterizations of nanostructured tungsten oxides. *Rom. Rep. Phys.* **2012**, *64*, 1213–1225.

9. Salje, E. Lattice Dynamics of WO3. *Acta Crystallogr. Sect. A Cryst. Phys. Diffr. Theor. Gen. Crystallogr.* **1975**, *31*, 360–363. [CrossRef]
10. Li, X.L.; Liu, J.F.; Li, Y.D. Large-scale synthesis of tungsten oxide nanowires with high aspect ratio. *Inorg. Chem.* **2003**, *42*, 921–924. [CrossRef]
11. Hariharan, V.; Gnanavel, B.; Sathiyapriya, R.; Aroulmoji, V. A review on tungsten oxide (WO3) and their derivatives for sensor applications. *Int. J. Adv. Sci. Eng* **2019**, *5*, 1163–1168. [CrossRef]
12. Magnéli, A. Structures of the ReO3-type with recurrent dislocations of atoms:homologous series' of molybdenum and tungsten oxides. *Acta Crystallogr.* **1953**, *6*, 495–500. [CrossRef]
13. Pickering, R.; Tilley, R.J.D. An electron microscpe study of tungsten oxides in the composition range WO2.90–WO2.72. *J. Solid State Chem.* **1976**, *16*, 247–255. [CrossRef]
14. Lundberg, M.; Sundberg, M.; Magnéli, A. The "Pentagonal Column" as a building unit in crystal and defect structures of some groups of transition metal compounds. *J. Solid State Chem.* **1982**, *44*, 32–40. [CrossRef]
15. Migas, D.B.; Shaposhnikov, V.L.; Rodin, V.N.; Borisenko, V.E. Tungsten oxides. I. Effects of oxygen vacancies and doping on electronic and optical properties of different phases of WO3. *J. Appl. Phys.* **2010**, *108*, 093713. [CrossRef]
16. Frey, G.L.; Rothschild, A.; Sloan, J.; Rosentsveig, R.; Popovitz-Biro, R.; Tenne, R. Investigations of nonstoichiometric tungsten oxide nanoparticles. *J. Solid State Chem.* **2001**, *162*, 300–314. [CrossRef]
17. Migas, D.B.; Shaposhnikov, V.L.; Borisenko, V.E. Tungsten oxides. II The metallic nature of Magnéli phases. *J. Appl. Phys.* **2010**, *108*, 093714. [CrossRef]
18. Kilaas, R. Optimal and near-optimal filters in high-resolution electron microscopy. *J. Microsc.* **1998**, *190*, 45–51. [CrossRef]
19. Bursill, L.A.; Hyde, B.G. CS Families drived from the ReO3 structure type: An electron microscope study of reduced WO3 and related pseudobinary systems. *J. Solid State Chem.* **1972**, *14*, 430–446. [CrossRef]
20. Pirker, L.; Višić, B.; Škapin, S.D.; Dražić, G.; Kovač, J.; Remškar, M. Multi-stoichiometric quasi-two-dimensional W_nO_{3n-1} tungsten oxides. *Nanoscale* **2020**, *212*, 15102–15114. [CrossRef]
21. Leftheriotis, G.; Papaefthimiou, S.; Yianoulis, P.; Siokou, A.; Kefalas, D. Structural and electrochemical properties of opaque sol–gel deposited WO3 layers. *Appl. Surf. Sci.* **2003**, *218*, 276–281. [CrossRef]
22. Katoh, M.; Takeda, Y. Chemical state analysis of tungsten and tungsten oxides using an electron probe microanalyzer. *Jpn. J. Appl. Phys.* **2004**, *43*, 7292. [CrossRef]
23. Zhang, C.; Boudiba, A.; Navio, C.; Bittencourt, C.; Olivier, M.G.; Snyders, R.; Debliquy, M. Highly sensitive hydrogen sensors based on co-sputtered platinum-activated tungsten oxide films. *Int. J. Hydrogen Energy* **2011**, *36*, 1107–1114. [CrossRef]
24. Lu, D.Y.; Chen, J.; Zhou, J.; Deng, S.Z.; Xu, N.S.; Xu, J.B. Raman spectroscopic study of oxidation and phase transition in W18O49 Nanowires. *J. Raman Spectrosc.* **2007**, *38*, 176–180. [CrossRef]
25. Remškar, M.; Kovac, J.; Viršek, M.; Mrak, M.; Jesih, A.; Seabaugh, A. W5O14 nanowires. *Adv. Funct. Mater.* **2007**, *17*, 1974–1978. [CrossRef]
26. Trapatseli, M.; Vernardou, D.; Tzanetakis, P.; Spanakis, E. Field emission properties of low-temperature, hydrothermally grown tungsten oxide. *ACS Appl. Mater. Interfaces* **2011**, *3*, 2726–2731. [CrossRef] [PubMed]
27. Hardcastle, F.D.; Wachs, I.E. Determination of the molecular structures of tungstates by raman spectroscopy. *J. Raman Spectrosc.* **1995**, *26*, 397–405. [CrossRef]
28. Gonzalez-Calbet, J.M.; Rosique-Perez, C.; Vallet-Regi, M.; Alario-Franco, M.A.; Rodríguez-Carvajal, J. Lithium insertion in reduced tungsten oxides. *Solid State Ionics* **1989**, *32*, 162–166. [CrossRef]
29. Woodward, P.M.; Sleight, A.W.; Vogt, T. Structure refinement of triclinic tungsten trioxide. *J.Phys. Chem. Solids* **1995**, *56*, 1305–1315. [CrossRef]
30. Thummavichai, K.; Wang, N.; Xu, F.; Rance, G.; Xia, Y.; Zhu, Y. In situ investigations of the phase change behaviour of tungsten oxide nanostructures. *R. Soc. Open Sci.* **2018**, *5*, 171932. [CrossRef]
31. Saqib, M.; Jelenc, J.; Pirker, L.; Škapin, S.D.; De Pietro, L.; Ramsperger, U.; Knápek, A.; Müllerová, I.; Remškar, M. Field emission properties of single crystalline W5O14 and W18O49 nanowires. *J. Electron. Spectros. Relat. Phenom.* **2020**, *241*, 146837. [CrossRef]
32. Zhang, Z.; Sheng, L.; Chen, L.; Zhang, Z.; Wang, Y. Atomic-scale observation of pressure-dependent reduction dynamics of W18O49 nanowires in an environmental TEM. *Phys. Chem. Chem.Phys.* **2017**, *19*, 16307. [CrossRef] [PubMed]
33. Merchan-Merchan, W.; Farahani, M.F.; Moorhead-Rosenberg, Z. Electron beam induced formation of tungsten sub-oxide nanorods from flame-formed fragments. *Micron* **2014**, *57*, 23–30. [CrossRef]
34. Khyzhun, O.Y. XPS, XES and XAS studies of the electronic structure of tungsten oxides. *J. Alloys Compd.* **2000**, *305*, 1–6. [CrossRef]
35. Khan, H.; Zavabeti, A.; Wang, Y.; Harrison, C.J.; Carey, B.J.; Mohiuddin, M.; Chrimes, A.F.; De Castro, I.A.; Zhang, B.Y.; Sabri, Y.M.; et al. Quasi physisorptive two dimensional tungsten oxide nanosheets with extraordinary sensitivity and selectivity to NO2. *Nanoscale* **2017**, *9*, 19162–19175. [CrossRef]
36. Korshunov, M.M.; Nekrasov, I.A.; Pavlov, N.S.; Slobodchikov, A.A. Band structure of tungsten oxide W20O58 with ideal octahedra. *JETP Lett.* **2021**, *113*, 57–60. [CrossRef]
37. Chen, J.; Lu, D.; Zhang, W.; Xie, F.; Zhou, J.; Gong, L.; Liu, X.; Deng, S.; Xu, N. Synthesis and raman spectroscopic study of W20O58 nanowires. *J. Phys. D* **2008**, *41*, 115305. [CrossRef]
38. Huang, P.; Kalyar, M.M.A.; Webster, R.F.; Cherns, D.; Ashfold, M.N.R. Tungsten oxide nanorod growth by pulsed laser deposition: Influence of substrate and process conditions. *Nanoscale* **2014**, *6*, 13586–13597. [CrossRef] [PubMed]

39. Lee, Y.-J.; Lee, T.; Soon, A. Phase stability diagrams of group 6 Magnéli oxides and their implications for photon-assisted applications. *Chem. Mater.* **2019**, *31*, 4282–4290. [CrossRef]

40. Zhao, Z.; Bai, Y.; Ning, W.; Fan, J.; Gu, Z.; Chang, H.; Yin, S. Effect of surfactants on the performance of 3D morphology $W_{18}O_{49}$ by solvothermal synthesis. *Appl. Surf. Sci.* **2019**, *471*, 537–544. [CrossRef]

41. Li, Y.; Chang, K.; Tang, H.; Li, B.; Qin, Y.; Hou, Y.; Chang, Z. Preparation of oxygen-deficient WO_{3-x} nanosheets and their characterization as anode materials for high-performance Li-ion batteries. *Electrochim. Acta* **2019**, *298*, 640–649. [CrossRef]

42. Zhuiykov, S. Material characterisation and transistor function of quasi two dimensional sub-stoichiometric WO_{3-x} nanoflakes. *Mater. Lett.* **2016**, *165*, 173–177. [CrossRef]

43. Pan, K.; Shan, K.; Wei, S.; Li, K.; Zhu, J.; Siyal, S.H.; Wu, H.-H. Enhanced photocatalytic performance of WO_{3-x} with oxygen vacancies via heterostructuring. *Compos. Commun.* **2019**, *16*, 106–110. [CrossRef]

44. Salje, E.K.H. Polaronic states and superconductivity in WO_{3-x}. *Condens. Matter* **2020**, *5*, 32. [CrossRef]

45. Chen, S.; Xiao, Y.; Xie, W.; Wang, Y.; Hu, Z.; Zhang, W.; Zhao, H. Facile strategy for synthesizing non-stoichiometric monoclinic structured tungsten trioxide (WO_{3-x}) with plasma resonance absorption and enhanced photocatalytic activity. *Nanomaterials* **2018**, *8*, 553. [CrossRef] [PubMed]

46. Parthibavarman, M.; Karthik, M.; Prabhakaran, S. Facile and one step synthesis of WO_3 nanorods and nanosheets as an efficient photocatalyst and humidity sensing material. *Vaccum* **2018**, *155*, 224–232. [CrossRef]

47. Mohamed, A.M.; Amer, A.W.; AlQaradawi, S.Y.; Allam, N.K. On the nature of defect states in tungstate nanoflake arrays as promising photoanodes in solar fuel cells. *Phys. Chem. Chem. Phys.* **2016**, *18*, 22217–22223. [CrossRef] [PubMed]

Surface Innovations

ice Publishing

Novel nanostructured and antimicrobial PVDF-HFP/PVP/MoO₃ composite

Urška Gradišar Centa MSc
PhD student, Condensed Matter Physics Department, Jožef Stefan Institute, Ljubljana, Slovenia (Orcid:0000-0001-5206-141X) (corresponding author: urska.gradisar@ijs.si)

Meta Sterniša PhD
Teaching Assistant and Researcher, Department of Food Science and Technology, Biotechnical Faculty, University of Ljubljana, Ljubljana, Slovenia (Orcid:0000-0002-2414-3618)

Bojana Višić PhD
Assistant Research Professor, Solid State Physics Department, Institute of Physics Belgrade, Belgrade, Serbia; Center for Solid State Physics and New Materials, Jožef Stefan Institute, Ljubljana, Slovenia (Orcid:0000-0002-2065-0727)

Žiga Federl BSc
Student, Faculty of Mathematics and Physics, University of Ljubljana, Ljubljana, Slovenia

Sonja Smole Možina PhD
Professor, Department of Food Science and Technology, Biotechnical Faculty, University of Ljubljana, Ljubljana, Slovenia (Orcid:0000-0001-7949-8128)

Maja Remškar PhD
Professor, Condensed Matter Physics Department, Jožef Stefan Institute, Ljubljana, Slovenia (Orcid:0000-0002-8919-1768)

Contact surfaces represent a liability for the transmission of microbial contamination, leading to high consumption of detergents and biocides for their care and further increasing the already problematic antimicrobial resistance of microorganisms. This issue could be addressed by the use of antimicrobial nanocomposite coatings. In this research, a polymer nanocomposite of inert poly(vinylidene fluoride-*co*-hexafluoropropylene) (PVDF-HFP) and water-soluble polyvinylpyrrolidone (PVP) polymers with molybdenum trioxide (MoO₃) nanowires (NWs) was designed and characterised for to its surface properties and antimicrobial potential. The nanocomposite has an inhomogeneous structure with a positively charged and hydrophilic surface. The nanofiller reduces the surface roughness, changes the zeta potential from negative to positive, increases the wetting angle and thermal stability of the blend and maintains the polar β-phase in PVDF-HFP. The high specific surface area of the NWs leads to rapid release into water and causes pH decrease, followed by hydrolysis of PVP polymer and formation of carboxyl acid and ammonium salt. The antimicrobial activity of the nanocomposite inactivates both bacteria and fungi, indicating that the novel nanocomposite is a stable nanostructured coating unfavourable for microorganism colonisation. The antimicrobial activity of this nanocomposite is activated by water, which makes it an intriguing candidate for antimicrobial coating of contact surfaces.

Notation

A	surface area of the foils
C	average number of cells counted
D	dilution factor
E	electric field
E^*	elastic modulus
N	number of viable cells per square centimetre of the tested foil
R_a	average surface roughness of the foils
$\tan \delta$	loss tangent
T_s	sample temperature
V	volume of the solution used to wash the foils
ν	measured electrophoretic velocity
ε	electrical permittivity of the electrolytic solution
η	viscosity
ζ	zeta potential

1. Introduction

Contact surfaces pose a risk for the transmission of microbial contamination. Moisture from the air and organic molecules created by frequent contact with hands provides the right environment for microorganisms to colonise, grow and form a biofilm. In order to survive, microorganisms form biofilms that protect them from the negative effects of the environment, including biocides.[1] Antimicrobial coatings are a promising approach to preventing the adhesion and growth of microorganisms on different surfaces in hospitals and other public spaces (e.g. door handles, passenger hand straps on buses, buttons in elevators, handrails of shopping carts, tables in dining rooms and work surfaces in kitchens).[2] Therefore, the development of new surface treatments has become a topic of great interest, and more attention is being paid to the development of antimicrobial coatings.

Various synthetic approaches based on the immobilisation of microbes or the release of antimicrobial substances, such as metal derivatives and nanomaterials, polyammonium salts, natural antimicrobials and antibiotics, have been used in antimicrobial coatings.[3–7] However, the increasing problem of growing microbial resistance to antimicrobial agents has led to the search for new ones with a non-specific mechanism of action that can be achieved by using different metals. Silver (Ag), zinc (Zn) and titanium (Ti) and their oxides have been extensively studied for such purposes. When inorganic nanoparticles are incorporated into polymer nanocomposites, their physico-chemical properties

256

Surface Innovations
Volume 9 Issue 5

**Novel nanostructured and antimicrobial
PVDF-HFP/PVP/MoO₃ composite**
Gradišar Centa, Sterniša, Višić *et al.*

differ from those of the individual components and lead to the development of novel multifunctional materials with a variety of applications, including the possibility of use as an antimicrobial coating. For example, polymer/nanosilver composite multilayer coatings have shown controlled release of biocidal silver ions and relatively good biocompatibility and environmental safety.[8] Biocompatible poly(*N*-isopropylacrylamide) coatings with incorporated zinc oxide (ZnO) nanoparticles were reported as an alternative to nanosilver. These showed a bactericidal behaviour towards *Escherichia coli* at a low zinc oxide concentration (approximately 0.74 µg/cm^2).[9] Nanotitania/polyurethane composite coatings also showed antibacterial activity against *E. coli*, as 99% of the bacteria were inactivated in less than 1 h under solar irradiation.[10] Unfortunately, silver and zinc oxide nanoparticles are toxic to human cells,[11] while ultraviolet (UV) light is needed to activate the antimicrobial properties of titanium dioxide (TiO$_2$).[10]

Various molybdenum (Mo) oxides have already been proposed as an alternative to these inorganic particles for use in public and healthcare environments because of their low cytotoxicity, biocompatibility and good antimicrobial activity.[12] A good antimicrobial potential of molybdenum oxides has also been shown in other studies.[13–17] The antimicrobial activity has been attributed to an acidic surface reaction in the presence of water that produces molybdic acid, which dissociates into hydronium (H$_3$O$^+$) and molybdate (MoO$_4^{2-}$) ions.[14] Moreover, antimicrobial activity has been shown to be dependent on the energy gap of molybdenum trioxide (MoO$_3$) nanorods[15] and on a specific molybdenum trioxide crystallographic phase.[12] A further comparison of commercial and synthesised forms showed the better activity of the synthesised orthorhombic structure.[12]

In addition to the antimicrobial potential of the nanofiller used for the antimicrobial composite, the properties of novel nanocomposite coating must also meet other requirements. The embedded nanomaterials (or the ions dissolved from them) need to come into physical contact with the bacteria to affect them, and part of the host material must be chemically inert to form the coating matrix. Therefore, a mixture of a water-soluble polymer containing water-soluble nanomaterials and water-insoluble polymers as the coating matrix would be a preferred design.

Within the scope of this research, a polymer nanocomposite was designed from a mixture of poly(vinylidene fluoride-*co*-hexafluoropropylene) (PVDF-HFP) and water-soluble polyvinylpyrrolidone (PVP) polymers with the addition of molybdenum trioxide nanowires (NWs). PVDF-HFP was chosen as the chemically inert part of the nanocomposite, characterised by low crystallinity (approximately 50%), low-temperature glass transition (−35°C) and high thermal stability (up to 143°C).[18–21] PVP is a biocompatible and water-soluble polymer with low chemical toxicity, high water solubility and the ability to act as a dispersant.[22] This particular combination of polymers has been reported as a possible novel high-temperature proton-exchange membrane[23] and for applications in wound healing.[24] Modified

PVDF-HFP membranes with grafting of *N*-vinyl-2-pyrrolidone and iodine (I) immobilisation[22] and quaternised pyridinium groups[25] have been shown to have good antimicrobial activity.

The nanocomposite was prepared in the form of a thin, self-standing foil as a model of a contact coating. The surface morphology on the nanoscale, the structural properties and the wetting angle, as well as the optical vibration and dynamic mechanical properties, were evaluated, and the antimicrobial activity of this nanocomposite against bacteria and fungi was determined.

2. Experimental section

2.1 Nanomaterial used and preparation of the nanocomposite

Molybdenum trioxide NWs with a diameter of 100–150 nm and a length of up to 3 µm have a high degree of porosity and a specific surface area of 12 m^2/g. They are synthesised by oxidation of Mo$_6$S$_2$I$_8$ NWs (Nanotul Ltd, Slovenia) at 285°C for 24 h.[26] Molybdenum trioxide NWs grow in an orthorhombic crystal structure (JCPDS 76-1003). The solubility of molybdenum trioxide is 2.03 ± 0.09 mg/ml in pure water. The authors showed that 6 h exposure of HaCaT cells to molybdenum trioxide at a concentration of 1 mg/ml had no effect on the survival of these cells – that is, no cytotoxic effect was observed.[27]

For the preparation of the nanocomposite, PVDF-HFP, from Sigma-Aldrich, USA, and PVP K30, from Sigma-Aldrich, USA, were dissolved separately in dimethylformamide (DMF), from Carlo Erba Reagents, Italy, and mixed using a magnetic stirrer for 2 h at 400 revolutions per min (rpm) at 80°C. In the next step, the molybdenum trioxide NWs were added to PVP and the dispersion was mixed for 2 h. Finally, PVP with molybdenum trioxide was mixed with the dissolved PVDF-HFP for another 2 h. The same mass ratio of 69:23:8 (PVDF-HFP:PVP:molybdenum trioxide) was used to prepare all foils. They were prepared by casting of the nanocomposite solution onto a Teflon plate and drying for 2 h at 80°C. For comparison, a PVDF-HFP/PVP polymer blend without molybdenum trioxide was prepared by mixing (2 h) separately dissolved polymers in DMF and then cast and dried under the same conditions as the PVDF-HFP/PVP/molybdenum trioxide nanocomposite.

2.2 Physico-chemical characterisation

The morphology of the nanocomposite films was investigated with a Supra 36 VP field-emission scanning electron microscope (SEM), from Carl Zeiss, Germany. The samples were placed on adhesive carbon (C) tape and sputtered with a 10 nm gold (Au) layer, with the aim of increasing the conductivity of the electrons during the investigation. The Raman spectra and the topography of the nanocomposites were recorded with an alpha300 confocal Raman microscope from WITec, Germany, using green laser (532.3 nm) and equipped with an atomic force microscope (AFM). The power of the laser beam measured on the sample was 0.3 mW.

Surface Innovations
Volume 9 Issue 5

**Novel nanostructured and antimicrobial
PVDF-HFP/PVP/MoO₃ composite**
Gradišar Centa, Sterniša, Višić *et al.*

The concentration of molybdenum trioxide dissolved from the nanocomposite foils was determined by UV–Vis spectroscopy using a PerkinElmer Lambda 950 spectrometer (USA) and a quartz cuvette. The nanocomposite foil with a mass concentration of 5 mg/ml was added to water in a glass beaker at room temperature (RT) while mixed with a magnetic stirrer at 300 rpm for 6 h. For the calibration curve, the absorbance amplitude of the peak at 210 nm in several molybdenum trioxide–water solutions with known concentrations was used. The surface zeta potential was measured with an Anton Paar SurPass electrokinetic analyser (Austria) with an adjustable gap cell and sample dimensions of 20 × 10 mm. The time for four measuring cycles was 5 min. The electrolyte used was a 0.001 M potassium chloride (KCl) solution in ultrapure water. The zeta potential was automatically calculated from the electrophoretic mobility, based on the Smoluchowski equation, $v = (\varepsilon E/\eta)\xi$, where v is the measured electrophoretic velocity, η is the viscosity, ε is the electrical permittivity of the electrolytic solution and E is the electric field.[28]

The wetting angle of the coatings for distilled water was measured at three points of each sample with an optical tensiometer Attension Theta Lite TL100 (Sweden) and the sessile drop method. All measurements were performed at RT, and the results are presented as the mean value with the associated standard deviation. The dynamic contact angle (CA) of water on the polymer blend and nanocomposite foil was determined according to the Wilhelmy plate method[29] with a Krüss K100 processor tensiometer (Krüss, Germany). The surface tension of demineralised water was obtained from the Krüss LabDesk database (72.8 mN/m).[30] A new sample and fresh water were used for each test cycle. The sample was first immersed in the liquid with the film normal perpendicular to the direction of immersion and then pulled out in reverse. The measurement began when the liquid buoyancy force acting on the sample was first detected and the sample reached an immersion depth of 2 mm. The immersion speed and pull-out speed were 6 mm/min. The sensitivity of force detection was set to 0.001 N. The maximum immersion depth was 7 mm. The advancing and receding CAs were determined with the Krüss LabDesk software.

The pH values were measured with a SevenExcellence multiparameter meter, from Mettler Toledo, Switzerland, with an InLab Expert Pro-ISM probe. The polymer blend and the nanocomposite foil with a mass concentration of 5 mg/ml were added to water in a glass beaker at RT. The samples were mixed with a magnetic stirrer at 300 rpm, and the pH was measured at 1 min intervals. While dissolving, they were submerged under the water surface.

The dynamic mechanical properties of the coatings were investigated with a DMA/SDTA861 dynamic mechanical analyser, from Mettler Toledo, Switzerland, in tension mode. The validity of Hooke's law – that is, the range in which the material behaves elastically – was measured with a displacement between 1 and 20 μm.
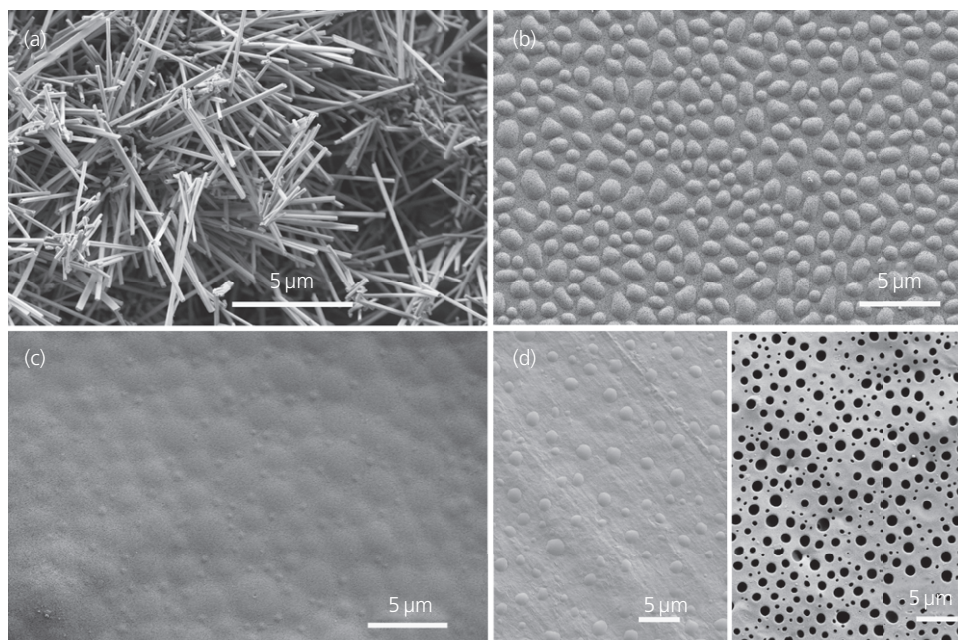
2.3 Antimicrobial test

The antimicrobial activity against Gram-positive bacteria (*Staphylococcus aureus* ŽMJ72 and *Listeria monocytogenes* ŽM58), Gram-negative bacteria (*E. coli* ŽM370 and *Pseudomonas aeruginosa* ŽM519), yeasts (*Candida albicans* ŽMJ32 and *Pichia anomala* ŽMJ6) and moulds (*Penicillium verrucosum* ŽM23 and *Aspergillus flavus* ŽM25) was evaluated. All microorganisms were from the culture collection of the Laboratory for Food Microbiology at the Department of Food Science, Biotechnical Faculty (designations ŽM and ŽMJ). The bacteria were stored in tryptic soy broth (Biolife, Italy) and the fungi in malt extract broth (Biolife, Italy) with 15% glycerol (Kemika, Croatia) at −80°C, revitalised on tryptic soy agar (TSA; Biolife, Italy) or malt extract agar (MEA; Biolife, Italy) and incubated at 37°C for 24 h for the bacteria or at 30°C for the yeasts and at 25°C for 5–7 days for the moulds (I-105 CK incubator, Kambič, Slovenia). Standardised inocula with a cell concentration of 5 log colony-forming units (CFU)/ml were prepared.

The antimicrobial potential of the material was evaluated using a modified ISO 22196 method.[31] An inert foil (polyethylene (PE)) was used as negative control, while the PVDF-HFP/PVP polymer blend was used for comparison with the PVDF-HFP/PVP/molybdenum trioxide nanocomposite. The inoculum of individual bacteria, yeast or mould was applied to PE, the PVDF-HFP/PVP polymer blend and the PVDF-HFP/PVP/molybdenum trioxide nanocomposite foils and covered with a PE foil to keep them humid. All three foil types were tested in three parallel experiments. After the test periods (0, 3 and 6 h for all test microorganisms and an additional 24 h for the fungi), the microorganisms were washed from the coatings with a neutraliser (soybean casein digest broth with lecithin and polyoxyethylene sorbitan monooleate), mixed on an orbital shaker for 10 min, diluted in saline solution and plated using the pour plate method with TSA for the bacteria and MEA for the fungi. The number of viable cells was calculated as $N = (100 \times C \times D \times V)/A$, where N is the number of viable cells per square centimetre of the tested foil, C is the average number of cells counted, D is the dilution factor, V is the volume of the solution used to wash the foils (10 ml) and A is the surface area of the foils (400 mm²). The results for each microorganism at each time point were compared with analysis of variance and post hoc Tukey test in the SPSS software program.

3. Results

3.1 Surface topography of the PVDF-HFP/PVP blend and PVDF-HFP/PVP/molybdenum trioxide nanocomposite

The surface topography of the investigated materials is shown in Figure 1. The molybdenum trioxide NWs have relatively homogeneous sizes, with a length of up to a few micrometres and a diameter of 100–150 nm (Figure 1(a)). The surface of the PVDF-HFP/PVP blend (Figure 1(b)) is nanostructured with rounded PVP islands with diameters of 200–500 nm. The PVDF-HFP/PVP/molybdenum trioxide nanocomposite (Figure 1(c)) has

Surface Innovations
Volume 9 Issue 5

**Novel nanostructured and antimicrobial
PVDF-HFP/PVP/MoO₃ composite**
Gradišar Centa, Sterniša, Višić *et al.*

Figure 1. SEM images of (a) molybdenum trioxide NWs, (b) PVDF-HFP/PVP polymer blend, (c) PVDF-HFP/PVP/molybdenum trioxide nanocomposite and (d) PVDF-HFP/PVP polymer blend after 6 h in water and (e) PVDF-HFP/PVP/molybdenum trioxide nanocomposite after 6 h in water

a domain surface structure with a diameter of a few micrometres and PVP islands in the submicrometre range. After 6 h exposure of the polymer blend and the nanocomposite foils to water, partial removal of the PVP islands from the surface of the polymer blend was observed (Figure 1(d)), but they were completely removed from the surface of the molybdenum trioxide nanocomposite, leaving a porous surface (Figure 1(e)).

The surface topography of the polymer matrix (Figure 2(a)) and the polymer nanocomposite (Figure 2(b)) on the nanometre scale was revealed using an environmental AFM. The bright PVP islands in the matrix are about 200 nm high, whereas in the nanocomposite, the height was twice reduced and smaller islands are visible. The addition of molybdenum trioxide NWs reduced
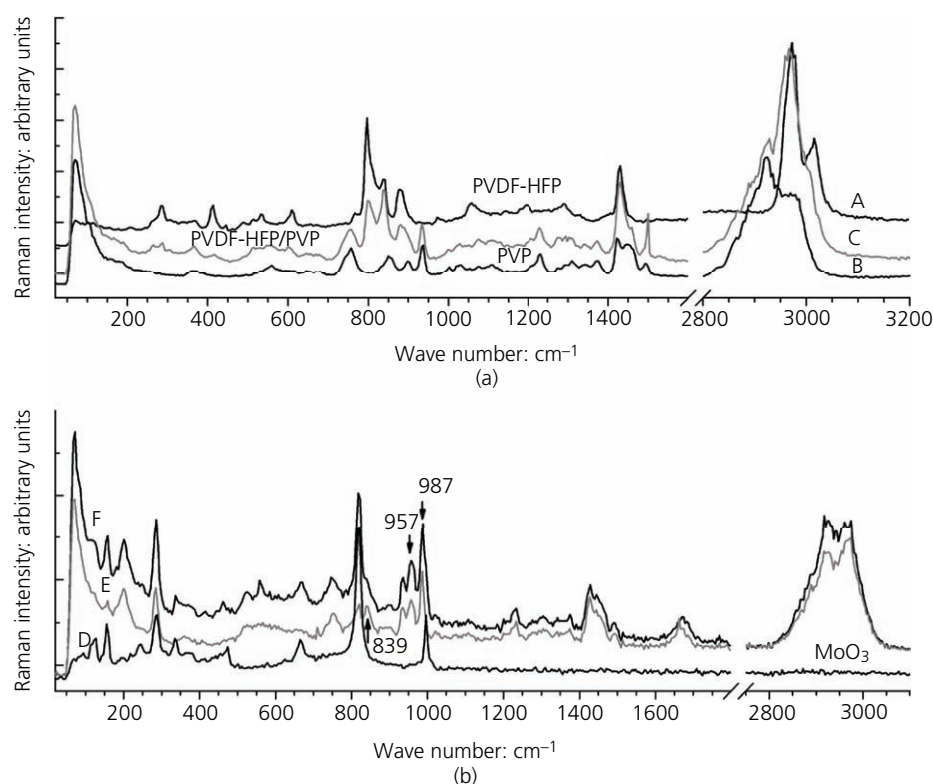
the surface roughness of the polymer nanocomposite with respect to that of the polymer matrix.

3.2 Vibration analysis of the PVDF-HFP/PVP blend and PVDF-HFP/PVP/molybdenum trioxide nanocomposite

Raman spectroscopy was used to study the polymer blend (Figure 3(a)) and the effect of molybdenum trioxide NWs (Figure 3(b)) on their vibration states. The positions of the Raman peaks are listed in Tables 1 and 2 and attributed to specific components. It is important to note that the Raman peak at 839 cm^{-1} indicates the presence of the polar β-phase of PVDF-HFP,[34] which increased strongly in the polymer blend (Figure 3(a), spectrum C). In the spectrum recorded between the PVP islands (Figure 3(b),
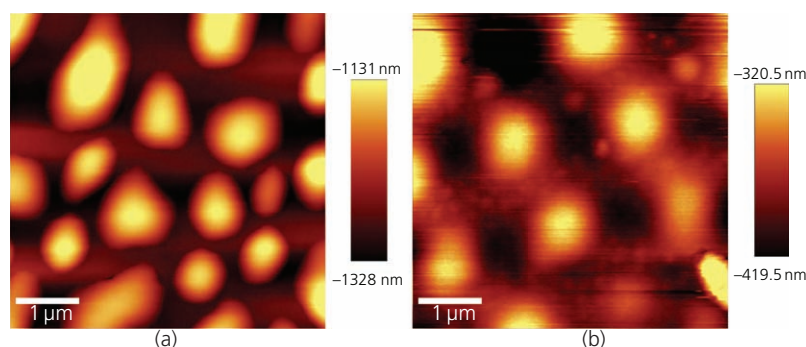
Figure 2. AFM images: (a) PVDF-HFP/PVP polymer blend; (b) PVDF-HFP/PVP/molybdenum trioxide nanocomposite

Surface Innovations
Volume 9 Issue 5

**Novel nanostructured and antimicrobial
PVDF-HFP/PVP/MoO₃ composite**
Gradišar Centa, Sterniša, Višić *et al.*

Figure 3. Raman spectra: (a) polymers (A, PVDF-HFP; B, PVP) and polymer blend (C, PVDF-HFP/PVP); (b) molybdenum trioxide (D) and PVDF-HFP/PVP/molybdenum trioxide nanocomposite (E, between islands; F, island)

Table 1. Positions of Raman peaks in the spectra of the PVDF-HFP/PVP blend, pure PVP and pure PVDF-HFP

PVDF-HFP/PVP blend		PVP		PVDF-HFP	
Position: cm⁻¹	Relative intensity: %	Position: cm⁻¹	Literature[32,33]	Position: cm⁻¹	Literature[28]
71	100	70	72	—	—
285	78	—	—	283	284
558	63	560	556	413	—
747	64	—	746	610	—
757	53	758	758	797	—
839	63	850	—	839	839 β-phase
—	—	898	—	—	—
—	—	—	—	876	—
934	53	937	934	—	—
—	—	—	—	1058	—
—	—	—	—	1194	—
1233	50	1232	1233, 1228	—	—
—	—	—	—	1290	—
1429	62	1422	1421	—	1430
1445	59	1447	—	—	1445
1490	53	1492	1494	—	—
1668	54	1660	1665, 1663	—	—
2924	78	2922	2928	—	—
2974	78	2969	—	2972	2971
—	—	—	—	3015	—

spectrum E), the presence of the molybdenum trioxide peaks is less expressed than in the spectrum recorded on the PVP islands (Figure 3(b), spectrum F), where the molybdenum trioxide peaks dominate. This indicates that most of the molybdenum trioxide is located on the PVP islands. The polar β-phase in PVDF-HFP is distinctive in spectrum E (between the islands), while in spectrum F (on the islands), it appears as a weak shoulder on the strong molybdenum trioxide peak centred at 819 cm⁻¹. However, in both

Surface Innovations
Volume 9 Issue 5

Novel nanostructured and antimicrobial
PVDF-HFP/PVP/MoO$_3$ composite
Gradišar Centa, Sterniša, Višić *et al.*

Table 2. Position of Raman peaks in the spectra of the PVDF-HFP/PVP/molybdenum trioxide nanocomposite taken on the PVP islands, on the area between the PVP islands and on pristine molybdenum trioxide NWs, with peaks assigned

| Islands | | Between islands | | Molybdenum trioxide | | | Assignment |
| | | | | This study | | Literature[34–36] | |
Position: cm^{-1}	Relative intensity: %	Position: cm^{-1}	Relative intensity: %	Position: cm^{-1}	Relative intensity: %	Position: cm^{-1}	
72	100	72	100				PVP
124	60	124	72	127	64	130	Molybdenum trioxide
158	74	158	70	156	69	159–161	Molybdenum trioxide
201	73	200	73	197	58	199	Molybdenum trioxide
217	sh	217	sh	218	59	219	Molybdenum trioxide
248	sh	249	sh	246	62	249	Molybdenum trioxide
286	78	285	73	289	71	295	PVDF-HFP, molybdenum trioxide
337	59	—	—	335	64	339–340	Molybdenum trioxide
474	56	—	—	474	61	470–482	Molybdenum trioxide
668	62	—	—	665	63	666–667	Molybdenum trioxide
817	85	821	69	821	100	820–823	Molybdenum trioxide
839	63	839	68	—	—	—	PVDF-HFP β-phase
935	64	935	68	—	—	—	PVP
957	68	957	70	—	—	—	New peak
987	77	987	78	—	—	—	New peak

sh, peak shoulder

nanocomposite spectra (E and F), two new peaks are observed at 957 and 987 cm^{-1}. The peak at 957 cm^{-1} is assigned to O=Mo=O symmetric polarised stretching modes,[32] while the narrow intense peak at 987 cm^{-1} is generally assigned to the terminal oxygen (Mo^{6+}=O) stretching mode.[33,35,36]

3.3 Mechanical properties of the PVDF-HFP/PVP blend and PVDF-HFP/PVP/molybdenum trioxide nanocomposite

The curves of the elastic modulus (E^*) and the loss tangent (tan δ) of the polymer blend (a, b) and the polymer nanocomposite (c, d) are shown in Figure 4. The spectra are rather featureless, with broad glass-transition peaks at −55 ± 3°C (full width at half maximum
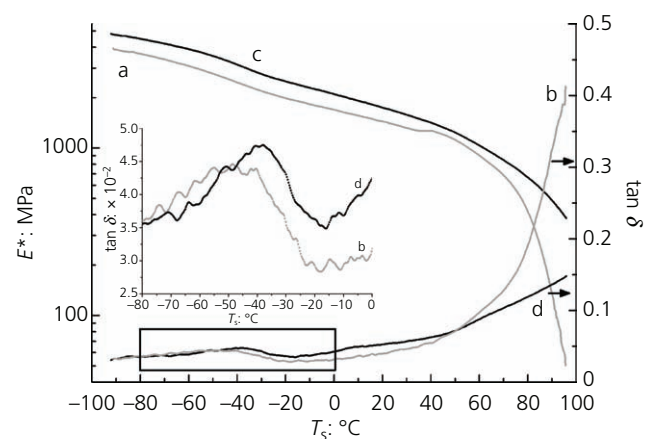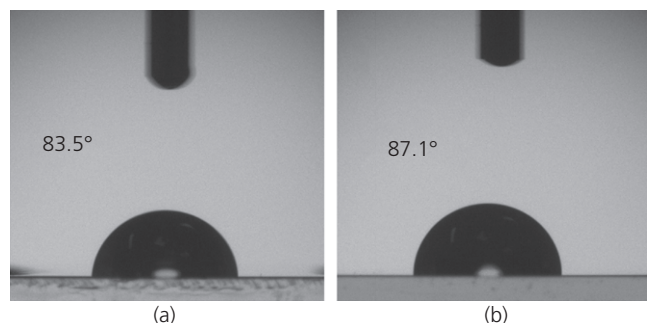

Figure 4. Elastic modulus E^* and tan δ: a, b, PVDF-HFP/PVP blend; c, d, PVDF-HFP/PVP/molybdenum trioxide nanocomposite

(FWHM): 37 ± 1°C) (blend) and at −38 ± 3°C (FWHM: 26 ± 1°C) (nanocomposite). The broadness of the peaks indicates the inhomogeneity of the polymer blend. The smaller FWHM of the convolution peak of the nanocomposite indicates that the molybdenum trioxide filler reduces the degree of inhomogeneity, corresponding to the smoother surface of the nanocomposite in relation to that of the pure polymer blend revealed by the AFM (Figure 2). The related glass-transition temperatures of the constituent polymers are −35°C (PVDF-HFP[19]) and 170°C (PVP[37]). For PVDF-HFP, a transition temperature of 50°C was also observed.[19] Above this temperature (50°C), where the tan δ curves in Figure 4 intersect, the pure polymer blend entered the elastic flow region, while the nanocomposite shows higher thermal stability with a rubber-like plateau extending to the final temperature (95°C) of the measurement. This thermal stabilisation of the PVDF-HFP part of the blend by the molybdenum trioxide nanofiller is evidence of the interaction between the molybdenum trioxide NWs and the PVDF-HFP chains during crystallisation of the polymer blend.[38] The addition of molybdenum trioxide to the polymer blend increased the complex elastic modulus E^* of the polymer nanocomposite over the entire temperature range.

3.4 Wetting angle and surface charge of the PVDF-HFP/PVP blend and PVDF-HFP/PVP/molybdenum trioxide nanocomposite

The degree of the surface hydrophilicity of the PVDF-HFP/PVP blend and the PVDF-HFP/PVP/molybdenum trioxide nanocomposite foils was investigated by static and dynamic CA measurements. Figure 5 shows the water CAs of the polymer blend (Figure 5(a)) and the polymer nanocomposite (Figure 5(b)). The molybdenum trioxide NWs increased the CA of the nanocomposite (87.1 ± 0.1°) compared with that of the polymer blend (83.5 ± 0.1°). The surfaces

Surface Innovations
Volume 9 Issue 5

**Novel nanostructured and antimicrobial
PVDF-HFP/PVP/MoO₃ composite**
Gradišar Centa, Sterniša, Višić *et al.*

Figure 5. CA test: (a) PVDF-HFP/PVP polymer blend; (b) PVDF-HFP/PVP/molybdenum trioxide nanocomposite

of the samples are chemically heterogeneous and have nanostructures at the atomic scale. For this reason, the dynamic CA was also measured using the Wilhelmy plate method.[39] The advancing CA was 87.5 ± 0.2° for the nanocomposite and 83.8 ± 0.2° for polymer blend. In both cases, the receding CA was 0°. The addition of nanoparticles can modify the wettability of polymer surfaces, as they can alter the chemical composition of the surface or the surface morphology – for example, surface roughness.[40] The surface roughness of the nanocomposite was twice smaller than that of the polymer blend, and therefore, the authors observed a slightly larger value of the CA. Increasing the surface roughness decreases the

Table 3. Results and parameters of the zeta-potential measurements

	pH	Zeta potential: mV	Gap height: μm
PVDF-HFP/PVP polymer blend	6.57 ± 0.02	−26.3 ± 0.6	98.04
PVDF-HFP/PVP/molybdenum trioxide nanocomposite	5.62 ± 0.01	+ 10 ± 3	100.57
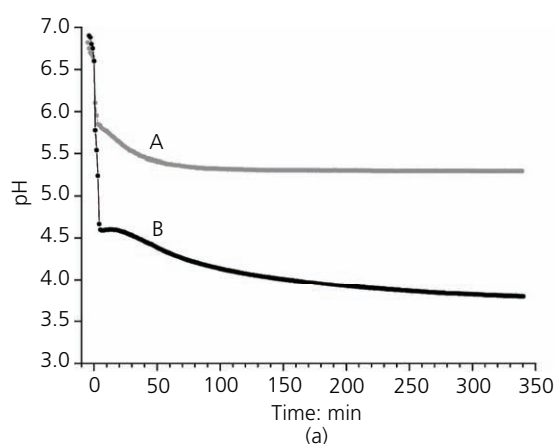
CA.[41] The values of the advancing angles indicate that the nanocomposite is slightly less hydrophilic than the pure polymer blend, although it can still be considered hydrophilic (CA < 90°).

Since the electric charge of a material surface is considered one of the most important physical factors influencing biological interactions,[42] the surface charges of the PVDF-HFP/PVP blend and the PVDF-HFP/PVP/molybdenum trioxide nanocomposite were determined (Table 3). It was found that the polymer blend without molybdenum trioxide is negatively charged, while the addition of molybdenum trioxide NWs causes a change in the surface zeta potential to a positive value.

3.5 Solubility kinetics of the PVDF-HFP/PVP blend and PVDF-HFP/PVP/molybdenum trioxide nanocomposite in water
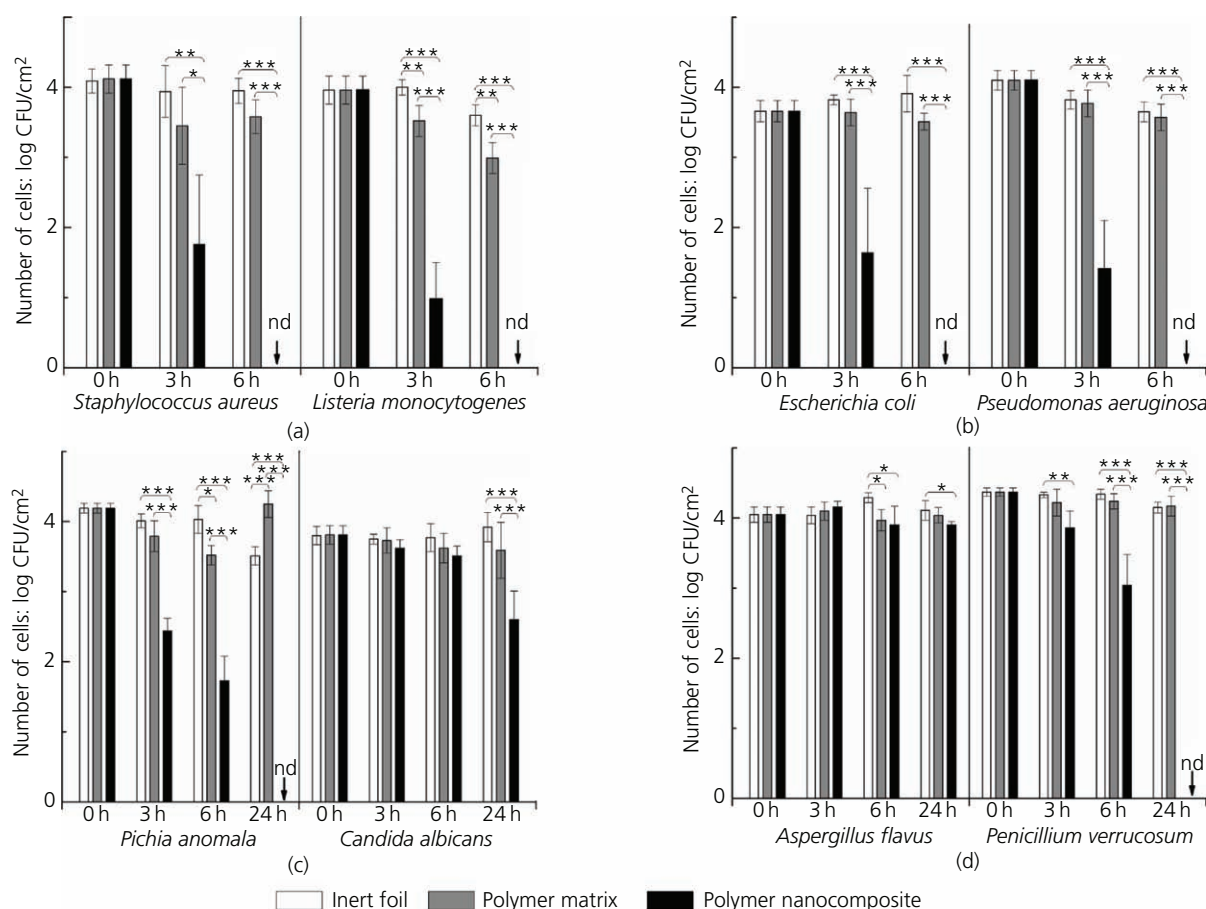
The polymer blend of water-soluble PVP and water-insoluble PVDF-HFP and the polymer nanocomposite PVDF-HFP/PVP with added water-soluble molybdenum trioxide at a concentration of 5 mg/ml were added to distilled water at RT, and the pH of the solutions was measured every minute for 340 min. The pH values of the solutions are shown in Figure 6(a). In the case of the polymer blend without molybdenum trioxide (curve A), the pH value reached a saturation value of 5.3 in 90 min. In the case of the molybdenum trioxide nanocomposite (curve B), the pH value dropped to 4.6 in the first 5 min and approached 3.8 after 6 h. The temporal development of the concentration of dissolved molybdenum trioxide NWs is presented in Figure 6(b). After a relatively short time, about 90 min, the concentration of molybdenum trioxide dissolved from the nanocomposite reached a saturation value of 0.09 mg/ml.

3.6 Antimicrobial activity

The antimicrobial properties of the PVDF-HFP/PVP/molybdenum trioxide nanocomposite were tested against Gram-positive bacteria *S. aureus* and *L. monocytogenes* (Figure 7(a)), Gram-negative
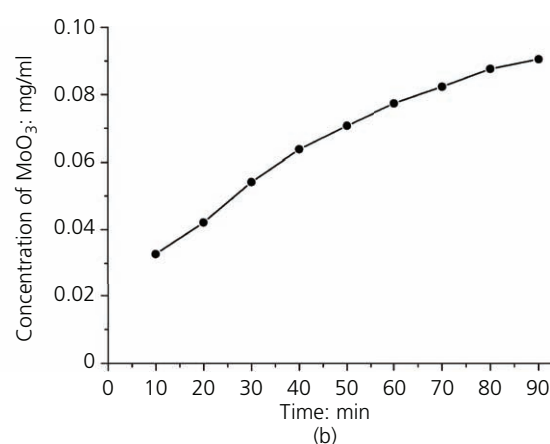
Figure 6. (a) Time evolution of pH values during dissolution in water of the PVDF-HFP/PVP blend (curve A) and PVDF-HFP/PVP/molybdenum trioxide nanocomposite (curve B); (b) concentration of dissolved molybdenum trioxide from the nanocomposite

Surface Innovations
Volume 9 Issue 5

**Novel nanostructured and antimicrobial
PVDF-HFP/PVP/MoO$_3$ composite**
Gradišar Centa, Sterniša, Višić *et al.*

Figure 7. Kinetics of the antimicrobial activity of inert PE foil (empty columns), PVDF-HFP/PVP blend (grey columns) and PVDF-HFP/PVP/ molybdenum trioxide nanocomposite (black columns) against (a) Gram-positive bacteria (*S. aureus* and *L. monocytogenes*), (b) Gram-negative bacteria (*E. coli* and *P. aeruginosa*), (c) yeasts (*C. albicans* and *P. anomala*) and (d) moulds (*P. verrucosum* and *A. flavus*). The abbreviation 'nd' means that the presence of microorganism was not detected. Asterisks indicate statistically significant difference (*$p < 0.05$; **$p < 0.01$; ***$p < 0.001$) between the compared parameters for each microorganism at a given time

bacteria *E. coli* and *P. aeruginosa* (Figure 7(b)), yeasts *C. albicans* and *P. anomala* (Figure 7(c)) and moulds *P. verrucosum* and *A. flavus* (Figure 7(d)). An inert PE foil was used as the negative control. A pure PVDF-HFP/PVP polymer blend was also tested and showed a statistically significant reduction in *L. monocytogenes* after 3 and 6 h. A reduction was also observed in *P. anomala* and *A. flavus* after 6 h, but these differences were no longer present after 24 h.

The antimicrobial activity of the PVDF-HFP/PVP/molybdenum trioxide nanocomposite was more pronounced against bacteria compared with that against fungi. The reduction trend in the number of colonies is evident for all four tested bacteria with a statistically significant reduction of 2–3 log after 3 h of incubation and with a complete bactericidal effect in 6 h (Figures 7(a) and 7(b)). For the yeasts, the antimicrobial effect was stronger against *P. anomala*, with statistically significant reductions of 1.7 log and 2.5 log in 3 and 6 h of incubation, respectively, and a fungicidal effect in 24 h (Figure 7(c)). The number of colonies of *C. albicans* was reduced less, but a

statistically significant reduction of 1.2 log in 24 h was achieved (Figure 7(c)). Species-specific differences in antimicrobial activity were also observed in the moulds, where the nanocomposite reduced the number of *P. verrucosum* already after 3 h with a reduction of 0.5 log in 3 h and by 1.3 log in 6 h in a statistically significant way and showed a fungicidal effect in 24 h. In the case of *A. flavus*, however, this difference was observed after 6 and 24 h (Figure 7(d)).

4. Discussion

The growth of microbes on different surfaces depends on several physical and chemical conditions. The most important physical conditions are the appropriate temperature, pH value, surface topography and the presence of water, while the most important chemical condition is the availability of nutrients. The physical properties of the surface, such as topography, wetting angle and surface zeta potential, influence the adhesion of microbes and their interaction with the surface. The surface roughness (R_a) of the investigated foils determined with AFM was 420 nm for the PVDF-HFP/PVP blend and half (210 nm) for the PVDF-HFP/

263

Surface Innovations
Volume 9 Issue 5

**Novel nanostructured and antimicrobial
PVDF-HFP/PVP/MoO₃ composite**
Gradišar Centa, Sterniša, Višić *et al.*

PVP/molybdenum trioxide nanocomposite. It is already known that a small increase in the average surface roughness (R_a) value reduces bacterial adhesion.[43] The addition of molybdenum trioxide NWs to the PVDF-HFP/PVP blend causes a slightly higher CA of the PVDF-HFP/PVP/molybdenum trioxide nanocomposite. Nevertheless, both foils retain their hydrophilic character, which is unfavourable for the attachment of microorganisms.[44] The existence of the β-phase of PVDF-HFP both in the pure polymer blend and in the nanocomposite is explained by an interaction between the $>CF_2$ group of PVDF and the carbonyl groups of PVP, as reported for the case of esters.[45]

Both PVP and molybdenum trioxide are water soluble and lower the pH value of the solutions towards the acidic region. The slightly acidic solution of PVP is explained by the carboxyl groups that are located at the beginning of each PVP chain.[46] The high specific surface area of molybdenum trioxide NWs leads to a very rapid dissolution in water. In the first step, molybdic acid is formed, which then dissociates further to form molybdate and hydroxonium ions.[13] The acidic environment of the dissolving molybdenum trioxide NWs intensifies the hydrolysis reaction of the PVP polymer. It has been reported that the rate constant of the hydrolysis/hydration reaction of PVP in water increases with acidity.[46] The dependence of the co-operative solubility is evident from the time dependence of the pH value, which in the case of a polymer blend solution reached the final pH value (5.3) in 1.5 h, while it decreased steadily to 3.8 in 6 h due to the dissolution of the nanocomposite. The solubility also influences the distribution of the surface charge. The zeta potential of the polymer blend is −26.3 mV, indicating the presence of negatively charged ions during the dissolution of PVP. The addition of molybdenum trioxide NWs to the polymer blend causes a change in the zeta potential from negative to positive, probably due to the protonation of the carboxylate anions. The interaction between the molybdenum trioxide NWs and the PVP polymer is also evident in the emergence of two new Raman peaks at 957 and 987 cm^{-1} and in the thermal stabilisation of the PVDF-HFP component of the blend with added molybdenum trioxide, which increased the complex elastic modulus E^* over the entire temperature range.

A consistent and statistically significant antimicrobial activity of the polymer blend was observed only for the Gram-positive bacterium *L. monocytogenes*, but the polymer also reduced *S. aureus* for 0.5 log after 6 h of incubation. This is consistent with a report that the polymers are generally more active against Gram-positive bacteria due to the difference in cell membrane structure.[47] The PVDF-HFP/PVP/molybdenum trioxide nanocomposite proved to have good bactericidal activity, as it inactivated both Gram-positive and Gram-negative bacteria after 6 h of incubation. However, species-specific differences were observed in fungi, as the nanocomposite was fungicidal against yeast *P. anomala* and mould *P. verrucosum* but only reduced the number of yeast *C. albicans* and mould *A. flavus*. This can be explained by the optimal growth rate of *A. flavus* in the pH range of 3.5–6.0,[48] while *C. albicans* has the ability to adapt to changes in extracellular pH and colonise tissues with diverse pH in vivo.[49]

5.   Conclusion

A novel nanostructured polymer composite was designed from inert biocompatible PVDF-HFP and water-soluble PVP polymers with incorporated molybdenum trioxide NWs. The nanofiller reduces the surface roughness, increases the wetting angle, changes the zeta potential from negative to positive, increases the thermal stability of the blend and preserves the polar β-phase in PVDF-HFP caused by the interaction between the two polymers. The high specific surface area of molybdenum trioxide NWs allows a fast dissolution and a consequent reduction in the pH value. The acidic environment enables hydrolysis of the PVP polymer, which could contribute to the antimicrobial function by forming carboxyl acid and ammonium salt. The synergy in the dissolving processes for PVP and molybdenum trioxide leads to sufficiently low pH values, although a relatively small amount of molybdenum trioxide (0.09 mg/ml in 1.5 h) is released from the nanocomposite. These characteristics indicate that the PVDF-HFP/PVP/molybdenum trioxide nanocomposite is a stable nanostructured coating that has a good antimicrobial potential and is unfavourable for colonisation by microorganisms. The advantage of the reported PVDF-HFP/PVP/molybdenum trioxide nanocomposite is the activation of its antimicrobial effect by water. Instead of using different disinfectants with different degrees of toxicity, which require frequent applications, the PVDF-HFP/PVP/molybdenum trioxide nanocomposite dissolves in water during the cleaning process or in water brought along by adhering microbes or condensed from the air humidity. The potential of its long-term antimicrobial and virucidal activity needs further investigation.

Acknowledgements

REFERENCES
1. Satpathy S, Sen SK, Pattanaik S and Raut S (2016) Review on bacterial biofilm: an universal cause of contamination. *Biocatalysis and Agricultural Biotechnology* **7**: 56–66.
2. Palza H (2015) Antimicrobial polymers with metal nanoparticles. *International Journal of Molecular Sciences* **16**: 2099–2116.
3. Glinel K, Thebault P, Humblot V, Pradier CM and Jouenne T (2012) Antibacterial surfaces developed from bio-inspired approaches. *Acta Biomaterialia* **8**: 1670–1684.
4. Vasilev K, Cook J and Griesser HJ (2009) Antibacterial surfaces for biomedical devices. *Expert Review of Medical Devices* **6(5)**: 553–567.
5. Thome J, Holländer A, Jaeger W, Trick I and Oehr C (2003) Ultrathin antibacterial polyammonium coatings on polymer surfaces. *Surface and Coatings Technology* **174–175**: 584–587.
6. Greenhalgh R, Dempsey-Hibbert NC and Whitehead KA (2019) Antimicrobial strategies to reduce polymer biomaterial infections and their economic implications and considerations. *International Biodeterioration & Biodegradation* **136**: 1–14.

Surface Innovations
Volume 9 Issue 5

**Novel nanostructured and antimicrobial
PVDF-HFP/PVP/MoO₃ composite**
Gradišar Centa, Sterniša, Višić *et al.*

7. Ogunsona EO, Muthuraj R, Ojogbo E, Valerio O and Mekonnen TH (2020) Engineered nanomaterials for antimicrobial applications: a review. *Applied Materials Today* **18**: article 100473.

8. Guo L, Yuan W, Lu Z and Li CM (2013) Polymer/nanosilver composite coatings for antibacterial applications. *Colloids and Surfaces A: Physicochemical and Engineering Aspects* **439**: 69–83.

9. Schwartz VB, Thétiot F, Ritz S *et al.* (2012) Antibacterial surface coatings from zinc oxide nanoparticles embedded in poly(*N*-isopropylacrylamide) hydrogel surface layers. *Advanced Functional Materials* **22(11)**: 2376–2386.

10. Charpentier PA, Burgess K, Wang L *et al.* (2012) Nano-TiO₂/polyurethane composites for antibacterial and self-cleaning coatings. *Nanotechnology* **23**: article 425606.

11. Bondarenko O, Juganson K, Ivask A *et al.* (2013) Toxicity of Ag, CuO and ZnO nanoparticles to selected environmentally relevant test organisms and mammalian cells in vitro: a critical review. *Archives of Toxicology* **87(7)**: 1181–1200.

12. Shafaei S, Lackner M, Meier M *et al.* (2013) Polymorphs of molybdenum trioxide as innovative antimicrobial materials. *Surface Innovations* **1(4)**: 202–208, https://doi.org/10.1680/si.13.00021.

13. Zollfrank C, Gutbrod K, Wechsler P and Guggenbichler JP (2012) Antimicrobial activity of transition metal acid MoO₃ prevents microbial growth on material surfaces. *Materials Science and Engineering: C* **32**: 47–54.

14. Krishnamoorthy K, Veerapandian M, Yun K and Kim SJ (2013) New function of molybdenum trioxide nanoplates: toxicity towards pathogenic bacteria through membrane stress. *Colloids and Surfaces B: Biointerfaces* **112**: 521–524.

15. Kumar A and Pandey G (2017) Synthesis, characterization, effect of temperature on band gap energy of molybdenum oxide nano rods and their antibacterial activity. *American Journal of Applied and Industrial Chemistry* **3(3)**: 38–42.

16. Desai N, Mali S, Kondalkar V, Mane R and Hong C (2015) Chemically grown MoO₃ nanorods for antibacterial activity study. *Journal of Nanomedicine & Nanotechnology* **6**: 338–344.

17. Chaves-Lopez C, Nguyen HN, Oliveira RC *et al.* (2018) A morphological, enzymatic and metabolic approach to elucidate apoptotic-like cell death in fungi exposed to h- and α-molybdenum trioxide nanoparticles. *Nanoscale* **10(44)**: 20702–20716.

18. Laxmayyaguddi Y, Mydur N, Shankar Pawar A *et al.* (2018) Modified thermal, dielectric, and electrical conductivity of PVDF-HFP/LiClO₄ polymer electrolyte films by 8 MeV electron beam irradiation. *ACS Omega* **3**: 14188–14200.

19. Sundaram NTK and Subramania A (2007) Microstructure of PVdF-*co*-HFP based electrolyte prepared by preferential polymer dissolution process. *Journal of Membrane Science* **289(1–2)**: 1–6.

20. Malmonge LF, Malmonge JA and Sakamoto WK (2003) Study of pyroelectric activity of PZT/PVDF-HFP composite. *Materials Research* **6(4)**: 469–473.

21. Cao JH, Zhu BK and Xu YY (2006) Structure and ionic conductivity of porous polymer electrolytes based on PVDF-HFP copolymer membranes. *Journal of Membrane Science* **281**: 446–453.

22. Shawky AI, Noor MJMM, Nasef MM *et al.* (2016) Enhancing antimicrobial properties of poly(vinylidene fluoride)/hexafluoropropylene copolymer membrane by electron beam induced grafting of *N*-vinyl-2-pyrrolidone and iodine immobilization. *RSC Advances* **6**: 42461–42473.

23. Guo Z, Xu X, Xiang Y, Lu SA and Jiang SP (2015) New anhydrous proton exchange membranes for high-temperature fuel cells based on PVDF–PVP blended polymers. *Journal of Materials Chemistry A* **3(1)**: 148–155.

24. Wang M, Fang D, Wang N *et al.* (2014) Preparation of PVDF/PVP core–shell nanofibers mats via homogeneous electrospinning. *Polymer* **55**: 2188–2196.

25. Yao C, Li X, Neoh KG, Shi Z and Kang ET (2009) Antibacterial activities of surface modified electrospun poly(vinylidene fluoride-*co*-hexafluoropropylene) (PVDF-HFP) fibrous membranes. *Applied Surface Science* **255(6)**: 3854–3858.

26. Varlec A, Arčon D, Škapin SD and Remškar M (2016) Oxygen deficiency in MoO₃ polycrystalline nanowires and nanotubes. *Materials Chemistry and Physics* **170**: 154–161.

27. Božinović K, Nestić D, Gradišar Centa U *et al.* (2020) In-vitro toxicity of molybdenum trioxide nanoparticles on human keratinocytes. *Toxicology* **444**: article 152564.

28. Zhang Y, Yang M, Portney NG *et al.* (2008) Zeta potential: a surface electrical characteristic to probe the interaction of nanoparticles with normal and cancer human breast epithelial cells. *Biomedical Microdevices* **10**: 321–328.

29. Wilhelmy J (1863) Über die Abhängigkeit der Kapillaritäts-Konstanten des Alkohols von Substanz und Gestalt des Benetzten Festen Körpers. *Annalen der Physik* **119**: 177–217 (in German).

30. Ström G, Fredriksson M and Stenius P (1987) Contact angles, work of adhesion, and interfacial tensions at a dissolving Hydrocarbon surface. *Journal of Colloid and Interface Science* **119(2)**: 352–361.

31. ISO (International Organization for Standardization) (2007) ISO 22196:2007: Plastics – measurement of antibacterial activity on plastics surfaces. ISO, Geneva, Switzerland.

32. Kalampounias AG, Tsilomelekis G, Berg RW and Boghosian S (2012) Molybdenum(VI) oxosulfato complexes in MoO₃−K₂S₂O₇−K₂SO₄ molten mixtures: stoichiometry, vibrational properties, and molecular structures. *Journal of Physical Chemistry A* **116(35)**: 8861–8872.

33. Sharma RK and Reddy GB (2014) Synthesis and characterization of α-MoO₃ microspheres packed with nanoflakes. *Journal of Physics D: Applied Physics* **47(6)**: article 065305.

34. Singh P, Borkar H, Singh BP, Singh VN and Kumar A (2014) Ferroelectric polymer–ceramic composite thick films for energy storage application. *AIP Advances* **4**: article 087117.

35. Beattie IR and Gilson TR (1969) Oxide phonon spectra. *Journal of the Chemical Society A: Inorganic, Physical, Theoretical* **969**: 2322–2327.

36. Dieterle M and Mestl G (2002) Raman spectroscopy of molybdenum oxides. *Physical Chemistry Chemical Physics* **4**: 822–826.

37. Turner DT and Schwartz A (1985) The glass transition temperature of poly(*N*-vinyl pyrrolidone) by differential scanning calorimetry. *Polymer* **26**: 757–762.

38. Remškar M, Iskra I, Jelenc J *et al.* (2013) A novel structure of polyvinylidene fluoride (PVDF) stabilized by MoS₂ nanotubes. *Soft Matter* **9**: 8647–8653.

39. Strobel M and Lyons CS (2011) An essay on contact angle measurements. *Plasma Processes and Polymers* **8(1)**: 8–13.

40. Manoudis PN and Karapanagiots I (2013) Modification of the wettability of polymer surfaces using nanoparticles. *Progress in Organic Coatings* **77**: 331–338.

41. Juárez-Moreno JA, Ávila-Ortega A, Oliva AI and Cauich-Rodríguez JV (2015) Effect of wettability and surface roughness on the adhesion properties of collagen on PDMS films treated by capacitively coupled oxygen plasma. *Applied Surface Science* **349**: 763–773.

42. Cai K, Bossert J and Jandt KD (2006) Does the nanometre scale topography of titanium influence protein adsorption and cell proliferation? *Colloids and Surfaces B: Biointerfaces* **49(2)**: 136–144.

43. Taylor RL, Verran J, Lees GC and Ward AJP (1998) The influence of substratum topography on bacterial adhesion to polymethyl methacrylate. *Journal of Materials Science: Materials in Medicine* **9**: 17–22.

44. Oliveira R, Azeredo J, Teixeira P and Fonseca AP (2001) The role of hydrophobicity in bacterial adhesion. In *Biofilm Community Interactions: Chance or Necessity?* (Gilbert P, Allison D, Brading M, Verran J and Walker J (eds)). BioLine, Cardiff, UK, pp. 11–22. See http://citeseerx.ist.psu.edu/viewdoc/download?doi=10.1.1.625.340&rep=rep1&type=pdf (accessed 11/12/2020).

45. Manna S and Nandi AK (2007) Piezoelectric β polymorph in poly (vinylidene fluoride)-functionalized multiwalled carbon nanotube nanocomposite films. *Journal of Physical Chemistry C* **111**: 14670–14680.

46. Frank HP (1954) The lactam-amino acid equilibria for ethylpyrrolidone and polyvinylpyrrolidone. *Journal of Polymer Science* **12**: 565–576.

47. Tashiro T (2001) Antibacterial and bacterium adsorbing macromolecules. *Macromolecular Materials and Engineering* **286**: 63–87.

48. Kosegarten CE, Ramírez-Corona N, Mani-López E, Palou E and López-Malo A (2017) Description of *Aspergillus flavus* growth under the influence of different factors (water activity, incubation temperature, protein and fat concentration, pH, and cinnamon essential oil concentration) by kinetic, probability of growth, and time-to-detection models. *International Journal of Food Microbiology* **240**: 115–123.

49. Davis D (2003) Adaptation to environmental pH in *Candida albicans* and its relation to pathogenesis. *Current Genetics* **44**: 1–7.

How can you contribute?

To discuss this paper, please submit up to 500 words to the journal office at journals@ice.org.uk. Your contribution will be forwarded to the author(s) for a reply and, if considered appropriate by the editor-in-chief, it will be published as a discussion in a future issue of the journal.

ICE Science journals rely entirely on contributions from the field of materials science and engineering. Information about how to submit your paper online is available at www.icevirtuallibrary.com/page/authors, where you will also find detailed author guidelines.

Article

Hydrophilicity Affecting the Enzyme-Driven Degradation of Piezoelectric Poly-L-Lactide Films

Lea Gazvoda [1,2], Bojana Višić [3,4], Matjaž Spreitzer [1] and Marija Vukomanović [1,*]

1 Advanced Materials Department, Jožef Stefan Institute, 1000 Ljubljana, Slovenia; lea.udovc@ijs.si (L.G.); matjaz.spreitzer@ijs.si (M.S.)

2 Jožef Stefan International Postgraduate School, 1000 Ljubljana, Slovenia

3 Condensed Matter Physics Department, Jožef Stefan Institute, 1000 Ljubljana, Slovenia; bojana.visic@ijs.si

4 Institute of Physics Belgrade, University of Belgrade, Pregrevica 118, 11080 Belgrade, Serbia

* Correspondence: marija.vukomanovic@ijs.si; Tel.: +386-1-477-3547

Abstract: Biocompatible and biodegradable poly-L-lactic acid (PLLA) processed into piezoelectric structures has good potential for use in medical applications, particularly for promoting cellular growth during electrostimulation. Significant advantages like closer contacts between cells and films are predicted when their surfaces are modified to make them more hydrophilic. However, there is an open question about whether the surface modification will affect the degradation process and how the films will be changed as a result. For the first time, we demonstrate that improving the polymer surface's wettability affects the position of enzyme-driven degradation. Although it is generally considered that proteinase K degrades only the polymer surface, we observed the enzyme's ability to induce both surface and bulk degradation. In hydrophilic films, degradation occurs at the surface, inducing surface erosion, while for hydrophobic films, it is located inside the films, inducing bulk erosion. Accordingly, changes in the structural, morphological, mechanical, thermal and wetting properties of the film resulting from degradation vary, depending on the film's wettability. Most importantly, the degradation is gradual, so the mechanical and piezoelectric properties are retained during the degradation.

Keywords: poly-L-lactic acid; enzymatically catalyzed degradation; piezoelectricity; bulk erosion; surface erosion

1. Introduction

Poly-L-lactic acid (PLLA), a biosynthetic thermoplastic polyester, is widely used in the biomedical field because it is biocompatible and biodegradable [1,2]. It can also be formed into different shapes (2D coatings and films, micro- and nano-powders, 3D scaffolds, etc.) with different properties, depending on the requirements [3]. Accordingly, PLLA is used in drug-delivery systems [4], tissue engineering [5], wound dressing [6], implantation [7] and many more [8,9].

A very poorly explored and particularly important aspect of PLLA's application in biomedicine is associated with the possibility of processing it into a piezoelectric material. Due to its helix structure, PLLA exhibits shear piezoelectricity [10]. When PLLA is oriented and crystalline, usually as fibers or films, the chains are strained, the molecular dipoles are aligned, and a voltage difference is observed [11]. Such a structure, formulated as a piezoelectric scaffold, can be applied for piezo-stimulation and promoting cell proliferation. The low piezoelectric effect of PLLA (compared to piezoceramics) is comparable to the piezoelectricity of natural biomacromolecules (i.e., collagen) [12] and can be efficient enough to relate with biological systems [13]. It makes this polymer particularly appropriate for regenerative medical use to accelerate the wound-healing process. When applied for wound healing, the safe biodegradation of piezoelectric PLLA films is very important. The process needs to be steady, and the biodegradation (followed by a change of mechanical,

structural, morphological and piezoelectric properties) should follow the kinetics of the tissue regeneration so that at the end, no material residues are left in the system when the new tissue is formed.

When PLLA is in contact with biological media, cleavage of the ester bonds occurs in the bulk matter, usually by hydrolysis, into lactic acid, carbon dioxide and water [14]. Under in vivo conditions, due to the inflammation process during the injury, the degradation process is enhanced by the enzymes present that degrade the polymer matrix [1]. Since PLLA is more hydrophobic, swelling of the polymer film occurs with the diffusion of water inside the polymer bulk, which triggers the degradation inside the material [14]. However, when enzymes are present, it is generally considered that surface degradation is favorable since the diffusion of enzymes inside the film is aggravated [15]. Proteinase K catalyzes the degradation of PLLA several times faster in amorphous than in crystalline regions [16]. At the surface, degradation is limited to just the amorphous parts [15]. Crystalline residues, remaining after the degradation of the connected amorphous areas, are released into the surrounding liquid medium or accumulate on the surface and increase crystallinity [15]. Polymer crystallinity and chain orientation have been determined to have an important role in the process of enzyme-induced PLLA degradation. H. Tsuji et al. showed that the initially higher crystallinity of the PLLA films slows the degradation process and that the higher polymer-chain orientation also limits the enzyme intake into the bulk [15]. In addition, Rangari et al. observed that during the hydrolysis of the amorphous part on the surface in uniaxially prepared crystalline PLLA films, crystallinity plays the dominant role in determining the extent of the degradation, compared to the orientation of the polymer chains [16].

Understanding the degradation mechanism in biologically relevant surroundings is a key issue for using a piezoelectric polymer in biomedical applications. Although there is a detailed study of the structural changes that follow enzymatic degradation (change in crystallinity, chain orientation, chain mobility, etc.), very little knowledge is available on the change in the piezoelectric and mechanical properties of PLLA films during the degradation process. All the information regarding PLLA degradation is available for polymers with a hydrophobic surface. However, the hydrophobic surface is the main disadvantage of PLLA, potentially resulting in a low cell affinity and an inflammatory response [17]. A particular lack of information was observed for the case of the degradation of surface-modified PLLA hydrophilic films. With that in mind, we focused our investigations on two questions:

(i)   How will the degradation be affected if the surface of the PLLA film is modified from hydrophobic to hydrophilic (more favorable to cells)?

(ii)   What will happen to the mechanical and piezoelectric properties of the PLLA once the film is immersed in a liquid medium containing proteinase K (as an imitation of the inflammation response at the site of a wound)?

Therefore, in this study, we compare the enzymatically catalyzed degradation process of a uniaxial drawn piezoelectric PLLA film with and without surface modification, and with it the mechanical and piezoelectric changes that occur during the degradation process to achieve a more stable and gradual loss of piezoelectric properties during the process. Films with improved wettability should have greater potential for medical applications due to the proposed better affinity of the cells for the film.

2. Materials and Methods

2.1. Materials

Poly-L-lactic acid (PLLA) having a molecular weight with an approximate value of 150 kDa (Goodfellow, Cambridge, Ltd., UK), bovine serum albumin (BSA) (Fisher scientific, Leics, UK), methylene blue (MB) (Alfa Aesar, Thermo Fisher GmbH, Kandel, Germany) were used. Enzyme proteinase K was purchased from ITW Reagents (AppliChem GmbH, A3830,0500, Darmstadt, Germany) and was used as received. TRIS buffer, sodium hydroxide (NaOH), methanol (MeOH), hydrochloride acid (HCl), were purchased from

Sigma-Aldrich Chemie GmbH, Steinheim, Germany. Distilled water was purified using a Milli-Q system (Purelab Option-Q, ELGA, High Wycombe, UK).

2.2. Processing PLLA Films

Piezoelectric polymer films were prepared using the following procedure, optimized in our previous study [18]. PLLA granules (1 g) were melt-pressed between two metal plates at 200 °C under a pressure of 56 kN for 3 min and immediately quenched in cold water (4 °C) (amorphous sheet). To prepare piezoelectric films, the amorphous sheet was cut into a dumbbell-shape film and uniaxially stretched with a homemade tensile stretcher to a draw ratio of 5 at a temperature above the glass transition (90 °C), using a drawing rate of 40 mm/min. Surface modification, such as alkaline etching, was performed to prepare hydrophilic films. Films were submerged overnight in a 0.04 M NaOH medium, prepared in a water/MeOH mixture (70/30 *V/V*) to cleave the ester bonds on the surface.

2.3. Enzymatic Degradation

The drawn films were immersed in 0.1 mg/mL proteinase K solution with pH 8.5. The enzyme solution was prepared using a 0.5 M TRIS buffer, adding HCl to adjust the pH value. 5 mL of enzyme solution containing films was maintained at 37 °C in a water bath while gently shaken. The degradation study was carried out for 10 days. Films were washed with water and left to dry before the analyses. Enzymatic activity during the degradation process was monitored using an absorbance multiplate reader (Synergy H1, BioTek, Bad Friedrichshall, Germany). A sample of 500 μL of enzymatic medium taken from the degrading sample was added to 500 μL of 1 mg/mL BSA protein and digested for 2 h. Absorbance at 290 nm was continuously measured to determine the half-time needed for protein degradation. Measurements were made in two parallel samples for enzymes with different polymer films and a bare enzyme. Further enzymatic activity was stopped by heating the sample at 90 °C. A total of 15 μL of the sample with 3 μL of added loading buffer were put on 15% polyacrylamide gel to separate the degraded BSA proteins based on size using SDS-page electrophoresis.

2.4. Characterization Methods

Gravimetric determination, crystallinity and orientation changes were calculated using the following equation:

$$\Delta X \ (\%) = 100\% \times (X_{t0} - X_t)/X_{t0}, \tag{1}$$

where ΔX represents the weight changes (w), crystallinity (X) and orientation ratio (D) from the beginning ($t0$) to a certain time of degradation (t).

Orientation was determined using a Fourier-transform infrared spectrometer in attenuated total reflectance (ATR) mode (PerkinElmer Spectrum 100, Waltham MA, USA). Spectra were recorded in the 600–4000 cm^{-1} wavenumber range with a spectral resolution of 4 cm^{-1} and the accumulation of 10 spectra using a polarizer. Changes in the orientation were determined using the previous equation, where D represents the ratio between changes of the vertical ($\parallel$) and horizontal ($\perp$) absorbance (A) of the C=O peak (1756 cm^{-1}) using the following equation [19,20]:

$$D = A_{\parallel}/A_{\perp}. \tag{2}$$

Crystallinity was determined using a NETZSCH STA 449 (Jupiter) thermal analyzer for differential scanning calorimetry (DSC) in an Ar/O atmosphere (40/10). A total of 3–4 mg of each sample were put in platinum crucibles and heated from 40 °C to 200 °C with a 20 °C/min heating rate due to the temperature calibration under these conditions. The enthalpy of cold crystallization (ΔHc) and the enthalpy of melting (ΔHm) were determined

by calculating the surface under the peak of the crystallization or melting, respectively. Bulk crystallinity was determined with the following expression:

$$X_c \, (\%) = 100\% \times (\Delta H_m - \Delta H_c)/\Delta H_{100\%}, \tag{3}$$

where the value for $\Delta H_{100\%}$ is taken as 93.6 J/g, which is a theoretical value for 100% crystalline PLLA films in the α crystalline form [21].

Morphological changes during degradation were observed with a scanning electron microscope (JSM-7600 F, Jeol Ltd., Tokyo, Japan). To observe changes in the hydrophilic properties, methylene-blue staining was used to observe the color change due to more carboxylic groups on the surface [22]. Water wetting angles were measured using a Theta Lite contact-angle meter, Biolin Scientific.

Dynamic mechanical properties of the PLLA samples were studied under tension mode on the films in a rectangular shape (9 mm long, 3–3.5 mm wide and 0.1 mm thick). The measurements were performed with a Mettler Toledo DMA/SDTA861e. The dynamic responses were tested from 0 °C to 130 °C at the heating rate of 3 K/min. The dynamic force amplitude was 1 N, and the validity of Hooke's law (linearity measurement) was tested on every sample to determine the displacement amplitude, which was 2–5 µm. The chosen frequency was 1 Hz. The storage modulus, loss modulus and tan δ were recorded as a function of the sample temperature. Since the measurements were made in the tension mode, the storage modulus corresponds to Young's modulus.

The piezoelectric properties were measured according to the description in a previous article [18]. Polymer films were cut at an angle of 45° from the stretching axis, seeing that the shear stress has a maximum value when measured at this angle [23]. The measurement was made using a PiezoMeter System PM300 (Piezotest Pte. Ltd., International Plaza, Singapore), which was adapted for thin-film d_{31} measurements. First, gold electrodes were sputtered on both surfaces of the polymer film. Then the film was clamped on both sides to stretch the film (frequency of 110 Hz and force 0.15–0.5 N). The voltage was measured with a voltmeter (Tenma multimeter) over a reference capacitor of 1000 pF. The piezoelectric coefficients g_{14} and d_{14} were calculated.

3. Results

PLLA films were made with a hydrophilic surface using alkali etching to improve their water wettability, which is favored for interactions with cells [24]. Before being applied for the degradation study, the stretched, oriented, and etched films remained stained after immersion in the methylene-blue solution, indicating a larger amount of carboxylic end groups on the surface (Figure 1a). Degradation was performed using a proteinase-K-buffered solution under simulated physiological conditions (gently shaking at 37 °C). After aging for 5 and 10 days in the enzyme solution, the polymeric films had macroscopically observable damage (Figure 1b). Normally, for PLLA polymers, proteinase K acts as a hydrolysis catalyzer, and degradation follows the surface mechanism [15]. For the case of non-etched, hydrophobic films, we initially observed the occurrence of surface erosion, along with some evidence of bulk erosion induced by autocatalysis (day 10). This result was more following the available literature on hydrophobic PLLA film degradation without any enzyme present [17]. However, in the case of more hydrophilic PLLA films, it was observed that the films were macroscopically more compact, without signs of bulk erosion, indicating a contribution of the surface modification to the degradation process and the following mechanism (Figure 1b).
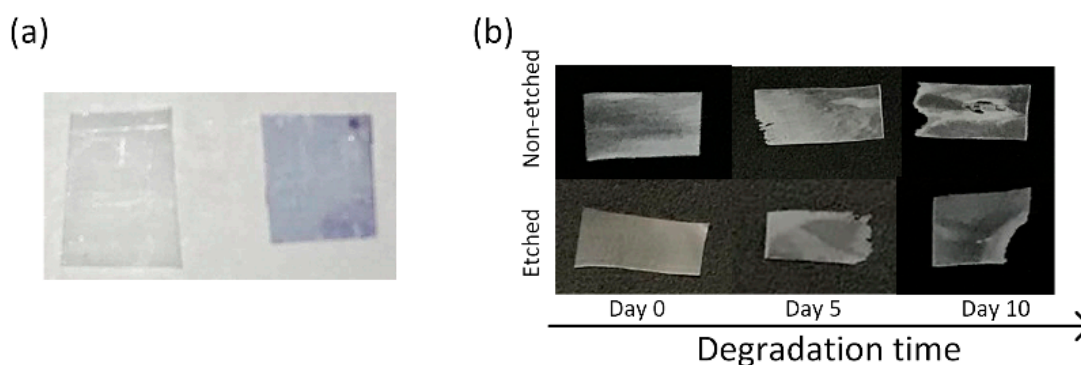
Figure 1. (**a**) Methylene blue staining of non-etched (**left**) and etched (**right**) PLLA films; (**b**) samples of enzymatic degradation of the non-etched (**top**) and etched (**bottom**) films after 0, 5 and 10 days.
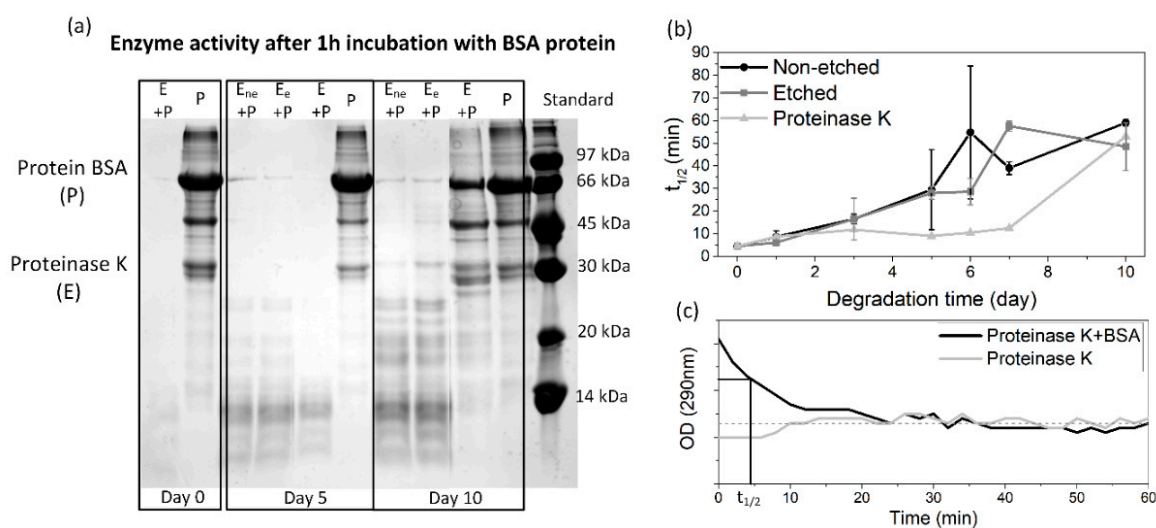
3.1. Enzymatic Activity

Since all of the polymeric films were degraded in the same solution for the whole 10 day period, the enzyme activity was periodically monitored to follow the progress of degradation. By lowering the pH value, as a result of the release of lactic acid residues into the medium during the degradation progress, the activity of the proteinase K was also expected to decrease. The detected degradation products (based on an SDS-page test) (Figure 2a) and the half time of the enzyme's degradation activity (Figure 2b) show a lowering of the activity along with the film's degradation. The enzyme activity was also decreased in a reference enzyme solution (without films); however, this drop was more pronounced when films were present. Figure 2c presents the activity of the initial enzyme solution with the reference BSA protein, observed with a continuous absorbance measurement, from where the half time of the total protein degradation was determined. After 10 days of degradation, the enzyme activity is significantly reduced compared to day 1 (from 5 to 50 min), even without the films being present. This was expected since no fresh enzymes were added during the degradation. Despite the observed decreases, it should be noted that the enzyme was active for the whole period during which the degradation progress was observed. Accordingly, all the observed changes in the aged PLLA films could be assigned to the process of degradation.

3.2. Structural Changes (Crystallinity and Orientation)

After 10 days of degradation, the weight losses, indicating the progress of the degradation, were similar for both the etched (35%) and non-etched (37%) films. Additionally, the drops in the pH, directly correlated with the degradation process, were comparable for the etched and non-etched films (from 8.5 to 4.6) since the equally released lactic acid residues lower the initial pH value. The initial hydrophilicity was changed only on the surface of the films, which could affect the location of the degradation; however, the total progress of the degradation remained the same.

The main differences in the degradation of the etched and non-etched films were the crystallinity and orientation. These properties were detected by comparing the FTIR spectra of the enzymatically degraded films with the spectra of the film reference (corresponding to films aged in a medium without the enzyme present), as presented in Figure 3. Typical changes in the surface crystallinity are observed closely at normalized spectra in the wavelength range 900–980 cm^{-1}. Following previous studies [16,18], the increase in the intensity of the peak at 922 cm^{-1} represents an increase in the crystallinity of the PLLA, which we also observed in the case of the non-etched (hydrophobic) films (Figure 3, left).

Figure 2. (**a**) SDS-page results for the enzymatic activity of the initial solution and after 5 and 10 days of degradation for enzymes in non-etched (Ene), etched (Ee) and control solutions (E), where activity was verified with degradation of the BSA protein (P); (**b**) calculated half time needed for BSA protein degradation for enzymes in non-etched, etched and control solutions, determined from measured optical density at 290 nm for each solution, where graph (**c**) presents the absorbance measurements for initial proteinase K solution with a marked half time of total degradation ($t_{1/2}$).
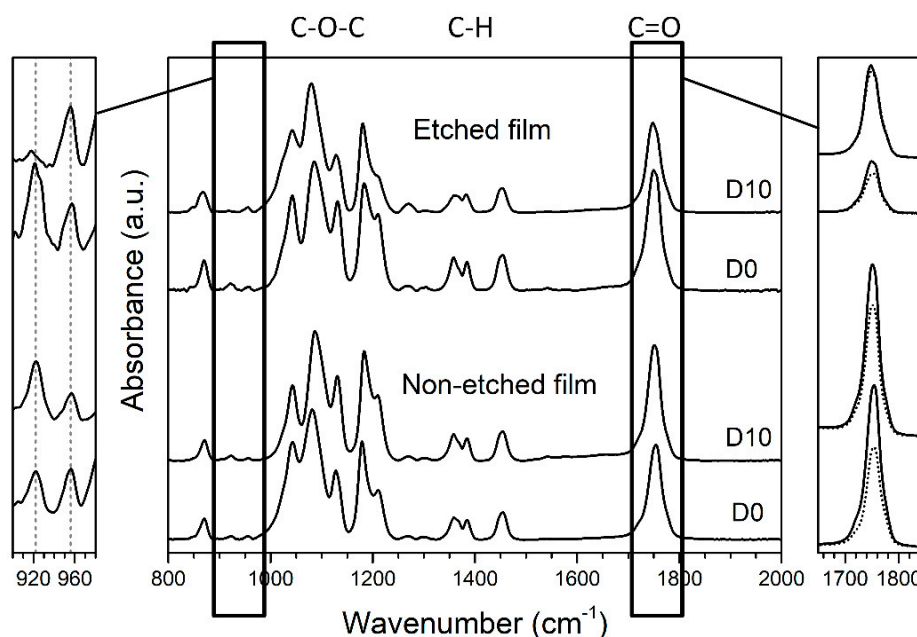
Figure 3. ATR FT-IR spectra (normalized to maximum peak absorbance) for non-etched and etched PLLA films (**middle**), degraded for 10 days in enzymatic solution (D10), compared to initial PLLA film (D0). On the (**left**), an enlarged, normalized spectrum between 900 and 980 cm^{-1} is presented to observe changes in the intensity of peaks that are specific for more crystalline (921 cm^{-1}) or more amorphous (956 cm^{-1}) films. On the (**right**), a polarizer was used to determine the changes in orientation of the C=O peak, comparing the intensities of horizontal (solid line) and vertical (dotted line) orientations without normalization of the spectra.

Orientation for the polymeric chains within the film was confirmed based on an observable peak at 1755 cm^{-1} that corresponds to the C=O stretching in the ester carbonyl group. As noted earlier, high anisotropy is obtained for oriented polymeric films when comparing the vertical and horizontal positions [19]. For our oriented PLLA films, the intensities of the C=O and C–O–C peaks are enhanced in the drawing direction (horizontal)

compared to the perpendicular direction (vertical) and shifted to slightly lower values (Figure 3, right). Comparable changes in the C=O and C–O–C peaks were also observed by T. Nobeshima et al. [20]. Regarding the influence of the water wettability, the orientation was decreased for both the hydrophobic non-etched and hydrophilic etched films during degradation (Table 1 and Figure 3).

Table 1. Summarized properties of degraded PLLA films over 10 days in solution with proteinase K.

Up to 10 Days of Degradation	PLLA Non-Etched	PLLA-Etched
pH change	From 8.5 to 4.6	From 8.5 to 4.6
Weight loss	37 wt %	35 wt %
Crystallinity change (DSC)	+27%	+5%
Orientation change (FT-IR: 1750 cm^{-1})	−24% of the initial ratio	−18% of the initial ratio
Piezo change	**After 5 days:**	**After 5 days:**
d_{14} g_{14}	2.68 pC/N (68.8% of initial) 0.092 Vm/N	2.32 pC/N (50.4% of initial) 0.066 Vm/N
	After 10 days	**After 10 days**
d_{14} g_{14}	Non-measurable with applied method	Non-measurable with applied method

Similar structural changes were revealed during the XRD study (Figure 4). As with the FTIR analysis, the XRD results clearly indicate the large increase in crystallinity of the non-etched samples. The polymer is in the α' phase since the specific (200)/(110) peak appears at the 2-theta position lower than 16.6°, following a previous report [25]. After 10 days, the additional, more ordered α phase is observed only for the etched film, detected as an additional XRD peak at 16.9° (Figure 4b).
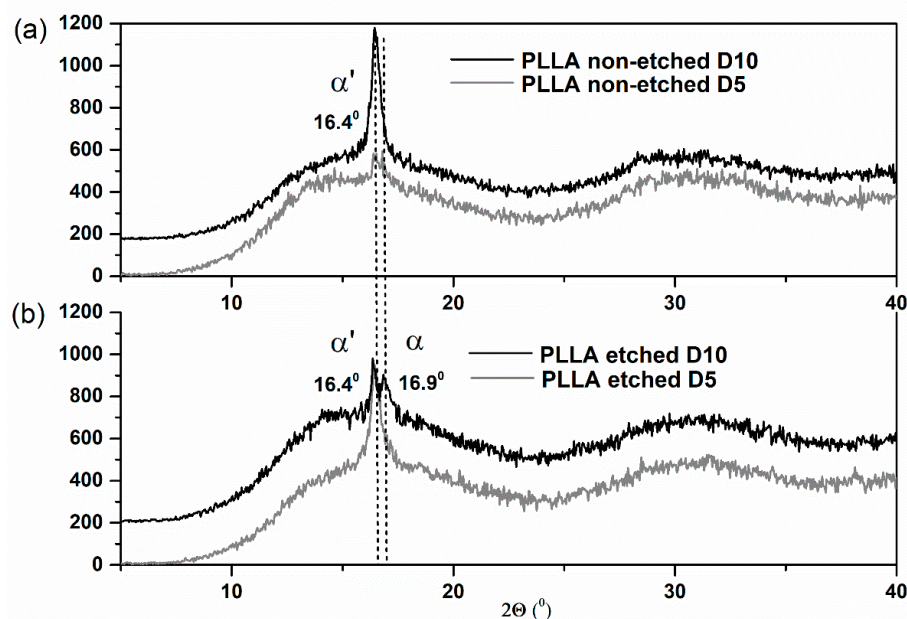
Figure 4. XRD patterns of hydrophobic non-etched (**a**) and hydrophilic etched (**b**) PLLA films obtained after 5 and 10 days of degradation by proteinase K (labeled with D5 and D10).

Investigating the thermal properties of PLLA films also revealed different responses to enzyme-catalyzed degradation for the etched and non-etched samples (Table 1, Table 2 and Figure 5). For the etched samples, the melting peaks are broad for all the measured

samples, indicating the presence of both crystalline forms: α' and α. Degradation promotes recrystallization (α' to α) since they are both detected in the final degradation stage, as seen in the XRD data. The crystallinity of the etched films, measured using DSC, is initially high (since etching removes part of the amorphous regions), and it was not changed much during the degradation. However, for non-etched samples, even though it starts at a lower value, the crystallinity increased significantly after 10 days of degradation, as also observed from the FTIR and XRD analyses. While the glass and melting temperatures (T_g and T_m) were shifted for non-etched films during degradation, similar changes were not observed in the etched films. H. Tsuji et al. also observed increased T_g values for the oriented and un-oriented films; therefore, T_g changes respond to the degradation process, like changes in the highly ordered structure, such as crystallinity or orientation [15].

Table 2. DSC data for etched and non-etched PLLA films for different periods of degradation.

| Up to 10 Days of Degradation	T_g	ΔH cryst. (J/g)	T_c	ΔH melt (J/g)	T_m	Crystallinity %
PLLA-non-etched	69 °C	21	117 °C	51	173 °C	31
PLLA-non-etched D5	72 °C	35	118 °C	50	173 °C	16
PLLA-non-etched D10	75 °C	/	/	55	167 °C	58
PLLA-etched	71 °C	/	/	49	172 °C	52
PLLA-etched D5	72 °C	/	/	57	170 °C	61
PLLA-etched D10	72 °C	5	109 °C	59	170 °C	57
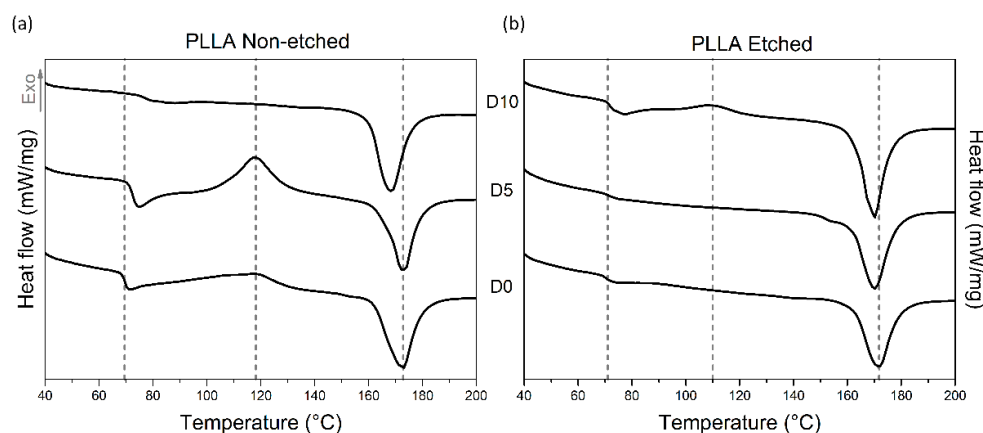
Figure 5. DSC curves of hydrophobic non-etched (**a**) and hydrophilic etched (**b**) PLLA films obtained after different periods of degradation by proteinase K, labeled by D0, D5 and D10.

3.3. Mechanical Properties

DMA measurements were performed for degraded samples to determine the changes in the mechanical properties. Since the non-etched films were very torn and porous after 10 days of degradation, measurements were not feasible. Therefore, the mechanical properties were measured only for the 5 day degradation period. On the other hand, in the case of the hydrophilic etched films, the compactness of the film was less damaged by degradation, so the mechanical measurements were normally made after 5 and 10 days of degradation.

Both etched and non-etched PLLA films have the same initial Young's modulus measured at 23 °C (2.4 GPa), comparable to values observed in the literature for PLA polymer [26], which confirms that alkali etching was performed only on the surface without compromising the inner parts (Figure 6a). After the enzymatic degradation, the values are significantly lowered for the non-etched samples, even after 5 days of degradation,

where the modulus is lowered by 92% (190 MPa), while it is only 1% for the etched samples (Figure 6a). As the degradation induces swelling and increased porosity in the bulk of the hydrophobic films (where degradation occurs), they cause a drop in the mechanical properties (observed through a drop in the storage modulus). These changes are not so pronounced in the case of the etched films before and after degradation since the dominant degradation events are taking place at the surface. In the case of the etched, hydrophilic PLLA films, Young's modulus drop occurs very slowly, only 16% for a degradation time of 10 days, clearly showing the lack of dominant bulk-erosion effects observed in non-etched films.
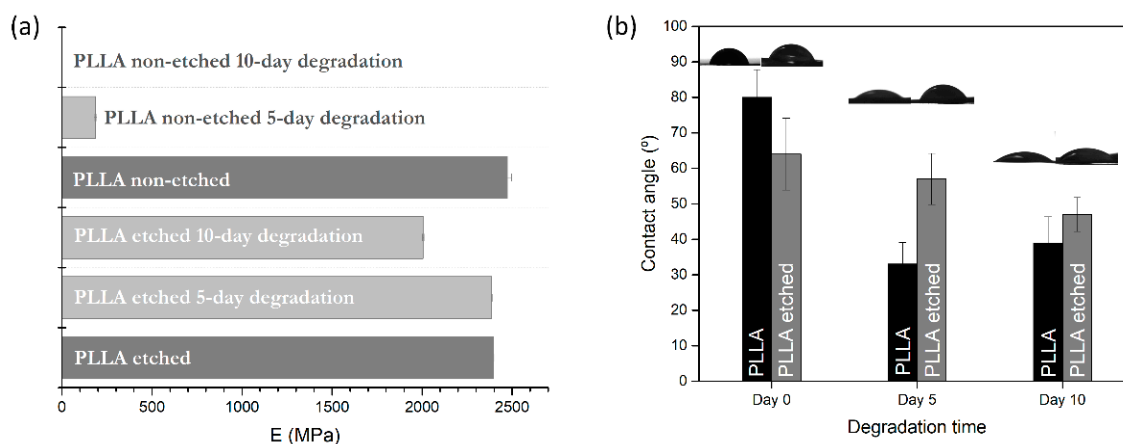
Figure 6. (**a**) changes in Young's modulus (at 23 °C) and (**b**) changes in wetting angle for water drop on polymer, for non-etched and etched samples after 0, 5 and 10 days of degradation.

3.4. Wetting-Angle Changes

Contact-angle measurements were made for pristine films and the films obtained after degradation. Interesting changes were observed for the non-etched films, where the wetting angle decreases more drastically than for the etched sample after 5 and 10 days of degradation (Figure 6b).

Alkali etching improved the hydrophilicity of the polymer surface by 25%, which resulted in more carboxylic end groups on the surface. During the degradation, a small lowering (−20%) of the initial wetting angle was observed in the etched films. The change could be associated with the change in the roughness observed in the SEM images for the etched films. On the other hand, due to the significant increase in the roughness and porosity of the non-etched hydrophobic films after degradation, their wetting angles decreased by 50%.

3.5. Piezoelectric Properties

Piezoelectric properties are highly dependent on the polymeric structure, the orientation of the polymer chains and the degree of crystallinity. Therefore, it was expected that the previously observed changes would affect them. According to those changes, proteinase-K-induced changes in the piezoelectric properties were lowered to 68% of the initial values for the non-etched sample and 50% for the etched polymer films (Table 1) after 5 days of aging. Further measurements after 10 days of degradation could not be performed since the degradation, with a mechanically unstable and porous film over the whole surface, did not allow measurements using the applied method.

3.6. Morphological Properties

After 10 days of degradation for the non-etched hydrophobic films, the main changes were observed in the cross-sections that reveal their inner (bulk) parts (Figure 7(a2,a3,b2,b3)). The initially dense and smooth layered structure in the cross-section of the starting films

before degradation (Figure 7(a2,a3)) turned into a porous, sphere-like structure obtained after the degradation progressed (Figure 7(b2,b3)). Both surfaces of the films, before and after the degradation (Figure 7(a1,b1)), are generally smooth, with a bubble structure observed on top of the degraded samples (Figure 7(b1)), indicating degradation events inside the film's bulk, such as progressive and intensive water swelling.
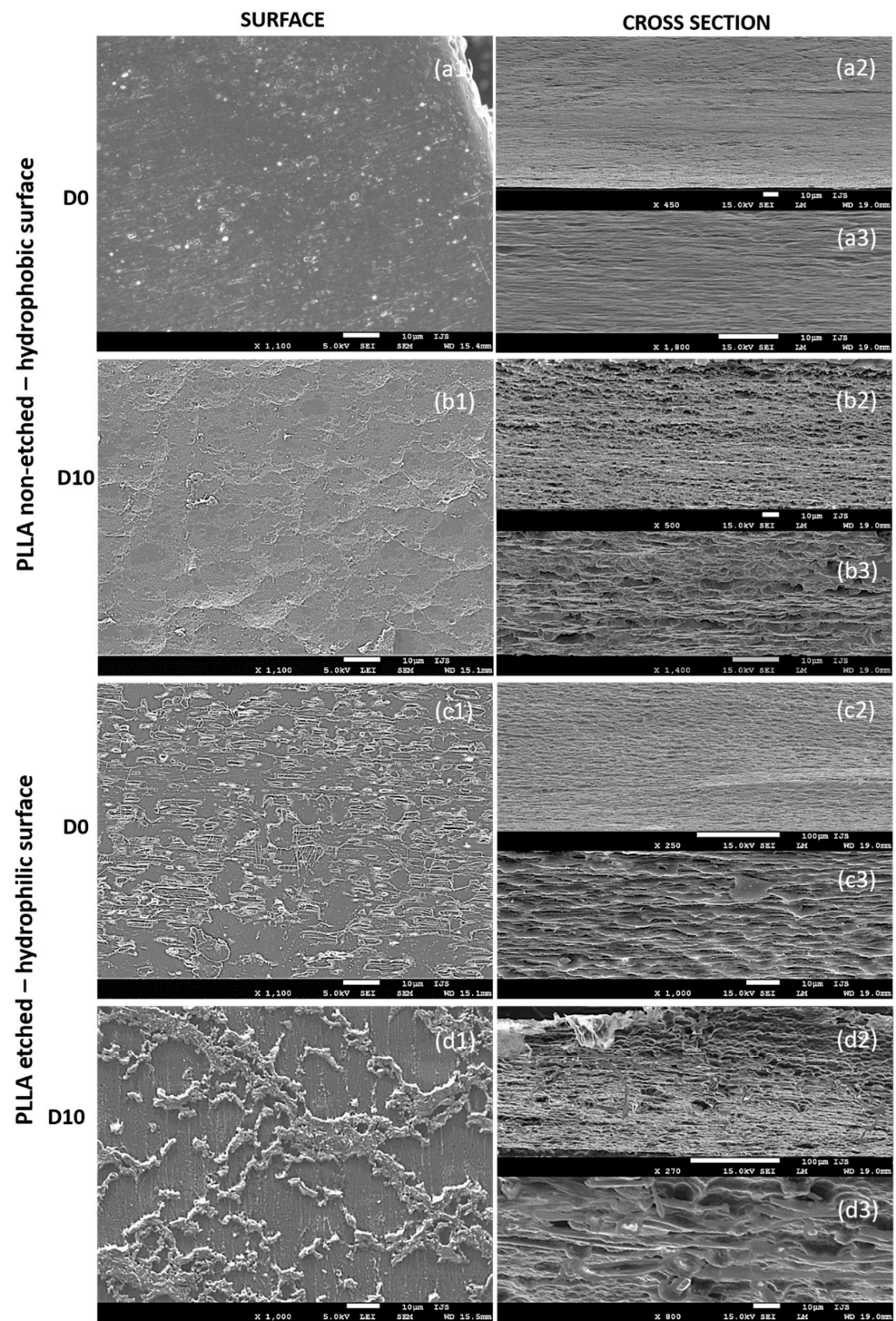
Figure 7. SEM images showing surfaces (1) and cross-sections (2, 3) of PLLA films with non-etched hydrophobic (**a1–a3,b1–b3**) and etched hydrophilic (**c1–c3,d1–d3**) surfaces before (D0) and after (D10) degradation with proteinase K.

Due to alkali etching, the hydrophilic films initially had a rougher surface with visible amorphous islands having short-edged chains (Figure 7(c1)). Such a structure is ideal for enzymatic degradation. As the degradation progressed, the roughness of the surface changed (Figure 7(d1)), indicating surface-erosion events. The inner parts of the films (observed in cross-sections, Figure 7(c2,c3,d2,d3)) did not change significantly and showed signs of delayed water swelling.

4. Discussion

Piezoelectric PLLA films were designed to optimize their applicability in electrostimulation, such as promoting mammalian cell growth. For the occurrence of effective electrical stimulation, film-cell contact is crucial, and surface properties are important. Therefore, to improve its properties for intended medical use and to ensure better cell affinity, hydrophilicity was improved by 25% using alkali etching of the polymer film, which resulted in more carboxylic end groups on the surface. The idea of the current study was to investigate the structural, mechanical, electric and surface properties of piezoelectric PLLA, with a hydrophobic and hydrophilic surface, in the presence of proteinase K as a degrading enzyme and a model of in vitro inflammation. This study is important since it can predict or explain further interactions of the surface-modified PLLA with living surroundings.

PLLA is a hydrophobic polymer that in general degrades through a hydrolysis reaction that occurs inside the bulk, driven by the swelling mechanism [14]. In the case of enzyme-driven degradation, when the enzyme proteinase K is present, surface erosion is reported as the main mechanism of degradation [15,16]. The reason is associated with the limited intake of the enzyme inside a polymer film.

According to our results, the structural, morphological, mechanical and piezoelectric changes obtained during the proteinase-K-induced degradation in PLLA films, two different degradation mechanisms are revealed due to the surface modification. In the case of the non-etched hydrophobic films, changes were mainly taking place in the polymer bulk. Due to the smooth surface and the strained, oriented chains observed with the electron microscope, enzyme–polymer contact is less probable; therefore, surface degradation is limited, and water diffusion inside the bulk is faster. Swelling occurs, which allows the enzymes to enter inside, meaning that bulk erosion is preferential. Enzymes cleave the tied and free amorphous parts from inside the bulk since proteinase K cannot degrade crystalline parts, resulting in increased overall crystallinity. Similar observations were made by Rangari et al., who also reported a slight increase in the crystallinity for oriented PLLA films due to the enzyme-catalyzed degradation of amorphous parts [16] but at the surface. The observed changes in crystallinity for the non-etched samples can be explained by the degradation of the free end and tie amorphous parts and possible accumulation of the cleaved crystalline parts trapped inside the film (increased crystallinity for day 10), as the degradation occurs there. However, the loss of crystallinity observed for day 5 can be associated with chain relaxation during the swelling mechanism. In both cases, for etched and non-etched films, the orientation of the polymeric films is lowered, which is expected since the swelling of the polymer in a water solution is inevitable after some time, making reorganization and mobility of the chains possible.

When observing etched films, their surface is hydrophilic with more amorphous end chains directly exposed to the outer water surroundings with the proteinase K enzyme. During the degradation, the film changes predominantly at the surface-with-surface erosion as the preferred mechanism. Therefore, only small changes are observed for bulk crystallinity and mechanical properties. Since the dense film is under amorphous clusters (as observed 7d1), the accumulation of crystalline residues is also less likely, and the loss of crystallinity is observed only on the surface.

F. Iñiguez-Franco et al. showed that increasing the hydrophilic properties of PLLA film using a chain extender, which incorporates more hydrophilic chain ends to form a branched structure, can result in hydrogen bonding between them and prevent the diffusion of water molecules inside the polymer matrix to start the bulk process [27]. This explanation can

be used to understand the changes we observed with the hydrophilic samples. In our case, the diffusion of water inside the films was slower, and enzyme travel inside the bulk was prevented. Therefore, enzymatically catalyzed hydrolysis occurs only at the surface (FTIR-921 cm^{-1} peak drop), inducing surface erosion. The loss of crystallinity for the etched sample occurred due to cleavage of the tie amorphous chain parts at the surface, releasing crystalline residues into the solution. Similar phenomena during degradation were previously explained by H. Tsuji et al. [15] on surface-eroded hydrophobic PLLA films. We also observed lowering the temperature of cold crystallization for the etched sample compared to non-etched films, which implies better orientation of the amorphous chains since the presence of oriented amorphous chains induces crystallization at a lower temperature. An interesting partial change from the α' to the α structural phase was observed only for etched films and further indicates the difference in degradation induced by surface wettability. This phenomenon could be explained by the recrystallization of polymer chains due to annealing in the medium at 37 °C since water can act as a plasticizer for PLLA. This was explained by H. Tsuji et al. as a possible event during degradation [15]. Since most of the degradation events in our etched films occur on the surface, this should also be the case for recrystallization.

The use of PLLA films for piezo-stimulation depends on their mechanical properties. PLLA is a semi-crystalline polymer; therefore, its properties depend largely on its crystalline phase. However, the balance of crystalline and amorphous regions is desirable since it enables the elasticity required for deformation in ultrasound that generates the voltage needed for promoting cell growth during stimulation. A difference in mechanical properties also implied a bulk-degradation event for non-etched and a surface-erosion event for the etched films during degradation. A huge loss of modulus, observed for non-etched films, could be connected to the swelling of the polymer film, as observed before [28], which could indicate that the degradation process was greater than that, which was evident with the weight loss. Due to swelling, there is an internal cleavage of the molecular bonds inside the film, which affects their compactness and strength, promoting degradation without the evident weight loss [1]. A similar situation was not detected in the etched films as their degradation took place at the surface.

Piezoelectricity in PLLA is a consequence of oriented and crystalline polymer chains inside the film [11]. A simple method like uniaxial drawing was used for preparing piezoelectric PLLA films. The drawing process above T_g aligns the chain molecules in the same direction in the entire film, inducing structural changes, such as crystallinity, due to the strain-induced crystallization [18]. Compared to the literature (10pC/N) [29], smaller values for d_{14} were obtained for our films (4–4.6 pC/N); however, negligible changes were observed after the surface modification with etching to improve the hydrophilic properties of the film (results presented in a previous article [18]). It is very important that the films retained their piezoelectric properties despite all the structural and mechanical changes during degradation. Changes in the piezoelectric properties after the degradation were observed for the first time. The preservation of piezoelectric properties is a consequence of changes in crystallinity and orientation. Bulk changes are not so pronounced in hydrophilic films, where most of the degradation events and the consequent modifications are taking place at the surface. However, the detected recrystallization, loss of surface crystallinity and relaxing orientation cause the loss of half of the initial piezoelectricity (50.4%, Table 1). In hydrophobic films, most of the degradation events and the following changes occur inside the films. Although there is a decrease in the orientation and an observed increase in the porosity, a smaller drop in the piezoelectric properties (68.8% of initial value remain, Table 1) was observed, possibly due to an increase in the crystallinity and the reorientation of fibers after drying the sample. However, our estimation is for the non-etched film to have a lower piezoelectric value during the degradation since the polymer is swollen from the start, compared to the etched sample, where the swelling was not observed after 5 days of degradation.

A combination of a hydrophilic surface with gradual changes to the films during degradation that maintains their piezoelectric properties is the optimal design for polymeric films initially developed for interactions with mammalian cells. With such a design, we could expect that the high affinity of cells for hydrophilic surfaces will enable close contact between the cells and films and provide the effective electrostimulation required for applying piezo-films in regeneration processes, particularly in wound healing.

5. Conclusions

Proteinase K can induce both bulk and surface degradation in PLLA films. The surface properties of the polymer films play a significant role in their degradation. As shown in the present study, their change is a powerful tool and makes it possible to change where the degradation occurs and defines the dominant degradation mechanism. If films are hydrophilic, enzyme-driven degradation occurs at the film surface, where they degrade the accumulated amorphous areas. On the other hand, if they are hydrophobic, water uptake and polymer swelling make it possible to transfer the enzyme to the bulk where the degradation occurs. When the surface chemistry is well balanced by degradation progress, so the mechanical, structural and piezoelectric changes to the films occur gradually, and very effective interactions with the cells are expected. The observed correlations are very important for further predictions during the interactions of piezoelectric PLLA films with living surroundings, particularly during electro-stimulated regeneration and wound healing, where the gradual loss of piezoelectric properties is useful for following the tissue regeneration.

References

1. De Silva, D.; Kaduri, M.; Poley, M.; Adir, O.; Krinsky, N.; Shainsky-Roitman, J.; Schroeder, A. Biocompatibility, biodegradation and excretion of polylactic acid (PLA) in medical implants and theranostic systems. *Chem. Eng. J.* **2018**, *340*, 9–14. [CrossRef] [PubMed]
2. Pappu, K.L.; Pickering, V.K. Thakur, Manufacturing and characterization of sustainable hybrid composites using sisal and hemp fibres as reinforcement of poly (lactic acid) via injection moulding. *Ind. Crop. Prod.* **2019**, *137*, 260–269. [CrossRef]
3. Rajabi, A.H.; Jaffe, M.; Arinzeh, T.L. Piezoelectric materials for tissue regeneration: A review. *Acta Biomater.* **2015**, *24*, 12–23. [CrossRef] [PubMed]
4. Jelonek, K.; Li, S.; Kaczmarczyk, B.; Marcinkowski, A.; Orchel, A.; Musial-Kulik, M.; Kasperczyk, J. Multidrug PLA-PEG filomicelles for concurrent delivery of anticancer drugs—The influence of drug-drug and drug-polymer interactions on drug loading and release properties. *Int. J. Pharm.* **2016**, *510*, 365–374. [CrossRef]
5. Mushtaq, F.; Torlakcik, H.; Vallmajo-martin, Q.; Can, E.; Zhang, J.; Röhrig, C.; Shen, Y.; Yu, Y.; Chen, X.; Müller, R.; et al. Magnetoelectric 3D scaffolds for enhanced bone cell proliferation. *Appl. Mater. Today* **2019**, *16*, 290–300. [CrossRef]

6. Gomaa, S.F.; Madkour, T.M.; Moghannem, S.; El-sherbiny, I.M. New polylactic acid/cellulose acetate-based antimicrobial interactive single dose nanofibrous wound dressing mats. *Int. J. Biol. Macromol.* **2017**, *105*, 1148–1160. [CrossRef]
7. Barroca, N.; Marote, A.; Vieira, S.I.; Almeida, A.; Fernandes, M.H.V.; Vilarinho, P.M.; Odete, A.B. Electrically polarized PLLA nanofibers as neural tissue engineering scaffolds with improved neuritogenesis. *Colloids Surf. B Biointerfaces* **2018**, *167*, 93–103. [CrossRef]
8. Shin, D.; Hong, S.W.; Hwang, Y.-H. Recent Advances in Organic Piezoelectric Biomaterials for Energy and Biomedical Applications. *Nanomaterials* **2020**, *10*, 123. [CrossRef]
9. Ates, B.; Koytepe, S.; Ulu, A.; Gurses, C.; Thakur, V.K. Chemistry, Structures, and Advanced Applications of Nanocomposites from Biorenewable Resources. *Chem. Rev.* **2020**, *120*, 9304–9362. [CrossRef]
10. Tajitsu, Y. Basic study of controlling piezoelectric motion of chiral polymeric fiber. *Ferroelectrics* **2009**, *389*, 83–94. [CrossRef]
11. Lovell, C.S.; Fitz-Gerald, J.M.; Park, C. Decoupling the effects of crystallinity and orientation on the shear piezoelectricity of polylactic acid. *J. Polym. Sci. Part B Polym. Phys.* **2011**, *49*, 1555–1562. [CrossRef]
12. Minary-Jolandan, M.; Yu, M. Nanoscale characterization of isolated individual type I collagen fibrils: Polarization and piezoelectricity. *Nanotechnology* **2009**, *20*, 085706. [CrossRef] [PubMed]
13. Murillo, G.; Blanquer, A.; Vargas-estevez, C.; Barrios, L.; Ibáñez, E.; Nogués, C.; Esteve, J. Electromechanical Nanogenerator-Cell Interaction Modulates Cell Activity. *Bioelectronics* **2017**, *29*. [CrossRef]
14. von Burkersroda, F.; Schedl, L.; Gopferich, A. Why degradable polymers undergo surface erosion or bulk erosion. *Biomaterials* **2002**, *23*, 4221–4231. [CrossRef]
15. Tsuji, H.; Ogiwara, M.; Saha, S.K.; Sakaki, T. Enzymatic, alkaline, and autocatalytic degradation of poly (L-lactic acid): Effects of biaxial orientation. *Biomacromolecules* **2006**, *7*, 380–387. [CrossRef]
16. Rangari, D.; Vasanthan, N. Study of Strain-Induced Crystallization and Enzymatic Degradation of Drawn Poly (l-lactic acid) (PLLA) Films. *Macromolecules* **2012**, *45*, 7397–7403. [CrossRef]
17. Casalini, T.; Rossi, F.; Castrovinci, A.; Perale, G. A Perspective on Polylactic Acid-Based Polymers Use for Nanoparticles Synthesis and Applications. *Front. Bioeng. Biotechnol.* **2019**, *7*, 1–16. [CrossRef]
18. Udovc, L.; Spreitzer, M.; Vukomanovic, M. Towards hydrophilic piezoelectric poly-L-lactide films: Optimal processing, post-heat treatment and alkaline etching. *Polym. J.* **2020**, *52*, 299–311. [CrossRef]
19. Vogel, C.; Wessel, E.; Siesler, H.W. FT-IR Spectroscopic Imaging of Anisotropic Poly (3-hydroxybutyrate)/Poly (lactic acid) Blends with Polarized Radiation. *Macromolecules* **2008**, *41*, 2975–2977. [CrossRef]
20. Nobeshima, T.; Sakai, H.; Ishii, Y.; Uemura, S.; Yoshida, M. Polarized FT-IR Study of Uniaxially Aligned Electrospun Poly (DL-Lactic Acid) Fiber Films. *J. Photopolym. Sci. Technol.* **2016**, *29*, 353–356. [CrossRef]
21. Farah, S.; Anderson, D.G.; Langer, R. Physical and mechanical properties of PLA, and their functions in widespread applications—A comprehensive review. *Adv. Drug Deliv. Rev.* **2016**, *107*, 367–392. [CrossRef] [PubMed]
22. Yanagida, H.; Okada, M.; Masuda, M.; Ueki, M.; Narama, I.; Kitao, S.; Koyama, Y.; Furuzono, T.; Takakuda, K. Cell adhesion and tissue response to hydroxyapatite nanocrystal-coated poly (L-lactic acid) fabric. *JBIOSC* **2009**, *108*, 235–243. [CrossRef] [PubMed]
23. Bernard, F.; Gimeno, L.; Viala, B.; Gusarov, B.; Cugat, O. Direct Piezoelectric Coefficient Measurements of PVDF and PLLA under Controlled Strain and Stress. *Proceedings* **2017**, *1*, 335. [CrossRef]
24. Webb, K.; Hlady, V.; Tresco, P.A. Relative importance of surface wettability and charged functional groups on NIH 3T3 fibroblast attachment, spreading, and cytoskeletal organization. *J. Biomed. Mater. Res.* **2009**, *41*, 422–430. [CrossRef]
25. Chen, X.; Kalish, J.; Hsu, S.L. Structure Evolution of a α'-Phase Poly (lactic acid). *J. Polym. Sci. Part B Polym. Phys.* **2011**, *49*, 1446–1454. [CrossRef]
26. Leluk, K.; Frackowiak, S.; Ludwiczak, J.; Rydzkowski, T.; Thakur, V.K. The Impact of Filler Geometry on Polylactic Acid-Based Sustainable Polymer Composites. *Molecules* **2021**, *26*, 149. [CrossRef]
27. Iñiguez-franco, F.; Auras, R.; Ahmed, J.; Selke, S.; Rubino, M.; Dolan, K.; Soto-valdez, H. Control of hydrolytic degradation of Poly(lactic acid) by incorporation of chain extender: From bulk to surface erosion. *Polym. Test.* **2018**, *67*, 190–196. [CrossRef]
28. Subramani, R.; Izquierdo-alvarez, A.; Bhattacharya, P.; Meerts, M. The Influence of Swelling on Elastic Properties of Polyacrylamide Hydrogels. *Front. Mater.* **2020**, *7*, 1–13. [CrossRef]
29. Fukada, E. New Piezoelectric Polymers. *Jpn. J. Appl. Phys.* **1998**, *37*, 2775–2780. [CrossRef]